

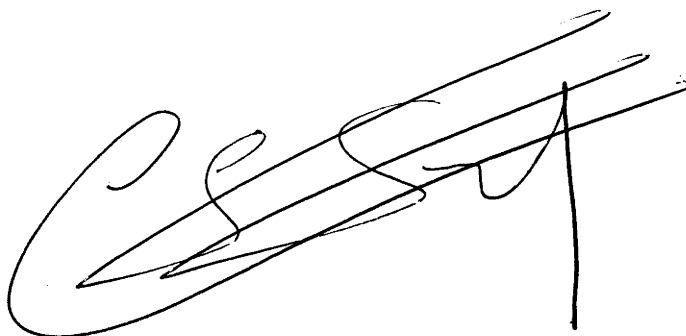
# A STUDY OF HIGH BRIGHTNESS PLASMA ION SOURCES

A thesis submitted for the degree  
of Doctor of Philosophy of  
the Australian National University

Orson Sutherland

February 2, 2005

This thesis contains no material which has been accepted for the award of any other degree or diploma in any university. To the best of the author's knowledge and belief, it contains no material previously published or written by another person, except where due reference is made in the text.

A handwritten signature in black ink, appearing to read 'Orson Sutherland', written in a cursive style with a large initial 'O' and a vertical line at the end.

Orson Sutherland  
February 2, 2005



# Acknowledgements

The human understanding is no dry light, but receives an infusion from the will and affections; whence proceed sciences which may be called “sciences as one would.” For what a man had rather were true he more readily believes. Therefore he rejects difficult things from impatience of research; sober things, because they narrow hope; the deeper things of nature, from superstition; the light of experience, from arrogance and pride, lest his mind should seem to be occupied with things mean and transitory; things not commonly believed, out of deference to the opinion of the vulgar. Numberless, in short, are the ways, and sometimes imperceptible, in which the affections color and infect the understanding.

*Francis Bacon*

I think it is quite fitting, as I write this small note of appreciation, that I should be listening to J. S. Bach’s Toccatas and Fugues: for me, they express imperious majesty, sobriety, rational thought but always an ever curious, arabesque creativity and stirring beauty. It is also a reminder of a time when all human enterprises of high art were passed on through the generations from the master to the apprentice. In my mind there is no doubt, for all the help that I have received from others, that my deepest thanks, with respect to this work, go to my supervisor R. W. Boswell. I flatter myself to believe that Rod may have made of me a Baconian. Upon reflection, this is all I ever really wanted from my time as a doctoral student. That I have produced this book and perhaps contributed something to science is a happy consequence of a much more meaningful and rich experience and one that has marked me both as a scientist and as a person. The clarity of thought that I have developed in my training under Rod’s supervision is probably now my most prized possession.

The logic now in use serves rather to fix and give stability to the errors which have their foundation in commonly received notions than to help the search after truth. So it does more harm than good.

*Francis Bacon*

I also reserve many thanks for Christine Charles who has been most generous with her time in helping troubleshoot experiments and discussing results. I have always been awe-struck by her organisation and I am constantly reminded not to forget the small things.

I would also like to thank Montague Giles for developing the ion cyclotron theory and Andrian Ankiewicz for his invaluable help with the Langmuir-Blodgett generalisations.

No tribute page in our laboratory would be integral or indeed just without the mention of Peter Alexander, our tireless technician. I think that we are blessed to have someone so skilled, so humble and so committed to the projects in the lab as our Peter. It will be a sad day when the time comes to fill his shoes but surely it is fair that even the most committed man may dream of an enjoyable retirement. I often wonder if among the "youth of today" we might find someone that will remotely resemble what we have in Peter... There is something about him of the old world decency and commitment that I don't detect among my peers.

In the same league is Dennis Gibson, from the Electronics Unit, who was instrumental in keeping WOMBAT's RF system running. He was always available for advice both in the design and construction of electronic circuits but also in trouble shooting probes. The younger fellas in the EU are going to have some trouble following in Den's foot steps when he finally decides he has had enough... nonetheless they are a great bunch of guys and I would like to acknowledge, in particular, David Anderson and Michael Birdsall.

Julie Dalco has gotten me out of many tight spots with her no nonsense approach to computer administration. But on this front, I owe a particular debt to Fenton Glass, who despite of (or is that because of ?) his major geekiness, has also become a good friend, one that I can always trust for a good laugh.

I'd like to thank all of my friends at the lab: Albert Meige, for reminding me to have fun; Devin Ramdutt, for reminding me to enjoy nature; Ane Aanesland, for reminding me that Latex syntax is important (and a special note of thanks for proof reading my thesis); Vicki Au, for reminding me that dressing well gets noticed; Peter Linardakis, for reminding me to stay in touch with old friends; Fernando Gesto, for reminding me to appreciate simple human emotions; Nicholas Plihon, for reminding me not to take things quite so seriously; Michael Irzyk, for reminding me to appreciate the finer things in life; John Keller, for reminding me to back myself; Helen Smith, for opening up the wonderful world of the Antarctic to me; Clive Michael, for reminding me to windsurf; Tristram Alexander, for reminding me just to take it easy; Hyun Jin Yoon, for reminding me to be patient.

I also owe thanks to my family who have supported and encouraged me. When I first started this undertaking it was generally assumed that I would be the first

PhD in the family. Subsequent research has uncovered that this is not at all the case with a number of relatives (especially females) having Doctorate's and in particular a noted historian. Nonetheless it is vindication for my parents and I hope an inspiration to my siblings. This thesis is certainly something that they should feel a part of.

For me, writing this thesis was an singularly egocentric experience and I recognise the hypocrisy of my comportment, simultaneously expecting understanding from those around me whilst putting on a steely air of control. I had no right to brood. However, I will say in my defence and all those that have and will suffer this fate, those who haven't written a PhD thesis (or who didn't find it a challenging experience) just can't understand; so perhaps we ought not expect them to. Nonetheless, my Jane tried her darndest and stuck by me when she had every reason to leave.

As a final note and a bit of a tribute to Jane's wit, I would like to share with you a Haiku that she wrote as a bit of a joke after reading the introduction to this thesis. She wrote several, but the one that I have presented here I personally think is brilliant. Those of you who know Jane will recognise her sense of humour. I hope that you will join me in agreeing that this is a most excellent work. It is pertinent, ingeniously humorous but simultaneously melancholic. A post-modern deconstruction of industrial man, forlorn amongst his machines.

Ions of argon  
In a vacuum, through a mask  
March single file

*SwX*



# Abstract

This thesis is concerned with the extraction of high brightness focused ion beams (FIBs) from radio frequency (RF) plasmas and presents both an experimental study of heating mechanisms in a helicon plasma ion source and a new perspective on the theory of extraction optics. Four prototype ion sources suitable for use with FEI Co. FIB columns are presented.

A new approach for the design of extraction optics which considers a more rigorous treatment of the plasma sheath, plasma/beam interface and beam distributions is presented. The theory treats the beam as an angular section of a complete classical diode as first considered by Langmuir and Blodgett but generalises the solutions to take into account the non-zero potential present in the plasma sheath. It also takes into account the convexity of the beam distribution solutions and proposes that to minimise emittance growth the electric field at the exit of the extractor must be zero requiring at least two stages comprising a total of 5 electrodes. The precise electrode geometries are then found by solving Laplace's equation in two dimensions in the charge free region.

This theory makes the assumption of cold plasma ions which can lead to a significant departure from experimental reality. It is also known from thermodynamic considerations that the inherent brightness of an ion source is limited by the temperature of the extracted species. Therefore some effort was made in this work to develop a high density, cold ion, plasma source. In particular, a source capable of densities up to  $10^{14} \text{ cm}^{-3}$  at the point of extraction is presented and both parallel and perpendicular heating mechanisms are investigated in some detail. In addition, it is shown how the parallel ion energy distribution can be controlled by "balancing" the RF antenna to minimise chromatic aberrations. Further improvements in ion energy spread are shown to be gained by the use of smaller extraction apertures and magnetic confinement of the source plasma. Finally, with the optimal mix of these parameters, the measured ion energy spread is shown to be within the 3 eV resolution of the measurement technique (as measured by Noel Smith of FEI Co.), and may, with subsequent measurements due for late 2004/ early 2005 be shown to be significantly less than this.

The use of a magnetic field can considerably increase the plasma density but also allows for a multitude of wave types to propagate in the plasma that can couple energy to ions. To investigate this, measurements were made in the large volume helicon reactor WOMBAT operating with similar parameters to the ion source. Un-

der certain operating conditions ion cyclotron and ion acoustic wave activity was observed. Generation of the ion cyclotron wave is explained by a filamentation type instability (developed by Montague Giles) whilst the ion acoustic waves are believed to be driven by strong pressure gradients at the edge of the plasma column. It is shown that these waves exist for a relatively narrow range of parameters and can be avoided whilst still obtaining high densities.

Collisional mechanisms can also play a role in increasing ion temperature and were studied using particle-in-cell simulations by Helen Smith. It was found that for pressures less than 10 mTorr (where the ion source was operated), the contribution of collisions to ion energy was less than 0.1 eV. Significant increases in ion energy were only observed for pressures in excess of 20 mTorr, but were always less than 1 eV.

# Contents

<b>Acknowledgements</b>	<b>v</b>
<b>Summary of Thesis</b>	<b>ix</b>
<b>1 Introduction</b>	<b>1</b>
1.1 Nano-Fabrication . . . . .	1
1.2 FIBs . . . . .	6
1.3 Quantifying FIBs . . . . .	8
1.3.1 Aberrations . . . . .	9
Spherical Aberrations . . . . .	10
Chromatic Aberrations . . . . .	11
1.3.2 Emittance . . . . .	13
1.3.3 Beam Brightness . . . . .	14
Thermodynamic Limit . . . . .	15
1.4 Ion Source Technology . . . . .	17
1.4.1 Liquid Metal Ion Sources . . . . .	17
1.4.2 Duoplasmatrons . . . . .	20
1.4.3 Multicusp Plasma Sources . . . . .	22
1.4.4 Penning Sources . . . . .	24
1.4.5 RF Ion Sources . . . . .	25
1.5 Towards a High Brightness Plasma FIB . . . . .	27
1.5.1 Electrode Design . . . . .	31
Empirical Studies On High Intensity Beams . . . . .	32
The Pierce Gun . . . . .	32
Extending Pierce's Method . . . . .	35
Generalising Langmuir-Blodgett's Laws . . . . .	35
Blocking Electrodes . . . . .	37
Engineering the Electric Field . . . . .	38
1.5.2 High Density Cold Ion Plasma Source Design . . . . .	39
Helicon Plasmas . . . . .	39
Parallel Ion Energy Distribution . . . . .	41
Perpendicular Ion Energy Distribution . . . . .	43

<b>2</b>	<b>Electrode Design for the Extraction of Very High Brightness Ion Beams</b>	<b>45</b>
2.1	Statement of Problem . . . . .	46
2.2	Beam Distributions . . . . .	49
2.2.1	The Basic Solution to Poisson's Equation . . . . .	51
	Spherical Symmetry . . . . .	51
	Cylindrical Symmetry . . . . .	53
2.2.2	Non-Zero Initial Gradient . . . . .	53
	Spherical Symmetry . . . . .	55
	Cylindrical Symmetry . . . . .	56
	The Plasma Sheath . . . . .	56
	Sheath Potential at the Meniscus . . . . .	57
	Potential Gradient at the Meniscus . . . . .	59
	Discussion . . . . .	59
2.2.3	Solving Poisson's Law Backwards . . . . .	61
2.2.4	Presence of Electrons . . . . .	62
2.2.5	Non-Zero Initial Velocity . . . . .	63
2.3	Laplace's Equation . . . . .	64
2.3.1	Strip Beam . . . . .	65
2.3.2	Wedge Beam . . . . .	66
2.3.3	Cylindrical Beam . . . . .	67
2.3.4	Conical Beam . . . . .	69
2.4	Method for the Design of Electrodes . . . . .	70
2.4.1	Introduction . . . . .	70
2.4.2	The Extraction Gaps . . . . .	70
	Stage 1 . . . . .	70
	Stage 2 . . . . .	71
	The problem . . . . .	71
2.4.3	Blocking Electrodes . . . . .	72
2.4.4	Beam Neutralisation . . . . .	72
2.5	An Example: A Diverging Wedge Beam . . . . .	73
	Extraction Gap Stage 1 . . . . .	73
	Extraction Gap Stage 2 . . . . .	74
	Blocking Gap Stage 1 . . . . .	76
	Blocking Gap Stage 2 . . . . .	76
2.5.1	Closing remarks . . . . .	76
	Simulations . . . . .	78
	Plasma Density Range . . . . .	82
<b>3</b>	<b>Diagnostics</b>	<b>85</b>
3.1	Langmuir Probes . . . . .	85
3.2	Ion Source Diagnostics . . . . .	90
3.2.1	Density Measurements . . . . .	90
3.2.2	Beam Measurements . . . . .	92
	Extracted Current . . . . .	92



	Angular Divergence . . . . .	92
	Beam Distributions . . . . .	93
	Simulation . . . . .	96
3.3	WOMBAT Diagnostics . . . . .	99
3.3.1	Langmuir Probes in WOMBAT . . . . .	99
	The Study of Basic Plasma Parameters . . . . .	100
	Spectral Measurements . . . . .	101
3.3.2	Microwave Interferometer . . . . .	101
3.3.3	Retarding Field Energy Analyser . . . . .	102
<b>4</b>	<b>Development of a Compact High Density Plasma Ion Source</b>	<b>107</b>
4.1	The Experimental Concept . . . . .	109
	Vacuum System and Gas Feed . . . . .	109
	RF System . . . . .	112
	Extraction System . . . . .	113
	Diagnostic Chamber . . . . .	115
4.2	The Prototypes . . . . .	115
4.2.1	Prototype 1 . . . . .	115
	General Description . . . . .	115
	Ray-Tracing Simulations . . . . .	117
	Plasma Density Measurements . . . . .	118
	The Effect of Power, Magnetic Field and Antenna Position . . . . .	119
4.2.2	Prototype 2 . . . . .	122
4.2.3	Prototype 3 . . . . .	124
4.2.4	Summary of Prototypes . . . . .	126
<b>5</b>	<b>Perpendicular Ion Heating</b>	<b>127</b>
5.1	A Brief Introduction to Electromagnetic Waves in Cold Plasmas . . . . .	127
	Circular Polarisation and Resonance . . . . .	130
5.2	Wave Particle Interactions . . . . .	132
5.2.1	Ion Landau Damping . . . . .	132
5.2.2	Doppler Shifted Ion Cyclotron Resonance . . . . .	135
5.2.3	The Experimental Set-Up . . . . .	136
	Vacuum Vessel . . . . .	137
	Magnetic Field System . . . . .	138
	RF System . . . . .	140
	Ar II Plasma Column . . . . .	143
5.2.4	Ion Cyclotron Waves . . . . .	146
	Experimental Evidence of Ion Cyclotron Waves . . . . .	146
	Four Wave Resonant Interaction . . . . .	150
	Ion Cyclotron Parameter Space . . . . .	154
	Discussion . . . . .	155
5.2.5	Ion Acoustic Waves . . . . .	158
	Experimental Observation . . . . .	159
	Localisation . . . . .	161

Pressure . . . . .	163
Power . . . . .	163
Magnetic Field . . . . .	163
A Comparative Study . . . . .	165
<b>6 Parallel Ion Heating</b>	<b>167</b>
6.1 Charge Exchange and Elastic Scattering Collisions . . . . .	167
6.2 Parallel Ion Energy Spread . . . . .	176
6.2.1 Measuring Ion Energy Spread with a Mass Spectrometer . . . . .	176
Energy Callibration of the Mass Spectrometer . . . . .	176
Initial Energy Spread Results . . . . .	179
6.2.2 Reducing Capacitive Coupling . . . . .	181
Balanced Antenna . . . . .	181
200 $\mu\text{m}$ Extraction Aperture . . . . .	182
Half Split Faraday Shield . . . . .	184
<b>7 Concluding Remarks</b>	<b>187</b>
7.1 Extraction Optics . . . . .	189
7.1.1 Generalising the Langmuir-Blodgett Laws . . . . .	189
7.1.2 Low Aberration Electrodes . . . . .	191
7.1.3 Electrons and the Extraction Optic . . . . .	192
7.2 Plasma Source . . . . .	193
7.3 Ion Energy Spread . . . . .	194
7.4 Other implications of the work . . . . .	196

# Introduction

## 1.1 Nano-Fabrication

It is an observable trend that the number of personal computers, mobile telephones and other portable micro-processor based technologies is increasing as the functionality of such devices improves and their accompanying cost falls. The processing speed of micro-processors as well as the memory capacity of mass storage devices is largely a function of the number of transistors that can be printed per integrated circuit (IC) chip. According to the Semiconductor Industry Association [86] road map, transistor density has been growing exponentially from  $10^7$   $\text{cm}^{-2}$  in 1995 to  $1.1 \cdot 10^8$   $\text{cm}^{-2}$  in 2004 and will continue to do so in coming years attaining  $5.6 \cdot 10^8$   $\text{cm}^{-2}$  by 2010. Interestingly, the cost per chip has remained stable at around USD 100 per unit and is expected to remain so. Although the transistor density is increasing exponentially, the aggressive pace of contemporary systems designs means that there is also a need to increase chip size from  $250 \text{ mm}^2$  in 1995 to  $620 \text{ mm}^2$  in 2010 to keep up with demands for increased processing power and memory capacity at lower cost. This has two immediate implications: increased lithographic exposure resolution (90 nm line width in 2004) to furnish the need for increased transistor density, but also with the growing wafer size, increased exposure fields. Increasing the wafer size is essential to maintaining throughput and hence keeping the per chip cost down but it also puts new and as yet largely unanswered challenges

to chip manufacturers as they are driven to increase wafer size from 300 mm in 2004 to 400 mm by 2007.

In the manufacture of ICs the enabling technology has been optical lithography which, due to enhancements in stepper and lens technology, has seen it push the need for next generation lithography (NGL) machines further and further into the future. The technology that experts claimed was defunct a decade ago is still supplying the micro-electronics industry with ICs. However, despite it being generally accepted that optical lithography is the technology of choice down to 200 nm, the current push by chip manufacturers from 90 nm down to 65 nm feature size and beyond will require a sustained technology evolution for which many of the technical challenges have no contemporary solutions. According to Gross [45] in 1997, photolithographers seemed unanimous in thinking that the only and final step forward for optical lithography then seemed to be to push the wavelength barrier one last time into the deep UV (193 nm) to reach 150 nm resolution. Today, many IC fabs have already implemented 193 nm DUVL machines for resolutions of 120 nm and below. However, the optical adjustments required to work in DUV make this form of optical lithography progressively more expensive. As a simple example, exposures at wavelengths much below 157 nm have to be done under vacuum which drives up the cost of the machine and slows throughput. Moreover, much below 126 nm, the physical properties of all optical components including the mask and even air act as reflectors opening the way for the new field of extreme UV lithography (EUVL) and a complete redesign of much of the existing lithography technology. Typically EUV research centres around wavelengths close to 13 nm and has been shown to successfully produce features of less than 70 nm in dimension [89]. However, for use in mass production there is quite some way to go for this technology which still must overcome a number of technical issues with mask fabrication ([53], [92], [82], [49]) as well as resist technology ([118],[52]).

At even more extreme wavelengths is the field known as proximity x-ray lithography (PXL). Again, this technology has proven its ability to mill features as small as 35 nm but is hampered by current mask technology which has trouble keeping pace, especially in the context of mass production [1]. The trade-off in increased resolution is closer proximity between the mask and the wafer which can be as little as  $5\mu m$ . At this distance mask rigidity, thermal expansion effects and particulate contamination become real issues for mask maintenance and lifetime. Moreover, PXL is a unity demagnification system which puts tight constraints on the contribution of mask alignment, beam uniformity and mask feature resolution to the edge to edge overlay budget [45]. Mizusawa *et al.* [93] have presented a production ready exposure tool for PXL but as yet there have not been any real solutions to mask and resist technology. In addition, the 1 nm range x-rays are generally produced using a synchrotron so that the manufacturing floor would need to be significantly altered to accommodate between 10 and 20 exposure stations for every x-ray source [89].

Many of the technical difficulties associated with diffraction through the mask are avoided by using electrons or ions as the exposure medium. At 100 keV, electrons have a DeBroglie wave length of  $4 \cdot 10^{-3}$  nm whilst Hydrogen ions have a wave length on the order of  $5 \cdot 10^{-5}$  nm. For ions, diffraction limits are well below 5 nm even with a numerical aperture (NA) as small as  $10^{-5}$  rad. That electrons and ions are able to expose resist has been known for over 2 decades [89, 39], but they are particularly effective since they provide very even dose and minimal scatter in the resist [106]. Standard resists can be used without modification and in the case of ions the exposure can be extremely rapid, about 0.5 s, with exposure fields up to  $100 \text{ mm}^2$  [46]. On the other hand, electron beam exposure requires much greater currents than ion beam exposure and so is limited by space charge effects in the focusing optics resulting in longer exposure times. In addition electron sources can

only expose fields on the order of  $1 \text{ mm}^2$  due to a relatively large NA of  $10^{-3}$  rad. Nonetheless, electron projection lithography (EPL) has been in use for some time in areas where throughput is less critical such as in the fabrication of lithography masks [89, 120, 39].

Up until recently, ion projection lithography (IPL) was shaping up to be a leading contender as an NGL device for high throughput fabrication of ICs. Most of the underlying technology such as stepper, mask and resist already existed and did not need to be modified. Loeschner *et al.* [84] had shown that IPL could effectively write 100 nm lines over an area of  $12.5 \times 12.5 \text{ mm}^2$  whilst Kaesmaier *et al.* [65] had demonstrated, using analytical modelling, that these sub-fields could be “stitched” together to expose an entire wafer using a new stitching technology. The main constraint in these systems was the ion source which typically produced ions with anywhere between a 2 and 15 eV energy spread. In early experiments Duoplasmatrons were used as a source of ions but these systems had an energy spread of between 10 and 15 eV [46]. This severely limited the resolution of the IPL device as a whole through blurring produced by chromatic aberrations in the optical column. In more recent tests a multicusp ion source developed at Lawrence Berkeley National Laboratory (LBNL) by Leung *et al.* was employed [80]. With a magnetic filter integrated into the system ion energy spreads as low as 1 - 2 eV were measured [80, 76]. It was this source that formed the basis of the most recent results at the Fraunhofer Institut in Berlin [77] and IMS in Vienna [65]. However, the short life-time of the multicusp source especially for the filament device will no doubt exclude it as a viable option for production ready machines [76]. Some work is still being undertaken on an immersed, porcelain coated RF antenna design which has shown more promise for life-time considerations but which has a higher ion energy spread [77]. Though it is claimed that the filament driven multicusp source has an ion energy spread of as little as 1 eV and is suitable for high brightness applications,

Scipioni *et al.* reported that this same source produced only an intermediate brightness of  $1650 \text{ A.cm}^{-2}.\text{sr}^{-1}$ . In any case, modelling performed at Siemens-Munich AG [46] has shown that assuming a virtual source size of  $10 \mu\text{m}$  and an energy spread of 1 eV (unfortunately an equivalent brightness was not quoted) that 100 nm features with a pattern density of 50% can be printed over a  $22 \times 22 \text{ mm}^2$  area at a rate greater than 75 wafers per minute (WPM). Kaesmaier *et al.* ([65]) subsequently showed results from modelling that produced sub-50 nm resolution using stitching techniques.

It would seem, therefore, that a leading candidate for NGL is ion projection lithography, as it has a demonstrated production capability and has clear and apparently solvable technical challenges for evolution over several generations of shrinkage. One of the main challenges facing IPL is treated in some detail in this thesis, notably the design of a high current density plasma ion source with low ion energy spread. However, perhaps the greatest obstacle to IPL, according to the 2003 SEMATCH road map, will be the incumbent technology of optical lithography which it appears, despite a number of technical challenges in all aspects of the production process, will be able to continue on to 2009 and to feature sizes as small as 15 nm, by driving into the EUV. It is still unclear whether the process cost will become prohibitively expensive as more sophisticated methods are required to allow for ever decreasing wavelength, but SEMATECH ([107]) is confident that the next decade will almost certainly be dominated by optical lithography. According to Loeschner, IPL is now almost defunct but novel multi-beam lithography techniques are being developed as an alternative to optical processes should SEMATECH's prediction be wrong (L. Scipioni, FEI Co., private communication). These multi-beam systems still have at their core variable species, high current density, low ion energy spread plasma sources so that the research presented in this thesis is of some importance to their endeavours.

## 1.2 FIBs

Another area of direct relevance to the semiconductor industry both in terms of the mass production lithography process and the related field of metrology is the production of focused ion beams or FIBs. These become relevant in both mask modification and correction, surface analysis, failure analysis, defect characterisation and process control functions.

Masks are commonly made using a plasma etch technique but often have imperfections, typically an unintended opaque spot in a clear field or vice-versa, which left untreated would result in errors in the IC. With the increasing size of dies the probability of imperfections augments as the inverse of the area:

$$Y = \frac{1}{1 + D.A} \quad (1.1)$$

where  $D$  is the density of random defects and  $A$  is the die area on wafer. For multi-level structures to obtain a final yield of as little as 50%, the yield of any single layer must be greater than 88% [39]. Imperfections are virtually unavoidable and can have cost and performance ramifications further along the production process if not treated early. FIBs are ideal for mask correction because they can be used to sputter away and deposit material at the location of the imperfection with a nano-metric scale beam of ions. It is tempting to ask whether FIBs could be used to direct-write the entire mask as they can reproduce features on the order of 10 nm, but alas the process is far too slow for high-throughput production and hence is not cost effective.

Because FIBs have such high precision milling capabilities, they are also finding use in tunnelling electron microscopy (TEM) sample preparation [61], [60], [96], [108], [128], [129]. TEM is a method for analysing the chemical composition and thickness of layers on the surface of a material. A thin slice, usually between 50 - 100 nm thick, 10  $\mu\text{m}$  long and 5  $\mu\text{m}$  deep is cut from the surface under examination using a



FIB and then eutectically soldered to leads for transfer to a TEM workstation where its various stratifications can be analysed, much like geological analysis of soil. A similar technique can be used to troubleshoot components in ICs. Wang *et al.* have developed a electron holoscopy technique for the 2 dimensional characterisation of p-n junctions [126]. The technique is based on TEM where a wedge shape sample is cut from the circuit using a FIB in a similar fashion to standard TEM sample preparation techniques.

Another important measurement in the design, development and fabrication of ICs is the size of critical features such as linewidth, wall profiles and edge-to-edge overlay. Undercut profiles and pattern shift effects originating from the etching and mask imaging processes respectively can impact on design tolerances and mask performance during the lithography process and must be controlled precisely. The slope of the interface between the clear and opaque regions of a mask, usually called the mask walls, define the undercut profile and is directly related to the transmittance of the mask. Pattern shift on the other hand, which is defined as:

$$\Delta S = W_c - W_m \quad (1.2)$$

where  $W_c$  is the pattern width of the copy and  $W_m$  is the pattern width of the master mask, determine the final size of the reproduced circuit layer. Obviously, in contemporary multi-layer designs edge-to-edge overlay is critical and hence control of the pattern shift is fundamental.

Design tolerances, development cycle time, manufacturing yield and circuit performance depend on the accurate measurement and control of these type of feature sizes. In order to achieve adequate circuit performance, these features must be controlled to with-in 10% of the total feature size. For 100 nm linewidths this means an error of 10 nm or less, but ideally should far less than this. Wagner *et al.* pointed out that “gross differences in measurement accuracy” can exist between different metrology tools and even between applications of the same tool [125]. In

their paper they demonstrated that FIBs can be used for accurate critical resist dimension metrology. Orloff *et al.* go further and point out that FIB imaging (or scanning ion microscopy, SIM) is often preferred over higher resolution scanning electron microscopy (SEM) techniques because there are different contrast mechanisms available with either secondary electron or secondary ion detection [95].

### 1.3 Quantifying FIBs

Focused ion beams constitute any group of largely mono-energetic ions with directed velocity, extracted, focused and accelerated from a source of ions, typically by a series of electrodes that create a shaped static electric field. The term largely mono-energetic is used because in all practical systems, the source of ions is not cold and has some distribution of temperatures which is imparted on the individual beamlets both parallel and perpendicularly to the directed motion. Typically, the ion temperature in the source is several orders of magnitude less than the energy gained from the extraction field and so in many applications can be ignored entirely. However, for the work presented in this thesis ion temperature is a significant parameter.

Beam geometry plays an important role in the development of the theory in this work. In a macroscopic sense FIBs are differentiated by the geometry of the aperture through which they are extracted. FIBs extracted through rectangular apertures are referred to as strip or wedge beams whereas beams extracted through circular apertures are denominated cylindrical or conical depending on whether they are convergent, divergent or parallel.

A beam is defined as laminar if after passing through an ideal convergent lens all the trajectories converge on one point. A consequence of this definition is that both convergent and divergent groups of mono-energetic ions can be laminar. The

extent to which a beam is laminar is strongly tied in with the quality of the beam which will be discussed in the following sections on aberrations and beam brightness.

### 1.3.1 Aberrations

The same type of lens errors which are found in light optics are found in charged particle beam lenses. These errors are referred to as aberrations and occur when rays leaving a point on the object converge on different image points.

In charged particle optics, aberrations arise from various sources. If it is assumed that the charged particles emanating from the source are strictly mono-energetic and that the extraction optics are perfectly aligned, then any deviation from the ideal image is referred to as geometric aberration. These are also commonly called third-order aberrations as they arise when the beam diverges from the paraxial ray approximation. In the basic linear optical theory the half angle of arrival (or departure) of a ray,  $\theta$ , is assumed to be smaller than  $\pi/20$  so that the error in the approximation  $\sin(\theta) \approx \theta$  is less than 0.1%. In many ion sources (especially plasma sources), relatively large extraction apertures are required hence  $\sin(\theta)$  can no longer be closely approximated by the first order term in the series expansion:

$$\sin(\theta) \approx \theta - \frac{\theta^3}{3!} + \frac{\theta^5}{5!} - \dots \quad (1.3)$$

In light optics  $\theta$  often has large values as many of the aberrations can quite easily be compensated for, however, in ion optics, due to complications in the physics,  $\theta$  can not be increased too much. Nonetheless, even if an angle as extreme as  $\theta = \pi/4$  is considered, the error incurred by making the third-order approximation is only 0.5%. Therefore, deviations from the paraxial approximation can be analytically investigated with quite a good degree of accuracy by considering only the first two terms of the series expansion 1.3. This is called third-order theory and will not be presented here in any great detail except to mention the various aberration types

that it describes: distortion, anisotropic distortion, curvature of field, astigmatism, anisotropic astigmatism, coma, anisotropic coma and aperture defect (otherwise known as spherical aberration) [35]. It is this last aberration type that will be of most interest to this work as it has the most dramatic impact on the final spot size in FIB systems. The other aberration types pertain more to the high-fidelity reproduction of patterns as in projection lithography applications.

If it is now no longer assumed that the electrode apertures are perfectly concentric and parallel, then a deviation in the Gaussian image plane occurs, even in the paraxial limit, due to aberrations of asymmetry.

To further complicate the picture, any axial energy spread in the plasma ions results in a non-uniform extraction velocity leading to an error phenomenon called chromatic aberration. Axial energy spread can result both from inherent ion heating mechanisms in the plasma and fluctuations in the plasma potential. Thermal effects can be caused by collisions and wave-particle interactions as discussed in chapters 5 and 6 whilst oscillations in the plasma potential result from capacitive coupling at the RF driving frequency between the antenna and the plasma (again c.f. chapter 6). Oscillations in the plasma potential effect the velocity of the particles as they transit the sheath and when this transit time is comparable to the ion plasma period can result in a distribution of exit velocities (c.f. *Parallel Ion Energy Distribution*).

### Spherical Aberrations

A lens exhibits spherical aberration when its focal lengths for paraxial and marginal rays are different. Typically for a convergent lens, the latter are more strongly focused so that there exists a continuity of focal points along the axis up to the paraxial focal point as shown figure 1.1. A screen placed normal to the axis at the paraxial focal point would show a bright central spot surrounded by a series of concentric circles coalescing into each other. Of all the third-order aberrations,

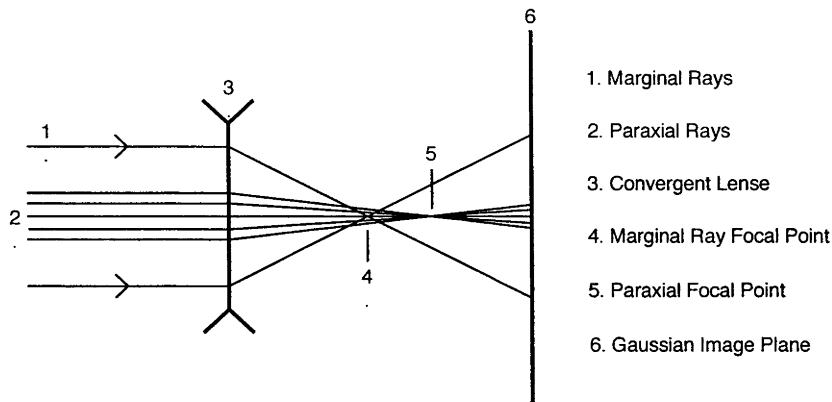


Figure 1.1: Ray tracing of convergent lens effected by spherical aberrations.

spherical aberrations are the only type to exist for a point on the axis. It is largely due to the aperture size and is the same for all points on the object. The aberration figure in the Gaussian plane is a circle of radius proportional to the cube of the aperture radius [35].

The theory presented in Chapter 2 is aimed in large part at minimising spherical aberrations in the extractor where for zero ion temperature all particle trajectories are laminar.

### Chromatic Aberrations

Just as in light optics, where different wavelengths of light “see” different indexes of refraction, ions of different velocities can be thought of as changing the refractive index of the medium through which they travel, resulting in differential optical behaviour. Thus slower ions (longer wavelengths) are focused more sharply than faster ions (shorter wavelengths) and the image becomes marred. All real ion sources have some ion thermal energy distribution producing variations in focus that reduce beam brightness. The energy spread in a plasma might be a small fraction of the total extraction energy, but in high brightness applications it may still be enough

to preclude the focusing of nano-metric beam spots. If only chromatic aberrations are considered the minimum spot size,  $d$ , for a beam with an axial energy spread of  $\Delta E$  is:

$$d = C\alpha\left(\frac{\Delta E}{E}\right) \quad (1.4)$$

where  $C$  is the chromatic aberration coefficient of the focusing lens,  $\alpha$  is the half-angle of the beam arriving at the final focal spot and  $E$  is the total beam energy. This equation shows that the final spot size is proportional to the ratio of the axial energy spread and the total energy of the beam. It also demonstrates that the length of the focusing column is a practical constraint on the system as the final spot size is directly proportional to the half angle of arrival.

Unlike light optics where chromatic aberrations can be almost completely removed, ion optics can not be designed to do so. The defect is with the object, or ion source, and even a well designed lens will be subject to chromatic aberrations if the ion source is not sufficiently cold or oscillations in plasma potential can not be reduced below a suitable threshold.

This effect is particularly important in low energy FIB applications where the beam energy can be on the order of 100 eV. In this case, an axial energy spread of 10 eV, not uncommon for both Duoplasmatron and liquid metal ion source (LMIS) systems represents an unacceptably large portion of the total beam energy and results in strong chromatic blur. The relatively low inherent thermal ion energy spread of RF ion sources ( $< 1$  eV) makes this technology particularly suitable for low energy FIB applications.

At higher extraction energies ( $> 10$  keV), chromatic blur is minimised and often becomes less important than both geometric and spherical aberrations.

### 1.3.2 Emittance

Any force that acts over a length scale large compared with the inter-particle spacing preserves the phase-space volume of the beam distribution [56]. In one dimension, phase-space is a plot of velocity versus position in a given direction for all the particles in a beam in a given plane. Non-linear field components and fringing fields (third-order aberrations) of focusing lenses can stretch and distort the distribution. To designate the quality of a beam a figure of merit is commonly employed based on the effective volume occupied by the distribution, called emittance. This quantity describes the transverse motion of particles in a beam and in one dimension of phase-space is defined as the area of the smallest ellipse to circumscribe all the points in the distribution:

$$\epsilon_x = \frac{1}{\pi} \int \int dx.dv_x \quad (1.5)$$

The beams most common in FIB applications have cylindrical symmetry and so  $\epsilon_x = \epsilon_y$ .

As a simple example, figure 6.4 shows the phase-space representation of an ideal diverging wedge beam and the same beam distorted by spherical and chromatic aberrations. Transversally, an ideal wedge beam has infinite extent in the y direction and hence all space charge forces cancel so that its emittance is determined solely by the distribution of points in the  $x - v_x$  plane. These points lie about a line and the closer the beam particles are to this line the lower the emittance and hence the more laminar the beam is.

The angle of the line is directly related to the angle of divergence of the envelope where a positive slope represents a divergent beam and a negative slope a convergent beam. Distributions lying around the horizontal axis are parallel beams.

Non-linear forces distort the distribution. A distribution that emanates from the plasma with particles lying close to a line in phase-space will be distorted into an 'S'-shaped distribution by spherical aberrations in the extractor whilst space charge

and particle thermal effects will lead to a broadening of the distribution away from the line. Thus, as no source of ions is ever ideally cold the phase-space distribution can never be a perfect line.

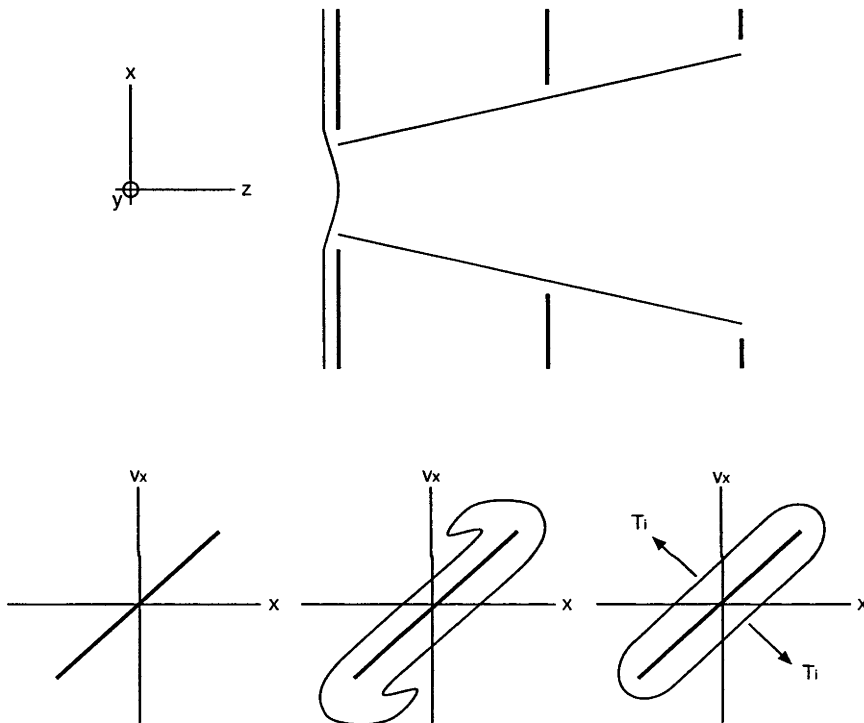


Figure 1.2: Trace and phase space diagrams. Top: trace space diagram of diverging wedge beam through 3 electrodes. Bottom: phase space diagrams. Bottom left: ideal wedge beam. Bottom center: wedge beam with spherical aberrations. Bottom right: phase space broadening due to ion temperature.

### 1.3.3 Beam Brightness

Another useful figure of merit is beam brightness providing information not only on the beam quality but also its intensity. Brightness is directly related to the quantity of current that can be delivered to a focused spot and thus is the primary



metric for FIB applications. In its basic form it is defined as the current density per unit solid angle in the axial direction:

$$B = \int \frac{dI}{d\Omega.dS} \quad (1.6)$$

As FIBs commonly have Cartesian symmetry in the transverse direction, brightness can be expressed as a function of emittance:

$$B = \frac{I}{\pi^2 \epsilon_x \epsilon_y} \quad (1.7)$$

If  $\epsilon_x = \epsilon_y$  then the beam is isotropic and brightness can be expressed in terms of the average emittance  $\epsilon$ :

$$B = \frac{I}{\pi^2 \epsilon^2} \quad (1.8)$$

Importantly, this expression shows that brightness is directly proportional to beam current and emittance, noting that if emittance is conserved, then beam brightness is constant throughout the extraction and transport regions.

### Thermodynamic Limit

Even with close to ideal lenses there is an ultimate limit to the brightness that can be achieved with any given source which is dependent on ion temperature. The thermodynamic limitations to brightness derive from the fact that the particles emitted from the plasma have a Maxwellian energy distribution with a most probable energy of  $kT_i$  and an average energy of  $2kT_i$ , where  $k$  is the Boltzman constant and  $T_i$  is the mean ion energy in eV. If it is assumed for simplicity that the ions are accelerated in a parallel, uniform electrostatic field which adds only to parallel energy, leaving the perpendicular energy unchanged, and that the parallel velocity is much greater than the perpendicular velocity, then the half-angle of divergence is given by:

$$\theta \simeq \frac{v_{\perp}}{v_{\parallel}} \quad (1.9)$$

The electric field accelerates the ions through a potential drop,  $V$ , so that the parallel velocity can be written:

$$v_{\parallel} = \sqrt{2\frac{e}{M_i}V} \quad (1.10)$$

where  $e$  is the elementary charge and  $M_i$  is the ion mass. A similar reasoning can be applied to obtain the perpendicular ion velocity by equating the most probable energy to the kinetic energy:

$$v_{\perp} = \sqrt{\frac{2kT_i}{M_i}} \quad (1.11)$$

Since brightness is defined in terms of solid angle,  $\theta$  must be converted to steradians. This is done by noting that solid angle is the area defined by the surface of intersection between a cone of half-angle  $\theta$  and the unit sphere, where the cone apex is concentric with the centre of the sphere. A simple calculation yields the solid angle,  $\alpha$ , as a function of half-angle,  $\theta$ :

$$\alpha = 2\pi(1 - \cos(\theta)) \quad (1.12)$$

Since  $\theta \ll 1$  equation 1.12 can be rewritten in terms of a Taylor series:

$$\alpha \simeq 2\pi\left(1 - \left(1 - \frac{\theta^2}{2!}\right)\right) = \pi\theta^2 \quad (1.13)$$

and the beam can be considered quasi-parallel. If, in addition, it is assumed that the current density is uniform across the whole area of the extraction aperture, then the current density can be assumed to be isotropic so that the brightness can be rewritten:

$$B \simeq \frac{j}{\alpha} = \frac{j}{\pi\theta^2} = \frac{j e V}{\pi T_i} \quad (1.14)$$

where  $j$  is the current density and  $T_i$  is in eV. This equation was first derived by Langmuir in 1937 and demonstrates that brightness increases as a function of current density and extraction potential and decreases as the inverse of ion temperature. In the thermodynamic limit, the denser and colder the plasma the brighter it is as an ion source. It must be stressed, however, that this is an upper limit to brightness, in

reality lens aberrations play an important role in decreasing the effectiveness of FIB systems. Ultimately, however, even without considering spherical and chromatic aberrations it shows that FIB extraction is limited by irreversible emittance growth caused by inherent thermal mechanisms in the plasma. In addition, it demonstrates that the brightness of a plasma ion source is limited by practical constraints on the maximum plasma density (effecting extractable current) and extraction voltage that can be attained in real systems.

As an example, if ions are extracted at 10 kV from a plasma of density  $10^{19} \text{ m}^{-3}$  with an ion temperature of 0.1 eV, then the thermodynamic limit on beam brightness is approximately  $10^4 \text{ A.cm}^{-2}.\text{sr}^{-1}$ . This is relatively low when compared with LMIS systems which can provide beams with brightness two orders of magnitude higher than this. It doesn't seem unreasonable, however, to design a source with a density of  $10^{14} \text{ cm}^{-3}$  and an extraction potential of 100 kV which would provide comparable results. It should also be mentioned that there are numerous applications for inert gas ion sources of intermediate brightness on the order of  $10^3 - 10^4 \text{ A.cm}^{-2}.\text{sr}^{-1}$  which are well with-in the limits of the technology presented in chapter 4 (N. Smith, FEI Co., private communication) . A typical application is surface analysis where a relatively high current beam on the order of 100 nA with a micron resolution is applied to a surface at intermediate (10 keV) and low (100 eV) energies.

Equation 1.14 underpins the primary emphasis of this work which is the development of low spherical aberration electrodes supplied by a cold ion plasma source.

## 1.4 Ion Source Technology

### 1.4.1 Liquid Metal Ion Sources

The semiconductor industry has had sub-micron milling capability for some decades in the form of LMIS. It is still today the brightest known source of metal

ions<sup>†</sup> [116] and is used on almost all FIB systems employed in the semiconductor industry [88]. Focused spots with diameters under 10 nm and current densities between 1 and 10 A.cm<sup>-2</sup> are now routinely obtained [95, 2]. The LMIS FIB system has found extensive use across a wide range of applications in the manufacture of ICs including design modification, failure analysis, defect characterisation and process control functions. However, they are unsuitable for low energy FIB applications because they have a minimum axial energy spread of 5 eV [94].

The device works by field emitting ions from the tip of a sharp needle (usually tungsten) over which a liquid metal such as gallium has spread by capillary effect. The liquid metal is stored in a reservoir and, being usually solid at room temperature, is heated to ease the flow over the tip. In the case of gallium, the metal is liquid at room temperature in vacuum and the heating process is mostly to evaporate surface contaminants and gallium oxide. An electrode in the form of an annulus, concentric with the emitter and some distance below it applies an electric field to the tip where it is concentrated and exerts a stress on the metal surface lifting it into a cone of some 10 nm in diameter at its apex. The cone, referred to as the Taylor cone [119], does not sharpen without limit because the field emission of ions at the tip is a sufficient restoring force to maintain stability. Two explanations for this have been proposed. The first reasons that the sharper the tip becomes the greater the field that is concentrated there and as a result the higher the emission current. As the emission current increases space charge builds up in front of the tip, blocking the effect of the applied field. The alternative analysis provides that the hydrodynamic properties of the liquid metal flow down the needle limits the available current and as a result determines the I-V characteristics of the source. It has been found that the radius of the needle tip and its surface roughness play an important role in the current emission characteristic of the source, making the latter hypothesis more

---

<sup>†</sup>Though gaseous field emission ion sources (GFIS) have been shown to produce greater brightness than LMIS, they have severe engineering limitations with respect to stability and life-time.

generally accepted but by no means proven beyond reasonable doubt [88].

The metals used for LMIS can be of any composition as long as they wet the

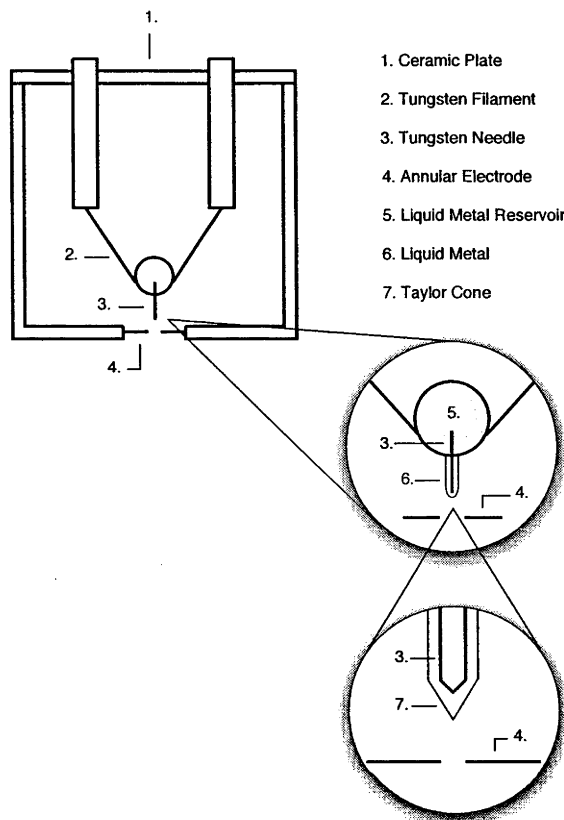


Figure 1.3: Conceptual diagram of a LMIS system with close-ups of the field emission tip.

needle, do not corrode the surface and have a low vapour pressure in the molten state. Typically, metals with melting temperatures below  $300^{\circ}\text{C}$  are employed. Alloy sources include: Au/Be/Si or Pd/As/B and require a mass separator stage to isolate a single ion species for implantation into the sample. It is also preferable in FIB optics to have only a single ion species, and indeed a single ion isotope, so that stray B fields (for example from a magnetic objective lens of a coincident electron column) do not mass separate the beam and hence smear it at the sample. With nanometric spot sizes, even  $^{69}\text{Ga}$  and  $^{71}\text{Ga}$  can take slightly different

trajectories through the final focusing lenses if a nearby magnetic lens or ion pump magnet is not well enough screened. By far the most commonly used metal in LMIS, especially in industry, is gallium (and in particular isotopically pure  $^{69}\text{Ga}$ ) since it is almost liquid at room temperature and yields long life-time sources. A typical LMIS construction is shown in figure 1.3. A small tungsten needle is spot welded to the apex of a tungsten filament formed into a loop and anchored in a heat proof insulating base. The liquid metal is then held between the loop in the filament and the shank of the needle by surface tension. For metals that are not liquid at room temperature a current is passed through the filament to heat the metal.

#### 1.4.2 Duoplasmatrons

The Duoplasmatron has found wide use in a number of research and industrial settings [56]. For example, in the early work on IPL it was the preferred source of ions for resist exposure [112, 89, 46, 65, 84]. It was also commonly used in secondary ion mass spectrometry (SIMS) [23]. Typically, the Duoplasmatron is used for the production of relatively high current beams with peak currents up to several hundred milli-Amperes [111]. However, for high brightness applications, it is limited by a relatively large axial energy spread of between 10 - 20 eV [111, 123]. Perhaps the Duoplasmatron's biggest disadvantage is its short life time. Though, Coath and Long [23] claim "long lifetime" to be among its chief advantages, Noel Smith's (of FEI Co.) experience with Duoplasmatrons working at both Cambridge Mass Spectrometry (in the U.K.) and Physical Electronics (in the U.S.A.) was that the best possible life time for these devices was 1000 hours for the cold cathode model, though 250-500 hours was more typical. Life times well in excess of 1000 hours are required for efficient use "in-line" in a semiconductor fabrication process. Even in less production critical environments, longer life-times are desirable. Often the cathodes need refurbishing after just a few days operation. Hot cathode models

perform even less well than this. The quoted lifetime for the Peabody Scientific hot cathode Duoplasmatron was 150 hours. Hot cathodes are typically used for inert gases and cold cathodes for oxygen.

The main cause of the Duoplasmatron's short lifetime is sputtering of the cathode by high energy ions of between 300-400 eV. The sputtering itself reduces the useful lifetime of the device by eroding the cathode, but the most common cause of premature failure is sputter deposited material blocking the source aperture and even in some cases the intermediate electrode aperture (N. Smith, FEI Co., private communication).

Intermediate brightness' have been reported for Duoplasmatron supplied ion beam systems. The device used by Stengl *et al.* [112] in 1986 on their early IPL studies at IMS produced a current density of  $10 \mu\text{A}\cdot\text{cm}^{-2}$  on the target and, it was claimed, a

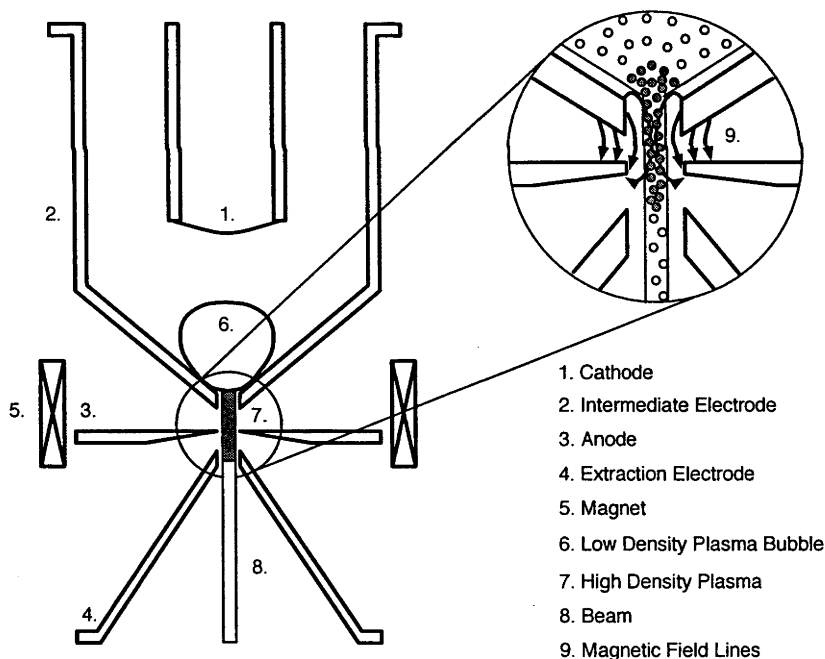


Figure 1.4: Conceptual diagram of a Duoplasmatron.

brightness in excess of  $10^4 \text{ A}\cdot\text{cm}^{-2}\cdot\text{sr}^{-1}$  with  $\text{H}^-$  ions. Coath and Long [23] 10 years

later quoted a brightness of  $1.7 \cdot 10^3 \text{ A.cm}^{-2}.\text{sr}^{-1}$  with  $\text{Ar}^+$  ions at an extraction energy of 15 keV from a Duoplasmatron optimised for FIB applications. However, the large axial energy spread of these systems makes them unsuitable for low energy ( $< 1 \text{ keV}$ ) and nanometric FIB applications.

The original Duoplasmatron was designed by von Ardenne [124] in 1963 and a generic device is illustrated in figure 1.4. It works by thermionic emission of electrons from a tungsten filament ionising neutral gas atoms as they are accelerated towards an anode. An intermediate electrode, called the focusing electrode stands between the cathode and the anode (usually floating) and funnels the neutral gas towards a narrow aperture where a plasma bubble is produced. This relatively diffuse plasma supplies electrons to a second, much denser, magnetically confined plasma produced between the intermediate and anode electrodes. This dual low density/ high density plasma system is the origin of the device's name.

Humphries [56] states that extraction voltages in the range of 50 kV can be applied for moderate current applications, though Stengl *et al.* [112] applied between 60 and 90 kV in their work.

### 1.4.3 Multicusp Plasma Sources

The multicusp ion source, sometimes called the magnetic bucket source, is characterised by an array of permanent magnets that covers the walls of the plasma chamber as shown in figure 1.5. In filament type multicusp sources, thermionic electrons are emitted from a hot filament, typically constructed from tungsten, and accelerated towards the chamber walls which act as an anode. Multipole fields of a few kilo-Gauss localised near the wall reflect a large portion of the primary incident electrons, increasing their residence time in the source and thus promoting ionisation and higher densities. The magnetic fields do not effect the emittance of the extracted beam as the axis of the source, where most of the ionisation occurs,



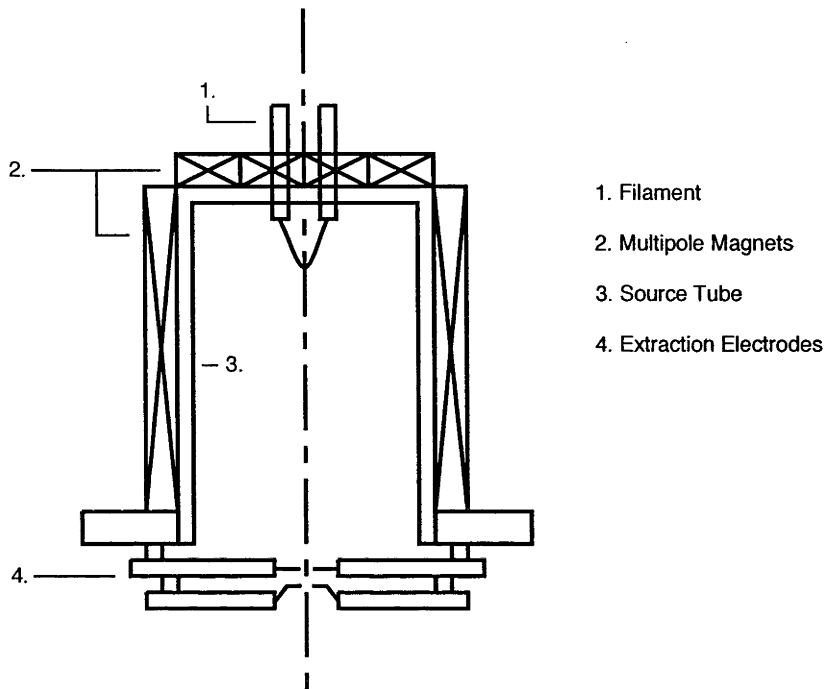


Figure 1.5: Conceptual diagram of a Multicusp source

is field-free [56].

It has been shown by workers at LBNL that the addition of a magnetic filter just upstream from the extraction aperture can significantly reduce the ion energy spread of the beam ions improving brightness [80, 76, 81, 77]. Measurements using a 2 grid retarding field energy analyser have shown energy distributions as low as 1 eV can be achieved with the filter in place [77] as compared to 6 eV without it. Unfortunately, the filament, working by evaporation, has a limited operational life-time of around 100 h and is thus unsuitable for use in IC production tools.

This problem can be solved by replacing the filament, anode/cathode structure with an RF system. Because of the array of magnets on the chamber wall, the antenna can not be wound around the outside of the source and instead must be immersed in the plasma. Sputtering of the RF antenna can be reduced by using a porcelain

coating but stochastic heating of ions in the antenna near field can not and leads to increased ion energy spreads [76]. Lee *et al.* [76] reported that the LBNL magnetic filter was not effective in reducing the ion energy spread in the extracted beam and claimed RF induction fields were penetrating into the post filter region causing ion energy spreads as high as 8 eV. More recently Leung [81] presented results showing that the use of a magnetic filter reduced the ion energy spread from 10 eV to as low as 2 eV.

#### 1.4.4 Penning Sources

The Penning Ionisation Gauge (PIG) source has not commonly been used in IC fabrication or research programs, though some recent interest has been shown in this technology at the University of Maryland [48, 47]. At first glance it appears to be an attractive option for IPL and FIB applications because it has a relatively

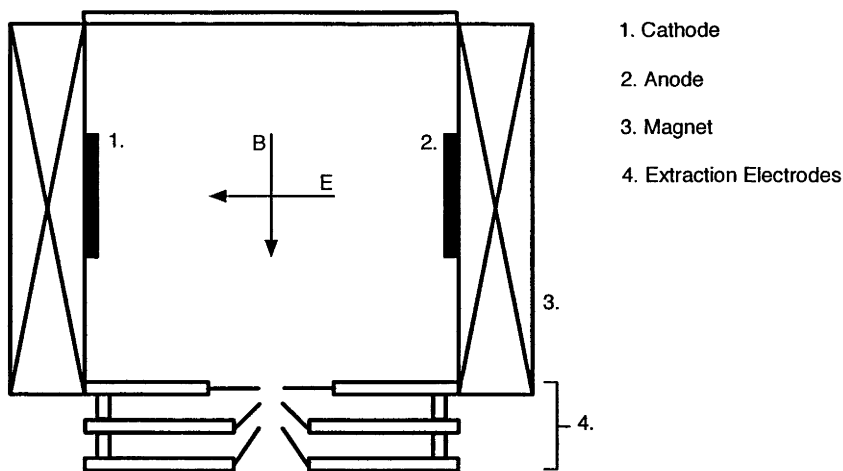


Figure 1.6: Conceptual diagram of a Penning ion source

high current density of several  $\text{A}\cdot\text{cm}^{-2}$  and a reasonably low ion energy spread of about 3 eV or less. Guharay *et al.* [48] have presented results showing ion energy

spreads as low as 0.6 eV for emission current densities of  $1 \text{ A.cm}^{-2}$  but report that perpendicular ion energy increases with beam intensity (higher extraction voltages). No mention was made of the overall source stability, though Humphries mentions this as a chief disadvantage of these systems [56]. He singles out plasma instabilities resulting from the crossed electric and magnetic fields as the cause of increased ion temperature and large spatial and temporal variations in the plasma parameters under various operating regimes.

Typically, PIGs are used for high current applications such as particle accelerators [4, 62].

As with the Duoplasmatron, the PIG ion source is limited in practice by short life time due to sputtering erosion of the cathode. Again, both hot and cold cathodes are employed, where hot cathodes are typically used for inert gases and cold cathodes are used for oxygen.

The device works by the emission of electrons from either a hot or cold cathode which ionise neutral gas particles as they are accelerated towards the anode. The discharge is struck in a small cavity formed between the anode and the cathode in which an axial magnetic field and a radial electric field is applied as shown in figure 1.6. Electrons are trapped radially by the magnetic field and axially by the electric field and as a result follow complex trajectories with-in the volume of the source leading to longer residence times and hence ionisation.

#### 1.4.5 RF Ion Sources

Given the apparent lack of RF ion sources in use by the semiconductor industry, it is perhaps surprising that the first attempt to form a FIB was done using a system adapted from a standard RF ion implanter dating back to 1973 [88]. It produced a beam diameter of  $3 \mu\text{m}$  and was used to expose Polymethylmethacrylate (PMMA) and perform maskless implantation of Silicon. Because of the low brightness, the

processes were very slow, but the potential of the system was demonstrated. A number of RF plasma ion sources have been developed by various research groups over the years, but these sources are often multi-aperture devices for use in large area processing of materials, neutral beam injectors for fusion and space propulsion. Single aperture RF devices other than the multicusp type developed at LBNL are more rare and certainly are not commonly used in the semiconductor industry. An exception to this is a single aperture helicon ion source developed at the Korea Advanced Institute of Science and Technology (KAIST) by Hwang *et al.* for use in both a neutron spallation source and in accelerator driven transmutation technology. This device produced a 200 mA beam at 50 kV with a divergence angle of 260 mrad [57]. No brightness measurements were presented.

Examples of multi-aperture ion sources are those described by Hayes *et al.* [51] and Irzyk *et al.* [59], where the work of Irzyk *et al.* is of particular interest here because it was based on a helicon reactor developed at the Australian National University (ANU) and is similar in concept to the devices presented in this work. In his PhD thesis, Irzyk showed that a helicon discharge was an efficient way to produce a high-density, uniform plasma for ion extraction applications [58].

As will be shown later in this work, densities in excess of  $10^{12}$  cm<sup>-3</sup> can be achieved with as little as 150 W of RF power and 5 mTorr of neutral gas pressure. These types of discharge work primarily by inductive coupling and so fluctuations in the plasma potential due to capacitive coupling are minimised. Measurements performed at FEI Co. on the third prototype source presented in chapter 4 demonstrated that ion energy spreads of less than 3 eV could be obtained in the extracted beam without the need for magnetic filtering. If an axial magnetic field is applied to the system then wave modes can be generated in the plasma further increasing the ionisation rate. Helicon (whistler wave) plasma discharges are extremely efficient and much research has been performed in the preceding decades to understand the mecha-

nisms driving this [99, 37, 34].

Even in inductive and wave coupling modes, some amount of residual capacitive coupling exists between the driving antenna and the plasma, causing the plasma potential to oscillate (c.f. equation 3.11). This contributes significantly to parallel ion energy spread and hence chromatic aberrations (especially at low extraction energies) and is one of the primary avenues of research in the development of the high brightness RF ion source presented in this work.

As perpendicular ion energy has a strong impact on the effectiveness of the extraction system, it must also be studied closely. One set of phenomena that are common to all plasmas of a certain pressure are charge-exchange collisions which occur in the plasma pre-sheath. These could lead to a fundamental limit on the minimum perpendicular ion energy spread that can be achieved in any plasma ion source and can only be avoided by changing the pressure regime which does not necessarily translate to benefits in other plasma parameters. Finally, in magnetised plasmas, resonant interactions between the RF driving frequency and low frequency waves such as ion cyclotrons can lead to increased perpendicular ion energy. All these phenomena are studied in this work.

## 1.5 Towards a High Brightness Plasma FIB

To this day, the only demonstrated ion beam technology capable of the resolution required for nano-fabrication has been LMIS. However, for all its benefits the technology is restricted because it can only function with metals that are liquid at low temperature (typically 300°C). These metals interfere with the target's optical and electrical properties either directly or indirectly. In-process contamination is the most salient reason to look for an alternative to LMIS. For example, Scipioni *et al.* showed that quartz doped with even small doses of Ga reduced the transparency of the sample by 70% at wavelengths of 157 nm and beyond [106]. Since quartz is

used in photolithographic masks, a loss of transparency impacts on the printing of circuitry, especially if the transmittance of the mask is not uniform over its surface. Contamination is also encountered in semiconductor metrology where FIBs are often used to cross-section devices during various phases of production and perform metrology on subsurface features. Typically, only one device per wafer is sacrificed for the purposes of quality control, the rest being returned to the production line in order to complete the fabrication process. However, sputter deposited material from the milling process can cross contaminate the surrounding chips on the wafer. Any foreign matter on the chips can have nefarious effects on performance, but in particular the use of liquid metals, especially the most commonly used gallium (a group III dopant), can have a strong impact on the electrical performance of the end devices. This causes hesitancy to use metals “in-line” as part of the production process.

This restriction of LMIS to a small number of metals is a major disadvantage of the technology. Techniques have been tried for the production of EUVL masks [53] that involve the deposition of a buffer layer onto substrates to avoid contamination of neighbouring areas during FIB correction, but the masks produced by this method are still not production ready. A viable and more generic alternative would be to extract inert gas ions from a plasma. Indeed Scipioni *et al.* [106] showed that irradiating quartz with a dose of Krypton ions from a multicusp source had only a negligible effect on transparency. In addition, the entire gamut of inert gases from H to Xe can be used in ion extraction from plasmas as well as chemically reactive molecules such as SF<sub>6</sub> and O<sub>2</sub> for enhanced ion emission in SIMS or sputter yield in milling applications.

Another disadvantage of LMIS is the relatively low extractable current obtained (as opposed to current density which is relatively high). For this plasmas are ideal as extracted current is a function of both aperture size and plasma density. Though

extracted current density is ultimately limited by plasma density, which in most real systems can be considered capped at  $10^{14} \text{ cm}^{-3}$ , it still represents current densities of between  $1\text{-}10 \text{ A.cm}^{-2}$  (depending on ion species) which is comparable to LMIS. However, as opposed to field emission systems which extract current from a nanometric point, plasma apertures can range from roughly 3 times the sheath width (tens of microns) to the entire diameter of the source as in the current free double layer of Charles *et al.* [19]. The relatively large apertures of plasma ion sources can be a disadvantage in low current applications such as mask correction where the current density required for low emittance extraction must be traded off against the smallest possible extraction aperture putting the interplay between current density and total beam current into sharp relief. Luckily, a solution, though not elegant, is to skim the extracted beam through an aperture of the requisite diameter reducing the down stream current. Skimmers, however, are subject to intense sputtering causing both secondary electron emission and beam contamination. Secondary electrons will migrate into the extraction region if the electrodes are not designed for this contingency and beam contamination can effect both the beam quality and the target's electrical and optical properties. Sputtering also implies a limited life-time for the skimmer and hence a disadvantage for "in-line" production settings.

From the discussion on the *Thermondynamic Limit*, it can be concluded that the inherent brightness of an ion source is related solely to the extractable current density and the perpendicular ion energy (assuming that the extraction energy is very much greater than the axial ion energy). However in practice, the degree of emittance growth from lens aberrations is directly related to the amount of demagnification required in the column optics (as opposed to the extraction optics) to reduce the object size down to the final spot size at the target. This was seen, for example, in equation 1.4 for chromatic aberration where the final spot size was directly related to the half angle of arrival or equivalently the demagnification power. This means

that the virtual source size (i.e. the effective emission surface) plays an important role in the overall system brightness.

In light of this, an LMIS system is particularly bright because its object size is defined by the tip of the Taylor cone, which has a diameter on the order of 10 nm. In reality, Coulomb interactions between ions near the tip increase the virtual source to 50 nm full width half of maximum (FWHM). On the other hand, plasma ion sources have a relatively large virtual source size, being defined by an extraction aperture of at least some tens, if not hundreds, of microns in diameter. Typical plasma ion sources have apertures on the order of a millimetre, but an aperture of 200  $\mu\text{m}$  was investigated in this work with some success (c.f. chapter 6). In principle the extraction aperture can have any size, however, for divergent or convergent beams, it must be greater than 2 sheath widths (roughly some tens of microns) to allow the meniscus to change shape. This is because for a plasma to “see” a hole (and hence have its shape changed) a sheath must be able to cover all parts of the indentation including the side walls and the base (even if the base is the plasma/beam interface). In practice, however, this is only an approximate rule of thumb and it is not clear how large an aperture must be before it does not effect the interaction between the extraction field and the meniscus.

In any case, if the aperture is 2 sheath widths or less then the plasma does not distinguish between the walls of the discharge chamber and the hole and the meniscus will remain flat for all applied extraction fields. At first glance this appears to be a considerable advantage as control of the emission surface is a major objective in low emittance ion extraction from plasmas, however in practice, electrode apertures have a minimum thickness (i.e. their edges are not infinitely sharp) and may be considerably greater than the aperture diameter. This would then introduce a highly non-uniform field structure inside the aperture itself and complicates the interface between the aperture and the extraction gap. This complex situation is



not considered in this thesis.

Though the virtual source size of a plasma ion source is approximately 3 orders of magnitude greater than an LMI source, it also has much smaller radial ion energy. This leads to less phasespace broadening in the extraction and focusing optics and therefore compensates aberrations produced by the demagnification lenses.

### 1.5.1 Electrode Design

The ultimate goal of electrode design for FIB applications is to produce a laminar beam with uniform current density. This maximises brightness by increasing the focusable current and minimising emittance through the elimination of aberrations. Since Langmuir first conceived of space-charge limited flow early in the last century, researchers have been devising ways to focus particles into beams for applications as varied as electron microscopy to neutral beam injectors for fusion reactors, however, it wasn't until Pierce [97] presented his theories on the analytical design of electrodes in the 1940s that a rigorous formalism was devised. Even today, extractors are mostly designed with computer codes using rules of thumb rather than purely analytical techniques. In many cases, such as the grids used in neutral beam injectors and ion thrusters, this is because the Pierce method leads to electrode geometries that are difficult to manufacture and reproduce in large number and that are liable to degradation under heavy ion impact. Instead more simple geometries are used and these must be modelled using computer simulation techniques. For the most part these codes are accurate [115] but the results are only as good as the experience of the operator, as many factors impact on the quality of the output. These codes include ray-tracing and particle-in-cell (PIC) methodologies and are discussed in more detail in chapter 3.

## Empirical Studies On High Intensity Beams

In the manufacture of multi-aperture grids for neutral beam injectors and plasma thrusters it is not practical to shape the apertures both for manufacturing and physical reasons, especially in the high intensity regimes where they are often run because sputtering leads to rapid deterioration of the delicate electrode features. Instead simple cylindrical orifices are punched or milled into the electrodes. Particle extraction from multi-aperture systems is closely related to the physics of single aperture devices [50, 25] and hence much of the early development work for gridded systems was done using the standard single aperture triode. Since the analytical method of Pierce was abandoned for more easily manufactured geometries researchers in the field such as Harrison [50] and Coupland [25] endeavoured to find useful relationships between electrode thickness, spacing and aperture diameter developing empirical relationships that could be used to predict the operation of similar devices and in particular multi-aperture systems. Harrison found that the perveance of electrodes designed without the Pierce principles did not suffer greatly in many of the cases that he studied [50], though a rigorous treatment of brightness was not presented by either Harrison or Coupland. It would seem that the motivation of neutral beam and gridded ion thruster research was more on beam intensity and low divergence rather than low emittance which is a requirement of FIB applications in the semiconductor industry.

## The Pierce Gun

Unfortunately simple aperture geometries are not adequate for low emittance devices and so a more rigorous approach was undertaken to develop electrodes for high brightness applications by a line of researchers starting with Pierce [97]. His basic method started by assuming a uniform sheet of non-relativistic particles, with no internally generated magnetic forces flowing in space-charge limited equilibrium

between two coplanar surfaces held at a differential electrostatic potential  $V_{ext}$ . The sheet was assumed to have finite thickness  $\pm x_0$ , but infinite width so that all forces acted in the x-z plane. Particles emerged from the source with negligible velocity compared to the  $\sqrt{2(e/m)V_0}$  gained in the extraction gap and were assumed to have no thermal energy following strictly rectilinear trajectories as dictated by the extraction field. Pierce noted that in a parallel beam of infinite extent, transverse forces due to space-charge were exactly balanced at every point yielding parallel particle trajectories perpendicular to the emission surface in the cold particle limit, and so reasoned that an electrostatic field applied by a pair of electrodes could, in the same way, serve to balance the space-charge forces in a beam of finite thickness. Mathematically, this involves solving Laplace's equation for the potential  $V(x, z)$  in the charge-free region:

$$\frac{\delta^2 V}{\delta x^2} + \frac{\delta^2 V}{\delta z^2} = 0 \quad (1.15)$$

subject to the boundary condition imposed by the potential distribution along the beam edge. Since the distribution along the beam edge is the same as that along any line perpendicular to the emission surface in a parallel beam of infinite extent, the boundary condition is given by the Child-Langmuir law for parallel diodes [73], which can be re-written in a form more suitable for the Pierce derivation as follows (a detailed derivation of Langmuir-Blodgett's laws is presented in Chapter 2):

$$V(x, z) = V_{ext} \left( \frac{z}{d} \right)^{\frac{4}{3}} \quad (1.16)$$

where  $d$  is the inter-electrode spacing for  $|x| \leq x_0$ . In planar geometry, Laplace's equation can be solved quite simply given these boundary conditions using conformal mapping. Defining the complex variable  $u = z + ix$ , the complex function  $f(u)$  is analytic if its derivatives are finite and continuous over the region of interest. It can be shown that any analytic function is a solution to Laplace's equation and therefore that the real part of any analytic function is also a valid solution to 1.15.

Following Pierce, it is noted by setting:

$$f(u) = V_{ext} \left( \frac{u}{d} \right)^{\frac{4}{3}} \quad (1.17)$$

that:

$$V(x, z) = \text{Re}(f(u)) = V_{ext} \text{Re} \left( \frac{z + ix}{d} \right)^{\frac{4}{3}} \quad (1.18)$$

In order to extract the real part of the function it is convenient to express the complex function in polar coordinates with the substitution  $z + i(x - x_0) = \rho e^{i\theta}$  so that 1.18 becomes:

$$V(x, z) = V_{ext} \left( \frac{\rho}{d} \right)^{\frac{4}{3}} \text{Re} \left( e^{i\frac{4}{3}\theta} \right) \quad (1.19)$$

where  $\rho = \sqrt{(x - x_0)^2 + z^2}$  and  $\theta = \tan^{-1}((x - x_0)/z)$ . The Pierce electrodes can then be determined by solving 1.19 with  $V(x, z) = 0$  for the emitter and  $V(x, d) = V_{ext}$  for the collector over the interval  $x \geq x_0$  (symmetry) and  $z \geq 0$ . For positive ion extraction,  $V_{ext}$  is negative but the solution to 1.19 is generic, being independent of  $V_{ext}$ . Once the inter-electrode spacing has been specified, any value of  $V_{ext}$  can be taken assuming the source of particles (positive or negative) is undepletable. It should also be noted that in the case of positive ion extraction the emitter is typically charged up to a positive  $V_{ext}$  and the collector kept at ground rather than the collector being charged negatively.

It is interesting to note that for the emitter, where  $V(x, z) = 0$ :

$$\frac{4\theta}{3} = \frac{\pi}{2} \quad (1.20)$$

That is, the charge free region of the emitter electrode is a straight line oriented at  $67.5^\circ$  with respect to the beam edge. This angle is commonly referred to as the Pierce angle and is the starting point for most modern particle gun designs.

Pierce's method only applies to parallel sheet beams, but subsequent theoreticians have proposed various methods to calculate electrode geometries for more sophisticated beam types [50, 28, 90, 103, 100]. As the mathematics becomes progressively

more complicated, theoreticians endeavoured to find simple relationships to express the electrode geometry of more complicated beam types [50]. However, the only rigorous treatment of all beam types was performed by Radley in 1964 [100]. In this work he presents a full analysis of Laplace's equation subject to Cauchy boundary conditions (that is Langmuir-Blodgett along the beam edge), including uniqueness and stability. Importantly, he finds the Pierce electrode by an alternative, more rigorous method and continues his investigations for higher order beam geometries including: strip and wedge beams, cylindrical and conical beams as well as hollow beams. It is perhaps the complexity of the mathematics which has prevented Radley's work from being used in the mainstream but in any case his work will be pivotal in the development of the theory presented here.

#### Extending Pierce's Method

Whilst Pierce's method and the work of others, particularly Radley, opened the way for a more rigorous formalism in the design of extraction electrodes, the direct application of their work to plasmas neglects three critical components:

- That the Child-Langmuir and Langmuir-Blodgett laws do not apply in their basic form to extraction from plasmas.
- That most real extractors consist of more than 2 electrodes in order to avoid deleterious effects from electrons.
- That the electric field as well as the potential need to be brought to zero by the end of the extractor in a fashion that ensures the classical diode symmetries are maintained.

#### Generalising Langmuir-Blodgett's Laws

The Child-Langmuir and Langmuir-Blodgett laws were initially developed to describe the space-charge limited flow of thermionic electrons between coplanar and

concentric surfaces referred to as planar, cylindrical and spherical diodes [73, 74, 75]. In the ideal case, planar diodes consist of infinite parallel plates, cylindrical diodes of infinitely long concentric cylinders and spherical diodes of concentric, closed spheres. Electrons were assumed to be produced thermionically from the emitter, which could be either the inner or outer surface depending on whether the flow was diverging or converging, and assumed to be undepletable in quantity (not source limited), cold and injected into the acceleration gap with negligible velocity. Importantly, the electric field at the emitter surface was assumed to be zero and was used as the primary justification for the description of the system as being space-charge limited. If this were not so then too many or too few electrons would flow into the extraction gap. If too many electrons are emitted, then the gap starts to develop a net negative charge repelling the entry of new electrons. If too few electrons are emitted, then the gap has a net positive charge and more electrons are attracted from the unlimited source of electrons in the emission surface. It is then clear that the equilibrium situation requires the electric field to be zero at the emission surface. However, in the extraction of ions from plasmas the emitter is the meniscus, across which exists a strong electric field typically of the order of a mega-Volt per meter. This can not be neglected and must be introduced into the derivation of the inter-electrode beam distribution calculation bringing about a corresponding change in the electrode geometries, including the Pierce angle which becomes a function of the sheath field and hence the plasma density.

In addition, the notion of ions being extracted from the plasma is a misnomer since ions are not “pulled” but rather fall through the sheath and cross the meniscus under the influence of the pre-sheath and sheath. This means that extraction from a plasma is not space charge limited as is assumed by Child-Langmuir and Langmuir-Blodgett’s laws but rather source limited and is a fundamental departure from the commonly held beliefs about ion extraction from plasmas.

As an interesting aside, it is noted that, even neglecting sheath potential, Pierce's method can only be applied directly to the extraction of ions from a plasma with care because the source of ions is not infinite. Instead, the extractable current,  $I$ , is directly related to the plasma density,  $n$ , by:

$$I = 0.6env_B\mathcal{A} \quad (1.21)$$

where  $v_B$  is the ion sound speed and  $\mathcal{A}$  is the area of the extraction aperture, so that for the meniscus to remain planar the extractor is sensitive either to inter-electrode spacing or applied extraction voltage. This means that a given applied voltage and inter-electrode spacing pair corresponds to only one current density and hence one plasma density and as a result each electrode design is unique, if it is to be used optimally as a low emittance device. It also means that the Langmuir-Blodgett laws can only be verified for plasmas, even neglecting the sheath potential, if the plasma density can be controlled accurately. Indeed, Rautenbach verified the scaling law [102]:

$$I = \kappa \left( \frac{e}{M_i} \right)^{\frac{1}{2}} V^{\frac{3}{2}} \quad (1.22)$$

where  $I$  is the extracted current from a plasma source,  $V$  is the extraction potential and  $\kappa$  is a geometric constant associated with the geometry of the extraction system. He was careful to specify that the "electrostatic field distribution remains invariant", however, the effect of the meniscus potential on beam geometry could not be verified because it was subsumed into the constant  $\kappa$  and so his experiments do not show that the flow of ions in an extraction gap is space charge limited as he claims but rather that they satisfy a 3/2 power law given by 1.22.

### Blocking Electrodes

In real systems the beam ions interact both with the extractor and the vacuum vessel and hence produce secondary electrons. This has an advantageous effect

on beam neutralisation in the post extraction transport region as these electrons can ionise the background gas and create a beam plasma that shields the beam's positive potential from the grounded vessel walls. However, electrodes designed directly from the Pierce methodology have only two electrodes and can not block these same electrons from migrating into the extraction region where they would alter the extraction field and hence degrade beam quality. The inclusion of a third electrode between the plasma electrode (the electrode in contact with the plasma) and the grounded electrode (the collector in the Pierce paradigm), biased at some sufficiently negative potential to block all on-coming electrons is satisfactory for this purpose (c.f. figure 4.1).

### Engineering the Electric Field

With three electrodes Pierce's method (and hence that of Radley) becomes strained because for the various diode assumptions to hold the electrostatic potential in the charge free region must be maintained from the meniscus to the last grounded electrode and not, as is usually assumed, solely between the first two electrodes. In addition the convexity of the Langmuir-Blodgett solutions both in their original and generalised forms implies a strong electric field at the exit of the extractor which balloons out of the aperture deflecting the beam trajectories and hence inadvertently increasing emittance. Probably of more importance, is the effect on the shape of the 0 V equipotential surface (the collector in the Pierce paradigm) which accordingly changes the beam geometry and hence the potential distribution in the extractor altering the extraction mechanism and degrading beam quality. This can be avoided by including two more electrodes configured to bring the electric field back to zero, whilst maintaining a blocking potential against the flux of electrons. In essence, a standard and an inverted Langmuir-Blodgett potential distribution are stitched together to create a low field/high field/low field distribution.



The mechanics of this process are presented in chapter 2.

### 1.5.2 High Density Cold Ion Plasma Source Design

Equation 1.14 shows that for a brightness of  $10^5 \text{ A.cm}^{-2}.\text{sr}^{-1}$ , current densities on the order of  $1 \text{ A.cm}^{-2}$  are required assuming an ion temperature of 0.1 eV and an extraction voltage of 10 kV. This implies a plasma density of  $10^{14} \text{ cm}^{-3}$ . With simple inductively coupled plasmas, densities on the order of  $10^{12} \text{ cm}^{-3}$  have been achieved with as little as 150 W and 5 mTorr. Higher power yields even greater densities, but the addition of a magnetic field can boost the density up an order of magnitude by allowing the generation of ionisation promoting wave modes. In chapter 4, a source design which employs a permanent magnet is presented that is capable of  $10^{14} \text{ cm}^{-3}$ .

#### Helicon Plasmas

It has been known for some decades that helicon (whistler wave) plasma sources have high density and require relatively little input power [12]. Densities in excess of  $10^{12} \text{ cm}^{-3}$  are typical but as will be shown in this work plasma densities of up to  $10^{14} \text{ cm}^{-3}$  are possible for as little as 1 kW input power. Helicon plasmas are magnetised inductively coupled discharges with electromagnetic waves that propagate parallel to the magnetic field. The dispersion relation for helicon modes was initially predicted in solids by Bowers in 1961 [18] and independently by Legendy in 1964 [78]. These same equations were developed (again independently) for plasmas by Klozenburg, McNamara and Thonemann [67] and demonstrated experimentally soon afterwards by Lehane and Thonemann [79] and Blevin [8]. In these experiments a plasma was struck by some other means and the structure of a test wave generated by a small loop immersed inside the plasma was measured using electrostatic probes.

The first plasma generated by helicon waves was produced by Boswell [12] in the late 1960's. The experiment consisted of a 5 cm diameter, 55 cm long glass tube inserted into two solenoids that were configured in a magnetic pinch arrangement [13]. The antenna structure for these first experiments was a 16 cm long double saddle configuration (often referred to as a Boswell type antenna) wound around the outside of the glass source tube. This antenna resonantly excited helicon waves of wave length twice that of the antenna length and results from these early experiments indicated that plasma production was associated with the amplitude of these waves. In addition the measured electron density was found to undergo discrete jumps as the magnetic field was increased in such a way as to return the axial wave length of the helicon to roughly twice the length of the antenna.

Systems utilising large amplitude helicon waves to produce plasmas are known for their high ionisation efficiency compared to other non-resonant RF excitation techniques such as capacitive and inductive coupling. Boswell found almost 100% ionisation in the above described experiment for as little input power as 180 W. High densities have also been found by Shoji *et al.* [109], Komori *et al.* [69] and Chen *et al.* [21] in similar experiments.

Many theories have been proposed, and much controversy generated, over the topic of why helicons are so efficient at creating plasma especially since measurements of the wave damping rate under conditions of low collisionality can not be accounted for by the low collision frequency. The collisionless process that has received the most attention, and for which a great deal of experimental evidence exists [130, 69, 85, 38, 30] is the wave-particle interaction of Landau damping, a mechanism where electrons close to the wave phase velocity are accelerated up to the ionisation velocity by the wave (in a process similar to surfing). The experimental justification for this hypothesis consists of three elements:

- Some experimental correlation with the theoretical Landau damping rate [85].

- Measurements of the electron distribution function using swept Langmuir probes or retarding field energy analysers which correlate to the wave phase velocity [130].
- Measurements of moving pulses of Ar II emission consistent with the wave phase velocity [38, 34].

More recently, Chen *et al.* has distanced himself from his earlier work on Landau damping and suggested that Trivelpiece-Gould (T-G) modes are the most likely channel of energy flow into the electron distribution function [22]. This is strongly contested by Boswell (R. W. Boswell, A.N.U., private communication) on the grounds of strong experimental evidence in favour of wave-particle interactions and the non-existent experimental evidence for T-G modes, which remain a purely theoretical consideration. But even on a theoretical level, the role of T-G modes is disputed by Legendy who considers surface modes as sufficient to describe the helicon dispersion relation. In any case the high ionisation efficiency of the helicon discharge makes it an ideal candidate for a high brightness plasma ion source.

In much of the helicon dispersion theory ions are assumed to be cold and though this may be sufficient for experimental verification of the helicon dispersion relation and other phenomena it is not adequate for the purposes of high brightness FIB extraction. As all RF plasmas, both magnetised and non-magnetised, are capable of coupling significant energy into both the parallel and perpendicular motion of ions and hence reduce the brightness of the source, the study of ion heating mechanisms is a major focus of this work.

### Parallel Ion Energy Distribution

The primary cause of axial ion energy spread in inductive and wave generated plasmas is residual capacitive coupling between the antenna and the plasma. This

capacitive coupling modulates the plasma potential as:

$$V = \tilde{V} \sin(\omega t + \phi) \quad (1.23)$$

where  $\omega$  is the RF driving frequency,  $\phi$  is the RF phase and  $\tilde{V}$  is the amplitude of the RF oscillation “seen” by the plasma and can range from milli-Volts to hundreds of Volts depending on the effectiveness of the RF coupling between the antenna and the plasma.

If the ion transit time through the sheath is comparable to the ion plasma period then ions entering the sheath are not effected by the RF modulation. However, if the ion transit time is less than the ion plasma frequency, the axial energy distribution function of the ions exiting the sheath is broadened. The smaller the transit time relative to the ion plasma frequency the stronger the ions are modulated by the RF [19]. The exact extent to which the ion distribution function is broadened is a difficult analytical problem, but it has been simulated by various schemes [19]. The ultimate effect of the RF modulation is to broaden the velocity distribution of the ions exiting the plasma through the extraction aperture causing chromatic aberration.

Thus axial ion energy spread is reduced by any means that decreases the capacitive coupling between the antenna and the plasma. In this thesis an RF matching technique is presented that reduces capacitive coupling considerably. It involves placing capacitors on either side of the RF antenna in a  $\Pi$  configuration and adjusting them so that the phase in the middle of the antenna is zero. In chapter 6, results are presented showing ion energy spread as a function of the antenna phase and demonstrates that proper antenna balancing can result in a considerable decrease in ion energy spread.

### Perpendicular Ion Energy Distribution

The sources of perpendicular ion energy generation are more numerous and complicated but in most cases they are considered less important than parallel ion heating. Phenomena common to all plasmas are charge exchange collisions in the pre-sheath. In an internal report produced for the FEI project, Helen Smith showed that there is some possibility of this mechanism driving ion heating. These results will be presented in more detail in chapter 6 but briefly they showed scattering from charge-exchange collisions are significant in converting parallel energy gained in the pre-sheath to perpendicular energy attaining as much 1 eV at 20 mTorr. However, at lower pressures (10 mTorr) perpendicular ion energy was only increased to 0.1 eV. This is an encouraging result for the RF sources presented in this thesis which typically operate at around 5 mTorr.

In the case of magnetic inductively coupled plasmas, such as helicons, a multitude of wave modes are possible within the cavity created by the plasma. In particular, instabilities can be driven by a number of mechanisms including parametric decay, shearing and filamentation. It has been found previously in a number of settings, including space and laboratory plasmas, that helicons can decay parametrically into ion acoustic waves [15]. More recently it has been shown that ion cyclotron waves can be generated by temperature anisotropy driven shear in high beta plasmas [105]. It is clear from the measurements in this work that under certain plasma conditions, the helicon can also act as a pump in a resonant 4 wave interaction which produces ion cyclotron waves. In a process that resembles a filamentation instability, energy from the helicon pump is down converted into the ion energy distribution function resulting in large amplitude azimuthal modes. This can represent a significant path for energy flow into the perpendicular ion energy distribution. As is shown in chapter 5 these instabilities only exist within a relatively narrow band of operational parameters which may or may not be those used in the final FEI device, but they are

studied as a potential ion heating channel and also as an interesting phenomenon in their own right.

# Electrode Design for the Extraction of Very High Brightness Ion Beams

The design of low emittance growth extractors begins with an accurate description of the beam potential profile. The extractor is then built around the beam in such a way as to maintain the chosen conditions. A fundamental building block in this approach is the notion that certain beam types can be thought of as sections of current flowing in complete classical diodes. Descriptions of charge and potential distributions in these diode systems can be obtained under a wide variety of conditions. The most basic situations were previously studied by Child, Langmuir and Blodgett [73, 74, 75]. However, to adequately describe the beam distributions in practical extractors, several generalisations of the standard Child-Langmuir and Langmuir-Blodgett relations are required.

Armed with an accurate description of the beam potential profile, solutions to Laplace's equation, as described by Radley [100], can be employed to calculate the necessary electrode shapes and positions to maintain the chosen beam distribution. Except for the first and last, electrodes must be shaped on both faces and are calculated specifically for each stage of the extractor. The minimum number of stages for low emittance growth extractors is 4.

Here a complete method is presented for the design of low emittance growth beams. The mathematics and practical implementation of the formulae are described.

## 2.1 Statement of Problem

We wish to determine electrode geometries for the extraction of FIBs from a high density plasma with a final energy of up to several tens of kilo-Volts which minimise emittance growth. Though there are several definitions of brightness, it is generally accepted that minimising emittance ensures the highest possible brightness for a given beam current. Briefly, emittance is a measure of the laminarity of the individual particle trajectories with-in a beam. In planar symmetry this means that particles follow rectilinear and parallel trajectories whilst in cylindrical and spherical symmetry they move along rectilinear paths that follow radial lines as though emanating from a single line or point.

In this work, we are primarily concerned with the extraction of diverging and converging ion beams from rectangular slits and circular apertures where parallel beams are considered to be a special, zero divergence, case of these two principle extraction regimes. This yields 4 basic beam types:

- Strip Beams: parallel beams extracted through a slit.
- Wedge Beams: diverging/converging beams extracted through a slit.
- Cylindrical Beams: parallel beams extracted through a circular aperture.
- Conical Beams: diverging/converging beams extracted through a circular aperture.

These beams can be thought of as sections of current flowing in complete diodes. Consequently, parallel beams can be treated in the same way as a planar diode, divergent/convergent beams extracted through a rectangular slit can be treated as a cylindrical diode and divergent/convergent beams extracted through a circular aperture can be treated as a spherical diode. In each case, the plasma/beam interface or plasma meniscus is the anode (emitter) and the 0 V equipotential surface



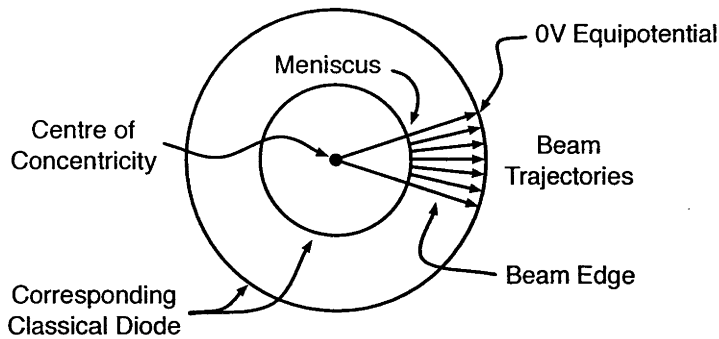


Figure 2.1: 2D representation of a diverging beam and corresponding classical cylindrical/spherical diode.

is the cathode (collector) as shown in figure 2.1. The purpose of the extraction electrodes is then to ensure that the meniscus and 0 V equipotential surfaces are parallel in the case of parallel beams and concentric cylinders or spheres in the case of diverging or converging beams. If this situation is maintained then, neglecting the inherent ion temperature in the plasma, the ions travel in perfect parallelism along radial lines from the meniscus to the 0 V equipotential and suffer no deflection. In other words the beams have zero emittance growth.

In accelerating the beam, however, a significant electric field can be produced in the direction of flow. This must be compensated otherwise upon exit of the extractor the electric field equipotentials in the beam will balloon outwards, as shown in figure 2.2, deflecting the ion trajectories.

Moreover, in practical systems the presence of electrons can not be ignored. In the transport region aft of the extractor, considerable advantage can be gained by the presence of electrons which neutralise the beam space charge. However, their presence in the extractor, especially in the acceleration gap, is highly detrimental to beam quality since they alter the charge density distribution and hence the potential structure through-out the extractor. The existence of an electric field at the exit to the extractor would serve to accelerate electrons into the extraction region

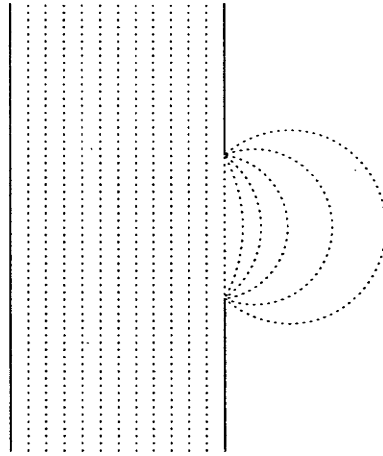


Figure 2.2: Equipotentials ballooning through an aperture. If the electric field on the left hand side of the aperture is greater than that on the right hand side, the equipotential lines balloon out towards the right.

in such quantity as to neutralise the electric field at the extractor exit. For both of these reasons the beam potential must be so engineered as to have zero electric field upon exit of the extractor.

Finally, the electrons in the beam plasma aft of the extractor have non-zero temperature and are generally distributed according to Maxwell's law. This means that higher energy electrons from the tail of the distribution are able to enter the extractor if a blocking field is not present. To this end a small negative potential of some hundred Volts is produced at the end of the extraction region to inhibit the passage of electrons. Again, to avoid ballooning of the electric field this potential must be produced so that the electric field upon exit of the blocking region is zero.

The potential distribution in the beam will then have the aspect of figure 2.3. There are two regions called the Extraction and Blocking regions both of which are divided into two stages. Stage 1 serves to take the beam from a low gradient to a high gradient and stage 2 vice versa. In the Extraction gap, stage 1 is necessary to match the beam potential to the plasma sheath and stage 2 to bring the electric field to zero. A similar rationale is behind the two stages of the Blocking region.

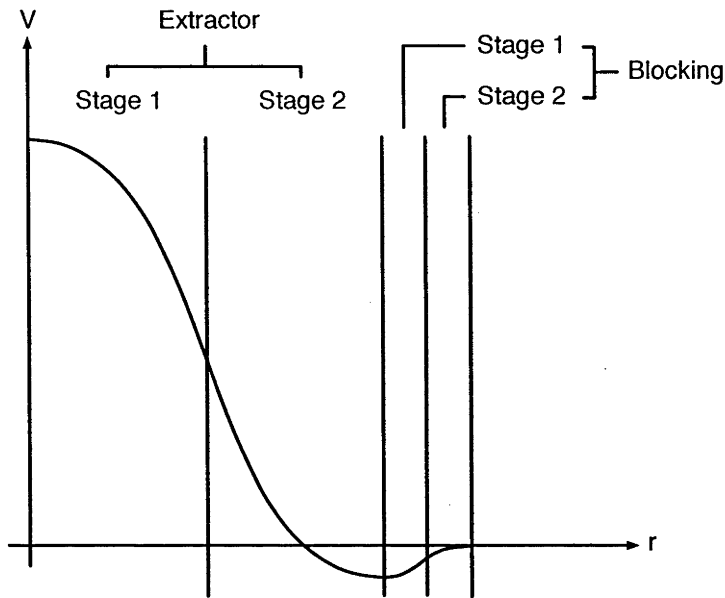


Figure 2.3: Potential distribution along the beam (direction of particle motion) for 5 electrode (4 stage) extraction system. Vertical lines represent the axial position of the electrodes. The 'r' axis is the position inside the hypothetical diode and demonstrates that the potential distribution is the same along any radius emanating from the center of concentricity as defined in figure 2.1.

## 2.2 Beam Distributions

The correct determination of the potential structure along the beam edge is crucial to the proper design of extraction electrodes. It is indeed the starting point in the design process and is one of the main features that distinguishes this method from others that the author is aware of.

In the previous section we showed the general shape of the potential along the beam inside the extractor for low emittance growth extraction (zero emittance growth in the ideal case). In this section we investigate the details of these distributions in each stage of the extractor.

The overall potential profile shown in figure 2.3 is four concatenated distributions. Each stage is bounded by two plane or two concentric surfaces (depending on the

beam type) so that each stage can be treated as separate, ‘complete’ diodes, each with its own set of boundary conditions as shown in figure 2.4. The complete distribution is then obtained by stitching these separate solutions together by matching the boundary conditions at each surface.

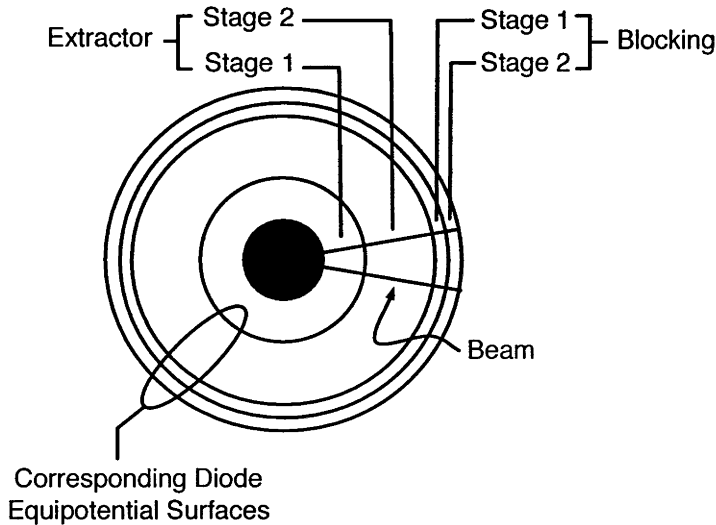


Figure 2.4: Diverging conical or wedge beam with electrode stages bounded by concentric equipotential surfaces corresponding to the emission and collection surfaces of classical diodes.

The potential and charge distributions in the beam at each stage of extraction are governed by Poisson’s law. The basic solution to this problem, using simple boundary conditions, in plane symmetry was solved by Child and Langmuir in 1911 and 1913 [73] respectively and in cylindrical and spherical symmetry by Langmuir and Blodgett in the 1920s [74, 75]. These initial solutions assumed only one charged particle species (notably electrons) and assumed zero potential gradient at the entry to the acceleration gap. In addition, initial velocity was ignored on account of it being several orders of magnitude less than the exit velocity. Though these basic distributions still have an important role in the design of electrodes, several generalisations are required for proper implementation of a low emittance extractor. In particular, distributions describing non-zero initial gradient, distributions describ-

ing non-negligible initial velocity, distributions tapering from a strong gradient to a zero gradient (the reverse of the standard Langmuir-Blodgett solution) and distributions describing the presence of Maxwellian electrons. A further requirement on these distributions (for the method presented here) is that they have the same form as the standard Langmuir-Blodgett series solutions since the Radley solutions to Laplace's equation are dependent on this form.

### 2.2.1 The Basic Solution to Poisson's Equation

The work published by Langmuir-Blodgett in the 1920s forms the basis for the beam distribution analysis that follows and is given in terms of simple and compact series solutions. In this section we present a cursory mathematical overview of Langmuir-Blodgett's contribution starting with spherical symmetry and working through to cylindrical symmetry.

#### Spherical Symmetry

In the case of ion beam extraction from a circular aperture, the charge and potential distributions in the beam are assumed to be analogous to those in a complete spherical diode. Following Langmuir and Blodgett [75], we state Poisson's equation between two concentric spheres:

$$\frac{1}{r^2} \frac{d}{dr} \left( r^2 \frac{dV}{dr} \right) = -\frac{\rho}{\epsilon_0} \quad (2.1)$$

where  $V$  is the potential at a point distant  $r$  from the common center and  $\rho$  is the ion charge density. The current flowing in the diode can be written in terms of the particle velocity  $v$ :

$$I = 4\pi r^2 \rho v \quad (2.2)$$

where the velocity can be written in terms of the voltage  $V$  by using the kinetic energy relation:

$$\frac{1}{2}Mv^2 = -eV \quad (2.3)$$

Combining equations (2.1), (2.2) and (2.3) yields:

$$r^2 \frac{d^2V}{dr^2} + 2r \frac{dV}{dr} = A\tilde{V}^{-\frac{1}{2}} \quad (2.4)$$

where  $\tilde{V} = -V$ , and:

$$A = \frac{I}{4\pi\epsilon_0} \sqrt{\frac{M}{2e}} \quad (2.5)$$

Equation (2.4) can probably not be integrated directly but a solution can be found in terms of a series. The form of the solution as a function of the ratio  $R = r/r_s$  presented by Langmuir and Blodgett is:

$$V(R) = \left(\frac{9}{4}A\right)^{\frac{2}{3}} f^{\frac{4}{3}}(R) \quad (2.6)$$

where  $f$  is the analytic function to be found. We use the same form here. The  $\left(\frac{9}{4}A\right)^{\frac{2}{3}}$  term serves to normalise for the constant term  $A$  related to the current and hence the plasma density and meniscus curvature, and the  $f^{\frac{4}{3}}(R)$  term to remove the square root from (2.4) and hence to simplify subsequent derivations. One further transformation is performed by setting:

$$\gamma = \ln(R) \quad (2.7)$$

so that a solution to (2.6) can be expressed in terms of a MacLauren series:

$$f = \sum_{n=0}^{\infty} a_n \gamma^n \quad (2.8)$$

By substituting (2.6) into (2.4) and imposing equation (2.7) we find:

$$3ff' + f'^2 + 3ff'' - 1 = 0 \quad (2.9)$$

where  $f' = df/d\gamma$  and  $f'' = d^2f/d\gamma^2$ .

From this form we immediately see that for  $f = 0$ ,  $f' = 1$ . The first six terms of

the series solution are then:

$$f = \gamma - 0.3\gamma^2 + 0.075\gamma^3 - 0.0143182\gamma^4 + 0.0021609\gamma^5 - 0.00026791\gamma^6 \quad (2.10)$$

where we note that this corresponds to the case  $V = 0$  and  $V' = 0$ .

### Cylindrical Symmetry

A similar derivation can be made for the case of cylindrical symmetry. Poisson's equation becomes:

$$r \frac{d^2V}{dr^2} + \frac{dV}{dr} = B\tilde{V}^{-\frac{1}{2}} \quad (2.11)$$

where:

$$B = \frac{I}{2\pi r l \epsilon_0} \sqrt{\frac{M}{2e}} \quad (2.12)$$

and  $l$  is the length of the extraction slit. The solution takes the form:

$$V = \left(\frac{9}{2}Br\right)^{\frac{2}{3}} g^{\frac{4}{3}} \quad (2.13)$$

where  $g$  is the analytic function to be found over the desired range of  $r$ . Again substituting (2.13) into (2.11) and setting (2.7), we find:

$$3gg'' + g'^2 + 4gg' + g^2 - 1 = 0 \quad (2.14)$$

Again, we immediately see that for  $g = 0$ ,  $g' = 1$  and the series becomes:

$$g = \gamma - 0.4\gamma^2 + 0.0916667\gamma^3 - 0.01424242\gamma^4 + 0.001679275\gamma^5 - 0.0001612219\gamma^6 \quad (2.15)$$

We note that this corresponds to the case  $V = 0$  and  $V' = 0$ .

#### 2.2.2 Non-Zero Initial Gradient

Since in this work we are primarily interested in the extraction of ions from plasma, the assumption that the electric field at the meniscus surface is zero, central to the Child-Langmuir and Langmuir-Blodgett derivations, is incorrect and so

will be generalised here. Furthermore, our final result will be presented in a similar, easy to use series formulation as the original Langmuir-Blodgett relation.

Figure 2.5 demonstrates the effect of non-zero initial gradient. The dashed line corresponds to the case of a divergent conical beam extracted from a plasma of density  $n = 10^{14} \text{ cm}^{-3}$  and is compared to the standard Langmuir-Blodgett distribution which assumes zero initial gradient.

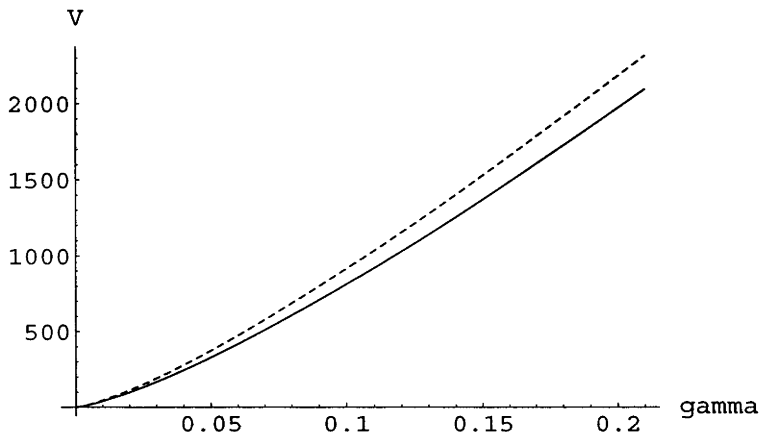


Figure 2.5: Generalised distribution (dashed line) versus Langmuir-Blodgett (solid line). Density  $n = 10^{14} \text{ cm}^{-3}$  and normalised gradient  $dV/d\gamma = 13001\text{V/unit}$ .

To understand why the gradient at the plasma/sheath interface or meniscus is non-zero we must consider the Bohm sheath criterion which stipulates the minimum ion velocity for entry into the sheath to maintain a stable sheath at a plasma boundary. In conjunction with some distribution relation for electrons, this defines a potential structure with-in the sheath. In particular, the electric field at the plasma boundary is non-zero and is typically several hundred kilo-Volts per meter. For continuity of the electric field across the plasma/beam interface the potential gradient must be equal on both sides of this surface. This is not assured by the original assumptions of Langmuir and Blodgett who were modelling particle flow from thermionic cathodes. In that case the source of particles was assumed to be undepletable and to



have no intrinsic electric field so that for equilibrium the boundary condition in the extractor was for the electric field to be zero at the entry to the acceleration gap. In the case of plasmas, the flux of ions is fixed and an intrinsic electric field does exist in the sheath which separates the beam from the bulk plasma. This strongly implies that particle beam extraction from plasmas is not space charge limited but rather is source limited and further that the voltage distribution in the beam is not given by the Langmuir-Blodgett relation as it is usually stated.

In this section we first present general solutions to Poisson's equation for the case of non-zero initial gradient. We then discuss the plasma sheath and how the gradient at the meniscus is obtained.

### Spherical Symmetry

Taking the first derivative of (2.6), we find that:

$$V'(\gamma) = \lambda\sqrt{p} \quad (2.16)$$

where  $\lambda = \frac{4}{3}(\frac{9}{4}A)^{\frac{2}{3}}$  and  $p = f'(\gamma)^2 f(\gamma)^{\frac{2}{3}}$ , for  $\gamma = 0$ . In the classic Langmuir-Blodgett derivation  $f(\gamma) = 0$  in (2.9) leads to  $f'(\gamma) = 0$ , for  $\gamma = 1$ , (assuming potential increases as a function of position in the extractor), so that  $p = 0$  and hence  $V'(\gamma = 0) = 0$ . In other words, the Langmuir-Blodgett derivation requires a zero initial gradient in potential. Numerically, however, it is possible to have  $f$  approach zero without requiring  $V'(0)$  to annul by setting  $f'(0)$  such that (2.16) holds for the desired value of  $V'(0)$ . For a given value of  $V'(0)$  and  $A$ , there is a limit to how small  $f(0)$  can be set, but in most practical cases it is several orders of magnitude less than unity.

We find that the solution depends only on  $p$ , rather than the individual values of  $f(0)$  and  $f'(0)$ , for the range of  $p$  which is of interest. The series coefficients,  $a_n$ , are expressed as a quadratic:

$$a_n = \alpha_n + \beta_n p + \gamma_n p^2 \quad (2.17)$$

where  $\alpha_n$ ,  $\beta_n$  and  $\gamma_n$  are the expansion coefficients found by a least squares method.

These terms are presented in the following table 2.1.

$n$	$\alpha_n$	$\beta_n$	$\gamma_n$
1	1.0035	4.049	-10.92
2	-0.3084	-8.008	25.11
3	0.08338	7.791	-25.85
4	-0.01825	-3.96	13.47
5	0.002870	1.0004	-3.448
6	-0.0002227	-0.09904	0.3441

Table 2.1: Expansion terms for the coefficients of the MacLauren series (c.f. equation 2.17). Spherical case. Note: the  $\alpha_n$  are very close to the original Langmuir-Blodgett series coefficients.

### Cylindrical Symmetry

We take the first derivative of the potential and write it in terms of the parameter

$p$ :

$$V'(R) = \mu(g^{\frac{4}{3}} + 2\sqrt{p}) \quad (2.18)$$

where  $\mu = \frac{2}{3}(\frac{9}{2}Be^\gamma)^{\frac{2}{3}}$  and  $R = 1$ , and note that in the limit the term in  $g$  disappears, so that  $V'(R) \approx 2\mu\sqrt{p}$ . This has the same form as the spherical case, so that by writing:

$$g = \sum_{n=0}^{\infty} b_n \gamma^n \quad (2.19)$$

and plotting the series coefficients in terms of the parameter  $p$  we obtain:

$$b_n = \delta_n + \epsilon_n p + \zeta_n p^2 \quad (2.20)$$

where  $\delta_n$ ,  $\epsilon_n$  and  $\zeta_n$  are coefficients found in the same fashion as for the spherical case. Results are presented in table 2.2.

### The Plasma Sheath

There are several ways to model the sheath. Lieberman [83] presents a method in terms of the Bohm sheath criterion and the Boltzman equation in one dimension,

$n$	$\gamma_n$	$\delta_n$	$\epsilon_n$
1	1.0034	3.989	-10.69
2	-0.4086	-8.223	25.43
3	0.1005	7.974	-26.22
4	-0.01866	-4.038	13.65
5	0.002658	1.0184	-3.491
6	-0.0002011	-0.1007	0.3482

Table 2.2: Expansion terms for the coefficients of the MacLauren series (c.f. equation 2.20). Cylindrical case. Note: the  $\gamma_n$  are very close to the original Langmuir-Blodgett series coefficients.

which is easily extended to spherical and cylindrical symmetry. This model is intuitively pleasing since it incorporates both the non-zero ion velocity  $v_B$  at the entry to the sheath, required by the Bohm criterion, and also the presence of electrons. Another popular method is the Child sheath [83], which is extended to spherical and cylindrical symmetry by the use of the standard Langmuir-Blodgett corrections. In this case, the pre-sheath/sheath boundary and the meniscus are considered to be concentric spheres for extraction from a circular aperture and concentric cylinders for extraction from a slit. Though solving the Boltzman sheath is possible in terms of a series and has been done by the author, it requires a somewhat more drawn out analysis than is necessary to demonstrate the thesis of this work, and so for simplicity, the Child sheath method will be employed with Langmuir-Blodgett corrections. As such, the pre-sheath can be ignored and we assume that the velocity of ions and the potential at the bulk plasma/sheath edge are zero. However, it should be noted that the Child sheath yields smaller gradients than the Boltzman sheath.

#### Sheath Potential at the Meniscus

To solve (2.4), we first note that in the case of extraction from a plasma  $I$  must equal the ambipolar flux for ions:

$$I^+ = 0.6en_s v_B \mathcal{A} \quad (2.21)$$

where  $n_s$  is the plasma density at the sheath edge and  $\mathcal{A} = 4\pi r_s^2$  is the area over which current is extracted,  $r_s$  being the radius of curvature of the sheath. It follows from (2.5) and (2.21), that the solution to (2.4) is strongly related to both  $n_s$  and  $r_s$ .

In addition, we require three boundary conditions. At the entry to the sheath we set  $V(1) = 0$  and  $dV(1)/dR = 0$ . To determine the sheath potential at the meniscus we equate ion flux, assumed constant through-out the sheath,

$$\Gamma_i = \frac{n_s v_B}{R^2} \quad (2.22)$$

to the electron flux at the meniscus,

$$\Gamma_e = \frac{n_s(\bar{v}_e) \exp(\frac{eV_m}{kT_e})}{4R^2} \quad (2.23)$$

where  $\bar{v}_e = (8eT_e/\pi m)^{\frac{1}{2}}$  is the mean electron velocity and  $V_m$  is the potential of the meniscus with respect to the plasma-sheath edge. Thus upon substitution of the Bohm velocity:

$$n_s \left(\frac{eT_e}{M}\right)^{\frac{1}{2}} = \frac{1}{4} n_s \left(\frac{8eT_e}{\pi m}\right)^{\frac{1}{2}} \exp\left(\frac{eV_m}{kT_e}\right) \quad (2.24)$$

which becomes:

$$V_m = -T_e \ln\left(\frac{M}{2\pi m}\right)^{\frac{1}{2}} \quad (2.25)$$

This can be expressed in a more convenient form by substituting the mass of the extracted ion species. Krypton is a typical gas used in ion beam extraction from plasmas and has a mass of  $M = 84$  au. Therefore in this case, (2.25) can be rewritten as  $V_m = -5.05T_e$ , which, assuming  $T_e = 3$  eV, is approximately  $-15$  V.

This now leads to suitable boundary conditions for (2.4):

$$\begin{cases} V = 0 & , r = r_s \\ V = -15 & , r = r_m \\ dV/dR = 0 & , r = r_s \end{cases} \quad (2.26)$$

where  $r_m$  is the radius of curvature of the meniscus.

### Potential Gradient at the Meniscus

Since both the voltage and its first derivative are zero at  $r_s$ ,  $f$  is independent of the parameter  $p$  and we have the familiar Langmuir-Blodgett relation:

$$\alpha(\gamma) = \gamma - 0.3\gamma^2 + 0.075\gamma^3 - 0.0143182\gamma^4 + 0.0021609\gamma^5 - 0.00026791\gamma^6 \quad (2.27)$$

This series expansion in conjunction with (2.6) and the boundary conditions now determine both the sheath width and the potential gradient at the meniscus edge. The sheath width is taken as the value of  $r_m - r_s$  for which (2.6) is equal to (2.25). The potential gradient at the meniscus edge is then equal to the first derivative of (2.6) taken at this value of  $r_m$ .

Assuming a constant electron temperature and gas type, equations (2.6),(2.7) and (2.27) show that the potential gradient at the meniscus edge is dependent on the bulk plasma density and the radius of curvature of the meniscus.

### Discussion

The extent to which the adjusted solution presented here deviates from that of Langmuir-Blodgett depends on the magnitude of the potential gradient at the sheath edge. From (2.16) we find that:

$$p = \alpha(\gamma_m)^{\frac{1}{3}} \frac{d\alpha}{d\gamma}(\gamma_m) \quad (2.28)$$

where  $\gamma_m$  is the value of  $\gamma$  at the meniscus edge. We note that  $d\alpha/d\gamma$  does not vary much with  $\gamma$  so that the the dominant term is  $\alpha^{\frac{1}{3}}$ . Consequently,  $p$  decreases with increasing density as the sheath becomes ever thinner, with the result that the first and second order terms in the quadratic expansions of the MacLauren series coefficients disappear in the limit where  $p$  tends to zero. Though it is noted that the constant terms (cf. tables 2.1 and 2.2) are not exactly equal to the Langmuir-Blodgett coefficients [74, 75], due to the fact that  $a_n$  and  $b_n$  are fitted for a given

range of  $p$ , they are sufficiently close that convergence between the generalised and the Langmuir-Blodgett series can easily be recognised. Nevertheless, the densities required for  $p$  to approach zero are unrealistically high for practical ion extractors. A density of  $10^{14} \text{ cm}^{-3}$  is on the limit of practicality and only engenders a  $p$  of  $1.537610^{-3}$ . Therefore in most practical circumstances, the generalised series coefficients are disparate to those in the Langmuir-Blodgett case, and increasingly so, as the plasma density is lowered (cf. figure 2.6).

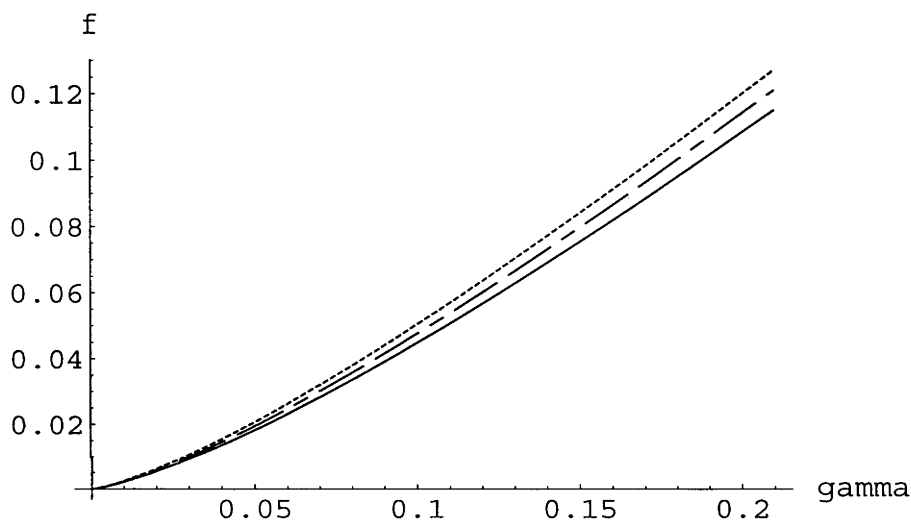


Figure 2.6: The function  $f$  versus  $\gamma$  for various values of the parameter  $p$  compared to the Langmuir-Blodgett distribution. Solid line: Langmuir-Blodgett distribution. Dashed line:  $n = 10^{14} \text{ cm}^{-3}$  ( $p = 0.013293$ ). Dotted line:  $n = 10^{13} \text{ cm}^{-3}$  ( $p = 0.028525$ ).

The range of  $\gamma$  over which the generalised series representation is accurate depends on the number of terms in the series. However, as can be seen in figure 2.7, the six term generalised series solution has an error of less than  $10^{-5}$  for  $\gamma < 3$ . By way of comparison a 4-term and 6-term Langmuir-Blodgett series is plotted against the exact solution, for an initial gradient of zero, in figure 2.8. There is a clear deviation from the exact solution at  $\gamma = 1.5$  and  $\gamma = 2.5$  respectively. As a reference to the scale magnitude of  $\gamma$ , we consider a  $5^\circ$  diverging beam extracted through a 1 mm

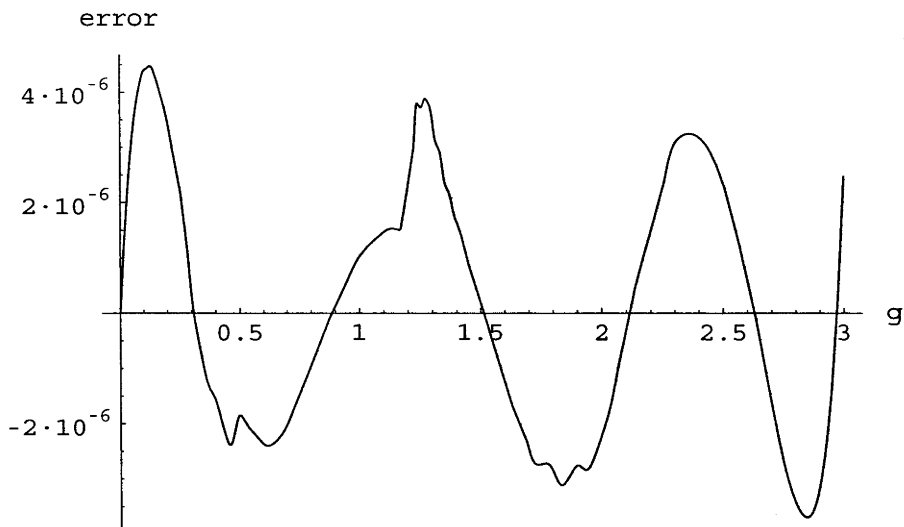


Figure 2.7: Error of the first 6 terms of the generalised series solution relative to the exact solution as a function of  $\gamma$  (here  $g = \gamma$ ). Spherical case.

circular aperture. In this case the meniscus curvature  $r_m = 5.737$  mm, so that a  $\gamma$  of 3 represents a beam length of 115 mm. The inter-electrode spacing in extraction gaps is typically only a few millimetres so that in most practical cases  $\gamma$  is less than unity.

Using a quadratic representation for the series coefficients  $a_n$  and  $b_n$ , the accuracy of the series solutions can be maintained to within  $10^{-5}$  for values of  $p < 0.1$ . This means that almost exact distributions can be calculated for densities down to  $2 \cdot 10^{11} \text{ cm}^{-3}$  and to within  $10^{-3}$  for densities down to  $10^9 \text{ cm}^{-3}$ .

### 2.2.3 Solving Poisson's Law Backwards

To solve this we consider the standard Langmuir-Blodgett problem in reverse, solving the differential equations from the exit of the extractor where the gradient is zero to the entry where it is large. This is tantamount to reversing the distribution in the case of a parallel beam or solving for the opposite convergence in the case of

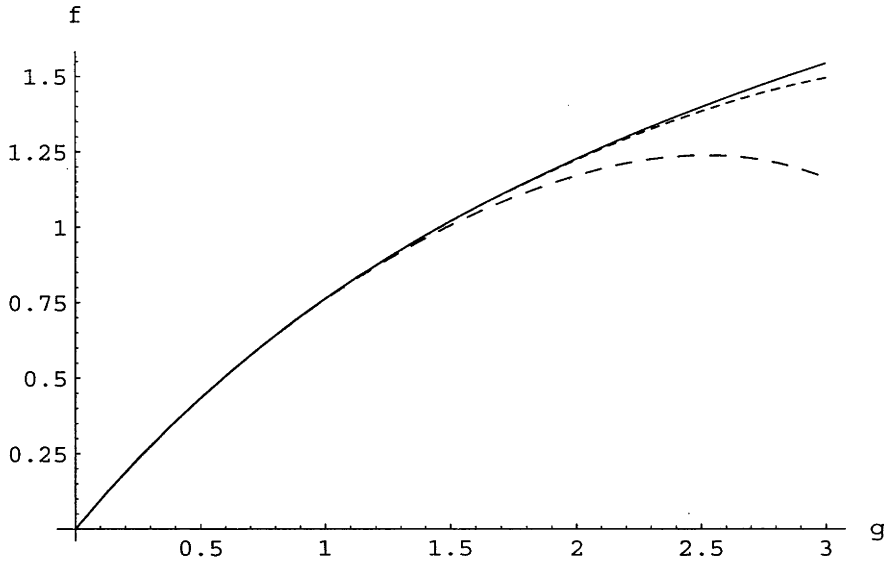


Figure 2.8: Range of the 4-term (long dash) and 6-term (short dash) series solutions as a function of  $\gamma$  (here  $g = \gamma$ ). The solid line is the exact solution.

divergent or convergent beams.

The  $f$  and  $g$  series as defined by 2.10 and 2.19 remain unchanged, however the definition of  $R$  and hence  $\gamma$  is altered. In the case of a diverging beam,  $R$  is taken to be the ratio of the current position to the first concentric surface and thus greater than unity. But in the case where Poisson's equation is solved backwards it is redefined to be the ratio of the current position to the second concentric surface and hence less than one. The inverse is true for a convergent beam.

### 2.2.4 Presence of Electrons

To account for the presence of a population of electrons arriving from the tail of a Maxwellian distribution we simply add an exponential term to the original differential equations to account for the Boltzmann relation.

Generalising for the presence of electrons involves only the RHS of Poisson's law:

$$\frac{\rho}{\epsilon_0} = \frac{e(n_i - n_e)}{\epsilon_0} \quad (2.29)$$



Since the electrons belong to a Maxwellian distribution their density as a function of potential is given by Boltzmann's relation:

$$n_e = n_0 \exp\left(\frac{eV}{kT_e}\right) \quad (2.30)$$

where  $n_0$  is some percentage  $\zeta$  of the ion density in the beam aft of the extractor to take into account the fact that neutralisation is not always 100%. The differential equations for spherical and cylindrical symmetry then become:

$$r^2V'' + 2rV' = 0.6ne\left[\frac{\tilde{A}}{\sqrt{V}} + \zeta \exp(C)\right], \quad \text{where } \tilde{A} = v_B \mathcal{A} \sqrt{\frac{M}{2e}} \quad (2.31)$$

and

$$rV'' + V' = 0.6ne\left[\frac{\tilde{B}}{\sqrt{V}} + \zeta \exp(C)\right], \quad \text{where } \tilde{B} = v_B \sqrt{\frac{M}{2e}} \quad (2.32)$$

where  $n$  is the ion density in the beam,  $\mathcal{A}$  is the area of the anode and  $C = \frac{eV}{kT_e}$ . Here the solutions take a very different form to those presented previously on account of the exponential term. However, it is possible to give a solution of the potential in terms of a MacLauren series, which when suitably normalised yields the correct form for implementation in the solutions to Laplace's equation. This has not been done here.

### 2.2.5 Non-Zero Initial Velocity

The problem is set out in the same fashion as in section 2.2.1 for negligible initial velocity, except that now the kinetic energy relation is written:

$$\frac{1}{2}Mv^2 - \frac{1}{2}Mv_0^2 = eV \quad (2.33)$$

This when rearranged yields:

$$v = \sqrt{2\frac{e}{M}V + v_0^2} \quad (2.34)$$

But since:

$$v_0^2 = \sqrt{2\frac{e}{M}V_{ext}} \quad (2.35)$$

where  $V_{ext}$  is the energy of the particles at the exit of the previous stage, the differential equations stipulated by Poisson's law become for spherical and cylindrical symmetries:

$$r^2V'' + 2rV' = \frac{A}{\sqrt{V + V_{ext}}} \quad (2.36)$$

and

$$rV'' + V' = \frac{B}{\sqrt{V + V_{ext}}} \quad (2.37)$$

And the solutions to these equations become:

$$V = \left(\frac{9}{4}A\right)^{\frac{2}{3}}f^{\frac{4}{3}} - V_{ext} \quad (2.38)$$

and

$$V = \left(\frac{9}{2}Br\right)^{\frac{2}{3}}g^{\frac{4}{3}} - V_{ext} \quad (2.39)$$

Importantly, upon substituting 2.38 into 2.36 and 2.39 into 2.37, 2.9 and 2.14 remain unchanged. This means that the initial velocity serves only to translate the solution vertically. The  $f$  and  $g$  series can still be obtained by the various means set out previously in this section.

## 2.3 Laplace's Equation

In a given region of the extractor, determining the electrode geometry amounts to solving Laplace's equation subject to the potential along the beam edge. Since in the three cases of interest, planar, cylindrical and spherical geometry, there is strong symmetry, this means that compact solutions can be obtained. These were presented by Radley [100] in 1957 along with a complete and rigorous mathematical derivation. A cursory overview of that paper is provided in the following.

However, before doing so, it is noted that in treating the instability issues of the solution, Radley remarks that in as much as small variations of the initial surface can produce large differences in the solution so, conversely, do relatively large variations in electrode shapes away from the beam surface produce only small variations in

the form of the beam surface. This will have important implications in the section *Method for Electrode Design* because electrodes will have to be curtailed to avoid overlap or break-down proximity.

### 2.3.1 Strip Beam

A strip beam can be thought of as an infinite plane diode in which the cathode is the plane  $x = 0$  and all charge in the region  $y > 0$  has been suppressed. To

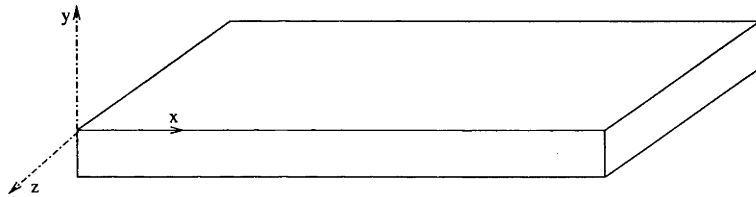


Figure 2.9: Strip Beam

determine electrodes that would extract a beam of this sort we must find a family of equipotentials in  $y > 0$  such that the conditions in  $y < 0$  are unchanged. The basic case of the potential distribution in space-charge limited flow when suitably normalised yields:

$$V = x^{\frac{4}{3}}, \quad \text{in } y \leq 0 \quad (2.40)$$

Since, assuming zero ion temperature, the trajectories are rectilinear and perpendicular to the emission surface defined by the extraction slit, the transverse forces on the beam at the beam edge are zero, so that  $\delta V / \delta y = 0$  there. Restating the conditions in polar coordinates, we have:

$$\left. \begin{array}{l} V = r^{\frac{4}{3}} \\ \frac{\delta V}{\delta \theta} = 0 \end{array} \right\} \text{ on } \theta = 0 \quad (2.41)$$

The solution in Cartesian coordinates is:

$$V(x, y) = \text{Re}\{z^{\frac{4}{3}}\} \quad (2.42)$$

where

$$z = x + iy = re^{i\theta} \quad (2.43)$$

so that the solution is given by the conformal mapping:

$$W = V + iU = z^{\frac{4}{3}} \quad (2.44)$$

first presented by Pierce [97] in 1940.

### 2.3.2 Wedge Beam

For a wedge beam it is assumed that the meniscus and 0 V equipotential surfaces are concentric cylinders. We therefore choose the coordinate system so that the origin is at the vertex of the wedge, and the beam surface lies on  $\theta = 0$ . Since the

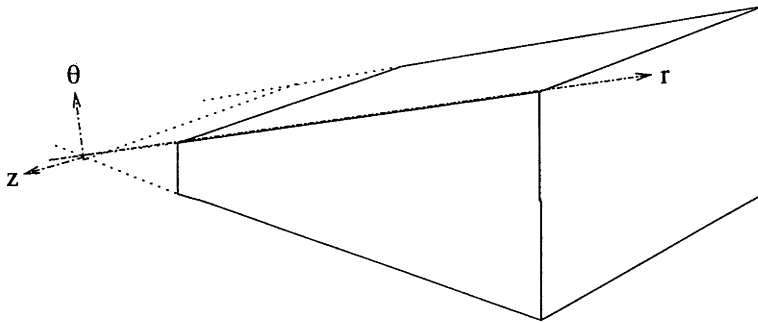


Figure 2.10: Wedge Beam

trajectories are rectilinear, lying along the lines  $\theta = \text{const.}$ ,  $\delta V/\delta\theta = 0$  on  $\theta = 0$ . We take the meniscus to be  $r = r_m$  and the cathode to lie somewhere in the region  $r > r_m$  in the case of divergent beams and  $r < r_m$  in the case of convergent beams. In what follows we shall assume that the ratio  $R = r/r_m$  is greater than unity or that the wedge is divergent. The potential distribution along the beam edge, when suitably normalised, is given by:

$$V = R^{\frac{2}{3}}\beta^{\frac{4}{3}} \quad (2.45)$$

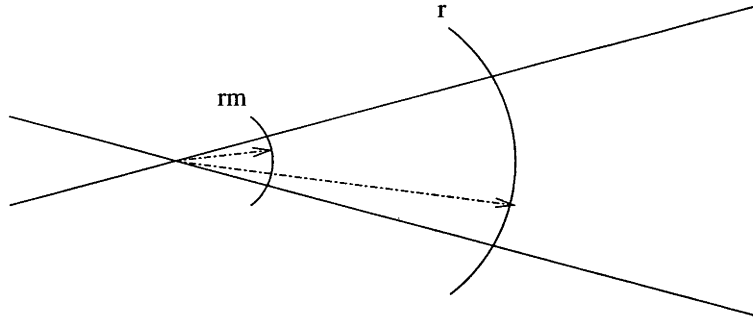


Figure 2.11: Illustration of the radial parameters  $r_m$  and  $r$  in a divergent beam.

where  $\beta$  is an infinite power series in the variable  $\gamma = \ln(R)$ . (2.45) can be rewritten in series form:

$$V = R^{\frac{2}{3}} \left[ \sum_{n=1}^{\infty} a_n \gamma^n \right]^{\frac{4}{3}} \quad (2.46)$$

Since  $a_1 = 1$ , this last expression may be expanded by the multinomial theorem, to give:

$$V = R^{\frac{2}{3}} \gamma^{\frac{4}{3}} \sum_{n=1}^{\infty} b_n \gamma^{n-1} \quad (2.47)$$

The coefficients,  $b_n$ , will be presented and discussed later. The potential outside the beam is obtained by writing  $Re^{i\theta}$  for  $R$  in (2.45). Thus  $\gamma$  is replaced by  $\omega = \gamma + i\theta$ , so that:

$$V = Re \left[ R^{\frac{2}{3}} e^{\frac{2}{3}i\theta} \omega^{\frac{4}{3}} \sum_{n=1}^{\infty} b_n \omega^{n-1} \right] \quad (2.48)$$

### 2.3.3 Cylindrical Beam

We employ for this case cylindrical polar coordinates  $(r, \theta, z)$ , with the axis of the beam along  $r = 0$ . By suitably normalising the coordinates, we may take the beam surface as  $r = 1$ . Since the system has axial symmetry, none of the variables involves  $\theta$ , so we may neglect this coordinate. The ion flow considered is a cylindrical section of an infinite plane diode so that we may again write:

$$\left. \begin{aligned} V &= z^{\frac{4}{3}} \\ \delta V / \delta r &= 0 \end{aligned} \right\} \text{ on } r = 1 \quad (2.49)$$

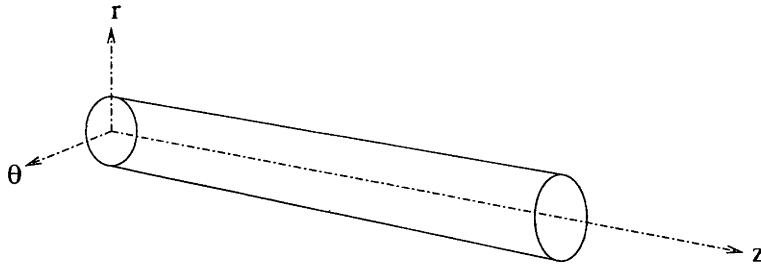


Figure 2.12: Cylindrical Beam

Applying Radley's analysis, the solution is:

$$V(r, z) = \frac{1}{2\pi} \frac{1}{(-\frac{7}{3})!(\exp(-\frac{14i\pi}{3}) - 1)} \int_C \frac{\exp(-pz)}{p^{\frac{4}{3}}} (J_1(p)Y_0(pr) - Y_1(p)J_0(pr)) dp \quad (2.50)$$

where  $p$  is a complex parameter,  $J$  and  $Y$  are Bessel functions of the first and second kind and  $C$  is the contour defined by:

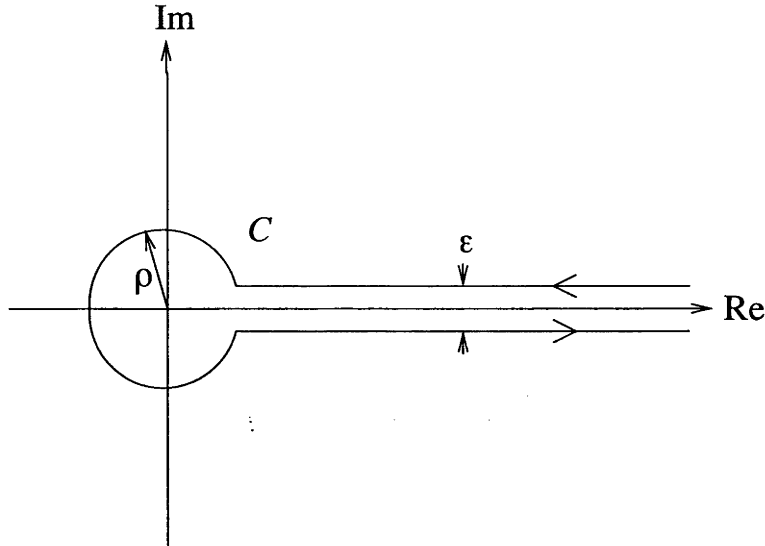


Figure 2.13: Contour of integration,  $C$ , in the complex plane.

In practice, the contribution of both straight line segments in  $C$  cancel and the contour reduces to a circle of radius  $\rho$ . In theory any value of  $\rho$  will work but we

found that values of between 1 and 5 produced the most rapid and accurate results.

### 2.3.4 Conical Beam

We employ spherical polar coordinates  $(r, \theta, \phi)$ , with a cone half-angle of  $\theta = \theta_0$ , the anode on the sphere  $R = 1$  and the cathode in the region  $R > 1$  in the case of a diverging beam and  $R < 1$  in the case of a converging beam. Again, we assume a diverging beam for the present derivation. Writing  $\gamma = \ln(R)$  and suitably

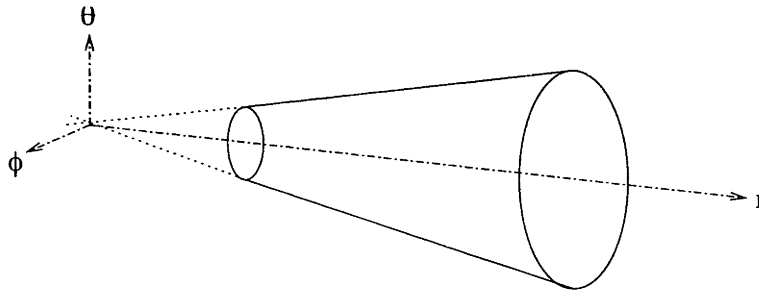


Figure 2.14: Conical Beam

normalising the potential we arrive at:

$$V = f^{\frac{4}{3}} \quad (2.51)$$

where

$$f = \sum_{n=1}^{\infty} c_n \gamma^n \quad (2.52)$$

The coefficients  $c_n$  depend on the boundary conditions for the beam as discussed in the previous sections. Again this series representation is expanded using the multinomial theorem and becomes:

$$V = \gamma^{\frac{4}{3}} \sum_{n=1}^{\infty} d_n \gamma^{n-1} \quad (2.53)$$

The boundary conditions to be applied are:

$$\left. \begin{array}{l} V = f^{\frac{4}{3}} \\ \frac{\delta V}{\delta r} = 0 \end{array} \right\} \text{ on } \theta = \theta_0 \quad (2.54)$$

and following Radley we arrive at:

$$V(r, \theta) = \sum_{n=1}^{\infty} \frac{d_n \sin^2(\theta_0)}{(\exp(-\frac{14i\pi}{3}) - 1)(-n - \frac{4}{3})!} \int_{\mathcal{C}} \frac{\exp(-\nu\gamma)}{\nu^{n+\frac{4}{3}}} (P_{\nu}(\mu)Q'_{\nu}(\mu_0) - Q_{\nu}(\mu)P'_{\nu}(\mu_0)) d\nu \quad (2.55)$$

where  $\nu$  is a complex variable,  $P_{\nu}$  and  $Q_{\nu}$  are Legendre functions of the first and second kind and  $\mathcal{C}$  is the contour defined in fig. 2.13. Again the straight line segments cancel so that the contour reduces to a circle, however, now the radius  $\rho$  is dependent on  $R$ .

## 2.4 Method for the Design of Electrodes

### 2.4.1 Introduction

The work presented by Radley [100], and others [50, 28]), in essence provides a solution for Laplace's equation but not a complete method for the design of low emittance extractors.

The first step in the design of electrodes is the choice of beam type, beam current and final extraction energy. For each choice there is a different electrode design. It must be determined from the first instance whether the beam is to be strip/wedge or cylindrical/conical and whether it is to be parallel, convergent or divergent. It must be kept in mind that the whole extractor is to act as if the beam was part of an entire diode from the plasma to the 0 V equipotential. A first glance at the electrode design will now show that the extractor apertures follow the beam shape so that they are just in contact with the beam at their respective positions.

### 2.4.2 The Extraction Gaps

#### Stage 1

The extraction gap stage 1 comprises the aft face of the Plasma electrode and front face of the Accel electrode. To determine the beam distribution in this region,



we must first take into account that the electric field at the plasma/beam boundary is non-zero due to the plasma sheath, then, given the beam form required the relevant solution can be arrived at by following the derivations of section 2.2. This in turn is substituted into the relevant solution from section 2.3. Note that in this region the potential distribution is convex and that the electric field at the exit of this region is very large.

### Stage 2

The extraction gap stage 2 comprises the aft face of the Accel electrode and the front face of the first Blocking electrode. The purpose of stage 2 is primarily to bring the electric field at the exit of stage 1 to zero. This prevents it from ballooning out aft of the Accel aperture and inducing strong aberration and readjustment of the beam charge distribution leading to non-uniformity in the beam and reshaping of the meniscus away from the ideal plane, cylinder or sphere. The potential distribution in this region is obtained by solving Poisson's law backwards and assuming a non-negligible initial velocity. Again this expression is substituted into the relevant solution from section 2.3.

### The problem

Unfortunately, it seems that we have stumbled into an immutable law of nature. Laplace's equation, it seems, can not be solved (in the Real domain) for a boundary condition that changes convexity because this would require that the equipotentials overlap, which in terms of electrodes means that they would need to occupy the same space. In fact, this is only a major problem for the intermediate electrode and a solution is to shape an electrode that is the median between the two ideal cases. It should be noted that close to the beam, the two equipotentials are almost identical and that away from the beam they are not strongly disparate.

Though the outer electrodes would eventually also overlap, and in practical terms

would approach each other so that the inter-electrode gap would lead to break down, Radley has indicated that the effect of the electrodes away from the beam edge is increasingly negligible. Thus as a best approximation to an ideal extractor, the outer electrodes are made to extend to just outside break-down distance and the intermediate electrode is made to be the average of the two ideal equipotentials.

### 2.4.3 Blocking Electrodes

The Extraction electrodes have accelerated the beam just beyond the desired extraction energy and have done so in such a way that the electric field at the exit of stage 2 is  $0 \text{ V.m}^{-1}$ . Since we are extracting positive ions, this means that the voltage at the exit of the Extraction region stage 2 is some negative value. The purpose of the Blocking electrodes is then to bring the beam potential back up to  $0 \text{ V}$  whilst ensuring that the electric field upon exit is  $0 \text{ V.m}^{-1}$ . Assuming that this Blocking potential is sufficiently high this impedes the flow of electrons from aft of the extractor to the Extraction region.

Since the potential gradient is zero upon entry to the Blocking electrode stage 1, the initial velocity generalisation of the Langmuir-Blodgett representation can be used for the beam potential. For stage 2, however, the presence of electrons can not be ignored since a population of higher energy electrons from the tail of the distribution will be able to penetrate some distance up the potential wall. To solve for this distribution the relation given in section 2.2.4 is employed. This potential distribution is then substituted into the relevant solution from section 2.3.

### 2.4.4 Beam Neutralisation

Beam neutralisation is necessary aft of the extractor to compensate the considerable beam space charge. In many practical situations, secondary electron emission from sputtering will be sufficient to provide a population of neutralising electrons. However, if this were not the case, some electron source would be required such as

a hollow cathode. In this situation emphasis should be given to ensuring that the electrons are as low energy as possible to avoid needing a large Blocking potential.

## 2.5 An Example: A Diverging Wedge Beam

As an example, we consider the case of a  $5^\circ$  diverging beam as extracted through a 1 mm wide, 1m long rectangular slit. The plasma source is assumed to be a Krypton plasma of density  $10^{13} \text{ cm}^{-3}$  at the sheath edge. The total extraction energy is 20 kV and the total blocking energy 200 V.

### Extraction Gap Stage 1

As previously mentioned, the problem can be considered analogous to that of a complete cylindrical diode. For a  $5^\circ$  diverging beam extracted through a 1 mm slit the meniscus curvature is  $r_s = 5.737 \text{ mm}$ . To calculate the potential distribution in the gap, the potential gradient at the meniscus edge must first be determined. The current density flowing across the meniscus yields  $B = 7.622 \cdot 10^8$  according to (2.12). The ratio of the sheath to the pre-sheath is given by first solving (2.6) for the boundary conditions set in (2.26):

$$\beta(\gamma_m) = \frac{15^{\frac{3}{4}}}{\sqrt{\frac{9}{2}Br_m}} = 1.71827 \cdot 10^{-3} \quad (2.56)$$

and then solving (2.19) to find  $\gamma_m = 1.71797 \cdot 10^{-3}$ . From (2.7) we get  $R = 1.00172$  so that the sheath width is given by:

$$1.00172r_s - r_s = 9.9 \mu\text{m} \quad (2.57)$$

The gradient at the sheath edge in terms of  $\gamma_m$  is:

$$\frac{dV}{d\gamma}(\gamma_m = 1.71827 \cdot 10^{-3}) = 11644 \text{ V/unit} \quad (2.58)$$

Since  $\gamma = \ln(r/r_s)$ ,  $d\gamma = dr/r$  which means:

$$\frac{dV}{dr}(r_m) \simeq \frac{1}{5.737 \cdot 10^{-3}} \frac{dV}{d\gamma} = 2.03 \cdot 10^6 \text{ V.m}^{-1} \quad (2.59)$$

According to (2.18),  $p = 1.43557 \cdot 10^{-2}$  which we note is well below the established limit of  $p_{\text{limit}} = 0.15$ . In combining table 2.2 and equation (2.20) we find the series expansion of  $g$ :

$$1.05846\gamma - 0.521406\gamma^2 + 0.209569\gamma^3 - 0.0738154\gamma^4 + 0.0165584\gamma^5 - 0.00157496\gamma^6 \quad (2.60)$$

and hence an expression for the voltage in terms of  $\gamma$  through relation (2.13).

Using the multinomial theorem we rewrite (2.60) to give the form:

$$1.0787 - 0.708501\gamma + 0.342937\gamma^2 - 0.140694\gamma^3 + 0.0419959\gamma^4 - 0.00842186\gamma^5 \quad (2.61)$$

Since the wedge is divergent  $\gamma = \ln(R)$ , and we solve (2.48) with

$$\begin{cases} R = \sqrt{\tilde{x}^2 + \tilde{y}^2} \\ \theta = \tan^{-1}\left(\frac{\tilde{y}}{\tilde{x}}\right) \end{cases} \quad (2.62)$$

where the non-normalised coordinates are:

$$\begin{cases} x = r_m \tilde{x} \\ y = r_m \tilde{y} \end{cases} \quad (2.63)$$

For the aft face of the plasma electrode we solve (2.48) for  $V = 0$ . To solve for the front face of the Accel electrode we solve for:

$$V = \frac{10100}{\left(\frac{9}{2}Br_m\right)^{\frac{2}{3}}} = 0.138575 \quad (2.64)$$

which is a direct consequence of (2.45).

### Extraction Gap Stage 2

At the entry to stage 2,  $V_{\text{ext}} = 10100$  V. The solution to the  $g$  series is given by the standard Langmuir-Blodgett relation but derived backwards. Hence we substitute:

$$g = \gamma + 0.4\gamma^2 + 0.0916667\gamma^3 + 0.01424242\gamma^4 + 0.001679275\gamma^5 + 0.0001612219\gamma^6 \quad (2.65)$$

into equation (2.48), but with  $\gamma = -\ln(r/r_d)$  where  $r_d$  is the radius of the concentric surface at the exit of the stage. At this point in the calculation  $r_d$  is unknown, but by an iterative process a value can be found such that the potential gradient at  $r_a$  at the entry to the stage is equal to that of the distribution at the exit of the previous stage. We define:

$$\gamma_a = -\ln\left(\frac{r_a}{r_d}\right) \quad (2.66)$$

so that:

$$e^{-\gamma_a} = \frac{r_a}{r_d} \quad (2.67)$$

and:

$$r_d = r_a e^{\gamma_a} \quad (2.68)$$

We solve for  $\gamma_a$  so that:

$$\frac{dV}{d\gamma}(\gamma_a^-) |_{\text{stage}_1} = \frac{dV}{d\gamma}(\gamma_a^+) |_{\text{stage}_2} = 63586 \text{ V/unit} \quad (2.69)$$

noting that the g series in stage 1 is different to that in stage 2. We find that  $\gamma_a = 0.35464$ . The voltage at  $\gamma_a$  is  $V = 0.239885$  according to (2.45).

The Decel 1 electrode front face is calculated by solving (2.48) for  $V = 0$  and the Accel aft face is calculated by solving (2.48) for  $V = 0.239885$ . It should be noted that the acceleration voltage in this gap is 17484 V which is significantly higher than 10100 V. To achieve a total acceleration energy of exactly 20000 V, an iterative approach will be required. But since this does not benefit the illustration of the method, this will not be done here.

Because the particles have an initial energy of 10100 V, the basic solution is shifted up by this amount.

The final Accel electrode will be the median of the Accel front face and Accel aft face. In practice this electrode should be made as thin as possible especially in the region close to the beam edge.

## Blocking Gap Stage 1

Since we require a blocking voltage of 200 V we assume that the voltage in this stage is 100 V. We solve the standard Langmuir-Blodgett relation to determine the gap size. This yields  $\gamma = 0.00712381$ . Then to solve for this stage we simply replace the standard Langmuir-Blodgett relation into (2.48). For the Decel 1 aft face we solve  $V = 0$  and for the Decel 2 front face we solve  $V = 0.00137203$ . The final solution is shifted up by 27584 V.

## Blocking Gap Stage 2

At this stage the solutions for the Poisson equation with the presence of Maxwellian electrons has not been resolved. For this reason we present an analysis that does not assume the presence of electrons.

The gradient at the entry to the stage is 18729 V/unit. We again use the Langmuir-Blodgett relation considered backwards. The gap spacing that gives a gradient of 18729 V/unit at the gap entry is  $\gamma = .007196$ . The normalised voltage at this point is  $V = 0.00138794$ . To solve for the Decel 2 aft face we solve (2.48) for  $V = 0$ . To solve for the ground front face we solve for  $V = 0.00138794$ .

## 2.5.1 Closing remarks

The electrodes defined in the the previous sections assumed, for convenience, negative ions being extracted from 0 up to 27584 V. The electrodes for the extraction of positive ions are identical except that the polarity of the field is reversed. Under this scheme ions are extracted from 27584 V down to 0 V. The electrodes are shown in figure 2.15 and a close up of the Blocking electrodes is shown in figure 2.16. These figures represent the calculated front and aft faces of the various electrodes, starting with the Plasma electrode on the left and finishing with the Ground electrode on the right. All the electrodes, except the Plasma electrode, terminate above the horizontal axis along a line that represents the beam edge ( $5^\circ$  half angle).

Only the aft face of the Plasma electrode is represented because the front face, in contact with the plasma, does not effect the extraction optics. The Accel and Decel 2 electrodes are both lines, being the median of the aft and front faces of the calculated electrode geometries. In reality these electrodes would have some thickness to ensure mechanical stability. The Decel 1 electrode (in the shape of an almond) is represented here with a foreshortened front face. This was as a result of an oversight in implementing the analytical solutions to Laplace's equation in Mathematica and can easily be remedied but was not done here due to time constraints. Nonetheless, in light of Radley's stability analysis on the solutions to Laplace's equation under Cauchy boundary conditions [100], the electrode presented here is probably sufficient to induce concentric equipotentials inside the beam as it does not need to extend far away from the beam to operate effectively.

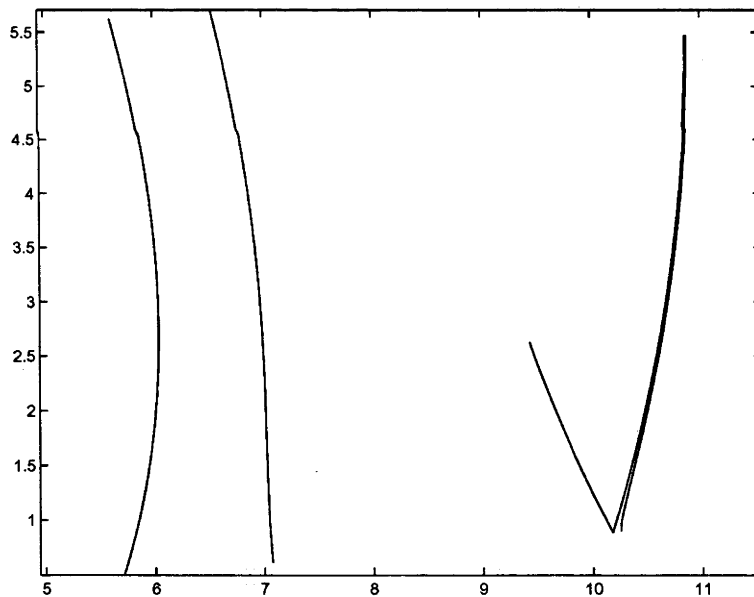


Figure 2.15: Electrode geometries for the extraction of a  $5^\circ$  diverging wedge beam.

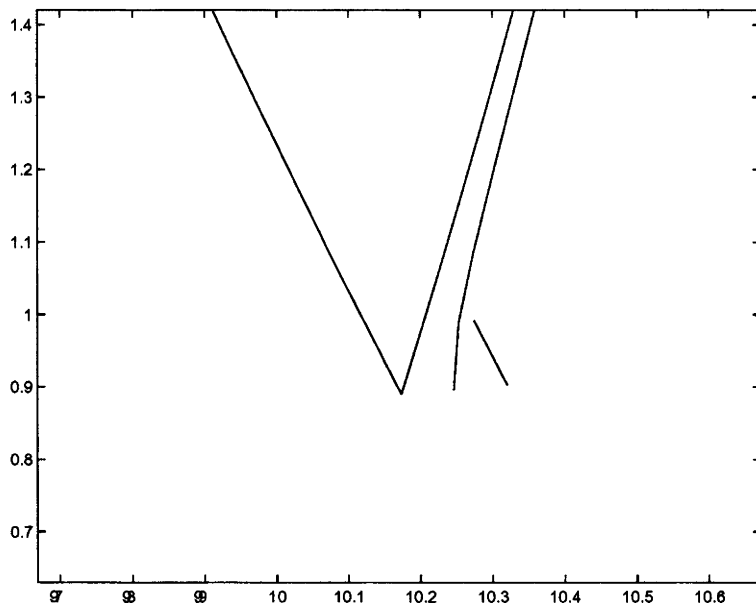


Figure 2.16: Electrode geometries for the extraction of a  $5^\circ$  diverging wedge beam. Close up of Blocking electrodes.

### Simulations

A short series of simulations was performed by Masis Mkrtchyan using Lorentz

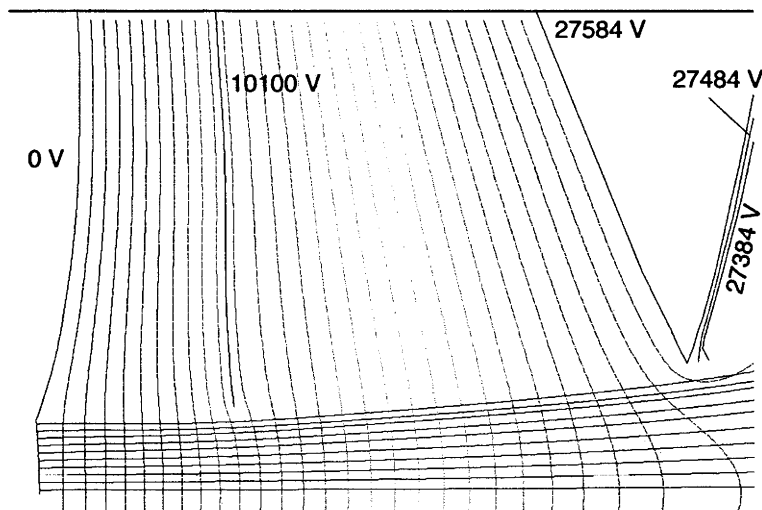


Figure 2.17: Lorentz 2D simulation of ideal electrodes. Courtesy FEI Co.



2D under contract to FEI Co. The simulations accounted for the electrodes' generated electric field and the beam space charge but did not model the plasma meniscus or the thermal energy of the emitted particles. Figure 2.17 shows the simulation of the ideal electrodes. The most striking feature of this result is the concentricity of the equipotential surfaces inside the beam, starting at the emission surface on the left and progressing all the way through the extractor to the right. There is some residual ballooning through the Blocking stage but this is most likely due to the absence of a fixed boundary at the right wall. This allowed the right boundary to charge up and Masis did not have the time to remedy this by placing a concentric 0 V sink at the exit to the extractor. It is noted, however, that the electric field on the ballooning equipotentials is very small as can be seen in figure 2.18 where the gradient of the potential distributions in the beam tapers off smoothly to zero. In

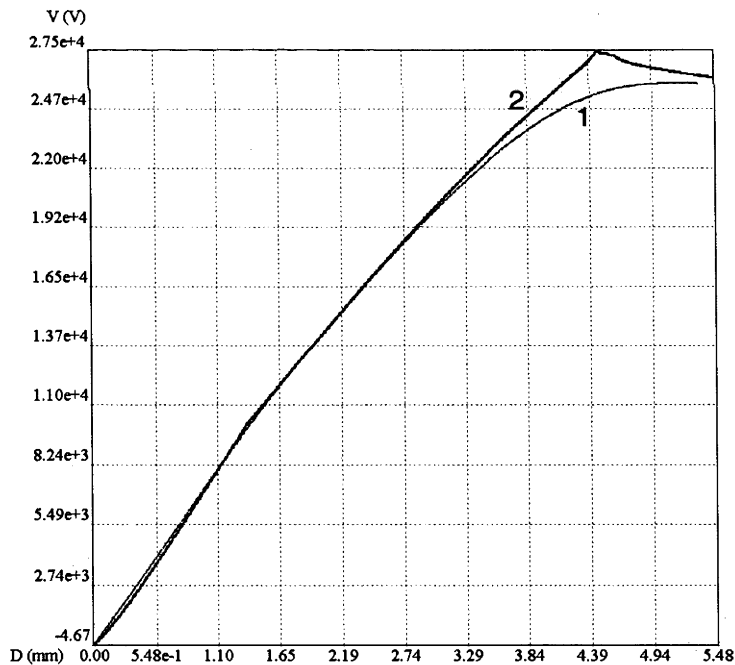


Figure 2.18: Potential distribution along the beam of the ideal electrode. 1: along the axis of symmetry. 2: along the chord joining the edge of the Plasma electrode and the edge of the Ground electrode.

particular, the chord joining the edge of the Plasma electrode to the final Blocking electrode is represented by curve 2 and shows the characteristic hump of the Blocking potential. Curve 1, which corresponds to the potential along the axis of the beam, does not have this hump and is almost certainly missing due to the equipotential ballooning through the Blocking electrodes. The absence of the Blocking potential along the beam axis would therefore be an artifice of the simulation.

The equipotentials around the Accel electrode (10100 V) deviate from the ideal curvature. This is probably because the electrode itself is an approximation, though the effect of neglecting the plasma meniscus field can not be discounted. In any case, with further investigation a more appropriate approximation to the Accel electrode could be determined if necessary.

Finally, the equipotentials close to the emission surface are more parallel than expected which causes the beam envelope to be parallel initially (instead of divergent) resulting in a slight kink under the Accel electrode. This is most likely due to the

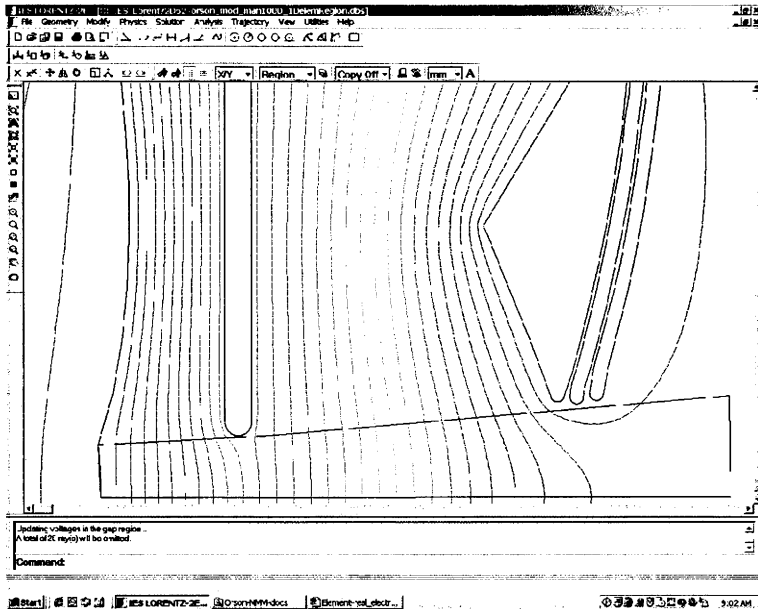


Figure 2.19: Lorentz 2D simulation of "real" electrodes. Courtesy of FEI Co.

meniscus field not being taken into account by the simulation and if it had would probably have resulted in the beam envelope following the electrode apertures more closely.

To assess how the electrodes might work with manufacturable dimensions a simple proof of concept design was simulated. The Accel electrode was designed to be a simple perforated sheet, but the Plasma and Decel 1 electrodes were close to ideal. As shown in figure 2.19 these "real" electrodes do not appear to perform significantly differently to the ideal case, however, the equipotentials just aft of the Accel electrode are no longer concentric but parallel due to the planar nature of the electrode. Nonetheless, this is an encouraging result especially since there is some scope to improve the Accel electrode.

Figure 2.20 shows the emittance at three locations in the beam for the "real" extractor and demonstrates that the design results in low emittance growth. In particular, the emittance at the exit to the extractor ( $\circ$ ) converges to the emittance value at

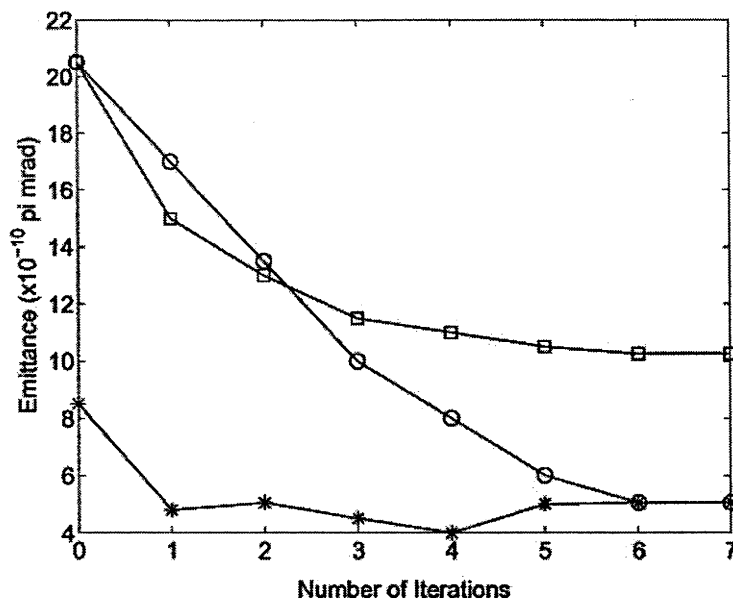


Figure 2.20: Emittance as a function of the number of iterations. \*: at the emission surface. □: mid-point between the emission surface and the exit surface. ○: at the exit surface.

the emission surface (\*) after 5 iterations of the code (required for the effect of the beam space charge to take effect). It is unclear why the emittance at the mid-point between the emission and exit positions ( $\square$ ) is double this value but it is probably due to the parallel equipotentials forcing the particles to follow non-rectilinear trajectories.

That there is any emittance at all (especially at the emission surface) is most likely due to the planar equipotentials in the first extraction gap and hence is a result of the meniscus potential not being taken into account by the simulation. Given that the particles are emitted at right angles to the emission surface and that this surface is a 2D cross section of a cylinder, the particles are initially accelerated along non-rectilinear trajectories as they enter the extraction gap. This deviates from the assumptions of the theory and as a result probably causes a small amount of geometric aberration.

No emittance plots were produced for the ideal case.

### Plasma Density Range

An important consequence of this work is that there is a limit to how high the extraction energy can be taken as a function of density and beam form. For example, at a plasma density of  $10^{14} \text{ cm}^{-3}$ , no wedge beam form can be extracted without aberration because the minimum voltage per meter required for extraction is in excess of the breakdown limit of  $10^7 \text{ V.m}^{-1}$ . Figure 2.21 compares extraction voltage as a function of inter-electrode spacing (in terms of the dimensionless variable  $\gamma$ ) for a  $5^\circ$  diverging and converging beam extracted from a  $10^{13} \text{ cm}^{-3}$  plasma. A line representing the  $10^7 \text{ V.m}^{-1}$  breakdown condition is plotted with these curves. At  $10^{13} \text{ cm}^{-3}$  extraction of all beam forms is possible, but for convergent beams the maximum extraction energy is capped at 20 kV in the stage 1 of the extraction region. Above this energy, the electrodes need to be too close for breakdown.

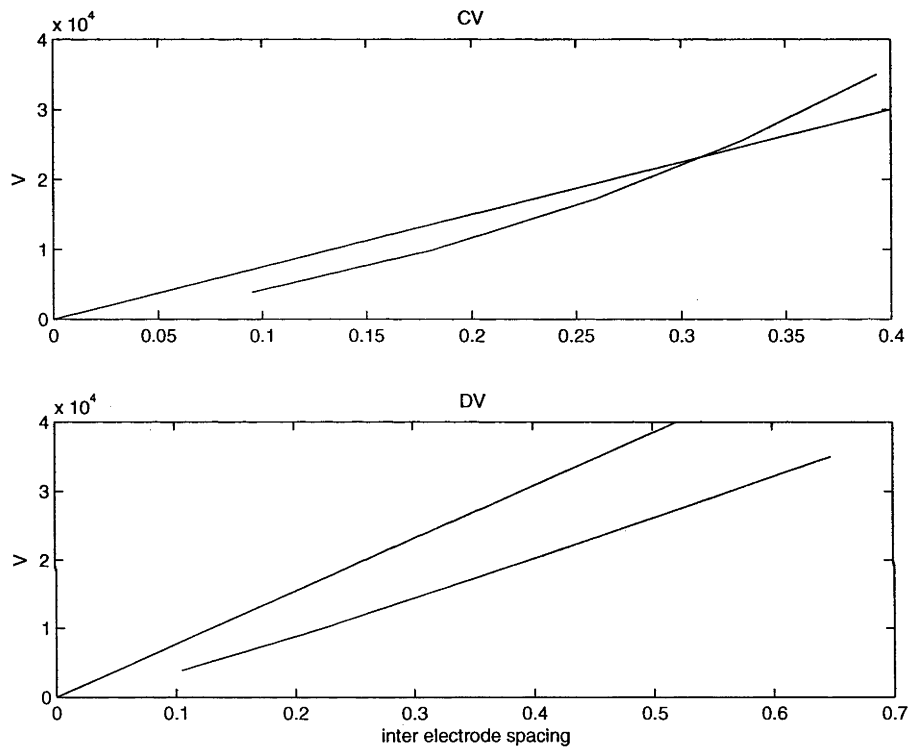


Figure 2.21: Evolution of Extraction Voltage as a function of inter-electrode spacing for a  $5^\circ$  convergent (CV) and divergent (DV) wedge beam. The plasma density is  $10^{13} \text{ cm}^{-3}$ . The breakdown limit is also graphed. It is the higher of the two curves in each respective graph.



# Diagnostics

## 3.1 Langmuir Probes

In its most basic form, a Langmuir probe consists of a small conducting surface, typically a cylinder or disk, to which a bias voltage is applied and a current is drawn from the plasma. If the bias voltage is swept over a sufficiently broad range then a current-voltage characteristic (I-V curve) is obtained that carries information about the plasma electron ( $n_e$ ) and ion ( $n_i$ ) densities, the electron temperature ( $T_e$ ), floating potential ( $V_f$ ) and plasma potential ( $V_p$ ). A large volume of literature exists on the physics of Langmuir Probes which can be cumbersome and is of limited interest to this work and so will not be reviewed in any great detail here, instead a simple interpretation of the measurement techniques used for this thesis will be outlined.

In the most simple model, ions are considered to enter the sheath surrounding the probe, of area  $A_s$ , at the ion sound speed,  $v_{Bohm}$  and fall perpendicularly towards the surface of the probe where they recombine with electrons producing a measurable current  $I^+$ . If the probe bias is sufficiently large and negative, then all neighbouring plasma electrons are repelled and the current measured on the probe is purely a function of the ion flux through the sheath [83]:

$$I^+ = 0.6en_i A_s v_{Bohm} \quad (3.1)$$

where  $e$  is the unit charge ( $1.6 \cdot 10^{-19}$  C),  $v_{Bohm}$  is the sound speed given by:

$$v_{Bohm} = \frac{kT_e}{M_i} \quad (3.2)$$

$k$  is the Boltzman constant,  $M_i$  is the ion mass and the factor 0.6 approximates the drop in density caused by the acceleration, in the presheath, of the ions up to the sound speed. Only  $A_s$  is a function of the bias voltage  $V_b$ , where for a cylindrical probe:

$$A_s = 2\pi s \quad (3.3)$$

and  $s$  is the sheath width given by the Langmuir-Blodgett law for space-charge limited flow between two concentric cylinders approximated by:

$$s = \frac{500V^{\frac{3}{4}}}{n^{\frac{1}{2}}T_e^{\frac{1}{4}}} \quad (3.4)$$

For a single sided disk probe a similar relationship can be derived, and provided the probe dimensions are much larger than the sheath thickness the relationship between the effective collection area  $A_s$  and the bias voltage can be ignored and replaced by the surface area,  $A_p$ , of the probe itself. This makes disk probes, in principal, simpler and more accurate to use for density measurements, but this is largely only true for low to medium density plasmas. For high density plasmas the probe dimensions must become so small, so as to not change the local plasma parameters, that probe construction becomes difficult and it is preferable to employ cylindrical probe tips which are much easier to build. Nevertheless, inside the column, measurements became unreliable and often led to probe degradation so that the best estimation of density could only be gained through microwave interferometry (c.f. 3.3.2).

For the purpose of calculating density, the electron temperature was approximated to be isotropic and 5 eV. This sits outside the range of 3-4 eV proposed by Ellingboe [37] and Porteous [99] (all be it for different experimental conditions) but on the



upper end of that proposed by Lieberman and Lichtenberg [83] for bounded equilibrium laboratory plasmas. As is detailed in chapter 5, the electron temperature in WOMBAT was highly anisotropic and varied between 1 and 8 eV, with large gradients particularly at the edge of the plasma column, making the above approximation somewhat strong. Nonetheless, it is noted that the sound speed goes as the square root of the electron temperature, so that for temperatures between 1 and 8 eV, the error in the ion velocity is less than  $\pm 30\%$ .

Attention is now turned to modelling the I-V curve in an effort to determine the electron temperature, the floating potential and the plasma potential. Ideally, to determine the electron temperature experimentally a full current-voltage trace, incorporating both ion and electron saturation currents, is required. In reality, electron saturation, even for very high bias voltages, was not attained and so some form of approximation was required. In a simple one dimensional model, the electron current collected by a probe of area,  $A_p$ , is:

$$I^- = eA_p \int_{v_{min}}^{\infty} v f(v) \cdot dv \quad (3.5)$$

where:

$$v_{min} = \left( \frac{2e(V_p - V_b)}{m_e} \right)^{\frac{1}{2}} \quad (3.6)$$

$m_e$  is the electron mass,  $f(v)$  is the electron distribution function to be found and  $V_b$  is the bias voltage on the probe. Typically, this is done by first stipulating a model for  $f(v)$  and then numerically fitting this to the experimental data. Commonly, the distribution function is assumed to be Maxwellian but it has been found by Cui [26], in WOMBAT, that for low pressures a bi-Maxwellian distribution can exist. There has also been some experimental evidence in the production of this work to suggest the presence of “hot electrons”, but this was not fully investigated and will be ignored here. If  $f(v)$  is assumed to be Maxwellian and the electrons are in

Boltzman equilibrium, then it can be shown that:

$$I^- \propto \exp\left(-\frac{eV_b}{kT_e}\right) \quad (3.7)$$

and the electron temperature can be determined by computing the inverse of the slope of  $\ln(I^-)$  as a function of  $V_b$ .

To determine  $V_f$ , we first recall that any floating object immersed in a plasma will attain a potential so as to have equal fluxes of electrons and ions to its surface and hence a net current of zero. On the I-V characteristic this corresponds to the point where the curve crosses the horizontal axis. Assuming, again, a Maxwellian distribution for the electrons, the null sum of fluxes yields the following approximate relationship:

$$V_p - V_f = \frac{kT_e}{2} \left( \ln\left(\frac{M_i}{2\pi m_e}\right) \right) \quad (3.8)$$

In reality, this relationship serves more to determine the plasma potential  $V_p$  than the floating potential which experimentally is very easy to measure by simply leaving a Langmuir probe open circuit and recording its potential to ground.

If it is assumed that  $V_f$  is known, equation 3.8 implies a strong relationship between electron temperature and plasma potential, both of which are often difficult to determine directly from a typical experimental I-V trace. However, for the data used in this work, a kink is still observed, roughly where  $V_p$  would be expected to lie (between 20 and 40 V) leading to an estimate of the plasma potential. The current-voltage characteristic can then be modelled by:

$$I(V) = a_0 - a_1V - a_2 \exp(a_3(V - V_p)) \quad (3.9)$$

where the  $a_i$ 's are the parameters to be determined by numerical fitting to the experimental data. The first two, linear, terms represent the ion saturation current and the exponential term models the Boltzmann distribution for the electrons. Some iteration was often required by varying  $V_p$  to obtain the best numerical fit but once

the numerical parameters had been determined, the electron temperature could be estimated by:

$$kT_e = \frac{1}{a_3} \quad (3.10)$$

Langmuir probes are an extremely expeditious way to measure local plasma properties due to their ease of manufacture and simplicity of use and are widely used in research and industry. However, measurements from these probes are open to broad interpretation especially in RF and magnetised plasmas, which remain areas of controversy (and the seed of lively debate at conferences). The literature is replete with reviews on the theory for a broad range of plasma conditions which include Chen [20], Godyak [44], Hershkowitz [54], Sugawara [114] and Lieberman and Lichtenberg [83]. Some of the issues are described briefly below.

A simple interpretation of the the I-V characteristic is made more difficult if significant RF radiation is present in the plasma. The plasma potential is caused to oscillate as:

$$V_p = \tilde{V}_p + V_{rf} \sin(\omega_{rf}.t) \quad (3.11)$$

where  $\tilde{V}_p$  is the background plasma potential,  $V_{rf}$  is the RF amplitude and  $\omega_{rf}$  is the RF frequency. As a result of the plasma potential oscillation, the electron distribution function is also perturbed as it is directly related to  $V_p$ . Experimentally, however, the problem arises because the equipment used to measure the probe current/voltage can only resolve the probe potential to some fractions of a millisecond, which is well above the RF period, and hence “sees” the time average effect of the oscillation. Nonetheless, if the electron population is assumed to be Maxwellian, then it can be shown that this does not significantly effect the electron temperature as long as:

$$V < \tilde{V}_p - V_{rf} \quad (3.12)$$

When the RF signal is more significant the I-V characteristic changes shape significantly and the interpretation of  $V_p$  becomes uncertain.

The presence of a static magnetic field adds an anisotropy to the motion of charged particles in plasmas where movement across field lines is restricted especially for electrons. This can lead to anomalous cross field diffusion and plasma flow where electrostatic fields are produced to ensure a net equilibrium in flux to the walls of the vessel. This seriously complicates the interpretation of Langmuir probe measurements as background parameters can be strongly influenced by flowing plasma. The presence of a magnetic field also increases the perturbing effect of the probe on the plasma as electrons are collected from the flux tube intersecting the probe tip leading to electron depletion and consequently anomalous current flow within the plasma [5, 6, 10].

## 3.2 Ion Source Diagnostics

### 3.2.1 Density Measurements

According to equation 1.14, brightness on the order of  $10^5 \text{ A}\cdot\text{cm}^{-2}\cdot\text{sr}^{-1}$  requires densities of at least  $10^{13}\text{cm}^{-3}$  at the extraction orifice (assuming  $T_i = 0.1 \text{ eV}$  and  $V_{ext} = 100 \text{ kV}$ ) so that the primary diagnostic focus of the prototype development was the measurement of density using Langmuir probes. Two probe designs were used for this purpose: an axially translating probe with a 5 mm long 50  $\mu\text{m}$  diameter cylindrical, dog-legged tip and a 2 mm diameter planar probe housed in a specially designed plasma electrode in such a way that the collection surface sat flush with the electrode surface and concentric with the usual position of the extraction orifice as shown in figure 3.1. A 1 mm hole was drilled into the grounded probe housing as close as possible to the insulating ceramic annulus to maintain the pumping relationship of figure 4.2.

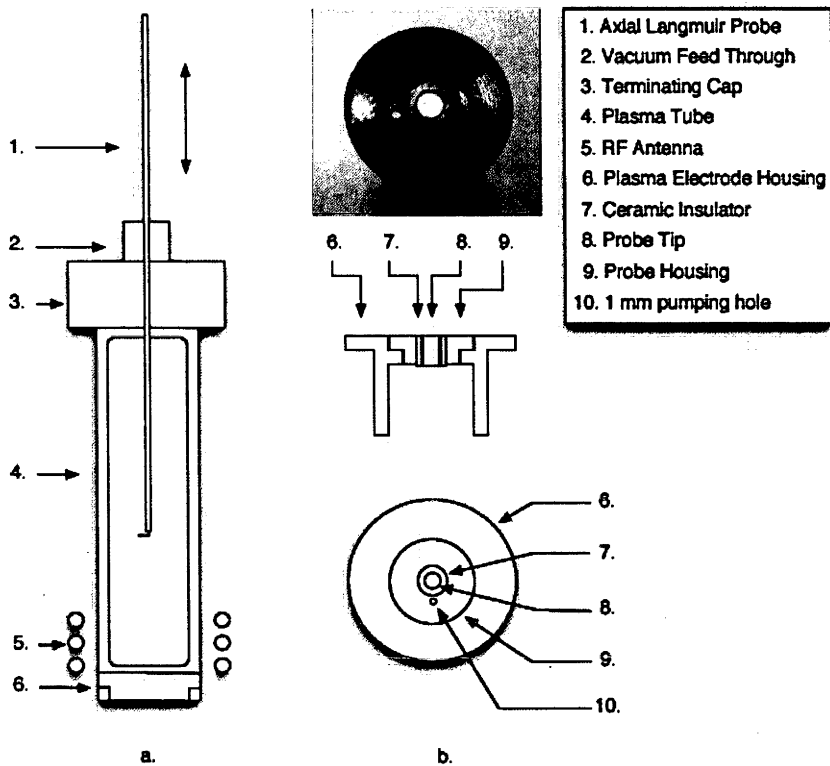


Figure 3.1: Diagram of ion source Langmuir probes. Left: axially translating dog-legged probe. Right top to bottom: photograph of probe insert, top and side section of plasma electrode with planar probe inserted.

The density was obtained by measuring the voltage drop across a  $1\text{k}\Omega$  sense resistor placed in series with the probe and a  $-90\text{ V}$  battery pack and then substituting  $I_{meas}^+ = V_{meas}^+ / R_{sense}$  into equation 3.1. For low power the plasma was not pulsed and hence  $V_{meas}^+$  was measured on a digital multimeter (DMM). For powers above  $200\text{ W}$  the plasma was pulsed on a 10% duty cycle of 10 ms on 90 ms off and the sense resistor potential measured on an oscilloscope. The rise time to steady state of an inductively coupled plasma is on the order of  $80\ \mu\text{s}$  so that the measured signal was a quasi square wave where the maximum was interpreted as the steady state ion saturation current. Under certain plasma conditions there was an “overshoot” in the signal which was interpreted as neutral gas pumping. In this case the ion saturation current was taken to be the flat portion of the curve aft of the overshoot.

During density measurements, the plasma was not biased, as this did not effect the power coupling mechanism and would have unnecessarily complicated the equipment and experimental set-up required.

### 3.2.2 Beam Measurements

#### Extracted Current

A basic condition for the existence of a plasma is the conservation of particle flux. This requires that an equal number of electrons and ions are lost to the plasma boundary. To compensate the loss of ions through the extraction aperture, electrons are removed by the extraction voltage bias electrode in equal number. This current was determined experimentally by measuring the potential drop across a  $5\text{ k}\Omega$  resistor placed in series with the bias electrode.

#### Angular Divergence

The variable shape of the plasma meniscus leads to three different basic beam forms. Assuming zero ion temperature, a sufficiently concave meniscus results in a convergent beam and a sufficiently convex meniscus produces a divergent beam. At some point between being convergent and divergent, the plasma meniscus is such that the extracted beam is parallel (figure 3.2). Though experimentally ion temperature is not zero and space-charge, especially in the acceleration gap of the extractor can not be ignored, the concept of a singular transition point between convergent and divergent beam forms leads to a simple experimental method for determining when a beam is parallel or slightly divergent in the transport region. However, it must be noted that if the ion beam past the third electrode is not completely space charge neutral and of low emittance it will be parallel only over a short distance so that a slightly convergent/divergent beam, having a larger waist, may have less

divergence further downstream than the beam that was first parallel after the extractor.

The Decel electrode in the initial prototypes (c.f. chapter 4) was 52 mm in length and 19 mm in inner diameter which represented a solid half-angle of  $10^\circ$  from the extractor orifice to the exit of the electrode system. For divergence angles greater than this, some portion of the beam struck the electrode resulting in a measurable current. This current increased as the beam became more convergent or divergent and as a result, a minimum in the Decel current was observed when sweeping the extraction voltage from a strongly divergent to a strongly convergent regime, whilst keeping the current density constant. Experimentally, the current was measured by placing a DMM between the Decel electrode and ground.

### Beam Distributions

To determine the distribution of the beam current from a line section, the device in figure 3.4 was built and placed in the diagnostic chamber of the experiment. Figure 3.3 shows a diagram of how it works: the primary beam (extracted and formed from the source plasma) is skimmed through a small orifice. The secondary beam thus formed is then scanned using a biased probe. In this way the divergence angle at any point in a given plane in the primary beam can be measured. The

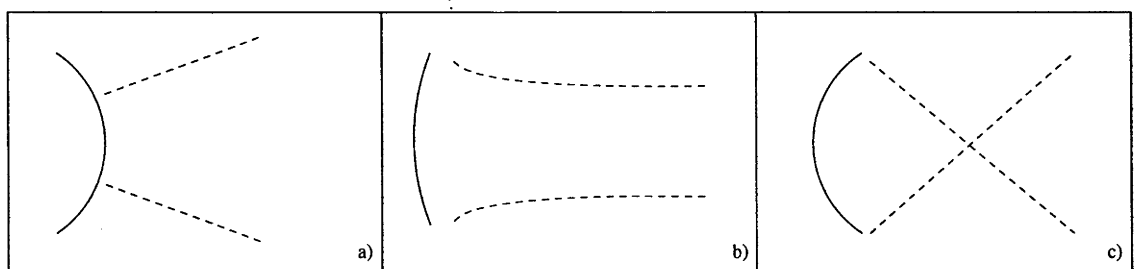


Figure 3.2: Diagram showing the evolution of the beam shape as a function of meniscus shape.

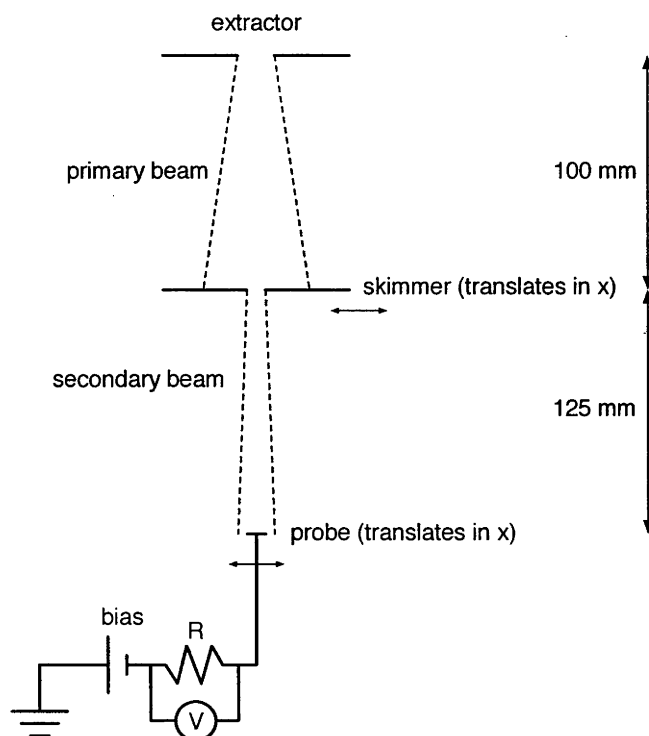


Figure 3.3: Diagram of the diagnostic instrument used to measure the distribution of the beam current from a line section.

limiting factor on the accuracy of this system is the diameter of the skimmer and probe. Though it is possible to manufacture skimmers and probes with dimensions on the order of some tens of microns, the experimental effort of aligning such small holes in a plane with the extraction orifice is tremendous. Though the skimmer and probe were very accurately aligned in the plane defined by the apparatus, this plane had to be made coplanar with the beam axis in such a way that the beam axis was perpendicular to the probe surface. Moreover, out of expediency this alignment had to be done by eye and so a diameter of  $300\mu\text{m}$  was chosen for both the skimmer and the probe. The holes were aligned in a darkened room with a torch placed over the extraction orifice (plasma side) causing a circle of roughly one millimetre in diameter to light up on the probe collection surface. The plane of the apparatus was then adjusted using shims until the light spot was concentric with the probe.



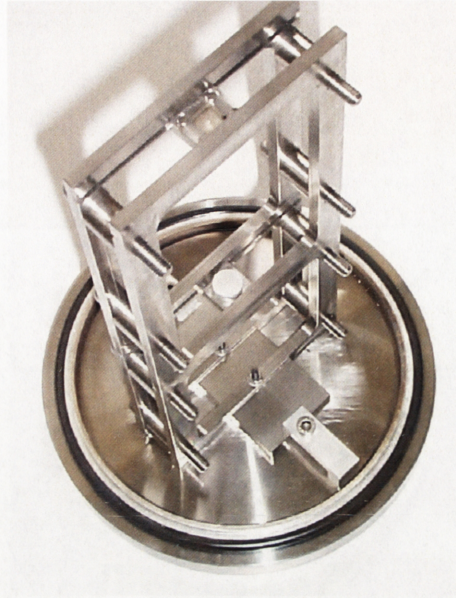


Figure 3.4: Beam divergence diagnostic apparatus clamped to base plate. Both the skimmer and the probe slide in coplanar rails and are driven by linear actuators.

To measure beam current at a given position, the probe was biased at  $-40\text{ V}$  to repel beam plasma electrons and the collected current measured across a  $10\text{ k}\Omega$  sense resistor. Of most interest was the secondary beam current distribution profile which gave an indication of the beam uniformity. Bell shaped curves represent high emittance beams whilst square distributions indicate a high level of uniformity and hence low emittance. Indeed, if all beam particles are emitted at right angles from a planar surface then, neglecting all geometric aberrations, their image through a skimming aperture is a spot of uniform current density of the same diameter as the skimmer. If, however, the beam is emitted from a surface with a distribution of angles as a result of inherent particle temperature then, again neglecting all geometric aberrations, the image is a broader spot with a peak in intensity under the skimming aperture (c.f. figure 3.5). The spot is not simply broader and uniform since the distribution of angles is a Maxwellian with the most probable angle being  $0^\circ$ , so that wider angles are less likely and hence the edges of the image are less

intense.

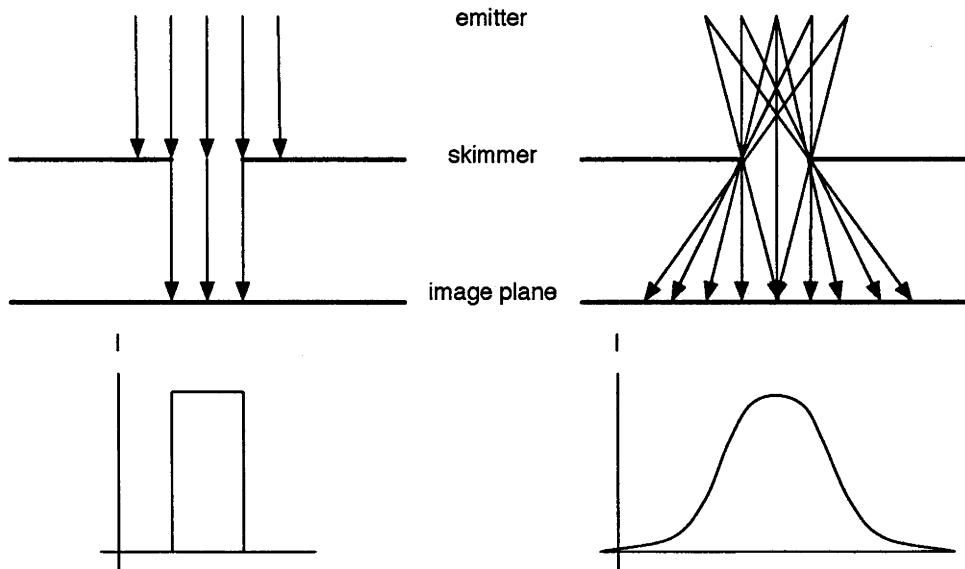


Figure 3.5: Diagram of beam current distribution through a skimmer. Left: a uniform beam of cold particles emitted at right angles to the emission surface. Right: a non-uniform beam of warm particles emitted with a distribution of angles.

Geometric aberrations in the extraction region further complicate the distribution, though experimentally it is difficult to determine how because:

- Building a series of extractors is expensive and time consuming.
- Experimentally, emittance is a difficult quantity to measure accurately and hence beam quality can not be easily determined.

### Simulation

Computer simulation techniques offer a compelling alternative to experimentally prototyped extractors and have been employed for over three decades in the design of electron and ion beam systems. Two simulation strategies were used in this work to simulate the plasma and ion beam: a commercially available ray-tracing code, called PBgun and a hybrid - PIC (particle-in-cell) called SEFI (Simulation d'Extraction de



Faisceaux d'Ions) written by Irzyk for his PhD thesis [58]. A study was undertaken to ascertain whether these codes could adequately model the plasma/beam interface and hence successfully predict the extracted current and beam form across a broad range of experimental extraction parameters [115] with a view to determining beam brightness. As brightness is a difficult quantity to measure accurately in an experimental setting, it is of some benefit to have an accurate computer estimation of this quantity.

It was found that SEFI could accurately predict the function of extracted current versus extraction voltage and that PBgun gave accurate simulations when the current or current density could be specified near the meniscus. Interestingly, it was also found that for a thin plasma aperture and a fixed current at the meniscus, PBgun gave roughly 60% of the functional dependence of the extracted current on the extraction voltage and the other 40% on variations in the plasma pre-sheath. Both codes had some error from beam crossing near the axis which changed the amount of meniscus curvature predicted. It was concluded that both codes gave a relatively accurate estimation of brightness and could be used to produce proof of concept electrode designs.

Ray tracing codes employ the Lorentz force law to calculate the trajectories of particles emanating from an emitting surface. Superficially, the problem is that of how to determine the electric field for use in this relation. The magnetic field is ignored since the beam particles are well below relativistic velocities and no external magnetic field is applied. The electric field potentials produced by the extraction electrodes are calculated using a numerical approximation to Laplace's equation. Space charge fields are determined from the beam charge density distribution. The field due to each trajectory is calculated using Poisson's equation and superposed to determine a space charge potential distribution for the extractor as a whole. This suggests an iterative approach to determining beam trajectories. First, the field is

determined from the electrode geometries and space charge fields, then the individual trajectories are calculated using the Lorentz force law. Once all the trajectories have been determined in this way, the space charge fields are recalculated and the process repeated until the simulation converges [9]. Collisions with neutrals are not incorporated into the simulation.

The question arises with simulations of this type as to how best to model the plasma meniscus [3][9]. PBGUN treats the plasma as a shaped anode and uses a fine mesh region near the emitting surface to simulate the sheath. The geometry of the emitting surface as well as the electron and ion temperatures, ion current and initial ion energy over the adjacent gridded area are specified by the operator. The sheath (and hence the meniscus) are then determined by space charge effects with the code calculating the electron space charge density using Poisson's equation and ion space charge density from the ion trajectories and the voltage on the grid points. The ion beams emanate from the emission surface with a Maxwellian distribution of angles, corresponding to the ion temperature and the plasma surface is made to be as close to the Bohm sheath boundary as possible as this increases the stability of the simulation and reduces the number of iterations needed for a given level of accuracy. SEFI is similar in concept to PBgun in that it employs the Lorentz force law to determine particle trajectories from the local field conditions but differs in its treatment of the plasma and the extracted particles. SEFI is a Particle-in-Cell code, thus the plasma and its sheath are self-organising and not modelled [7]. In addition, particles are treated individually rather than by the trajectory that they infer. PIC is a time dependent simulation method where particle and field "states" are calculated at regular intervals (usually on the order of the pico-second). At every time step the field is calculated using Poisson's law based on the position of each particle. All particles are then accelerated according to the Lorentz force law.

Because, in the simplest case, the code has to account for every particle in the sim-

ulation, it is computationally expensive. One way to decrease the convergence time to steady state is to assume a collisionless plasma in which electrons are distributed according to the Boltzman relation. Because in this case electrons would no longer need to be treated individually, a time step on the order of one tenth of a plasma oscillation would no longer be required and could instead be set to some fraction of the ion transit time between adjacent mesh elements. This yields at least a three order of magnitude improvement in computation time.

### 3.3 WOMBAT Diagnostics

#### 3.3.1 Langmuir Probes in WOMBAT

Several tip geometries were tried in the lead up to this work, including planar and large area cylindrical probes, but due to the high density of the plasma under investigation, a 4 mm long 250  $\mu\text{m}$  diameter Tungsten probe tip was finally settled upon. This tip was crimped to insulated copper wire and fed through a series of ceramic and stainless steel tubes as shown in figure 3.6 where the main purpose of the inner stainless tubing was to provide RF shielding to the probe wire and the ceramic tubing was to provide mechanical structure and insulation. The outer ceramic shell extended 300 mm from the end of a grounded stainless steel tube which served both as a ground reference point for the probe tip and the inner RF shielding (see in particular the locking ring in figure 3.6) and also as a smooth surface for translation in the vacuum feed-through. The probe end was extended this distance from the ground point to ensure that the only conducting surface in the plasma column was the probe tip.

Two such probes were built and mounted on computer controlled slides and were installed in the diffusion chamber 93 cm down stream from the antenna in the same plane through two ports separated by a right angle. As separate probes, they

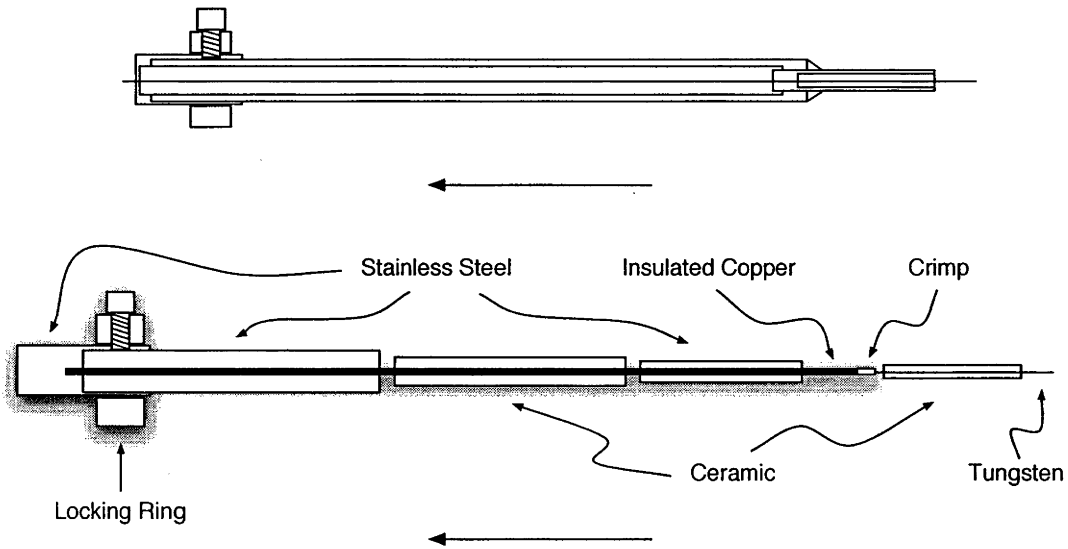


Figure 3.6: Sectional and exploded view of Langmuir probe assembly used on WOMBAT.

allowed radial measurements of density, floating potential, plasma potential and electron temperature but taken together they could be used to study the spectral properties of a wide range of perturbations.

### The Study of Basic Plasma Parameters

Radial measurements of local plasma density were made by biasing the probe to  $-60\text{ V}$  with respect to ground and measuring the ion saturation current as a function of the probe position. The ion saturation current was measured as a drop in voltage across a known sense resistor, either  $1\ \Omega$ ,  $10\ \Omega$  and  $100\ \Omega$  depending on the intensity of the current to be drawn. The density was then calculated by substituting  $I_{meas}^+ = V_{meas}^+ / R_{sense}$  into equation 3.1.

Radial floating potential profiles were obtained by simply connecting the probe directly to the  $1\ \text{M}\Omega$  input of a digital multimeter and measuring the probe potential as a function of position.

To obtain electron temperature measurements, the probe was swept over a  $100\ \text{V}$

range that scanned from well within the ion saturation current region to between 10 and 20 V above the plasma potential, observed as a knee in the I-V trace. As the electron current did not saturate, the plasma potential was taken to be the point where the first differential of current versus voltage ( $dI/dV_b$ ) was minimum. This value was then used to fit equation 3.9 to the experimental data and the electron temperature estimated by equation 3.10.

### Spectral Measurements

The probes were also used to detect real-time fluctuations in floating potential and density by either leaving them open circuit and connecting them to a heterodyne spectrum analyser via a DC block (a small capacitor) or by biasing them into ion saturation and monitoring the current fluctuations through a sense resistor (typically 10  $\Omega$ ) on a digital oscilloscope. To reduce the signal-to-noise ratio, the signals were windowed (typically 10-15 windows) and averaged.

As the probes were mounted on computer controlled slides these fluctuations were also measured as a function of radial position.

#### 3.3.2 Microwave Interferometer

Density measurements inside the plasma column using the Langmuir probes described above were often unreliable and resulted in the destruction of the probe tip, so a 35 GHz interferometer was used to determine line averaged densities and cut off.

Electromagnetic waves propagating perpendicular to the static magnetic field above the cut-off frequency have well known dispersion characteristics and are often used as a diagnostic for measuring plasma density. This is done using interferometry, where a low powered test signal (typically in the millimetre wavelengths) is launched

across the diameter of the plasma and its phase compared to a reference signal. It is simple to show, from the dispersion relation of ordinary waves, that the phase shift,  $\Delta\phi$  incurred by the test signal is related to the line averaged density of the plasma over the path length,  $L$ , travelled:

$$n = n_{co} \left( 1 - \left( 1 - \frac{\Delta\phi\lambda_0}{2\pi L} \right)^2 \right) \quad (3.13)$$

where  $\lambda_0$  is the free space wavelength of the signal and  $n_{co}$  is the cut-off density for waves of frequency  $\omega_{pe}$ , given by:

$$n_{co} = \frac{\epsilon_0 m_e}{e^2} \omega_{pe}^2. \quad (3.14)$$

For 35 GHz waves,  $\lambda_0 = 8.5$  mm and  $n_{co} = 1.52 \cdot 10^{13} \text{cm}^{-3}$ .

The line density was measured in two positions, 35 cm and 93 cm downstream from the antenna. The first position corresponded to a line segment spanning the source where the microwave horns were placed adjacent to the source tube through square windows cut into the RF shield. The second position, being in the diffusion chamber, required vacuum feed-throughs for the microwave waveguides so that the horns protruded 30 cm into the chamber, placed diametrically opposed across the plasma column.

### 3.3.3 Retarding Field Energy Analyser

In order to measure the ion energy distribution in the plasma a Retarding Field Energy Analyser (RFEA) was employed. These probes have been used in various incarnations for several decades but have been much less studied on a theoretical level than Langmuir probes [87, 55, 63, 64]. The main advantage of the RFEA is that it can permit the study of negative and positive charged particles separately and more importantly in a specific direction giving a level of spacial resolution not available to Langmuir probes. This has the result that charged particle beams can



be studied separately from the background plasma. and the background plasma can be studied in several directions revealing anisotropies.

RFEA probes are, however, complex due to the numerous grids used and the difficulty in optimising the grid bias potentials for reliable and reproducible results. The primary question in the design of such probes is how many grids to use. In ion collection mode, a two grid probe would have only a repeller to block plasma electrons from entering the probe, a discriminator to select ions by energy and a collector plate to measure the ion flux. However, any secondary electron emission from the collector would be measured as ion current and hence perturb the measurement. An alternative used in this work is to include a third grid, called the secondary, which serves to suck up secondary electron emission from the collector and which is then later subtracted from the collection current by electronic circuitry. A fourth grounded grid is placed at the entrance to the probe to give the plasma a solid ground reference and to help shield from RF.

The present RFEA is similar to that used by Charles [19] and consists of a grounded grid, three individually biased grids and a biased collector plate housed in a grounded stainless steel casing 35 mm in length, 20 mm in width and 15 mm in thickness connected to a 10 mm diameter 1200 mm long stainless steel tube used for translating the probe radially. The grids were made from Nickel and had 74% transparency. Each grid was glued into a sandwich between a 200  $\mu\text{m}$  Mylar shim punched with a 1 cm diameter hole to allow the passage of the particles and a copper ring (with a 1 cm inner diameter) which in turn was soldered to wires to allow biasing of the grids and the measurement of collection currents by an external circuit (see figure 3.9). The Mylar served to insulate between consecutive grids.

The probe can analyse electrons and ions separately but in this work was only used to study ion distribution functions so that the repeller was always biased negatively however the exact value of the repeller voltage was optimised for each new set of

operating conditions. The discriminator voltage was swept from 20 - 30 V below the plasma potential to between 80 and 100 V ensuring that the probe trace started well in the ion saturation region and reached well beyond the plasma potential. In previous work by Charles [19] it was found that the optimal bias for the secondary grid was -18 V and -9 V for the collector. This was not changed here. A narrow beam of particles was selected for analysis in the probe by a 200  $\mu\text{m}$  skimming aperture at the entrance to the probe (though this could be varied depending on the plasma density).

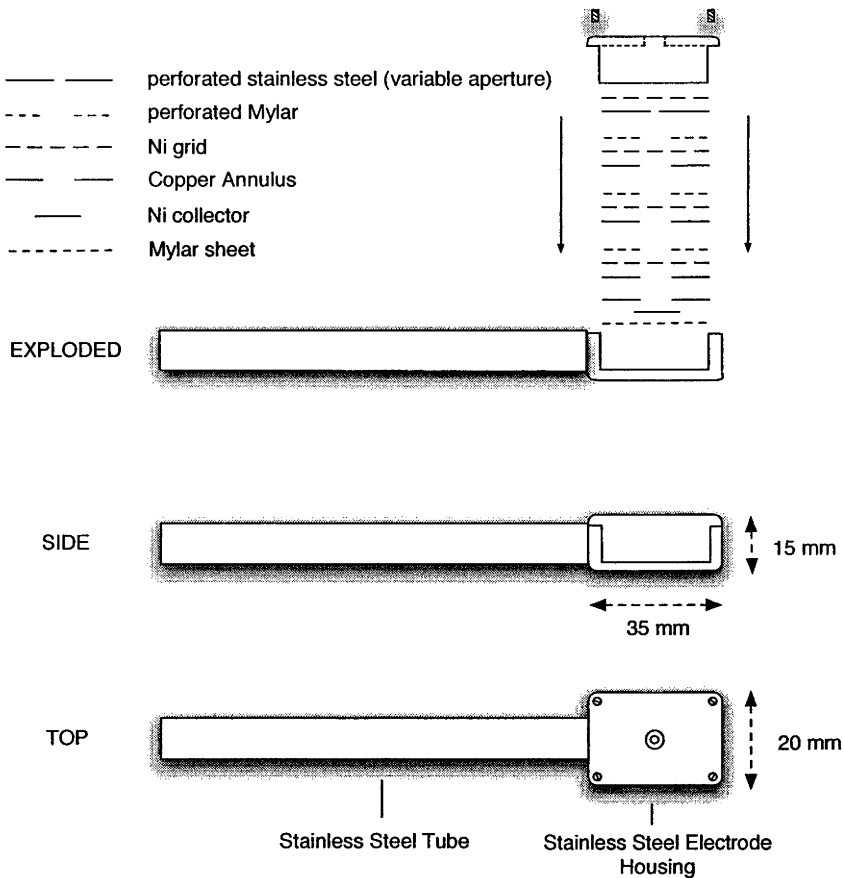


Figure 3.7: Sectional and exploded views of Retarding Field Energy Analyser (RFEA).

Since the probe collects only particles of energy superior to  $e.V_d$ , the collected cur-

rent, assuming that the coefficient of transmission for the grids is constant as a function of energy, is the integral of the ion velocity distribution function from  $(2.e.V_d/m)^{\frac{1}{2}}$  to infinity:

$$I(v_0) = T^i A e \int_{v_0}^{\infty} v f(v).dv, i = 4 \quad (3.15)$$

where:

$$\frac{1}{2} M_i v_0^2 = e V_d \quad (3.16)$$

and T is the coefficient of transmission for the grids, i is the number of grids, A is the area of the skimmer aperture,  $V_d$  is the discriminator voltage, v is the parallel velocity component and f(v) is the parallel velocity distribution function at the entrance to the probe. It is important to note that v is not related to  $V_d$  or any other potential inside the analyser.

By noting that:

$$f(v).dv = f(V_d)V_d = dn \quad (3.17)$$

we have the ion velocity distribution function in terms of the discriminator voltage:

$$f(V_d) = (T^4 A e v)^{-1} \frac{dI(V_d)}{dV_d} \quad (3.18)$$

The expression allows the ion energy distribution function to be calculated from the I-V relationship obtained experimentally. For a simple non-flowing plasma, this distribution has a single peak as shown in figure 3.8 corresponding to the plasma potential. The width of the peak describes the parallel energy spread of the ions and is directly related to the ion temperature and the RF oscillation of the sheath at the probe entrance. The presence of RF makes the direct measurement of the ion energy distribution function difficult.

If a mono-energetic beam is present then a second peak appears at the beam energy as shown in figure 3.8. Again the width of the peak is related to the beam's energy distribution, that is to say the temperature of the beam ions. The circuit shown in

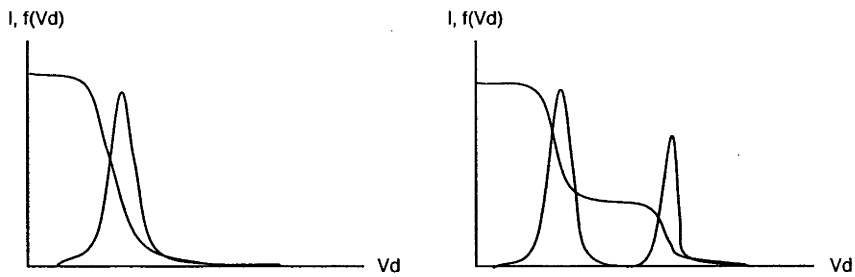


Figure 3.8: Current-voltage relationship and ion energy distribution function. Monotonically decreasing curves are ion current ( $I$ ) and peaks are their first derivatives ( $\propto f(Vd)$ ). Left, for a simple non-flowing plasma. Right, for a beam and plasma.

figure 3.9 was used to sum the collector and secondary grid currents as well as provide the bias voltage. The discriminator and repeller were powered by two separate programmable floating bipolar power supplies.

The probe was mounted on a computer controlled slide and introduced into the vacuum vessel via the same side port as the Langmuir probes allowing radial measurements of the ion energy distribution function 93 cm downstream from the antenna. As the probe could be rotated about its axis of symmetry, angular measurements could also be made in the plane of the source.

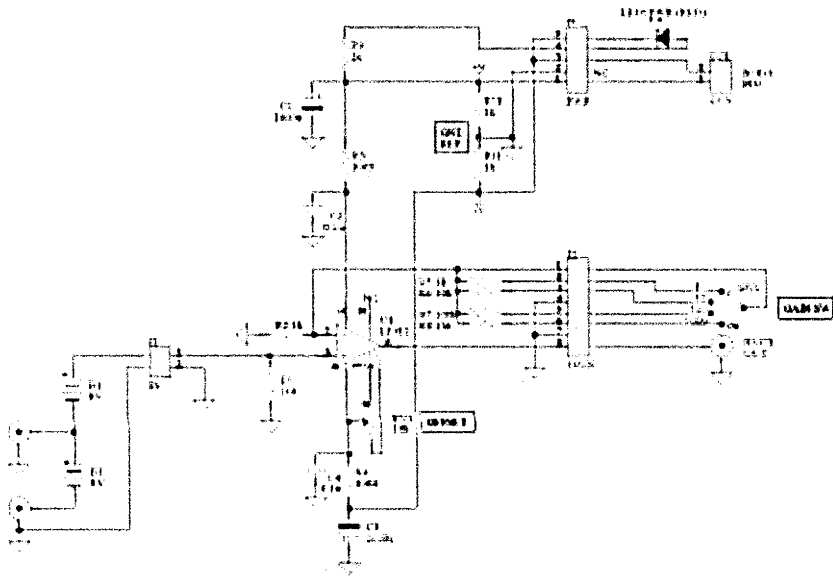


Figure 3.9: Diagram of RFEA circuit used to bias and collect current from secondary grid and collector plate.



# Development of a Compact High Density Plasma Ion Source

A large part of the ion source development presented in this thesis was undertaken with-in the framework of a contract between the A.N.U. and FEI Co. of Portland, Oregon in the U.S.A. to develop a high brightness inert gas plasma ion source for the semiconductor industry. Initially, the two major requirements for the source were that it produce densities of at least  $10^{13} \text{ cm}^{-3}$  and that it be suitably compact for use with existing FEI focusing columns. However, the ultimate aim of the research was to produce an inert gas plasma ion source capable of delivering a brightness of  $10^5 \text{ A.cm}^{-2}.\text{sr}^{-1}$  at 50 keV for which an ion energy of 0.2 eV or less is required. An intermediate goal was set for a brightness of  $10^3 \text{ A.cm}^{-2}.\text{sr}^{-1}$  at 10 keV.

Four prototypes were designed and built over a 3 year period and the first three are presented in this chapter. The author's involvement in this development process encompassed the design and testing of the first two prototypes in conjunction with Rod Boswell and Peter Alexander. The initial design was concerned with the consistent extraction of FIBs as well as the development of appropriate diagnostics. John Keller and Michael Irzyk were commissioned to perform computer aided design of the first extraction electrodes and also assisted in some preliminary beam measurements with the author. Over the development period of the first two prototypes, several Langmuir probe designs were tested to measure plasma density

in the source and the skimmer/probe assembly of 3.2.2 was designed and manufactured to perform direct measurements of the beam profiles. With the second prototype the emphasis shifted away from FIB extraction and concentrated more on increased plasma density in the source and overall miniaturisation of the device. Around the end of the first prototype's design cycle, Fenton Glass was employed as a research assistant to perform thermal and electrical breakdown testing on both the first and the second ion sources, After a third prototype had been designed by Rod and Peter, he also performed preliminary testing on it and Christine Charles made RF measurements on its "balanced" antenna. Two copies of the third prototype were manufactured with one remaining at the A.N.U. and the other being shipped to FEI Co. in Oregon where Walter Skoczylas performed life time testing

Prototype No.	1	2	3	4
Designers	Rod Peter Orson	Rod Peter Orson	Rod Peter	Rod Peter Walter Noel
Testers	Orson Fenton	Orson Fenton	Fenton	Ane Walter
Experimenters	Orson Michael John	Orson Fenton	Noel Christine	Ane Noel
Experiments	Density Beam Distr. Antenna Pos. Magnetic Field Temperature	Density Temperature	"Balanced" RF	Density RF

Table 4.1: Table summarising the design, testing and experimentation of the 4 prototypes developed over the three year period of this thesis. The participants in the project in chronological order are: Orson Sutherland, Rod Boswell, Peter Alexander, John Keller, Michael Irzyk, Fenton Glass, Christine Charles, Noel Smith, Walter Skoczylas and Ane Aanesland.

(a modified version with glass to metal seals had clocked over 600 hours at up to



400 W without degradation at the time of writing) and Noel Smith measured the ion energy distribution function of the extracted FIBs with a energy selective mass spectrometer (see chapter 6). From these measurements he was able to show that the “balanced” antenna configuration dramatically reduced ion energy spread in the extracted beam. A fourth ion source being designed in collaboration with these two scientists from FEI Co. was under construction at the time of writing.

A summary showing the 4 prototypes, their designers and the experiments carried out on them is presented in table 4.1.

## 4.1 The Experimental Concept

The standard experimental concept consisted of three interchangeable parts: an RF plasma source, a triode extraction assembly and a diagnostic chamber. The ion source itself (intended for use with FEI focusing columns) is considered to be comprised of the RF plasma source and the extraction assembly alone and the diagnostic chamber onto which the ion source was mounted for testing purposes, served to maintain vacuum, provide a transport region and sink for the extracted FIBs and a housing for diagnostic equipment. The interchangeability of the three main sections added flexibility to the development process, where, for example, improvements in the plasma source design did not require changes in the extraction set-up or the diagnostic chamber and vice-versa.

### Vacuum System and Gas Feed

The basic plasma source design consisted of a Pyrex tube terminated at one end by a cap (either insulating or conducting) and fitted at the other to the extraction assembly which formed part of the diagnostic chamber top plate sealing the vacuum vessel as shown in figure 4.1. A re-entrant design for the electrodes was used so that the plasma electrode was in close contact with the highest possible plasma density.

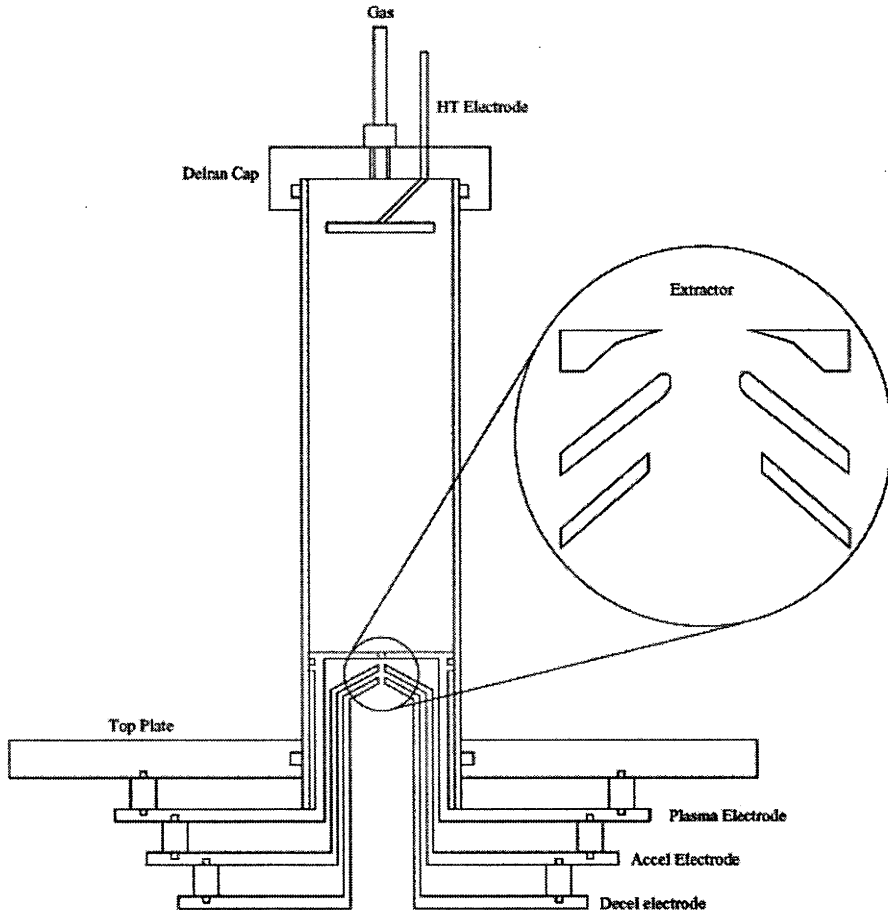


Figure 4.1: Sectional view of the basic experimental source set-up. The electrodes are bolted onto the diagnostic chamber top plate and the source tube slides over the plasma electrode.

Vacuum was maintained by a two stage pumping system consisting of a roughing pump (1st stage) and a turbo-molecular pump (2nd stage) mounted to a flange on the side of the diagnostic chamber providing a base pressure of  $10^{-6}$  Torr at a nominal pumping speed of  $100 \text{ L}\cdot\text{s}^{-1}$ . Because of the limited space on the source tube cap (the initial source designs only had enough space for the gas feed and the biasing electrode) the pressure in the source tube was deduced from the pressure measurement in the diagnostic chamber. A one off experiment was conducted to calibrate the measurement of the flow conductance represented by the extraction assembly by simultaneously measuring the pressure in the source tube and diagnos-

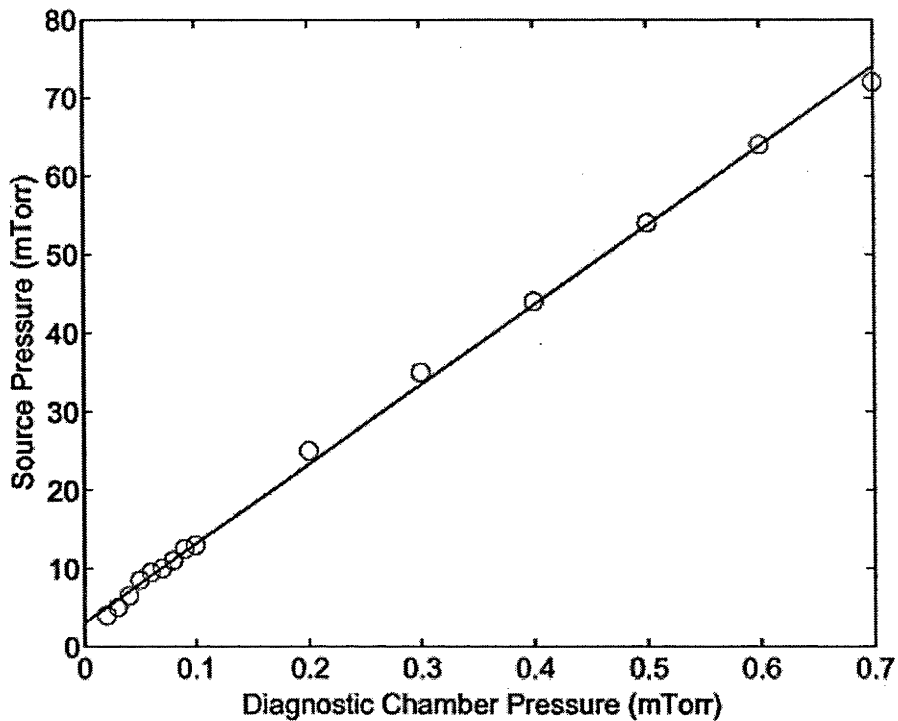


Figure 4.2: Source pressure versus diagnostic chamber pressure.

tic chamber for various gas flow rates with a Convectron mounted on a specifically designed source tube cap and an ion gauge mounted on the diagnostic chamber. The results of this experiment are shown in figure 4.2 where the relationship between the source tube and diagnostic chamber pressures is linear and represents a ratio of roughly 100 to 1 leading to a simple laboratory rule of thumb. The line on which the data sit does not pass through zero as the Convectron has an off-set of 3 mTorr when no gas is injected into the system, however this does not effect the linear relationship between the source and the diagnostic chamber pressure. The gas flow was controlled using a needle valve but was not monitored directly.

## RF System

All the ion sources were driven by either a single or a triple loop RF antenna wound coaxially around the source tube out of 3 mm copper wire. The effect of varying the antenna's axial position is presented later in this chapter but typically it was placed at the extraction end of the tube. For the first two prototypes, power was coupled to the antenna via the  $\Pi$  matching network shown in figure 4.3 at 13.56 MHz with powers ranging between 0 - 300 W, CW, and 0 - 1 kW, pulsed, with less than 5% reflected power for all experiments. The pulsed experiments were performed by modulating the RF power signal with a 10 Hz square wave oscillating on a 10% duty cycle. Since the pulse length was 10 ms, and the plasma rise time was roughly 80  $\mu$ s the plasma reached steady state with-in the pulse duration and the ion saturation current was equivalent to that in CW. Also, because the duty cycle was 10%, the heat load on the antenna and plasma tube was 100 W on average which was well with-in the operating limits of the source.

The value of the permanent capacitance C in the matching network was a function of the antenna and source tube geometries and was determined empirically using a grid-dip meter and was typically some hundreds of pico-Farads. Power was delivered with a single 1.2 kW RF power supply and forward and reflected power were measured using a directional coupler.

The third prototype was characterised by several important changes to the RF system. In particular, the plasma source tube was integrated into the matchbox so that the antenna could be connected directly to the tuning capacitors reducing stray capacitance, the antenna diameter was doubled and the antenna was no longer grounded at one end but rather connected at either end to the load and tune capacitors in what became known as the "balanced" antenna configuration. This system is described in more detail later in the chapter and the impact of the "balanced" antenna experiments on ion temperature are presented in chapter 6.

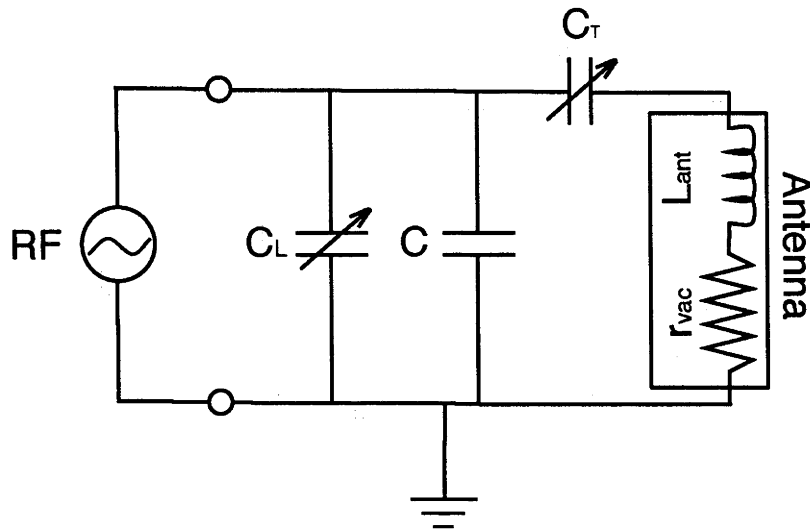


Figure 4.3: Initial matching network circuit for the FIB ion sources. The value of the permanent capacitance  $C$  varies as a function of the antenna and source tube geometry but is typically some hundreds of picoFarads.  $C_T = 0 - 500$  pF and  $C_L = 0 - 1000$  pF.

### Extraction System

The ion sources presented in this thesis were all fitted with a standard triode extraction optic rather than the five electrode system presented in chapter 2 because at the time of manufacture the theory had not yet been completed. The new electrode system will be installed into the fourth prototype and is scheduled for testing in early 2005. For the ion sources presented here, the extraction system consisted of three electrodes (hence triode) with single, concentrically aligned apertures computer designed for the extraction, focusing and acceleration of high brightness FIBs. In principle only two electrodes are required for the extraction of FIBs: an electrode which contacts the plasma and which charges up the extraction voltage and a grounded electrode which serves as a ground reference for the beam. However, the presence of electrons in the transport region, aft of the extractor, caused by secondary emission from the beam striking the chamber walls, leads to a flow

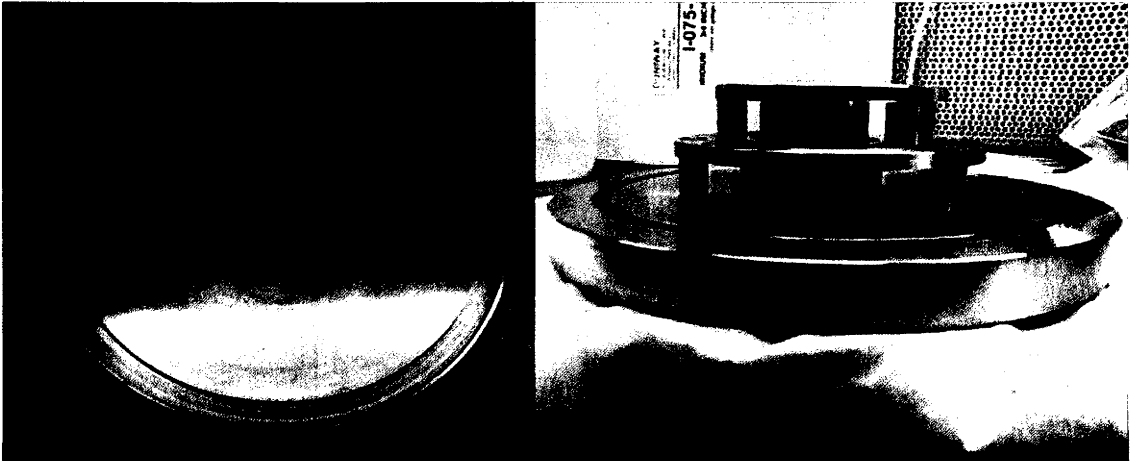


Figure 4.4: Photographs of the electrode assembly. Left: top view of the Plasma electrode protruding through the diagnostic chamber top plate, Right: side view of the diagnostic chamber top plate, Plasma and Blocking electrodes.

of electrons into the extraction region which degrades the quality of the focusing lens and hence decreases the brightness of the extracted beam. To avoid this, a third electrode, called the Accel electrode, is placed between the Plasma and Decel (grounded) electrodes and is biased sufficiently negatively to impede the counter flow of electrons. The extra electrode also provides further shaping to the extraction fields.

Typically, in ion source systems, the plasma electrode is powered directly by an HT source via a vacuum feedthrough, but because breakdown between the electrodes in the initial prototype could not be solved, the plasma electrode was floated and the plasma was charged by a bias electrode introduced through the terminating cap (and eventually the entire cap itself). Subsequent prototypes also used this floating plasma electrode configuration as the emphasis was more on attaining high plasma densities, compact source dimensions and low ion energies rather than perfecting the extraction system. However, in the fourth prototype which is a collaborative effort between FEI Co. and A.N.U., the entire RF source, including the RF power

supply and antenna will be floated at the extraction potential.

In addition to arcing in the extraction system, breakdown was also often observed across the glass source tube of the first two prototypes between the antenna and the plasma, causing in some extreme cases, the vacuum to be breached. The exact nature of the breakdown across the glass was not investigated but the effect was removed completely by doubling the antenna diameter in the third prototype.

### Diagnostic Chamber

The diagnostic chamber was a 30 cm long, 20 cm diameter stainless steel vacuum vessel which housed the turbo-molecular pump, the pressure gauges (an ion gauge and a convectron), a port for visual confirmation and a translating skimmer/Langmuir probe assembly used for beam analysis (c.f. 3.2.2). Except for the addition of new diagnostics, this portion of the experiment remained unchanged throughout the evolution of the source design.

Beam characterisation was only undertaken for the first prototype as later source developments were more focused on creating a compact, high density, low ion temperature plasma source.

## 4.2 The Prototypes

### 4.2.1 Prototype 1

#### General Description

The first source design used a 25 cm long, 5 cm diameter tube, a three turn antenna and a Delran terminating cap with the plasma electrode biased directly via a vacuum feedthrough. However, problems with arcing in the extraction system could not be solved and so a stainless steel bias electrode was introduced through the terminating cap and the plasma electrode was floated as shown in figure 4.5.



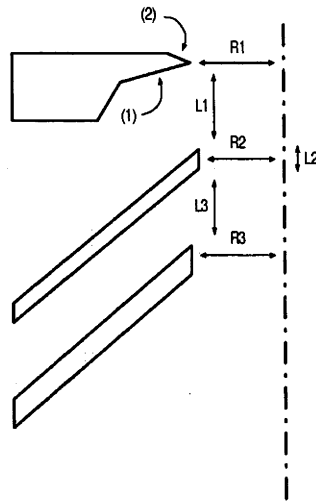


Figure 4.5: A close-up view of the discharge tube. The electrode that sets the plasma potential can clearly be seen at the top of the tube. The antenna is at the bottom of the tube near the extraction orifice. The square box houses the matching network.

The original extraction electrodes were designed by John Keller using PBgun and are summarised in table 4.2. The main feature of the electrodes was a two segment aft face on the plasma electrode, where the segment closest to the beam defined the Pierce angle and the second segment approximated a parabola to first order as shown in the figure of table 4.2. It was believed (at the time) that this configuration would increase the brightness of the beam in a convergent regime. Though the beam envelope was convergent in the acceleration gap (between the plasma and Accel electrodes), it became divergent in the Blocking gap (between the Accel and Decel electrodes). In light of the discussion of chapter 2, the equipotential line closest to the Accel electrode is of particular interest as it bulges out (as predicted by the theory of chapter 2) forming a divergent lens and so despite the strong neutralisation employed in the simulation the beam, which was initially convergent, becomes divergent in the transport region thus highlighting the importance of decreasing



the electric field as well as the potential to zero by the last electrode. However, the theory of chapter 2 had not been developed at this point and so could not be integrated into the electrode design.



Name	Value
L1	1.5 mm
L2	0.3 mm
L3	0.5 mm
R1	radius=0.75 mm
R2	radius=0.65 mm
R3	radius=0.75 mm

Table 4.2: Schematic diagram of the electrode configuration and tabularised summary. (1) Pierce angle. (2) Surface relieved to increase edge sharpness.

### Ray-Tracing Simulations

PBgun estimated that this extraction optic had a brightness of approximately  $10^3 \text{ A.cm}^{-2}.\text{sr}^{-1}$  at 10 kV, which fell short of the typical brightness produced by an LMI source ( $10^5 \text{ A.cm}^{-2}.\text{sr}^{-1}$ ) but which still represented a useful working brightness for industry as an inert or reactive gas plasma ion source, especially in light

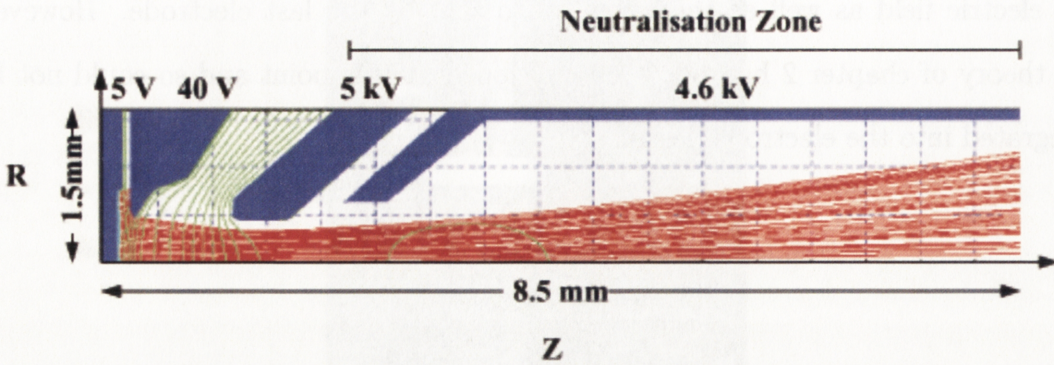


Figure 4.6: PBgun simulation of original electrode design. Courtesy John Keller.

of the low axial ion energy spread demonstrated in chapter 6 (N. Smith, FEI Co., private communication).

For these simulations, a plasma density of  $10^{12} \text{ cm}^{-3}$  and an ion temperature of 0.1 eV was assumed. Though the plasma density used in the simulation was based on experimental results (presented in the next section) ion temperature had not been measured and was therefore assumed to be on the order of a tenth of an eV, being a carry over from typical laboratory plasma assumptions where ion temperature is assumed to be less than 1 eV.

Experimental verification of extracted current and beam divergence showed surprisingly good correlation with the simulation [115] which lent some credence to the brightness estimation. However, further cross-sectional scans of the beam using the skimmer/probe assembly of 3.2.2 revealed bell shaped curves indicative of non-uniform beam current density and hence low brightness.

### Plasma Density Measurements

Axial measurements of the source plasma density were taken using the cylindrical probe described in 3.2.1 but the probe tip could not be placed closer than

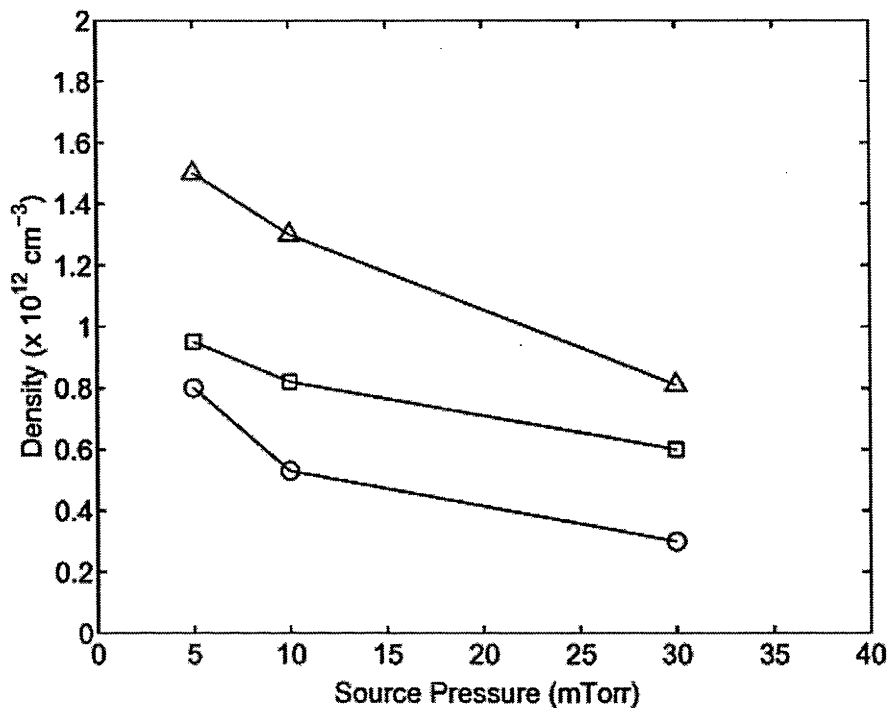


Figure 4.7: Density 2 mm above extraction orifice versus pressure for 3 input powers: ○: 50 W; □: 100 W; △: 200 W

2 mm to the plasma electrode (grounded for these experiments) because of arcing. Despite being limited to 200 W input power, a density of  $1.5 \cdot 10^{12} \text{ cm}^{-3}$  was achieved at a pressure of 5 mTorr. Figure 4.7 shows density versus pressure for various input powers at 2 mm above the bottom of the plasma source. Density was maximum relative to input power for a pressure of 5 mTorr. For lower pressures the density decreased. Noel Smith also reported a maximum in density at around 5 mTorr using the third prototype delivered to FEI (N. Smith, FEI Co., private communication).

#### The Effect of Power, Magnetic Field and Antenna Position

Because in these initial experiments the RF power was restricted to less than 200W to avoid overheating the device, despite blowing cold air diverted from the airconditioning system directly onto the experiment, higher densities could not be

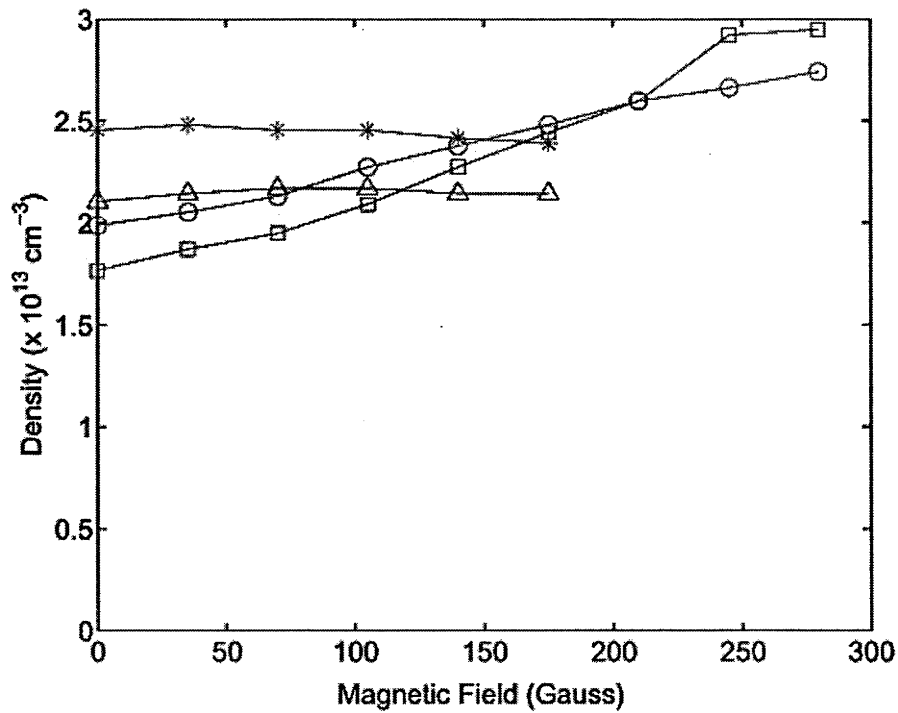


Figure 4.8: Density versus magnetic field at various antenna positions. Pressure was 5 mTorr. \*: 25 mm,  $\Delta$ : 35 mm,  $\circ$ : 45 mm,  $\square$ : 55 mm.

explored in CW. To investigate the potential of the system at powers up to 1 kW, the RF signal was pulsed at 10 Hz with a duty cycle of 10%. The axial Langmuir probe was also replaced with the planar probe described in 3.2.1 and the current collected monitored on a digital oscilloscope. A single loop antenna was investigated and antenna position, magnetic field and power were studied to obtain the highest possible density at the extraction orifice. Figure 4.8 shows the evolution of the plasma density as a function of magnetic field and antenna position for an input power of 1 kW. At lower magnetic fields it is advantageous to have the antenna closer to the extraction aperture. It is also observed that with the antenna close to the base (less than 35 mm) it is best to operate the source without magnetic field as it tends to hollow out the plasma and decrease the plasma density at the point of extraction. When the antenna is placed at 45 mm or more from the base,

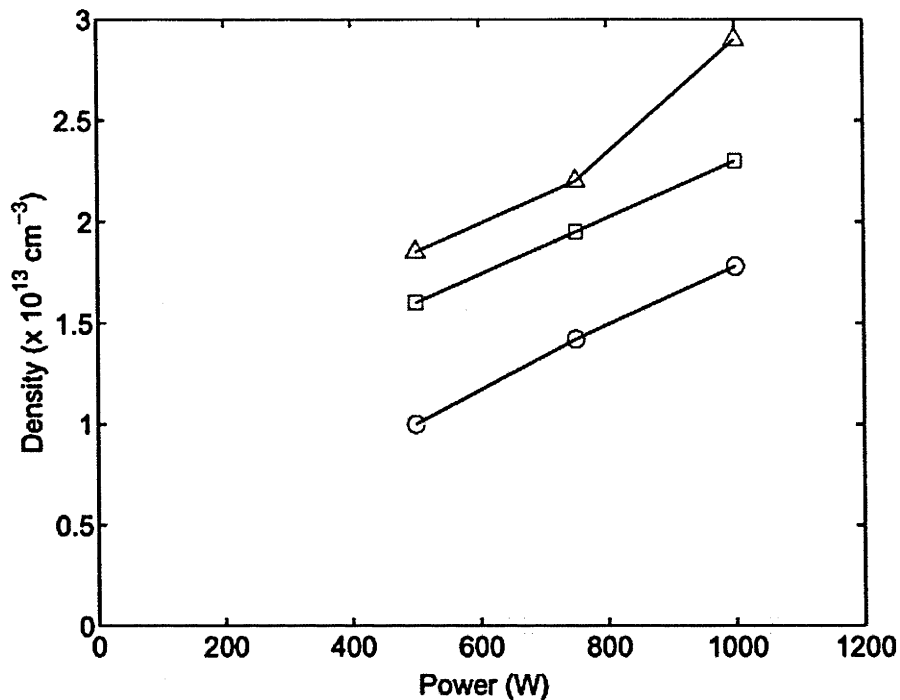


Figure 4.9: Density at the extractor measured as a function of power for three different magnetic field strengths. Pressure = 5 mTorr; antenna position = 55 mm above extractor.  $\circ$ : 0 Gauss,  $\square$ : 140 Gauss,  $\triangle$ : 280 Gauss.

density is an increasing function of magnetic field. Moreover, higher densities are possible under this regime than when no magnetic field is used but a field of at least 200 Gauss is required. Figure 4.9 shows the evolution of density as a function of power for three different magnetic field strengths when the antenna is 55 mm above the extraction aperture. Density is an increasing function of both power and magnetic field and at 1 kW and 280 Gauss, the plasma density is measured to be  $2.9 \cdot 10^{13} \text{ cm}^{-3}$ . The initial magnetic field experiments were limited to 280 Gauss by the solenoid power supply but the information learned in these experiments was used in subsequent prototypes where solid ring magnets were tested.



## 4.2.2 Prototype 2

The initial specifications required the source to fit into an insulating sleeve of 12 cm inner diameter and 20 cm in length, so a decision was taken to reduce the tube diameter from 5 cm to 2 cm and the Plasma electrode was modified accordingly. Initially, the tube length was maintained at 20 cm, but as the plasma was concentrated around the antenna region and the whole source had to fit inside the insulating sleeve, it was decided to reduce the source length to 10 cm. This had no appreciable effect on the plasma ball which remained concentrated around the antenna and so the new shorter tube became the standard dimension for the subsequent source evolution.

A new terminator cap was machined from stainless steel and connected directly to the HT source serving as the bias electrode for the extractor. Gas was still injected through the terminator cap though ceramic tubing was installed on the gas line between the source cap and the needle valve to avoid charging the gas lines up to

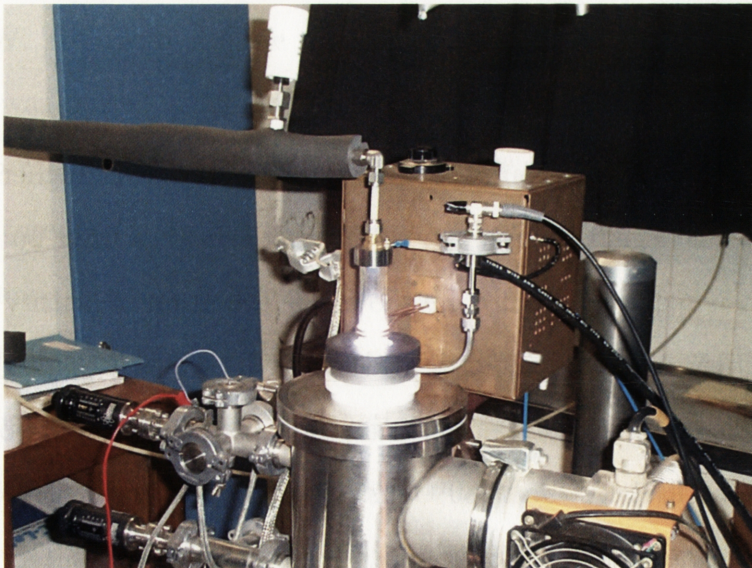


Figure 4.10: Photograph of prototype 2 installed on the diagnostic chamber. The 700 Gauss ring magnet is installed and a plasma is struck.

the extraction voltage.

As the prototype 1 source had shown that density was an increasing function of magnetic field for antenna positions above 45 mm, 350 Gauss and 700 Gauss solid magnets were used on the new source design. With the 350 Gauss magnet installed, a density of  $4 \cdot 10^{13} \text{ cm}^{-3}$  was measured using the planar probe described in 3.2.1 by pulsing the plasma with a peak power of 1 kW. A density of  $1 \cdot 10^{14} \text{ cm}^{-3}$  was measured with the 700 Gauss magnet.

Despite the thermal advantages of pulsing, it is not ideal for FIB extraction as the varying beam current effects the extraction optics and therefore a CW mode of operation must be achieved. However, with 1 kW of input power the heat loading on the source tube and extraction optics was considerable. Visually, the plasma was confined to a cylinder roughly 2 cm in length and 2 cm in diameter and was situated adjacent to the plasma electrode. The power input into the plasma must equal the power output and so a simple calculation assuming isotropic energy dissipation purely in the form of heat, based on the ratio of areas through which the power is dissipated, leads to a simple thermal model of the source. As the area of the plasma electrode is 1/6 of the total plasma area it absorbs 167 W of the 1 kW of injected power. The area of the glass tube in contact with the plasma represents 2/3 of the total plasma surface and so absorbs 667 W of power. The power per unit area absorbed by the glass and plasma electrode is  $5.3 \cdot 10^5 \text{ W.m}^{-2}$ , by assuming heat is transmitted purely by radiation and that the ambient temperature is 300 K, substitution into Stefan's law yields a temperature at steady state of 1750 K. This is surely an over-estimation of the temperature increase as conduction effects have not been taken into account and some output energy is lost as light emission, however, it does demonstrate that the source and extraction optic are under strong thermal load and that the vacuum o-rings which are rated for 500 K and which are in direct contact with both the source tube and the Plasma electrode are at risk of damage.



This was corroborated by Fenton Glass who made temperature measurements of the source tube and surrounding top plate with thermocouples. In particular, he found that for powers as little as 200 W the o-ring between the glass and the extraction assembly had hardened and deformed indicating that the Plasma electrode and the glass tube had heated to above 500 K at the level of the o-ring. Degradation of the o-ring results in out-gassing into the plasma contaminating the extracted beam and compromising the vacuum seal. The natural solution to this problem, implemented in prototype number 4 at the time of writing, was to braise the glass to the metal electrode housing using a glass-to-metal seal.

### 4.2.3 Prototype 3

Changes in the design requirements saw the end design shift away from the necessity to fit the source into the standoff sleeve and instead focused on integrating the plasma source into the matchbox itself. This meant that stray capacitance

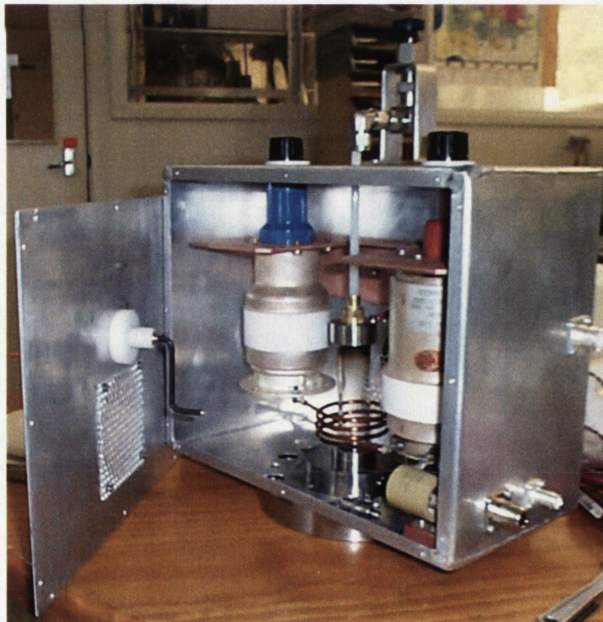


Figure 4.11: Photograph of prototype 3. The source is located inside the matchbox and the circuit configuration is “balanced”. The antenna is attached directly to the load and tune capacitors.



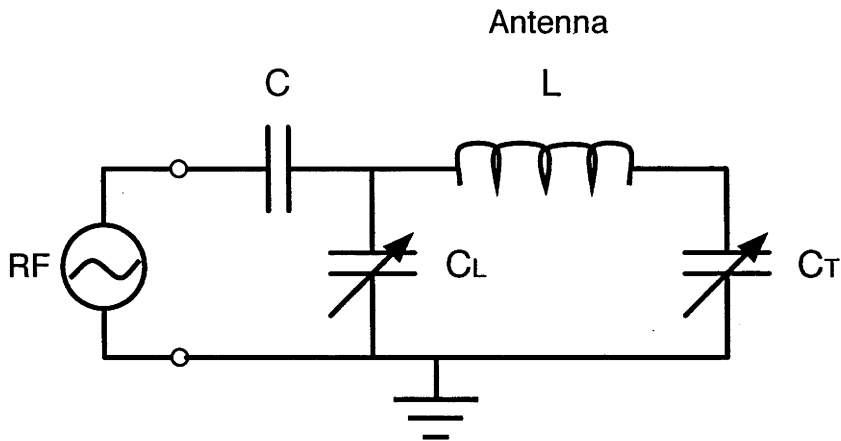


Figure 4.12: “Balanced” matching network circuit diagram.  $C$  is permanent capacitance (roughly 50 pF),  $C_L$  is the load capacitor and  $C_T$  is tune capacitor.

from connectors and leads was minimised as the antenna could be connected directly to the tuning capacitors. Cooling of the device was also made more simple as a fan could be mounted directly on the grounded housing. The matching network was no longer configured in the standard  $\Pi$  configuration typically employed in the laboratory with the capacitors now placed on either side of the antenna to ground as shown in figure 4.12. This allowed the antenna to be “balanced” so that a zero phase shift could be programmed at the middle of the antenna. It was suggested by J. Keller that this configuration could reduce the RF component of  $V_p$  as described by equation 3.11 and so reduce the broadening effect of RF on the ion energy distribution function in the extracted beam.

#### 4.2.4 Summary of Prototypes

	Prototype 1	Prototype 2	Prototype 3
Tube	5 cm Pyrex	2 cm Pyrex	2 cm Pyrex
Antenna	1&3 turn Copper Wire	1 turn Copper Wire	3 turn Copper Wire
B field	0 - 360 G Solenoid	350 G + 700 G Permanent Ring	No
Match Box	II	II	Balanced

Table 4.3: Summary of ion source prototypes

# Perpendicular Ion Heating

In the investigation of laboratory plasmas, ions in the bulk are commonly considered to be cold, that is, to have negligible velocity relative to the electron population which is assumed to be a Maxwellian distribution with a mean energy of between 3 and 5 eV. For the production of high brightness FIBs, ion energies much above 0.2 eV reduce the effectiveness of the extraction optics and therefore must be considered. As discussed in the introduction, both perpendicular and parallel ion energy effect on beam quality and both can be caused by collisional and non-collisional mechanisms. In this chapter, we consider the role of wave-particle interactions on perpendicular ion heating leaving a discussion on the effect of charge-exchange and elastic-scattering collisions to be considered in conjunction with parallel ion heating in the following chapter.

## 5.1 A Brief Introduction to Electromagnetic Waves in Cold Plasmas

In vacuum, electromagnetic (EM) radiation can propagate as a wave due to the coupling between oscillating electric and magnetic fields as described by Maxwell's equations. This coupling is enabled by the concept of displacement current where spatial changes in the electric field give rise to temporal changes in magnetic field and vice-versa. This ability to propagate in vacuum is unique among wave phenomena

which are without exception perturbations of a specific medium. EM waves can also propagate in matter, however, the EM coupling can be effected by the movement of charged particles which respond to the oscillations in the wave field. In the presence of plasmas, the propagation of the EM radiation exists as a hybrid of oscillating plasma parameters and the wave fields.

In the simplest case, the plasma response to an excitation at a particular frequency  $\omega$  is determined by the response time of the plasma particles to the oscillating wave fields due to their inertia. For example, plasmas are transparent to EM radiation down to the microwave range because neither ions nor electrons can react quickly enough to the oscillating fields. The natural frequency at which a charged species oscillates in a plasma is known as its plasma frequency  $\omega_p$ , and is given by:

$$\omega_p = \left( \frac{e^2 n}{\epsilon_0 m} \right)^{\frac{1}{2}} \quad (5.1)$$

where  $e$ ,  $n$  and  $m$  are the charge, number density and mass of the plasma species in question and  $\epsilon_0$  is the permittivity of free space. The plasma frequency of laboratory plasmas (densities less than  $10^{14} \text{ cm}^{-3}$ ) is in the microwave range, and therefore EM radiation propagates as in vacuum down to these frequencies at which point electrons become able to respond to the oscillating field. At and below the microwave range, electrons tend to cancel the incident fields and the plasma becomes progressively more opaque to the radiation. When the incident wave is totally reflected this is referred to as cut-off and corresponds to zero refractive index. That is, the wavelength of the propagating wave becomes infinite. Below this frequency, only electrostatic (ES) waves can propagate into the bulk of the plasma unless a DC magnetic field is applied.

In the presence of a DC magnetic field, a varied gamut of EM and ES wave types can be supported by the plasma because of the anisotropy introduced by the charged plasma particles (especially electrons) being bound to circular orbits about the magnetic field lines. The charged particle species have a natural orbit frequency,

called the cyclotron frequency  $\omega_c$  given by:

$$\omega_c = \frac{|e|B_0}{m} \quad (5.2)$$

where  $B_0$  is the magnitude of the applied DC magnetic field. The sign of the unit charge  $e$  defines the direction of orbit with respect to the magnetic field where positively charged ions rotate in a left-hand sense with respect to the direction of  $B_0$  while electrons rotate in the opposite sense. In a cold plasma (i.e., where  $T_e = T_i = 0$  eV) incident EM radiation propagating parallel to  $B_0$  at  $\omega_c$  will act to continually accelerate the particle species corresponding to that cyclotron frequency as they orbit around the field lines. This wave-particle interaction does work on the particles and therefore damps the oscillating field, limiting its propagation into the plasma. As the perturbation field approaches the cyclotron frequency from below, the effect of electron inertia results in a strong increase in the refractive index and the wavelength rapidly approaches zero producing a condition referred to as resonance. Incident field oscillations at frequencies above the resonance are evanescent, that is, they “see” a purely imaginary refractive index, and become decaying exponential oscillations with no propagating component.

The electron plasma frequency is modified in the presence of a DC magnetic field due to the cyclotron motion of the electrons. The right hand circularly polarised (RHCP) component of the incident wave field is cut-off at a higher frequency than  $\omega_p$  because the cyclotron motion shifts the RHCP frequency down in the electron frame of reference. Similarly, the left hand circularly polarised (LHCP) component is cut-off at a lower frequency than  $\omega_p$  because the LHCP frequency is shifted up in the electron frame of reference. A convenient way to summarise the various wave types that can propagate parallel to  $B_0$ , as discussed, is to plot the square of the refractive index ( $N^2$ ) as a function of frequency as shown in figure 5.1. The details concerning the calculation of these curves will not be given here but are derived from the left and right hand components of the dielectric tensor when the direction

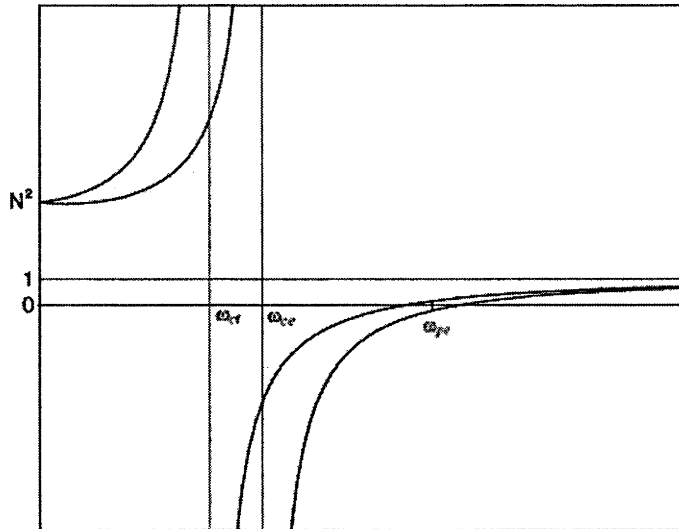


Figure 5.1: Variation of  $N^2$  as a function of  $\omega$  for propagation along  $B_0$ .

of propagation is along  $B_0$  [113, 30]. It shows the ion and electron cyclotron resonance frequencies as well as the LHCP and RHCP cut-off frequencies on either side of  $\omega_{pe}$ .

### Circular Polarisation and Resonance

The opposite cyclotron motion of ions and electrons make the segregation of wave types into LHCP and RHCP seem natural. This can be shown more rigourously, following the method of Stix and others [113, 104], by considering the motion of charged particles in the presence of a static and uniform magnetic field  $\tilde{B}_0$  and an oscillating electric field  $\tilde{E}(t) = E \cdot \exp(i \cdot \omega \cdot t)$ , for which the equation of motion is:

$$m \frac{d\tilde{v}}{dt} = e(\tilde{E}(t) + \tilde{v} \times \tilde{B}_0) \quad (5.3)$$

where  $\tilde{v}$  is the particle's velocity and  $\omega$  is the frequency of the electric field oscillation. The homogeneous solution to 5.3 is the velocity  $\tilde{v}_0$  which is independent of the

forcing term  $\omega$  and corresponds to oscillations at the cyclotron frequency. The solution to the forcing term,  $v_1$  is given by:

$$\left(i\omega + \frac{e}{m}\tilde{B}_0 \times\right) \tilde{v}_1 = \frac{e}{m}\tilde{E}(t) \quad (5.4)$$

which is solved by applying the conjugate operator  $(i\omega - (e/m)\tilde{B})$  to yield the parallel component of  $v_1$ :

$$v_{1,z} = -\frac{ie}{m\omega}E_z \quad (5.5)$$

the x component,

$$v_{1,x} = \frac{e}{m} \frac{i\omega E_x + s\omega_c E_y}{\omega_c^2 - \omega^2} \quad (5.6)$$

and the y component,

$$v_{1,y} = \frac{e}{m} \frac{i\omega E_y - s\omega_c E_x}{\omega_c^2 - \omega^2} \quad (5.7)$$

where  $E_x$ ,  $E_y$  and  $E_z$  are the x, y, and z components of the electric field vector  $E$  and  $s$  is the sign of the particle's charge. A LHCP electric field,  $\tilde{E}_L$ , has an x-component that lags its y-component by 90 degrees, so that it can be written  $\tilde{E}_L = E_x\tilde{x} - iE_y\tilde{y}$ , where  $\tilde{x}$  and  $\tilde{y}$  are the unit vectors in the  $x$  and  $y$  directions. Similarly, the x-component of the RHCP electric field leads its y-component by 90 degrees and can be written  $\tilde{E}_R = E_x\tilde{x} + iE_y\tilde{y}$ .

Substituting these definitions and analogous ones for the left and right hand gyrating particle velocities,  $\tilde{v}_L$  and  $\tilde{v}_R$ , into 5.6 and 5.7 the following is obtained:

$$\tilde{v}_L = \frac{ie}{m(s\omega_c - \omega)}\tilde{E}_L \quad (5.8)$$

and

$$\tilde{v}_R = -\frac{ie}{m(s\omega_c + \omega)}\tilde{E}_R \quad (5.9)$$

$E_L$ ,  $v_L$  and  $E_R$ ,  $v_R$  define orthogonal coordinates in a left and right hand rotating coordinate system.

Equations 5.8 and 5.9 clearly demonstrate the resonant effect of the wave-particle

interaction close to the respective particle cyclotron frequencies. The LHCP component,  $E_L$ , undergoes resonance with the ions at  $\omega = \omega_{ci}$  and the RHCP component,  $E_R$ , with the electrons at  $\omega = \omega_{ce}$  so that the particles are accelerated as the oscillation frequency approaches their respective cyclotron frequencies. It is this resonance between the EM waves and the plasma particles which is the basis for non-collisional ion heating.

## 5.2 Wave Particle Interactions

The discussion so far has assumed a cold plasma where electrons and ions have no thermal distribution and their motion is considered to be well described as that of separate fluids with defined velocities. The fluid model remains correct for both ions and electrons with finite temperature distributions if the forces acting on the particles are independent of their velocities in the fluid frame of reference. This is not the case for Doppler shifted particle resonances where the oscillation frequency of the propagating fields is either shifted up or down in the particle frame of reference. If the particle approaches the wave field with velocity  $\tilde{v}$  then the frequency of the oscillation in the particle frame of reference is:

$$\omega' = \omega - k \cdot \tilde{v} \quad (5.10)$$

where  $k$  is the wave number. For resonant interactions,  $\omega'$  may be replaced by  $n \cdot \omega_c$  where  $n$  is a signed integer giving rise to two important wave-particle phenomena, namely Landau damping and Doppler shifted cyclotron resonance (DSCR).

### 5.2.1 Ion Landau Damping

If  $n$  is set to zero then 5.10 reduces to:

$$v = \frac{\omega}{k} = v_\phi \quad (5.11)$$



where  $v_{\Phi}$  is the wave phase velocity. This condition describes a zero order resonance and is met if particles move at almost the same velocity and in the same direction as the wave field, in other words if the particles are almost stationary in the wave's frame of reference. If the particles are moving at just above or just below the wave phase velocity (but not enough to escape the wave field) then the particles are trapped between successive wave fronts and oscillate back and forth in a potential well created by the wave. If it is assumed that the wave has existed for all time then there is no net transfer of energy to the particles as they oscillate in the wave field in a manner similar to an undamped pendulum. Particles which move above the wave phase velocity with sufficient velocity to escape the wave's potential wells are alternatively accelerated and decelerated by the wave field but oscillate about a mean velocity which is different to zero. Particles with velocities very different to the wave phase velocity are not effected by the wave. In phase space  $((v_z, z)$ , where  $z$  is the direction of motion) the oscillations of the trapped particles are represented by circles of radius proportional to the oscillation amplitude. Particles that have a velocity very different from the wave phase velocity travel along straight lines and particles that have a velocity sufficient to escape the wave's potential wells but which are not significantly different to the wave phase velocity are sinusoids as shown in figure 5.2.

So far ion heating by zero order wave particle interaction has been limited to half a period of the ion orbit and net energy transfer from the wave to the particles is always compensated by an equivalent transfer in the opposite direction (assuming no collisions) so that no net ion heating and hence wave damping is possible. However, if the interaction is now considered as an initial value problem, where at time zero, more ions are moving at just below the phase velocity than above it, then when the wave is launched at  $t > 0$  it may be sufficiently damped that a large number of the freshly accelerated ions escape the wave field and net energy is lost from the wave.

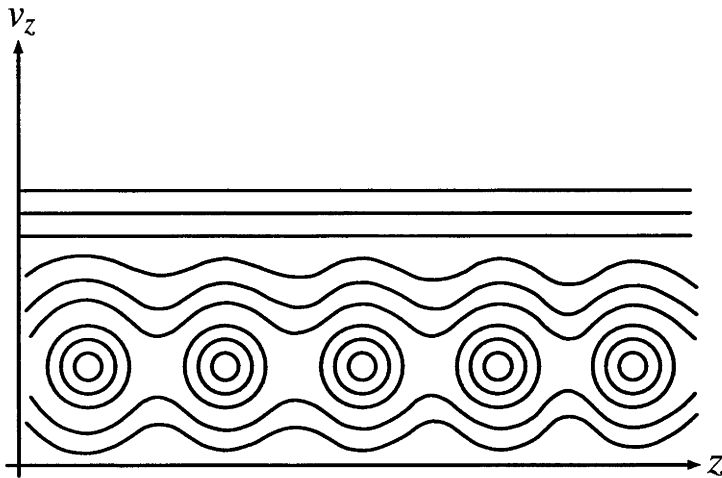


Figure 5.2: Phase space diagram of particles moving at close to the wave phase velocity interacting with a wave field. The circles represent trapped particles, oscillating back and forth in the wave potential wells.

This is referred to as ion Landau damping (IDL) and the number of wave periods required for the wave amplitude to be sufficiently small that all the ions are no longer trapped defines the damping length. When the ion sound speed approaches the ion thermal velocity from above (i.e. when  $T_e$  becomes less than or equal to  $T_i$ ), this mechanism becomes highly relevant to ion heating processes in the presence of ion acoustic waves (IAW), which by definition move at the ion sound speed [70]. This is because the wave phase velocity moves from a region where the derivative in the ion distribution function is small (for larger  $v_\phi$ ) to one where the derivative is large.

A linear theory describing these interactions was first presented by Landau in 1946 [72] based on a first order perturbation expansion of the linearised Vlasov equation in the absence of collisions. This theory demonstrated that the average rate of increase in particle energy was related to the number of particles streaming just below the wave phase velocity and can be expressed as follows (c.f. [113], p 117 for

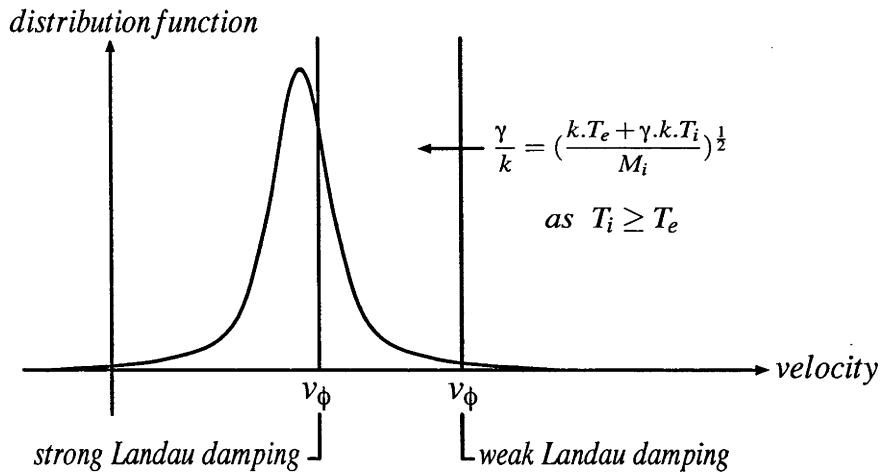


Figure 5.3: One dimensional ion velocity distribution function. As the ion sound speed approaches the ion thermal velocity from above ion Landau damping becomes more important because the derivative of the distribution where the vertical lines intersect it become larger.

details):

$$\left\langle \frac{d}{dt} \frac{mv^2}{2} \right\rangle = -\frac{\pi\omega e^2 E^2}{2mk|k|} \left[ \frac{df(v_0)}{dv_0} \right] \tag{5.12}$$

where  $f(v_0)$  is the initial velocity distribution of the particles at velocity  $v_0$ . For distributions in which the most probable velocity is below the wave phase velocity (c.f. figure 5.3) the derivative on the right hand side is negative and hence the average kinetic energy of the particles increases. If a large number of the ions have an initial velocity just below the wave phase velocity then the wave is strongly damped as energy is transferred from the wave to the ions.

### 5.2.2 Doppler Shifted Ion Cyclotron Resonance

If  $n$  is now set to 1 then, assuming ion cyclotron resonance, 5.10 yields:

$$\omega - k \cdot v_z = \omega_{ci} \tag{5.13}$$

where  $v_z$  is the velocity of the ions along the magnetic field lines. in the wave frame of reference. For frequency upshifting  $v_\phi$  and  $v_z$  are in opposite directions.

If we assume the EM oscillations are infinite plane waves, then as the LHCP part of the wave approaches the natural ion gyration around the magnetic field lines, the refractive index and hence also the wavenumber of the incident radiation tends towards infinity and the relative parallel velocity,  $v_z$ , of the particles approaches zero. In other words, along  $z$ , the ions are stationary in the wave frame of reference and are trapped. As a result of this resonance, the ions only “see” the radial component of the electric field as shown by equation 5.8. In the x-y plane (perpendicular to the applied magnetic field), the particles spiral outwards as the radial electric field accelerates them radially and they gyrate around the magnetic field.

If the infinite plane wave assumption is now relaxed and the resonance region is considered to be spatially limited, for example if there is a gradient in  $B_0$  or the wave field is damped by wave-particle interactions, then the particles will not be trapped by the wave field but will instead only “feel” the field for that fraction of the gyration which traverses the resonance zone. In general, a resonant cyclotron wave can not propagate over long distances in a uniform plasma as it is by definition damped by interactions with a given plasma particle species. It is not, for example, limited to coupling into only those particles in the portion of the distribution function for which the slope is negative, as in Landau damping. However, in non-uniform plasmas (for example plasmas contained in long tubes, where a strong radial gradient can exist in density and electron temperature), the cyclotron wave’s propagation properties are a function of position, so that the resonance region may be spatially restricted and the wave is only partially damped, otherwise propagating unimpeded (albeit with a smaller amplitude). If an ion cyclotron wave can be observed experimentally then it is not being strongly damped by wave-particle interactions and hence is not likely to be coupling large amounts of power into the

ion energy distribution function.

### 5.2.3 The Experimental Set-Up

In order to investigate the potential for wave-particle interactions in the ion source, experiments were undertaken in the large volume plasma device known as WOMBAT (Waves On Magnetised Beams And Turbulence) [17]. The size of the reactor allowed for several probes to be introduced simultaneously both in the source and diffusion chamber increasing the ease of use and diversity of diagnostic techniques employed to study the plasma. Originally conceived to simulate beam plasma interactions and space plasma phenomena over two decades ago, WOMBAT has proven to be a formidable experimental platform for the study of basic plasma physics with research contributing considerably to the understanding of plasma production by helicon waves [99, 37, 38, 34, 32, 33, 31]. Here, this body of work is extended by investigating the role of helicon waves in resonant interactions with ion-cyclotron and ion-acoustic waves.

#### Vacuum Vessel

WOMBAT has a volume of approximately  $6 \text{ m}^3$  and consists of a 50 cm long, 18cm inner diameter Pyrex source tube terminated at one end by a grounded aluminium plate and attached coaxially at the other to a 200 cm long, 100 cm inner diameter grounded stainless steel chamber shown in figure 5.4. The vessel was evacuated by a two stage pumping system consisting of a roughing pump (1st stage) and a turbo-molecular pump (2nd stage) mounted to the diffusion chamber end bell opposite the source and provided a base pressure of  $4 \cdot 10^{-6}$  Torr at a nominal pumping rate of  $330 \text{ L}\cdot\text{s}^{-1}$ . The pressure was monitored primarily using an ion gauge, as typically experiments were conducted for pressures below 1.2 mTorr, but the vessel

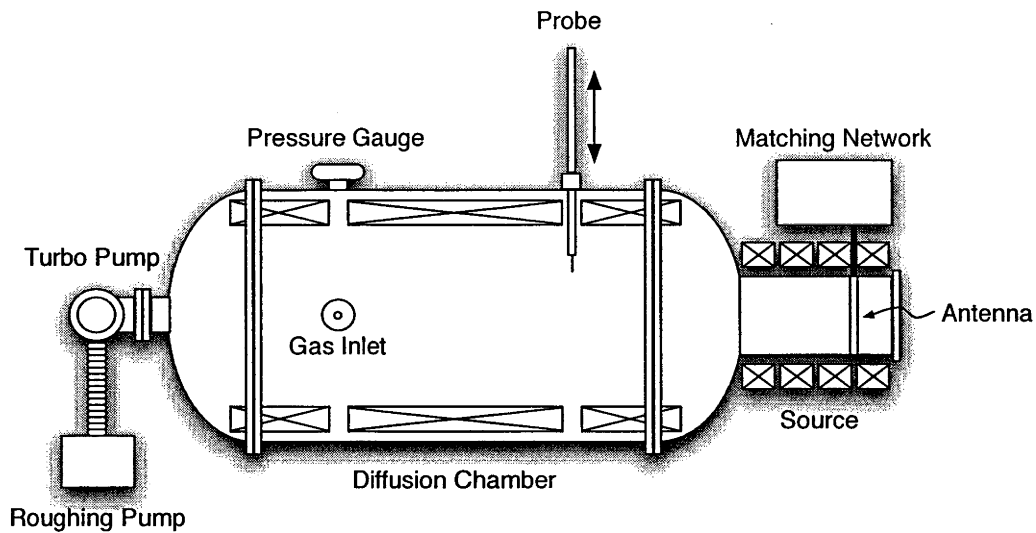


Figure 5.4: WOMBAT experimental set-up.

was also fitted with a convectron for higher pressures. Experimental conditions with pressures as high as 8 mTorr were investigated and in this range both gauges were in good agreement.

The Argon feed gas was introduced by a 50 sccm mass flow controller through a side port approximately 50 cm axially from the turbo pump end of the diffusion chamber (in the same plane as the pressure gauges) and it was found that the fill pressure could accurately be programmed using the ratio of 10 sccm per 1 mTorr for pressures below 1.5 mTorr.

### Magnetic Field System

WOMBAT is equipped with seven concentric solenoids to produce a time invariant axial magnetic field. Four are external to the source, mounted around the RF shield, but only the three solenoids internal to the diffusion chamber were used in the experiments presented here. These have a measured axial uniformity of 0.5% [26] and for operating conditions of 100 Gauss on axis result in the magnetic field geometry shown in figure 5.5 which was calculated by C. Charles using a code writ-

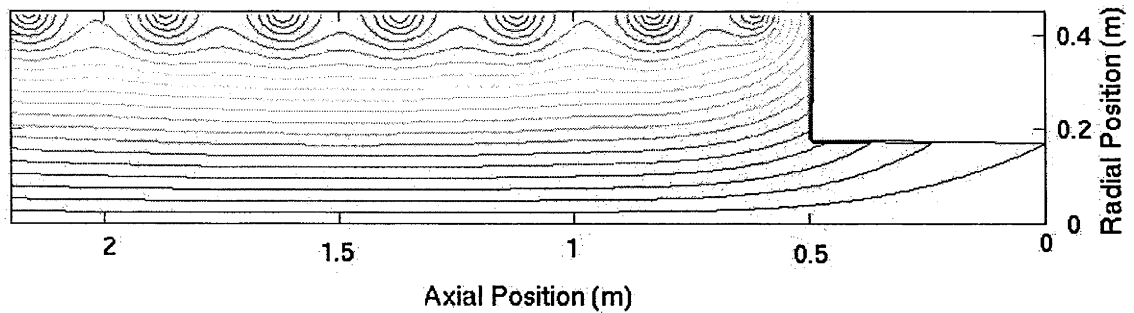


Figure 5.5: Magnetic field geometry (calculated) generated by the internal diffusion chamber solenoids corresponding to a field of 100 Gauss on axis under the coils.

ten by K. Gaff [41] that resolves the magnetic curl vector fields for the entire volume of the chamber based on the current profile and geometry of the coils. To achieve the measured field uniformity on axis in the calculation, the three experimental source solenoids were modelled using seven smaller coils. The resulting magnetic field geometry reveals a convergence in the field lines from the source to the diffusion chamber where a large portion of the central field lines intersect the glass source tube.

On axis measurements of the magnetic field magnitude using a Gauss meter are shown in figure 5.6. The field is highly uniform inside the diffusion chamber and, as expected, drops off roughly as the inverse of the square of the distance from the edge of the solenoid, so that with a diffusion chamber field of 110 Gauss, the field under the antenna is about 15 Gauss.

### RF System

Traditionally WOMBAT is driven by a double saddle (sometimes referred to as a Boswell-type) antenna [99, 27, 37] which launches waves with a half wavelength of the antenna length. However, in this thesis, the author, motivated by the intention not to strongly specify the helicon wavelength, followed the example of Degeling [30]

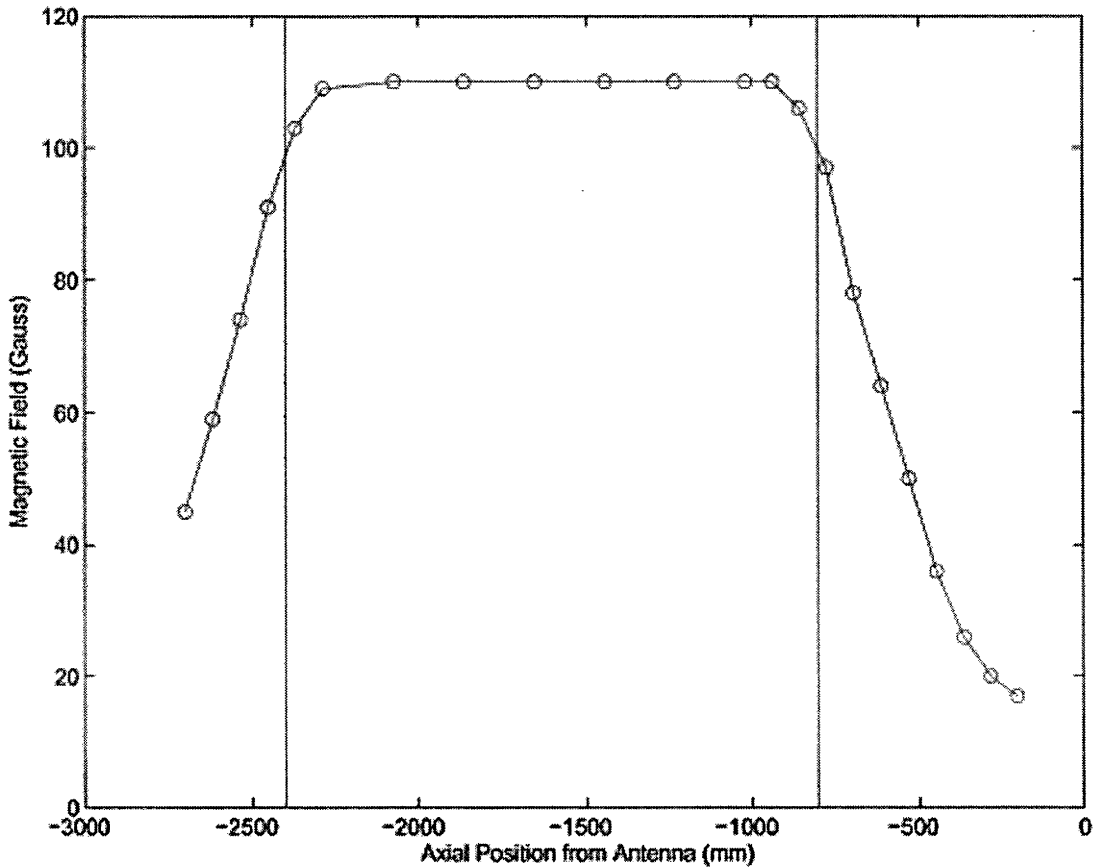


Figure 5.6: Measured magnetic field on axis produced by diffusion chamber solenoids. The antenna serves as a reference and is at 0 mm. The vertical lines represent the ends of the diffusion chamber solenoids.

and Ellingboe [36] and employed a double half-turn antenna which was believed to be more versatile in launching helicons over a broad range of operating conditions. WOMBAT is also typically driven at 13.56 MHz, however, a driving frequency of 7.2 MHz was chosen initially in order to reproduce the work of Degeling [30] on wave-particle interactions at lower frequency but which later was maintained (rather than switching back to 13.56 MHz) after the discovery of ion cyclotron waves, ion heating and four wave interactions.

The antenna, a double half turn, consisted of a single loop of copper, 200 mm in diameter, 10 mm in width and 3 mm in thickness connected at the top by a radial feed to the matching network, which was mounted in a grounded box located di-



rectly above the antenna. The bottom of the loop was connected to an aluminium cylinder mounted coaxially between the source and the solenoids which acted as an RF shield and a ground return path for the antenna current. As the device was inherited directly from Degeling the antenna was left axially aligned around the source and located 75 mm from the stainless steel terminating plate.

The matching network served to match the antenna/plasma system impedance to the output impedance of the RF generator ( $50\Omega$ ), ensuring that the maximum pos-

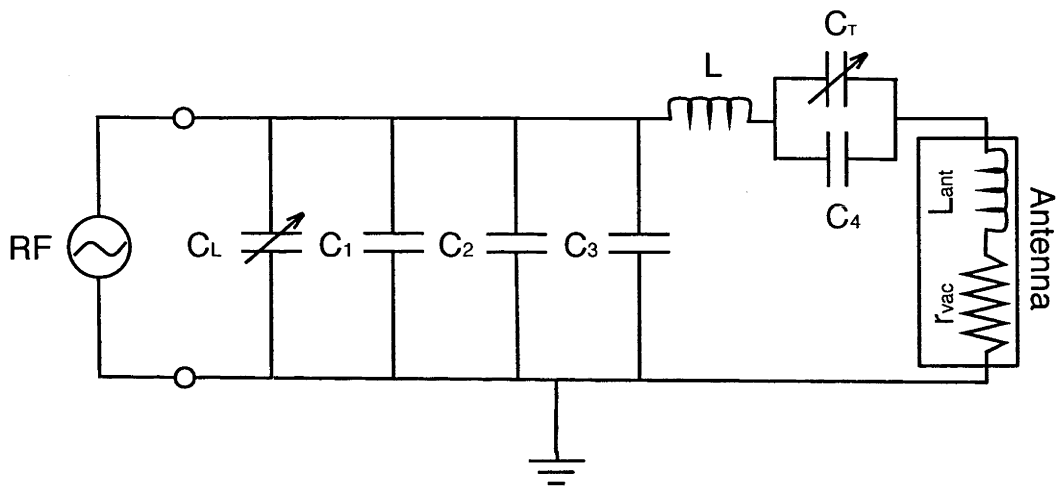


Figure 5.7: Matching network circuit diagram.  $L = 0.8 \mu\text{H}$ ,  $C_T = 0\text{-}500 \text{ pF}$ ,  $C_L = 0\text{-}1000 \text{ pF}$ ,  $C_1 - C_3 = 1200 \text{ pF}$ ,  $C_4 = 200 \text{ pF}$

sible forward power was transmitted to the plasma and not reflected back into the generator. This was motivated by two factors: the preservation of the RF power source and transmission lines and the accuracy of power measurements by the directional coupler which required low reflected power. In order to match the antenna/plasma system impedance to the output impedance of the RF generator, the antenna, which has a circuit equivalent inductance,  $L_{ant}$ , in the micro-Henry range and a resistance,  $r_{vac}$ , in the tenths of Ohms, is included in a network of capacitors and inductors organised in a  $\Pi$  configuration and designed to show a purely real input impedance of  $50\Omega$ . The exact circuit values of the capacitors and any extra in-

ductive components can be difficult to calculate as the antenna impedance changes as a function of the plasma parameters and all stray capacitance, inductance and resistance in the circuit originating from connecting straps or elsewhere must be known and integrated into the calculation. It was found that direct measurement with a grid dip meter or network analyser was a more effective method for finding the correct circuit elements, though a basic calculation allowed the rough circuit values to be found. The matching network used in this work is shown in figure 5.7. The tune capacitor,  $C_T$  is adjusted so that the real part of the circuit impedance reaches, but does not quite attain, the series resonance condition given by:

$$\omega(L_{ant} + L) = \frac{1}{\omega C_T} \quad (5.14)$$

where  $L$  is the extra inductance added to the circuit to ensure  $C_T$  is well below the 500 pF limit of the variable vacuum capacitor available for the experiment. The role of the tune capacitor is to program the inductive reactance of the antenna branch and hence the resonant frequency of the network whilst the load capacitor (a 1000 pF variable vacuum capacitor),  $C_L$ , and any permanent capacitance added to the shunt branch are used to tune the imaginary component of the circuit to zero. To determine the optimal inductance  $L$  and the value of the permanent shunt capacitors,  $C_i$ , with no plasma struck, a tracking generator was connected to the input of the matching network via a directional coupler and the reflected power measured as a function of frequency using a spectrum analyser as shown in figure 5.8. With the variable capacitors tuned to approximately the middle of their range, various inductors were tested until the circuit resonance was found to coincide with the desired driving frequency of 7.2 MHz. Permanent capacitors were then added to the shunt branch until the biggest dip in reflected power was achieved.

Up to 2.5 kW of CW or pulsed radio frequency (RF) power was available via a three-stage amplification system comprising a 13 dB variable frequency final stage, a 55 dB variable frequency pre-amplifier and a programmable digital synthesiser.

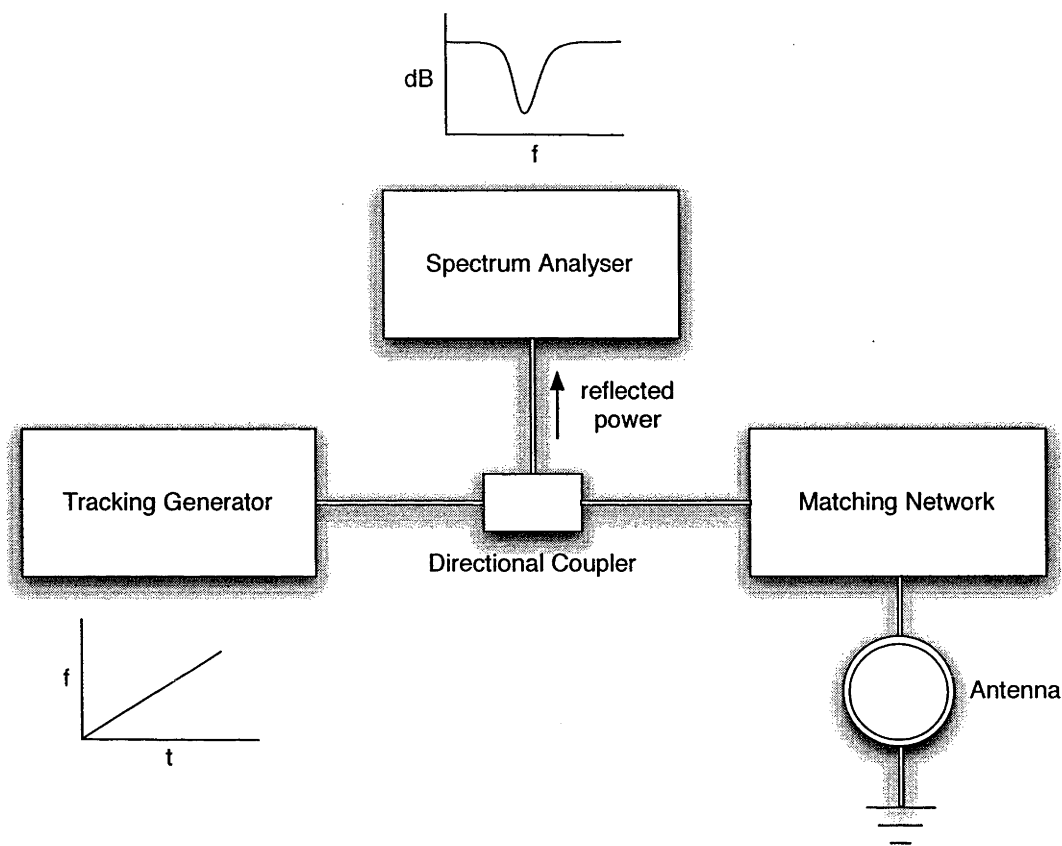


Figure 5.8: System diagram for measurement of matching network resonance condition. A dip in the spectrum analyser signal indicates the frequency at which the circuit is resonant. Changing the inductance and capacitance of the circuit changes the location of the dip in the frequency domain.

The forward and reflected power were monitored using a digital oscilloscope and a -51 dB directional coupler designed and manufactured in the school's electronics unit by D. Gibson.

### Ar II Plasma Column

The experimental set-up described in the previous sections resulted in a 2 m long plasma column along the length of the WOMBAT diffusion chamber. The column diameter was dependent on the applied magnetic field and decreased with an increase in field. For fill pressures of less than 1.5 mTorr, magnetic fields of

more than 130 Gauss and powers in excess of 1.9 kW, this plasma column radiated a powerful blue glow along its whole length. Under these conditions the column was roughly 8 cm in diameter, determined both by visual inspection and the full-width-half-maximum (FWHM) of the density profile as measured by the Langmuir probe described in 3.3.1. It was noted, however, that density measurements using a Langmuir probe proved unreliable inside the column and lead to the rapid destruction of the probe tip so microwave interferometry was used instead to estimate

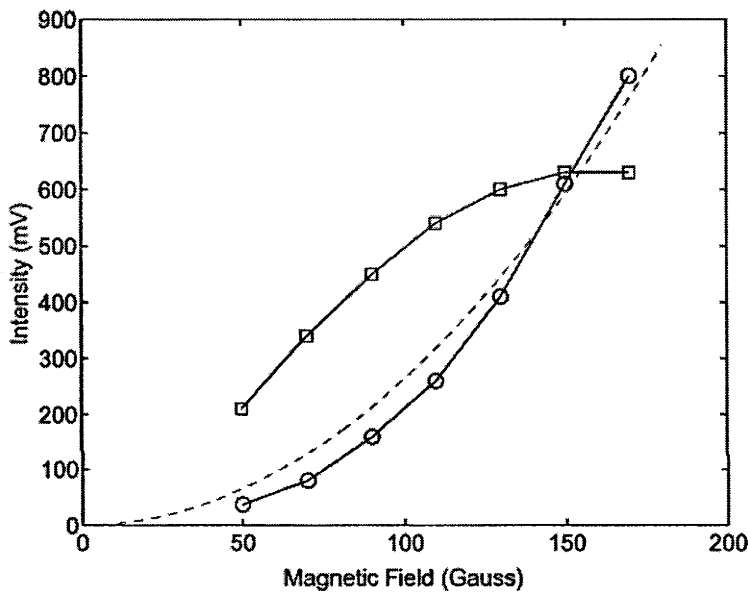


Figure 5.9: Relative Intensity of 488 nm (○) and 811 nm (□) wavelength radiation as seen from a side port of WOMBAT in the same plane as the Langmuir probes. Dashed line is  $B^2/38$ . Operating conditions: 0.6 mTorr and 2.5 kW.

the line averaged density. As only a 35 GHz interferometer was available for the experiment, it could only be concluded that the density inside the column was in excess of  $1.5 \cdot 10^{13} \text{ cm}^{-3}$  as the microwaves were cut-off under these conditions (c.f. 3.14).

The strong blue radiation is associated with a number of Ar II lines (particularly in the 400 nm range) which tend to indicate that the population of Ar ions was

greater than the population of neutrals and that the column was approaching complete ionisation (of the neutrals). Figure 5.9 shows the 488 nm Ar II and 811 nm Ar I emission as a function of magnetic field for a pressure of 0.6 mTorr and an RF power of 2.5 kW, as viewed by a monochromator through a fibre optic with an acceptance angle of  $40^\circ$  installed in a side port of the WOMBAT diffusion chamber. The 811 nm line saturates above 130 Gauss whilst for magnetic fields greater than 150 Gauss the 488 nm line continues to increase. The Ar II line goes as the square of the magnetic field which tends to indicate that it is proportional to the square of the electron density (for a helicon discharge) and hence the radiation is generated from the ground state of the ions and not the neutrals. The strong presence of the 811 nm line at all magnetic fields is probably due to the plasma surrounding the column which is over an order of magnitude less in density and hence dominated by Ar I emission. It was noted that this spectral behaviour was observed for all pressures between 0.6 mTorr (the lowest possible at these magnetic fields) and 1.5 mTorr. Though these spectral measurements do not of themselves offer an accurate estimation of the density they are a strong indication that the column is highly ionised.

In 1982 Boswell *et al.* [16] carried out similar experiments both at the A.N.U. and the University of Orleans using a 5 cm diameter discharge tube, 1 kW of RF power at a frequency of 7 MHz, a pressure of 7.5 mTorr and a magnetic field of 1 kilo-Gauss. The plasma created in that device was highly ionised with a core dominated by Ar II surrounded by an annulus principally composed of Ar I. The radial distribution of these populations was determined optically using a 1 m monochromator, by sliding a 1 mm slit across a Brewster window located at one end of the source tube. It can be seen from the data presented in that letter that the Ar II intensity was strongly peaked in the center of the discharge, dropping off as roughly  $1/r^2$ , whilst the Ar I emission was peaked close to the walls increasing roughly as  $r^2$ ,

where  $r$  was the radial distance from the center of the discharge tube. It was also reported in that letter that the gas was close to full ionisation.

At 1.2 mTorr (the most usual working pressure for the experiments presented in this chapter) the neutral gas density is  $3.84 \cdot 10^{13} \text{ cm}^{-3}$ . In light of the microwave data, if it is assumed that there is no gas pumping, then it is reasonable to assume that the peak plasma density inside the column was between  $1.5 \cdot 10^{13} \text{ cm}^{-3}$  and  $3.8 \cdot 10^{13} \text{ cm}^{-3}$ .

#### 5.2.4 Ion Cyclotron Waves

As the density is between  $1.5 \cdot 10^{13} \text{ cm}^{-3}$  and  $3.8 \cdot 10^{13} \text{ cm}^{-3}$  the density is set to  $10^{13} \text{ cm}^{-3}$  for simplicity. The Alfvén velocity at 158 Gauss is  $9.8 \cdot 10^3 \text{ m.s}^{-1}$  so that setting the Alfvén wavelength to 2 m (the length of the plasma column) yields an Alfvén wave frequency of 5 kHz which is roughly 0.7 times the theoretical ion cyclotron frequency.

Waves with a frequency close to 0.7 times the theoretical ion gyro frequency were observed in WOMBAT under these same conditions, in particular for magnetic fields greater than 130 Gauss. These waves produced fluctuations in the floating potential and density that were measured using the cylindrical Langmuir probe described in 3.3.1 and were observed simultaneously with upper and lower side bands on the helicon pump. To record this, the Langmuir probe was connected to the  $50\Omega$  input of a heterodyne spectrum analyser via a DC block (a small capacitor) and the analogue signal of the spectra was digitised using a 12-bit ADC. Fifteen digitised spectra were captured and averaged to increase the signal-to-noise ratio of the measurements. This number of averages was chosen to minimise the quantity of data acquired for the best possible signal-to-noise ratio.

## Experimental Evidence of Ion Cyclotron Waves

A typical set of spectra, measured here at a radius of 30 mm from the centre of the column for a magnetic field of 158 Gauss, is shown in figures 5.10 and 5.11. The helicon wave (7.2 MHz) has clear upper and lower sidebands at 5 kHz and 10 kHz from the center frequency and a low frequency wave exists at 5 kHz. Sidebands at three times the ion wave frequency were also occasionally observed. The low frequency wave was often less distinguishable from the background noise than

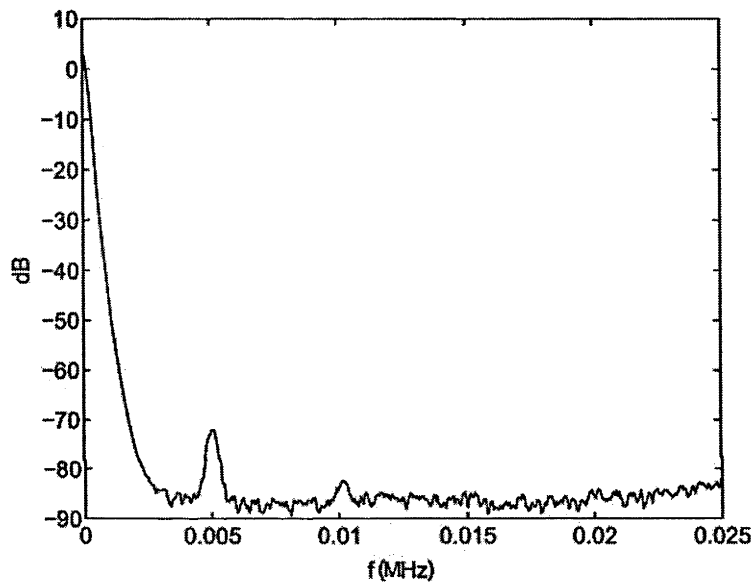


Figure 5.10: Ion cyclotron idler wave. Frequency spectrum for 0 to 25 kHz window, 1 kHz bandwidth. Operating conditions: 1.2 mTorr, 1.9 kW and 158 Gauss.

the helicon sidebands, its amplitude depending heavily on the correct tuning (not necessarily the lowest reflected power) and was rarely accompanied by waves that could be interpreted as harmonics. These waves were highly localised in the center of the column as can be seen from figure 5.12 with highest amplitudes for radii less than 10 mm. It was also observed, however, that the broadband noise was much higher in this region, reducing the signal-to-noise ratio considerably.

The amplitudes of both the upper and lower side bands follow the same evolution

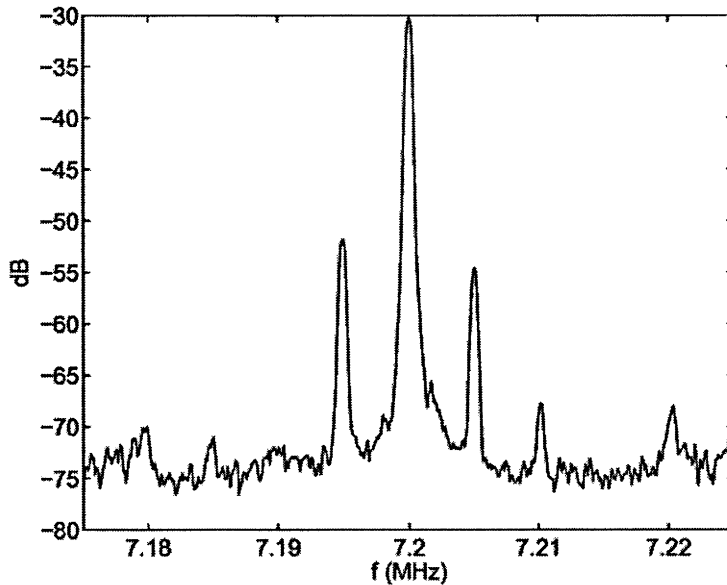


Figure 5.11: Pump and daughters: frequency spectrum centered on 7.2 MHz with 50 kHz span, 1 kHz bandwidth. Operating conditions: 1.2 mTorr, 1.9 kW and 158 Gauss.

as a function of radius, decreasing monotonically upon moving away from the center.

The low frequency wave as well as all the sidebands are observed to change frequency as a function of magnetic field, however the signal-to-noise ratio of the sidebands was generally higher than that for the low frequency wave. Figure 5.13 shows that the absolute value of the difference between the first harmonic upper and lower side band frequencies and the helicon frequency for magnetic fields between 130 Gauss and 158 Gauss is roughly linear and sits on a line 0.7 times the theoretical ion gyro-frequency. No measurements below 130 Gauss were taken because both the low frequency wave as well as the helicon sidebands were not present for these magnetic fields. As the low frequency wave is 0.7 the theoretical ion gyro-frequency and is a linear function of magnetic field, it is reasonable to assume that this wave is an ion cyclotron wave (ICW) mode with a lower bound threshold magnetic field of 130 Gauss, though it may be that the ICW still exists for lower magnetic fields but is



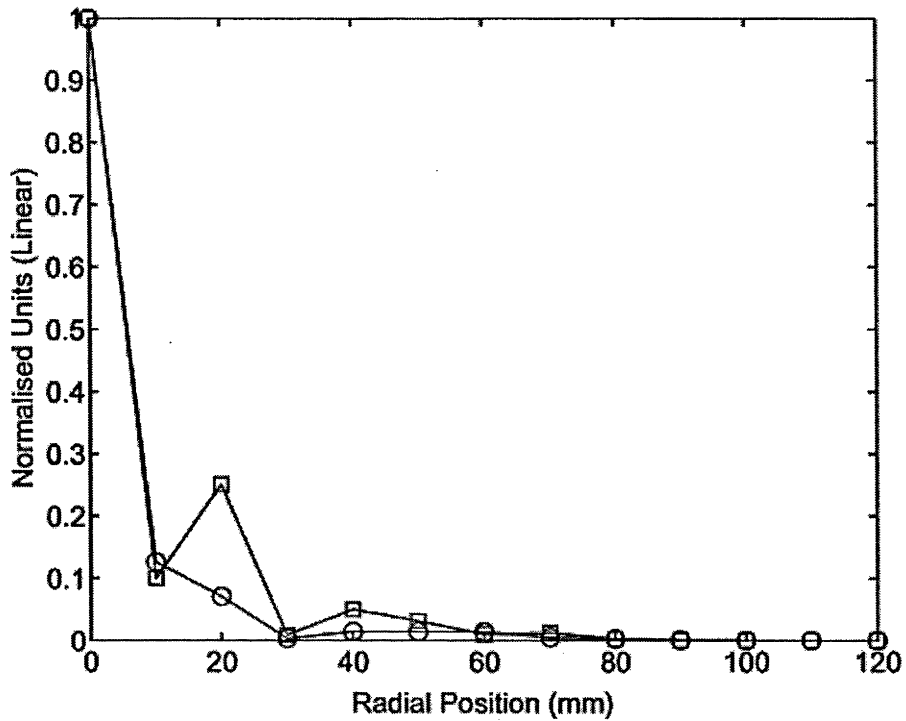


Figure 5.12: First harmonic upper (□) and lower (○) side band amplitude as a function of radial position. 0 mm is the center of the column. Operating conditions: 1.2 mTorr, 1.9 kW and 158 Gauss.

buried inside the surrounding broadband noise. An upper bound on the magnetic field could not be determined as the field in the diffusion chamber was limited to 158 Gauss by the solenoid power supply.

#### Four Wave Resonant Interaction

These experimental results were explained in terms of a filamentation theory developed in collaboration with Prof. Montague Giles and what follows is a brief summary of his theoretical discussion.

The electric field is separated into a high frequency helicon wave field,  $\mathbf{E}_h$ , and a low frequency electrostatic (ES) ICW field,  $-\nabla\phi$ :

$$\mathbf{E} = \mathbf{E}_h - \nabla\phi \quad (5.15)$$

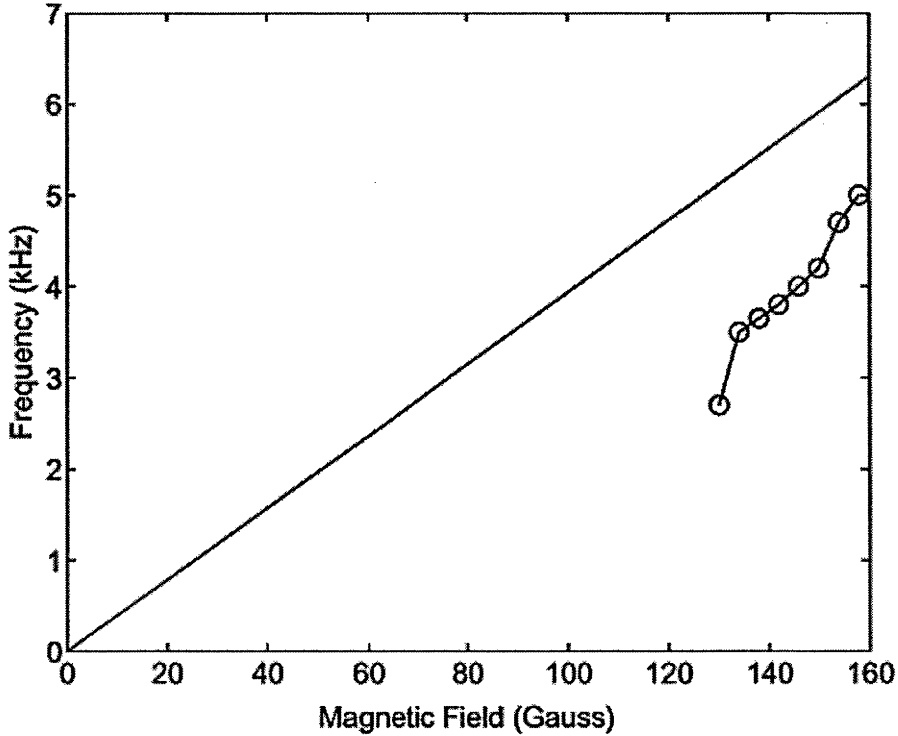


Figure 5.13: Absolute value of the difference between the first harmonic upper and lower side band frequencies and the helicon frequency as a function of magnetic field. Solid line: theoretical ion gyro-frequency; circles and solid line: experimental results. Operating conditions: 1.2 mTorr and 1.9 kW.

The quasi-neutrality condition (assumed) replaces Poisson's equation for the ES potential  $\phi$ , so that the ion and electron densities,  $n$ , are each the sum of the background plasma density  $n_0$  and a low frequency density fluctuation  $\delta n$ .

The magnetic field consists of the externally applied field  $\mathbf{B}_0$  and the high frequency helicon magnetic wavefield  $\mathbf{B}_h$ :

$$\mathbf{B} = \mathbf{B}_0 + \mathbf{B}_h \quad (5.16)$$

Let us assume that the helicon wave couples into the ES ion wave noise field at a frequency  $\Omega_c$  somewhat below the ion gyro-frequency,  $\Omega_i$ . When the Alfvén speed,  $v_A$ , is much smaller than the speed of light  $c$ , the low frequency branch of the ES ion wave field can only differ appreciably from  $\Omega_i$  if the angle of propagation  $\theta$

relative to the external magnetic field  $\mathbf{B}_0 = B_0 \mathbf{b}$  satisfies the condition  $\cos \theta \lesssim \sqrt{\mu}$ , where  $\mu$  denotes the ratio of the electron and ion masses,  $\mu = m_e/m_i$ . Under these circumstances the ion wave obeys the dispersion relation

$$\Omega_c = \frac{\Omega_i}{(1 + \mu \sec^2 \theta)^{\frac{1}{2}}}, \quad (5.17)$$

and gives rise to a low frequency fluctuation  $\delta n$  in the background plasma density  $n_0$ [91].

These almost transverse density fluctuations refract the helicon wave, so that upper and lower helicon sidebands appear. The mean Lorentz force due to the total helicon wave field then intensifies the density fluctuations in a positive feedback loop, allowing the instability to grow.

If we consider only the linear components of the the helicon Lorentz force, that is we ignore  $\mathbf{E}_h$  and  $\mathbf{B}_h$ , then from the ion equations of motion and continuity we see that the ES wave field causes the ion density to fluctuate according to:

$$\left( \frac{\partial^2}{\partial t^2} + \Omega_i^2 \right) \delta n = \frac{en_0}{m_i} \nabla^2 \phi \quad (5.18)$$

Since we have assumed quasi-neutrality, the ion density fluctuation  $\delta n$  also gives rise to an electron density fluctuation which is maintained through the generation of a low frequency electron current along  $\mathbf{B}_0$  driven by the mean helicon Lorentz force (and not by the electrons adiabatically maintaining a Boltzmann distribution).

Thus, the electron equations of motion and continuity give:

$$\frac{\partial^2 n}{\partial t^2} + \frac{en_0}{m_e} \frac{\partial^2 \phi}{\partial z^2} = 0 \quad (5.19)$$

which follows from the fact that the flow of electrons along  $B_0$  is determined by the ES field according to:

$$\frac{\partial v_{e,slow}}{\partial t} = \frac{e}{m_e} \frac{\partial \phi}{\partial z} \quad (5.20)$$

where  $v_{e,slow}$  is the low frequency component of the electron flow along  $B_0$ . Equations 5.19 and 5.20, when taken together, yield equation 5.18. However, when  $n$

and  $\phi$  represent a thermal ES field, these equations present no mechanism to cause amplification of the noise field.

But, when nonlinear (high frequency) effects are taken into account, the mean helicon Lorentz force due to the pump and its sidebands also contribute to the flow of electrons along  $\mathbf{B}_0$  (the ions are not effected by high frequencies) and provides the mechanism for the amplification. To derive a nonlinear dispersion relation for this instability, the cold plasma equations can be used together with Maxwell's equations. The total helicon wave field  $\mathbf{B}$  satisfies the linear wave equation and is supplemented here by the nonlinear perturbation of the refractive index, namely

$$(n_0 + \delta n) \frac{\partial \mathbf{B}}{\partial t} = -\frac{c^2 \Omega_e}{\omega_p^2} n_0 \mathbf{b} \cdot \nabla \mathbf{curl} \mathbf{B}, \quad (5.21)$$

where  $\omega_p$  and  $\Omega_e$  are the electron plasma and gyro-frequencies. The coupling of the density perturbation to the helicon wave field obeys the equation

$$\left\{ \left( \frac{\partial^2}{\partial t^2} + \Omega_i^2 \right) (\mathbf{b} \cdot \nabla)^2 + \mu \frac{\partial^2}{\partial t^2} \nabla^2 \right\} \frac{\delta n}{n_0} = -\frac{c^2}{V_A^2} \nabla^2 \left( \mathbf{b} \cdot \nabla \left\langle \frac{1}{B_0^2} \mathbf{b} \cdot \mathbf{curl} \mathbf{B} \times \mathbf{B} \right\rangle \right), \quad (5.22)$$

which includes, on the left, the linear terms associated with the linear dispersion relation (5.17), and on the right, the source term stemming from the helicon Lorentz force, where the angular brackets signify averaging over the high frequencies.

A dispersion relation for the instability can be derived from (5.21) and (5.22) by a standard analysis in which the solution is approximated as a 4-wave interaction.

The frequencies and wavenumbers of the waves involved are as follows (relative to a rectangular coordinate system with  $Oz$  parallel to  $\mathbf{B}_0$ ): (a) the pump wave,  $\omega_0, (0, 0, k)$ ; (b) the upper and lower sideband waves,  $\omega_{\pm}, (l, 0, k \pm m)$ ; and (c) the ion wave,  $\Omega, (l, 0, m)$ . The familiar helicon dispersion relation follows from (5.21), giving  $\omega_0 = k^2 c^2 \Omega_e / \omega_p^2$  and  $\omega_{\pm} = \omega_0 [(k \pm m)^2 + l^2]^{\frac{1}{2}} / k$ . Since  $m \ll l \ll k$ , we have  $\omega_{\pm} \simeq \omega_1 \equiv \omega_0 \sqrt{1 + l^2/k^2}$ , so that the difference frequency  $\Omega_1 \equiv \omega_1 - \omega_0 \simeq \omega_0 l^2 / 2k^2$ .

The result of the nonlinear stability analysis based on (5.21) and (5.22) is the

dispersion relation

$$(\Omega^2 - \Omega_c^2) (\Omega^2 - \Omega_1^2) = -\Omega_i^3 (P\Omega_1 + Q\Omega), \quad (5.23)$$

where

$$P = C \frac{km^2l^2}{k^3(m^2 + \mu l^2)} \quad (5.24)$$

and

$$Q = C \frac{ml^4}{2k^3(m^2 + \mu l^2)}, \quad (5.25)$$

in which

$$C = \frac{\omega_0}{\Omega_e} \left( \frac{\omega_p E_0}{\Omega_i B_0} \right)^2 \quad (5.26)$$

where  $E_0$  is the amplitude of the pump wave electric field.

Instability is associated with the terms on the right side of (5.23) and they will exert their greatest effect at the ion wavelength for which the coefficients are largest. From (5.25),  $Q$  is maximum when  $m/l = \cos \theta = \sqrt{\mu}$ , which satisfies the condition for the ion wave to propagate.  $P$  then reaches half its maximum value but this is as required because its full maximum is only achieved at unphysical wavelengths. Under these conditions, by (5.17),  $\Omega_c$  assumes the value  $\Omega_{c0} = \Omega_i/\sqrt{2}$ .

It can now be demonstrated that  $\Omega_{c0}$  is, in fact, the frequency of the most unstable wave. To do this, it is sufficiently accurate to substitute  $\Omega = \Omega_{c0}$  in the small correction terms on the right side of (5.23), which can then be written as  $-\Omega_0^4$ .  $\Omega^2$  can now be solved to get

$$\Omega^2 = \frac{\Omega_{c0}^2 + \Omega_1^2}{2} \pm i \left\{ \Omega_0^4 - \left( \frac{\Omega_{c0}^2 - \Omega_1^2}{2} \right)^2 \right\}^{\frac{1}{2}}. \quad (5.27)$$

This result shows that the growth rate is largest when

$$\Omega_{c0} = \Omega_1. \quad (5.28)$$

It is thus confirmed that the frequency of the most unstable wave is approximately  $\Omega_i/\sqrt{2}$  or  $0.7\Omega_i$ .

Equation (5.28) is a resonance condition which states that the linear helicon waves have difference frequencies which match the ion wave frequency. However, the nonlinear waves have frequency shifts which displace the sideband frequencies to  $\omega_0 \pm \Omega_c$ . Note further that (5.28) yields the transverse wavenumber of the ion wave as  $l \simeq k\sqrt{2\Omega_{c0}/\omega_0}$  which confirms that the required condition  $m \ll l \ll k$  is satisfied by this approximate solution.

### Ion Cyclotron Parameter Space

Over almost all of the operating range, the narrowband ICW and associated helicon sidebands could not be discerned from the background noise field. Even within the parameter space where the ICW was observed, it was found to be very sensitive to tuning with the optimal signal-to-noise ratio being obtained for a reflected power of roughly 10% (even though the matching network was capable of achieving very good impedance matching with reflected powers of less than 1% for all operating regimes).

It has already been shown that there was a lower bound in magnetic field of 130 Gauss for the ICW to be observed, though it was unclear whether this was a lower bound threshold for launching the ICW mode or if it corresponded to a degradation of the signal-to-noise ratio, that is, the ICW was still propagating but its amplitude was less than that of the surrounding broadband noise. An upper bound could not be determined due to limitations in the solenoid power supply.

For magnetic fields greater than 130 Gauss, a plasma could not be maintained at less than 0.6 mTorr for any power. This was true even when first striking the plasma at higher pressure and then gradually reducing it to the desired level. It is proposed that this was due to an increase in the effective mean free path for ionisation. Between 0.6 mTorr and 1.5 mTorr ICW were easily found, but above this pressure range they became progressively more dominated by the background noise.

The measurement of the ICW was more sensitive to power than pressure and mag-

netic field, appearing only in a very narrow band centered on 1.9 kW. Again the helicon sidebands were more easily discerned than the ICW themselves, but were also not observed at much outside this parameter range. At higher powers the broadband noise field was more prominent so it was difficult to determine whether the increased power "choked" the ICW or "smothered" it with noise. A similar observation was made at lower powers as the amplitude of the narrowband peak associated with the ICW and sidebands decreased gradually relative to the surrounding broadband noise rather than disappearing discontinuously.

### Discussion

Because it was difficult to discern between the ICW and surrounding noise when the signal-to-noise ratio was less than or equal to unity, the full range of parameters over which the mode existed and was capable of coupling energy to ions was difficult to determine. However, even though the operating conditions for which the ICW propagated may have been larger than the range over which it was discernible relative to the back ground noise field, its amplitude was reduced away from the optimal parameter range. What is less clear from the data presented here is the evolution of the ion temperature as a function of the ICW amplitude, in other words whether the decreased signal-to-noise ratio was a result of increased damping through ion heating or a change in operating conditions. This measurement was attempted using the RFEA described in 3.3.3 but no significant trend could be discerned. The size of the probe (a grounded 25 mm x 15 mm x 10 mm stainless steel box), however, may have perturbed the plasma and impeded the growth of the filamentation instability. A less invasive technique would have been to use laser induced fluorescence (LIF) but was not possible.

Ion heating is also associated with the ICW damping rate, which can be measured from wave amplitude as a function of position if the wavelength can first be deter-

mined. A measurement of the wavelength was attempted using an ensemble averaged cross-power correlation method. As these measurements were performed before the filamentation theory described in the section *Four Wave Resonant Interaction* was developed, it was assumed that the ICW was either an azimuthal or a longitudinal mode. Hence an experiment using two cylindrical Langmuir probes placed at right angles in a plane perpendicular to the chamber axis of symmetry (introduced through separate ports) and another experiment using a double tipped Langmuir probe was used. The double tipped probe (not described in chapter 3) briefly consisted of two 250 $\mu\text{m}$  diameter, 5 mm long probe tips separated by 3 mm, which could be rotated around the probe's axis of symmetry so that they were either in the transverse or longitudinal plane. The probe housing was inserted in the same radial port as the other probes (30 cm downstream of the source). The measurements themselves consisted of 84 ensembles, but the averaged cross-power spectra of the signals captured by the two probe tips showed no trend at any frequency for either experiment. As a result the wave damping rate could not be measured and hence an approximation of the perpendicular ion heating could not be obtained. However, in light of the theoretical discussion on filamentation instabilities it is now clear that the ICW was probably a transverse mode for which the previously described measurement technique was inappropriate.

The helicon dispersion relation can be obtained from (5.21), giving  $\omega_0 = k^2 c^2 \Omega_e / \omega_p^2$  which after some algebra can be rewritten to yield the helicon wavelength:

$$\lambda = 5.6 \cdot 10^7 \sqrt{\frac{B_0}{n_0 \cdot f}} \quad (5.29)$$

where  $f$  is the helicon frequency in Hz,  $B_0$  is in Gauss and  $n_0$  is in  $\text{cm}^{-3}$ . Assuming a helicon frequency of 7.2 MHz, a magnetic field of 158 Gauss and a density of  $10^{13} \text{cm}^{-3}$ , the helicon wavelength is roughly 8 cm which corresponds to a wavenumber of 78  $\text{rad.m}^{-1}$ . From the theoretical discussion, the transverse wave number cor-



responding to the ICW is then  $2.9 \text{ rad.m}^{-1}$  yielding a wavelength of roughly 2 m. The angle of propagation for the helicon sidebands can now also be calculated and is  $2^\circ$ .

From these results we can see that a half wavelength of the ICW could fit across the diameter of the WOMBAT diffusion chamber. Also, if we assume that the four wave interaction occurs on axis and starts under the antenna, then the ICW are launched in a cone with a  $2^\circ$  half angle and the helicon sidebands can only exist within 3 cm of the centre of the column at the position of the probe, 93 cm downstream of the antenna. If we assume that the instability is born at the constriction in the magnetic field (i.e. where it starts to become uniform, which is closer to the assumptions of the theory) then the probe is only 30 cm downstream of this point and the propagation cone of the helicon sidebands extends to 1 cm at the position of the probe. This corresponds well with the data of figure 5.12 which shows that the helicon side bands decay to less than 10% of their on axis maximum within 1 cm of the axis.

The ICW, however, satisfy equation 5.18 and can in principal, ignoring wave-particle and collisional damping, propagate beyond the 3 cm radial limit imposed on the helicon sidebands. The best signal-to-noise ratio was obtained at 3 cm from the center (along the proposed propagation cone) and decayed rapidly beyond this. However, the annulus confined between 3 and 6 cm from the center of the column corresponded to large broadband structures (approximately 450 kHz wide) which may have been responsible for reducing the signal-to-noise ratio rather than the waves themselves being damped. In addition, the theory presented above assumes  $n_0$  is spatially uniform whilst experimental evidence shows that it varies strongly with radius (c.f. figure 5.16) especially between 3 and 6 cm from the center of the column. Equation 5.18 shows that the ES wave field is dependent on  $n_0$  and it is possible that the decrease in the ICW amplitude is due to variations in density rather than

damping from wave-particle interactions (collisional damping can be ignored over these length scales, at this pressure). In any case, even if the narrowband signal can be differentiated from the background noise by ensemble averaging or some other technique, the measurement of the transverse ICW wavelength will only be possible over a range of a few centimetres and may be difficult to record at all as the signal amplitude falls off in much less than a wavelength.

### 5.2.5 Ion Acoustic Waves

Very pronounced wave activity was also measured at 100 kHz and to a lesser extent 200 kHz and was spatially localised at the edge of the plasma column. As opposed to the ICW, these higher frequency waves were found to be very stable over a broad range of operating conditions and were relatively insensitive to tuning. Their spectra are associated with helicon sidebands similar in nature to those presented in the previous section on 4 wave interactions where the absolute value of the frequency difference between the upper and lower sidebands and the helicon was equal to the ion wave frequency. However, the filamentation theory presented in conjunction with the ICW is not applicable to these higher frequency waves and so can not be employed here.

The 100 kHz oscillations are too low in frequency to be lower hybrid waves ( $f_{lh} \simeq 2$  MHz at 160 Gauss) and an order of magnitude higher in frequency than the ion cyclotron waves presented in the previous section. There was strong experimental evidence that these 100 kHz oscillations were IAW. Firstly, they were spatially localised in regions of high plasma pressure gradients. Secondly, measurements done collaboratively at the Ecole Polytechnique in Paris by Nicolas Plihon showed that the wave was an azimuthal mode propagating at the sound speed. IAW have been reported in conjunction with helicons before [98, 14, 66, 122], notably in relation

to the parametric decay process. Briefly, a resonant interaction between three or more waves can result in a parametric decay if it satisfies the conditions of energy and momentum conservation. Energy conservation requires that the frequency of the daughter waves add up to the frequency of the pump:  $\omega_1 = \omega_2 \pm \omega_3 \pm \dots$ ; and momentum conservation that the wave numbers sum up in a similar fashion:  $k_1 = k_2 \pm k_3 \pm \dots$ . Taken together, these relations lead to the simple rule that the group velocity of the pump and daughter waves should equal the phase velocity of the low frequency ion wave. It is tempting to couch the spectral data presented in figures 5.14 and 5.15 in terms of a parametric interaction but the wavelength of the helicon and its sidebands are bigger than those of the low frequency ion wave and so the wavenumbers can not be made to fit the momentum conservation relation. Instead, it is proposed that the free energy in the radial plasma pressure gradient resulting from the electron temperature and density gradients produced at the edge of the plasma column drove the IAW. The resulting oscillation of the refractive index at the ion wave frequency would then cause the helicon wave to be modulated producing upper and lower sidebands that, at least in the frequency domain, mimicked aspects of parametric decay.

### Experimental Observation

As with the cyclotron waves, the ion acoustic perturbations caused the floating potential to oscillate and could be measured with a floating Langmuir probe. This was done with the same experimental methodology as was used for the acquisition of the ion cyclotron spectral data of the previous section and employed the same cylindrical Langmuir probe of chapter 3 connected to a heterodyne spectrum analyser via a DC block, with the output digitised, windowed and averaged. It was found that at the edge of the plasma in a narrow annulus centered roughly 50 mm from the axis of the column, an ion wave with a clear peak in the 100 kHz range

could be discerned as shown in figure 5.14. This sharp peak coincided with the maximum of a large broadband structure of almost 450 kHz in width. At 10 kHz on either side of the 100 kHz narrowband wave were two clear peaks, which were not analysed in detail, but which could be interpreted as second harmonic sideband modulation of the ICW with the IAW.

As shown in figure 5.15, two sidebands 100 kHz above and below the helicon wave

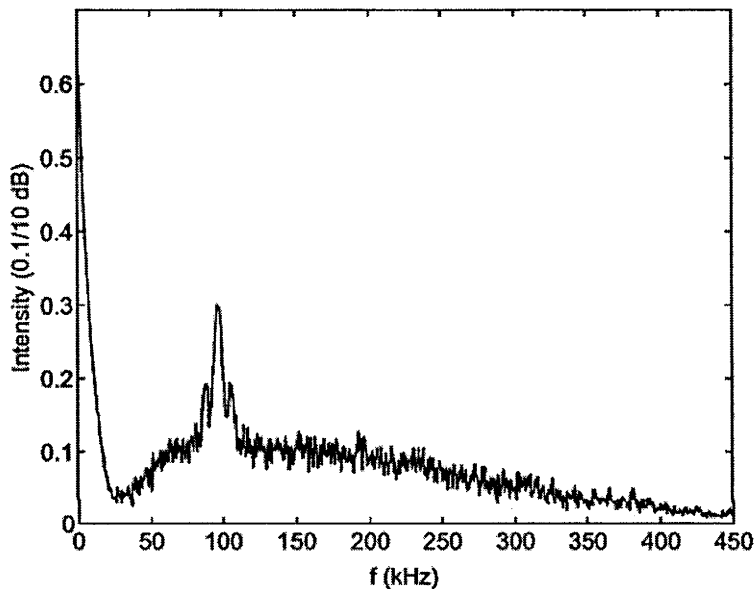


Figure 5.14: 100 kHz ion acoustic idler wave. Frequency spectrum for 0 to 450 kHz window, 3kHz bandwidth. Operating conditions: 1 mTorr, 2.5 kW and 110 Gauss.

(7.2 MHz) were observed. It was noted that these helicon sidebands were more clearly differentiated from the background noise field over a broader range of parameters than the low frequency IAW.

The parameter range used to study these 100 kHz waves in WOMBAT was 0.5 - 3 mTorr in pressure, 50 - 2500 W in forward power and 50 - 170 Gauss in magnetic field.

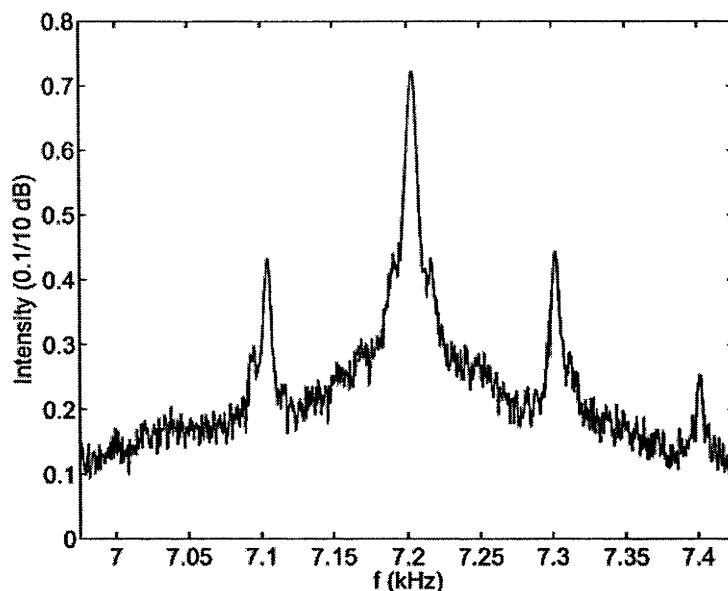


Figure 5.15: Helicon and side bands. Frequency spectrum centered on 7.2 MHz with a span of 500 kHz, 3 kHz bandwidth. Operating conditions: 1 mTorr, 2.5 kW and 110 Gauss.

### Localisation

Figure 5.16 shows normalised plasma density, electron temperature and floating potential as a function of radial position for 1 mTorr of pressure, 2.5 kW of RF power and 110 Gauss of magnetic field. The column diameter was 80 mm as defined by the FWHM of the density profile measured using the cylindrical Langmuir probe of 3.3.1. It was noted that, although the density measurements made inside the column were not always reliable, the FWHM was consistent across measurements of all parameters. At roughly 5 mm from the inside the column edge, all the plasma parameters had a maximum in gradient. A peak occurred in the radial position of the narrowband wave 50 mm from the center or 10 mm from the edge of the column as defined by the FWHM. By comparing figures 5.16 and 5.17 it was observed that the maximum amplitude of the 100 kHz waves was approximately 15 mm outside the point of highest gradient in the plasma parameters. Elsewhere in the plasma

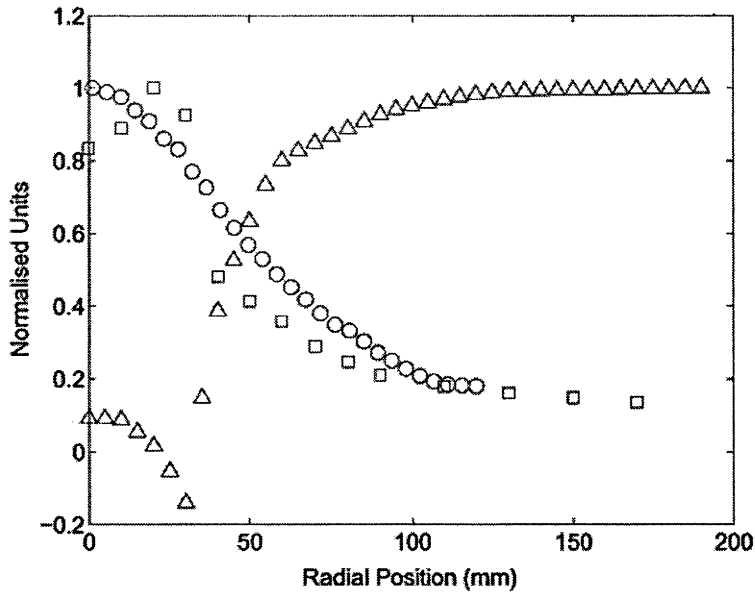


Figure 5.16: Normalised plasma parameters demonstrating the position of the high gradient region at the edge of the column.  $\circ$ : plasma density ( $\times 8.9 \cdot 10^{12} \text{ cm}^{-3}$ );  $\square$ : electron temperature ( $\times 8.1 \text{ eV}$ );  $\triangle$ : floating potential ( $\times 13.0 \text{ V}$ ). Plasma operating conditions: 1 mTorr, 2.5 kW and 110 Gauss.

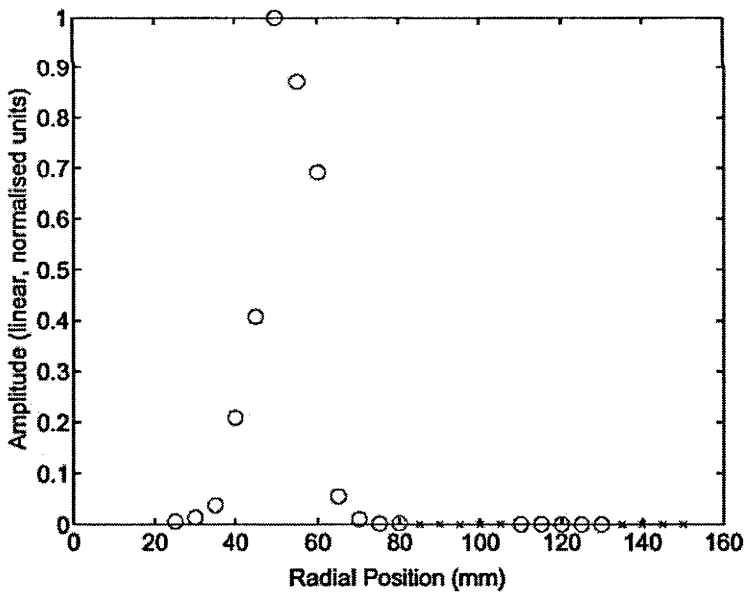


Figure 5.17: 100 kHz ion acoustic idler wave amplitude as a function of radial position.  $\circ$ : narrowband wave amplitude.  $\times$ : amplitude of broadband structure at 100 kHz.

(marked by crosses in figure 5.17) the 100 kHz wave was indistinguishable from the surrounding broadband structures. These results strongly suggest that the ion acoustic instability was generated by the radial pressure gradient ( $\nabla n.T$ ) present at the edge of the column and that the subsequent fluctuation of the refractive index modulated the 7.2 MHz helicon wave, producing the observed upper and lower sidebands.

The drift velocity of particles generated by  $E \times B$  forces is  $v = E/B$ . From figure 5.17 the electric field at 50 mm from the center of the column is approximately  $2 \cdot 10^2 \text{ V.m}^{-1}$  for a magnetic field of  $1.1 \cdot 10^{-2} \text{ T}$  so that the  $E \times B$  drift velocity is  $2 \cdot 10^4 \text{ m.s}^{-1}$ . This simple estimate is roughly 5 times the ion sound speed and demonstrates that there sufficient free energy in the  $E \times B$  field to drive the IAW instability.

### Pressure

Pressure did not significantly influence the narrowband 100 kHz wave in WOM-BAT, instead, increasing pressure was observed to increase the level of broadband structures in the frequency range. At higher pressures (greater than 3 mTorr), the range over which the 100 kHz wave could be clearly discerned as a function of radial position (relative to surrounding broadband structures), was significantly reduced. Similarly at very low pressures (less than 0.8 mTorr) no clear peaks could be discerned in the 100 kHz range. The optimal pressure range for the narrowband 100 kHz wave was 0.8 - 1.2 mTorr with a clear maximum in signal-to-noise ratio (100 kHz relative to broadband structures) at 1 mTorr.

### Power

For the IAW to be discernible from the broadband noise floor, a lower limit for the input power was observed to be 1600 W, below which no clear peaks were observed. However, broadband structures like that shown in figure 5.14 were still

present down to some hundreds of Watts (dependant on magnetic field and pressure). For powers above 900 W the broadband structures remained constant in amplitude. Thus for powers above 1600 W (with a pressure of 1 mTorr and a magnetic field of 110 Gauss) a corresponding increase in the 100 kHz signal amplitude resulted in an increased signal-to-noise ratio.

### Magnetic Field

The IAW was observed to increase in frequency with an increase in the magnetic field as shown in figure 5.18 where the wave frequency was 100 kHz at 100 Gauss

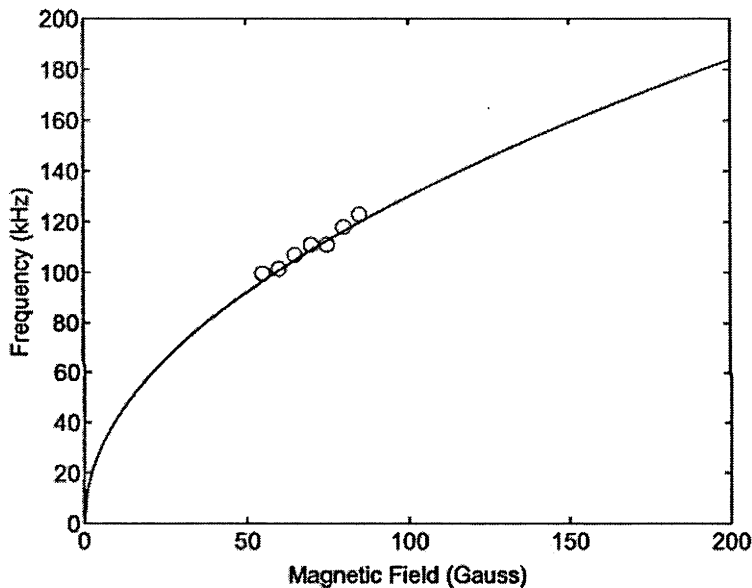


Figure 5.18: Idler frequency as a function of magnetic field.

and 123 kHz at 160 Gauss. Over the range measured it was found that the frequency was proportional to the square root of the magnetic field. A lower limit of 100 Gauss was observed for the applied magnetic field, below which no narrowband wave was observed. However, above this the peaks were clear and increased from 15 dB to 25 dB above the broadband noise floor. For the data presented in figure 5.18 the pressure was set to be in the middle of the optimal range (1 mTorr) and



the RF power chosen to maximise the narrowband peaks (2.5 kW). As the magnetic field was increased above 150 Gauss, the signal-to-noise ratio decreased so that at 170 Gauss the narrowband signal was only 5-10 dB above the noise floor. However, this was as a result of increased noise and not a reduction in the narrowband signal strength. Unfortunately, the field strength could not be increased beyond this limit and so it was not possible to determine whether there was also an upper limit to the magnetic field for which the narrowband structure was observable.

### A Comparative Study

Ion acoustic wave phenomena were also investigated in the smaller Ecole Polytechnique<sup>†</sup> (EP) helicon source which is typically used as a plasma processing tool. Though the E. P. helicon source is similar in conception to WOMBAT, there were a number of differences between the two experiments, notably chamber dimensions (source: 150 mm in inner diameter, 300 mm in length; diffusion chamber: 320 mm in inner diameter, 240 mm long), RF frequency (13.56 MHz), antenna geometry (Boswell type) and magnetic field set-up (uniform in the source and diffusion chamber). In addition, the RF power was limited to 1 kW and the magnetic field was not varied and set to 34 Gauss. Despite this, the two experiments both produced a low frequency ion wave on the order of 100 kHz in WOMBAT and 200 kHz in the EP machine with a maximum amplitude at the radius coinciding with the highest gradients in density, floating potential and electron temperature [24]. No low frequency waves were found in the centre of the discharge in either experiment, as opposed to many earlier helicon experiments [98, 66, 122].

These results suggest that the pump frequency, the plasma density and the volume of the plasma play little or no role in the observed behaviour of the waves. The mag-

---

<sup>†</sup>Laboratoire de Physique et Technologie des Plasmas, Ecole Polytechnique, 91128 Palaiseau Cedex France

netic field had a weak impact on the frequency of the ion wave which was observed to vary only as the square root in WOMBAT. A similar variation was observed in the EP machine as the pressure was varied. Unfortunately, from these experiments alone no definitive conclusion can be drawn from these variations because the form of the plasma itself changes as the magnetic field and pressure are altered and it is difficult to unfold what is causing the variation with the present set-ups.

Importantly for the A.N.U. ion source design, the wave activity was restricted to the edge of the plasma column, and, as no perturbations were observed along the central axis of the plasma would be unlikely to have any direct impact on ion extraction from a single centralised aperture.

# Parallel Ion Heating

This chapter is based on work not performed directly by the author, but is included in the spirit of completeness as it relates to the development of the A.N.U. compact plasma ion source.

It details the effect of collisional heating through charge exchange and elastic scattering collisions and demonstrates that the “balanced” matching network, smaller extraction apertures and magnetic confinement of the source plasma are effective in reducing parallel ion energy spread.

## 6.1 Charge Exchange and Elastic Scattering Collisions

As part of the FEI contract, Helen Smith was commissioned by the A.N.U. to produce a report detailing the effect of charge exchange collisions in the presheath on ion heating. She used the 1D planar PIC code `xpdp1` developed at Berkeley

Electrode Voltage, $V_{rf}$ (peak)	200 V
Source Frequency, $f_{rf}$	13.56 MHz
Electrode Separation, $d$	10 cm
Gas Pressure, $p$	10, 20, 40 mTorr

Table 6.1: Simulation parameters for a 1D PIC of a parallel plate discharge with variable pressure.

by Verboncoeur *et al.* [121] to simulate parallel plate discharges with either AC or

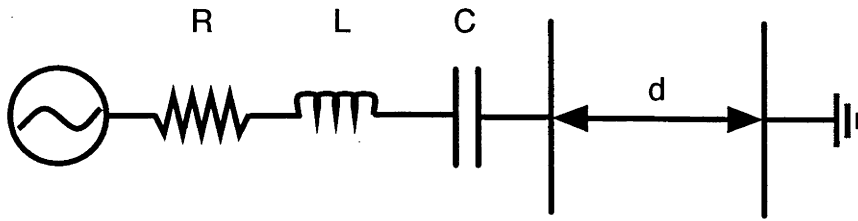


Figure 6.1: Circuit diagram of PIC simulation strategy.

DC applied voltage as shown in figure 6.1. The code employed a monte-carlo, null collision method to model collisions between neutrals and charged particles, with realistic collision cross-sections. Ion collisions were assumed to scatter isotropically, whilst electrons were treated anisotropically, depending on the relative electron energy. The simulations were used to model an RF discharge in Argon with variable pressure and the parameters are summarised in table 6.1.

According to the Bohm sheath criterion, ions must be accelerated up to the ion sound speed before entering the sheath to ensure its stability [83]. This leads to a small potential drop between the bulk of the plasma and the sheath edge known as the pre-sheath. Typically, the voltage drop in the presheath is assumed to be of the order of  $kT_e/2$ , and the ion energy distribution function is assumed to be a drifting Maxwellian, that is, isotropic with an offset velocity in the sheath direction. However, as the ions traverse the presheath they undergo elastic scattering collisions with neutrals which for large angle scattering can potentially transfer a substantial fraction of the ion velocity from the direction parallel to the voltage drop to the perpendicular. If a significant portion of ions are scattered in this way they gain energy in the perpendicular direction, resulting in non-thermal ion distribution functions.

Figure 6.2 shows typical time-averaged profiles of plasma potential, density and electron kinetic energy produced by the PIC code at steady-state. The presheath

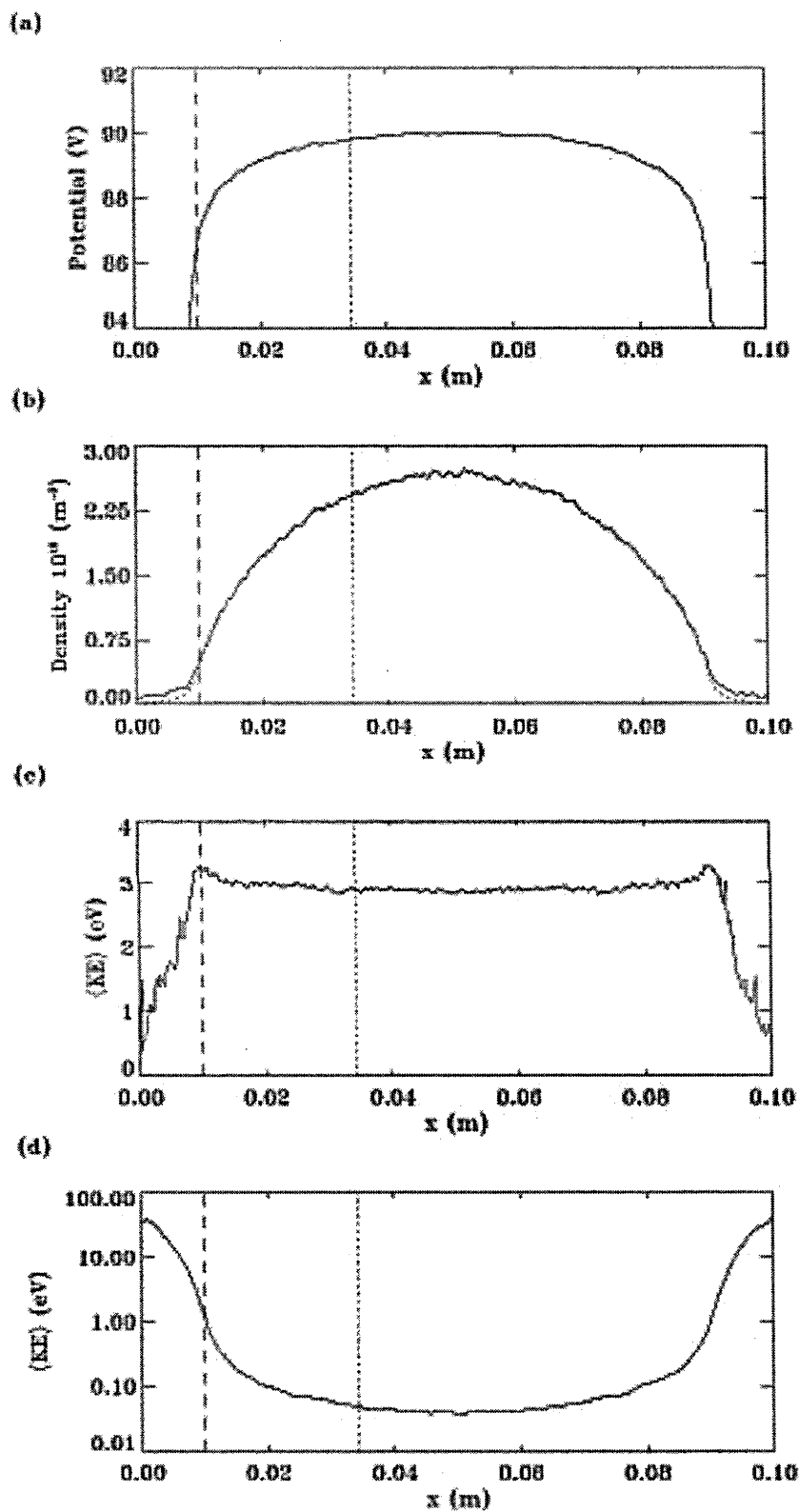


Figure 6.2: Time averaged profiles of a) plasma potential, b) density, c) electron energy and d) ion energy.

boundaries are difficult to define as the average ion energy rises monotonically from the center towards the boundary of the plasma with no clear transition between the bulk plasma, presheath and sheath. For the purposes of this study, the presheath was defined to start where the average parallel ion energy was 15% above that in the center of the discharge and ended at the point where the ion sound speed was attained. Assuming the electrons were in a Maxwellian distribution (which is verified in figure 6.3) their mean temperature can be related to the average kinetic energy by:

$$T_e = \frac{2}{3} \langle KE \rangle \quad (6.1)$$

and hence the ion sound speed,  $c_s$ , can be determined using:

$$c_s = \sqrt{\frac{eT_e}{M_i}} \quad (6.2)$$

For a pressure of 10 mTorr, the average electron kinetic energy was 3 eV in the

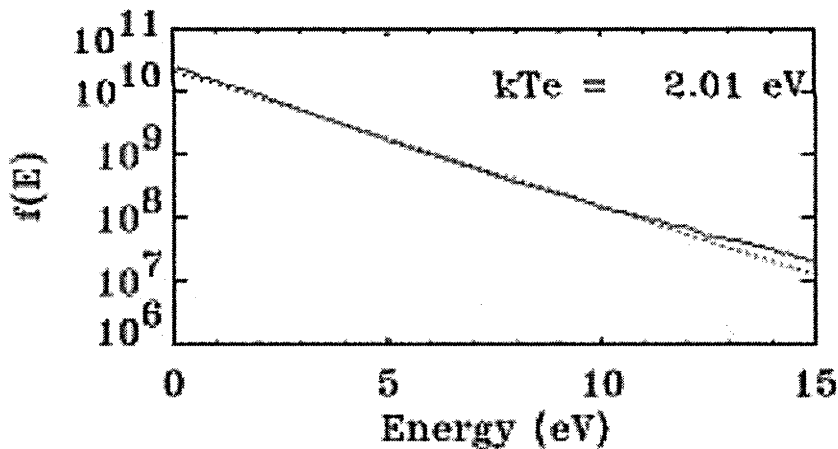


Figure 6.3: Log plot of electron energy distribution function in the center of the discharge showing that the electrons are in Maxwellian equilibrium. Dotted line: ideal Maxwellian; Solid line: simulated distribution function.

center so that the bulk electron temperature was 2 eV, yielding  $c_s = 2100 \text{ m.s}^{-1}$  or equivalently  $T_i = 1 \text{ eV}$  at the sheath edge. It was noted from figure 6.2(d) that average ion energy reached 1 eV at 1 cm from the plasma boundary which agreed

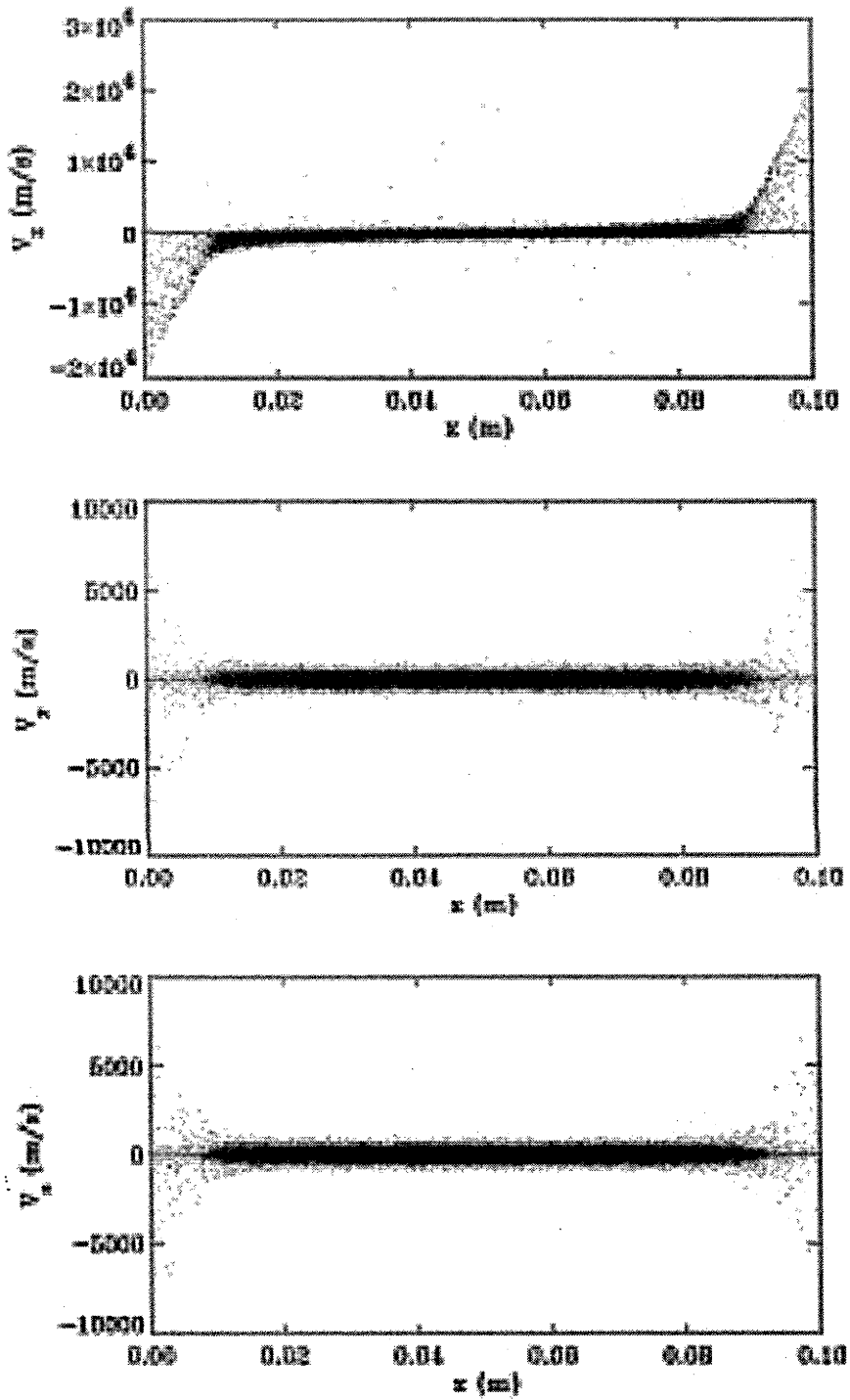


Figure 6.4: Phase space diagrams of: a)  $v_x$  vs.  $x$ , b)  $v_y$  vs.  $x$  and c)  $v_z$  vs.  $x$ .

well with the sheath width determined from visual inspection of the phase space diagram in figure 6.4. From figure 6.2(d) the average ion energy in the bulk plasma was 0.038 eV which corresponded well to the assumed neutral gas temperature of 0.026 eV. The average ion energy was 15% above the bulk energy at 3.4 cm from the plasma boundary giving a presheath width of 2.4 cm.

The charge exchange and elastic collision frequency profiles are shown in figure 6.5 and as expected are strongly dependant on the density profile, since, at low energy the cross-sections are relatively insensitive to energy [101, 29, 71, 40]. At 1 eV the charge exchange cross section is  $Q_{ce} = 76 \text{ \AA}^2$  and the elastic scattering cross-section  $Q_{es} = 58 \text{ \AA}^2$ . The mean free path for ion neutral collisions is given by:

$$\lambda_i = \frac{1}{(Q_{ce} + Q_{es})N_n} \quad (6.3)$$

where  $N_n$  is the neutral density equal to  $3.2 \cdot 10^{20} \text{ m}^{-3}$  at 10 mTorr. The mean free path for ion neutral collisions was therefore 2.3 mm, representing approximately one quarter of the sheath width and one tenth of the presheath.

Figure 6.6 shows the velocity distributions at various positions in the plasma notably in the center ( $x = 5 \text{ cm}$ ), at the presheath/bulk boundary ( $x = 3.4 \text{ cm}$ ), at three positions in the presheath ( $x = 2.5 \text{ cm}$ ,  $2 \text{ cm}$ ,  $1.5 \text{ cm}$ ) and at the presheath/sheath boundary ( $x = 1 \text{ cm}$ ). The perpendicular velocity,  $v_p$  was taken to be the RMS value of the two perpendicular components  $v_x$  and  $v_z$  relative to the potential drop along  $x$ . At the center of the discharge, the distribution function was a Maxwellian with a temperature of 0.026 eV, as expected, since the net force in the bulk was zero. At the presheath/bulk boundary the distribution showed a small directed velocity of around  $200 \text{ m.s}^{-1}$  attaining  $2000 \text{ m.s}^{-1}$  at 1 cm from the plasma boundary in good agreement with the calculated value.

As the ions progressed through the presheath they were observed to accumulate perpendicular energy attaining 0.1 eV at the sheath edge. Though this was 4 times the bulk ion energy, it was still a very positive result for high brightness FIB ap-



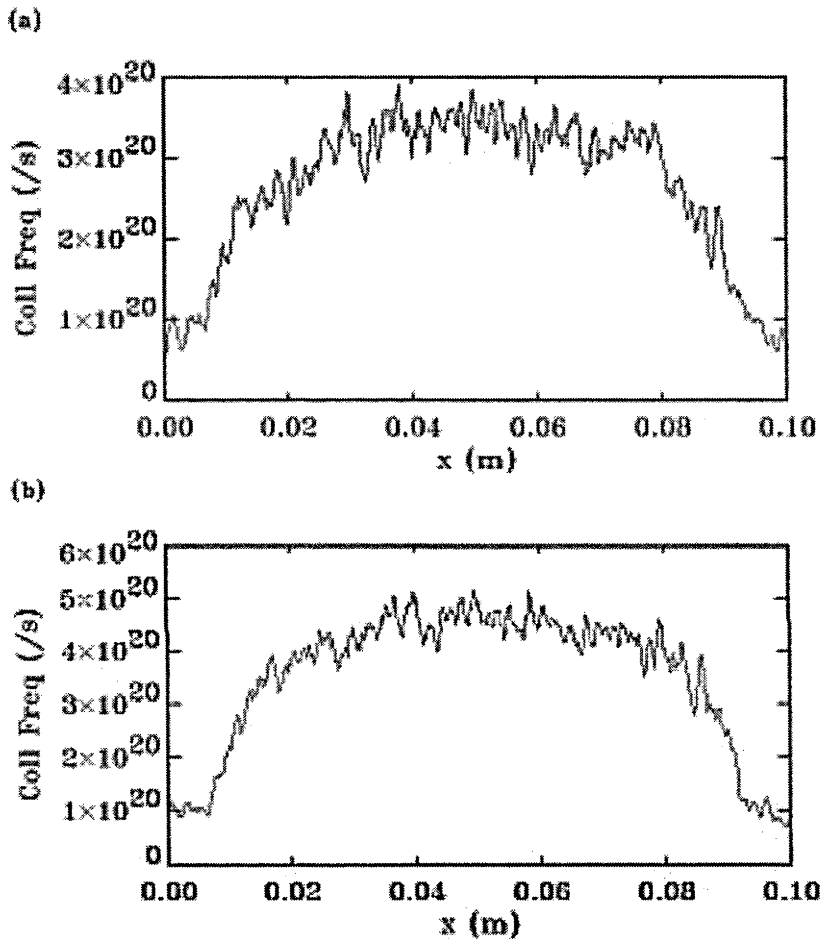


Figure 6.5: Profiles of the ion-neutral collision rate for: a) elastic scattering and b) charge exchange.

plications as the thermodynamic limits calculated for this work were usually based on an ion temperature of 1 eV. Even at higher pressures (20 mTorr and above) collisions in the presheath did not cause the perpendicular ion energy to increase beyond 1 eV as shown in figure 6.7.

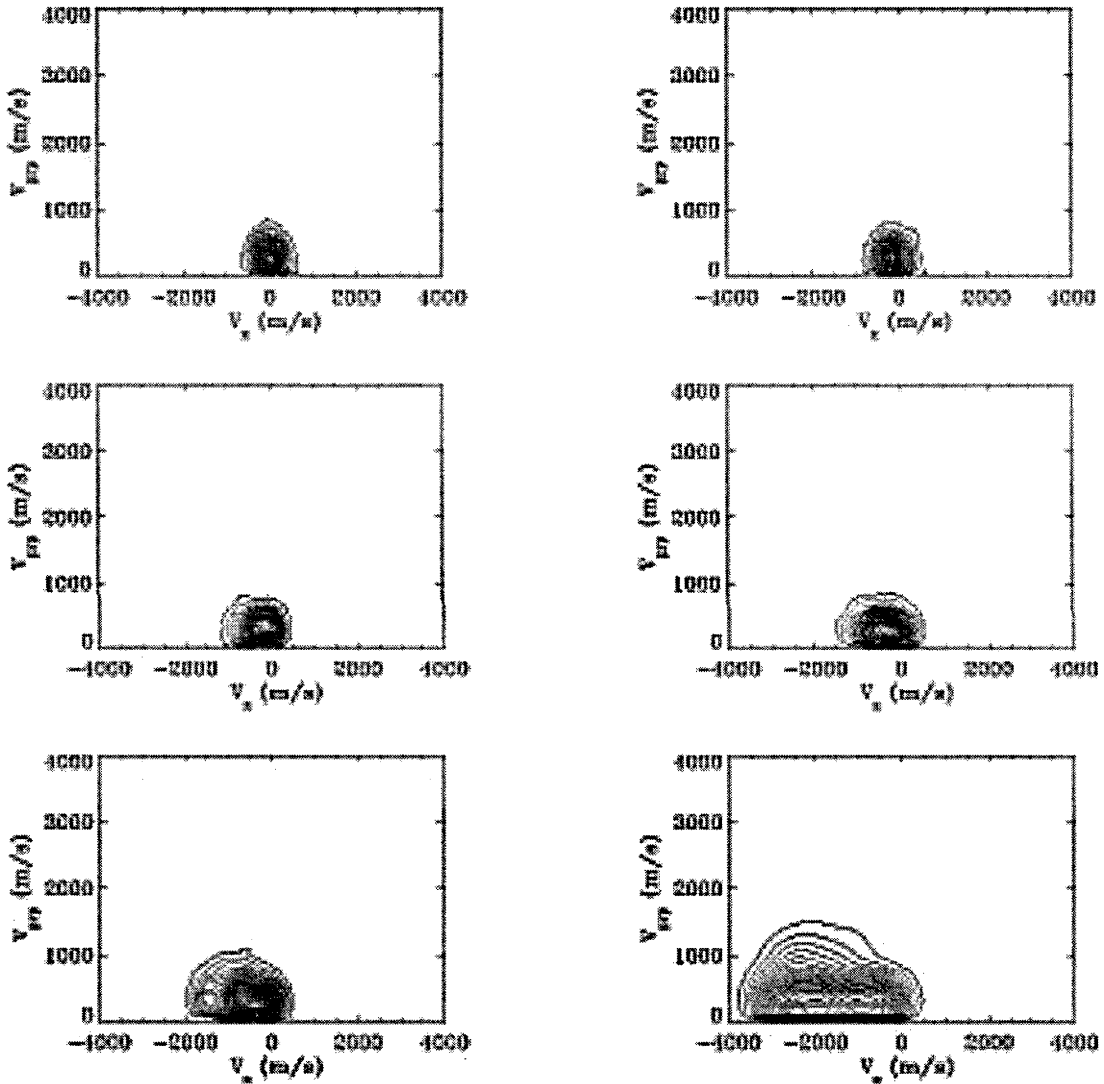


Figure 6.6: Ion velocity distributions for 10 mTorr. Top to bottom, left to right:  $x = 5$  cm, 3.4 cm, 2.5 cm, 2 cm, 1.5 cm and 1 cm.

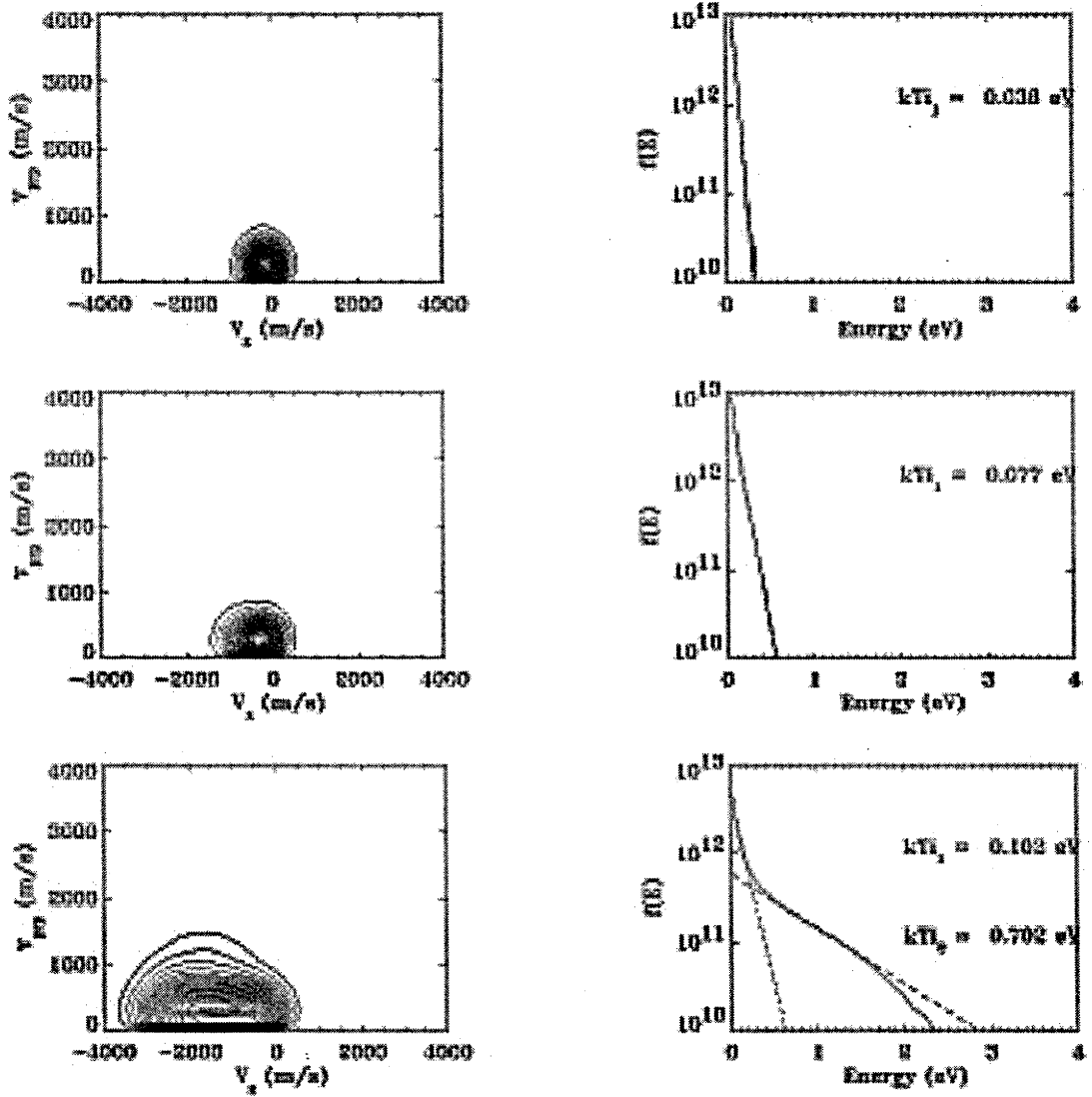


Figure 6.7: Ion velocity and energy distribution results for 20 mTorr. Top to bottom:  $x = 2.6$  cm,  $1.5$  cm and  $0.84$  cm.

## 6.2 Parallel Ion Energy Spread

### 6.2.1 Measuring Ion Energy Spread with a Mass Spectrometer

In order to measure the parallel ion energy spread of the system, N. Smith of FEI Co. installed the last prototype presented in chapter 4 onto a magnetic sector mass spectrometer and analysed a slightly divergent beam with an extraction potential of 3.6 kV. The energy resolution of the spectrometer is limited by the dimension of the magnetic sector entrance and exit slits which are optimised to achieve a reasonable working current (for which the slits should be as wide as possible) with the highest possible resolution (for which the slits should be as narrow as possible). The current emanating from the exit slit is collected by an electron multiplier tube and is directly related to the magnetic field necessary to ensure a beam of ions of mass  $M_i$ , charge  $q$  and energy  $V$  exit the magnetic sector at radius  $r_{exit}$  of the exit slit:

$$\frac{M_i}{q} = \frac{B^2 r_{exit}^2}{2V} \quad (6.4)$$

By scanning the magnetic field over a certain range and recording the collected current as a function of this variation, the energy distribution, including the thermal energy spread, of the extracted ions can be determined.

#### Energy Calibration of the Mass Spectrometer

The magnetic field is controlled by a Hall probe which measures the B field between the poles of the magnetic sector solenoid. This was calibrated as a function of beam energy by acquiring a broad mass range mass spectrum of the extracted beam as shown in figure 6.8 and identifying the Hall voltage of the  $40\text{Ar}^+$  as a function of beam energy (cf. figure 6.9). This relationship was approximately linear over the range with a slope of 49 eV/mV, but was more accurately described by a second order polynomial. For simplicity, the linear relationship was used.

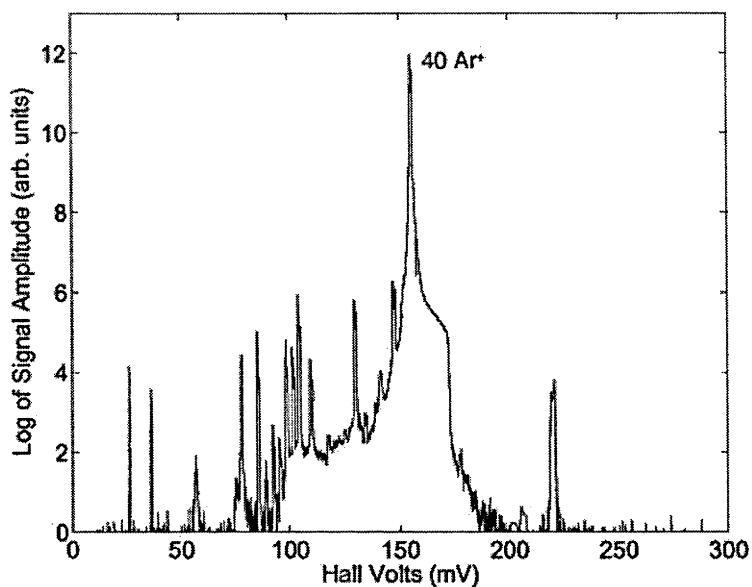


Figure 6.8: Broad mass range mass spectrum of extracted beam with operational parameters: RF power = 160 W; fill pressure = 10 mTorr; extracted current = 121  $\mu\text{A}$ ; extraction voltage 3602 V.

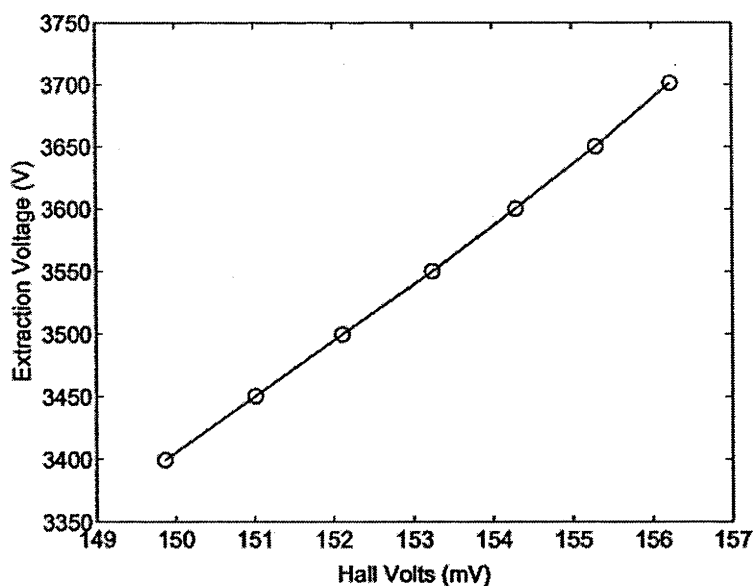


Figure 6.9: Extraction voltage versus Hall voltage. The relationship is roughly linear but is more accurately described by a second order polynomial.

Beams that traverse the mass spectrometer incur a phase-space transformation which can be described by the convolution of the extracted beam energy distribution function  $f_{entry}$  with the the transfer function  $F(E)$ :

$$f_{exit}(E) = F(E) * f_{entry}(E) \quad (6.5)$$

where  $f_{exit}$  is the measured beam energy distribution. If the energy spread caused by the transfer function is of the same order or greater than that of the beam, then it must be deconvolved from the measured quantity to obtain the true beam energy spread. If the measured energy spread is larger than that caused by the measurement equipment and the transfer function and true energy spread are assumed to be Gaussian, then the full-width-half-maximum (FWHM) of the measured energy spread is given by the quadrature relationship:

$$\Delta E_{measured} = (\Delta E_{beam}^2 + \Delta E_{spectrometer}^2)^{\frac{1}{2}} \quad (6.6)$$

where  $\Delta E_{measured}$  is the measured energy spread,  $\Delta E_{beam}$  is the actual beam energy spread and  $\Delta E_{spectrometer}$  is the energy spread introduced by the mass spectrometer. To get an idea of the energy transfer function, a Gallium LMI source was installed onto the mass spectrometer and operated with an emission current of  $2\mu\text{A}$ . These systems have been well studied and are known to have a FWHM energy spread of close to 5 eV in this energy range [117]. Given that the measured FWHM energy spread was 6 eV equation 6.6 gives the spectrometer energy resolution as 3.3 eV.

As the extraction energy of the Ga LMI source can be controlled quite accurately, it was also used to determine the 40 au (Ar) 3596 eV (3.6 kV less a 4 eV energy deficit [117]) Hall voltage reference point for displaying energy distribution data from the plasma source. The actual extraction voltage from a plasma is the anode potential plus the plasma potential which typically ranges anywhere between 15 and 30 V but since the plasma potential could not be measured in real time, the extraction voltage for the purpose of displaying data was taken to be that of the anode. The

Hall voltage reference was determined by setting the Ga ion beam energy to that of the 40 au, 3596 eV Ar ions via equation 6.4 and was found to be 153.8 mV. However, it was thought that the accuracy of the calibration introduced an error of roughly  $\pm 0.1$  mV into the Hall voltage corresponding to a  $\pm 5$  V error in the absolute beam energy.

### Initial Energy Spread Results

Figure 6.10 shows a typical energy distribution for the plasma source operating at 200 W without magnetic field. It was found that the FWHM of the distributions varied between 60-75 eV as a function of RF power, neutral pressure and tuning but that the approximate shape of the distributions remained independent of operating conditions.

It was reported by Woodworth *et al.* [127] that this type of double peaked energy distribution can be due to capacitive coupling between the antenna and the plasma

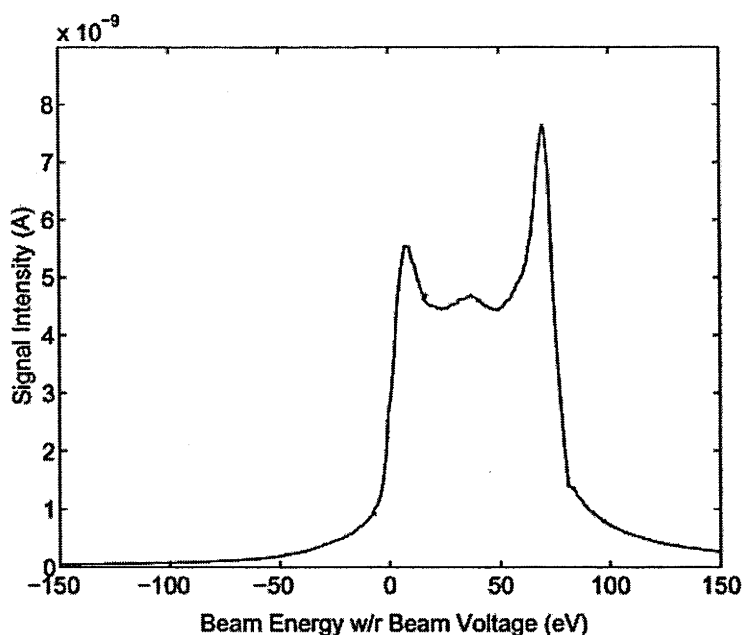


Figure 6.10: Energy spread for the source operating with no magnetic field. Peak-to-peak energy spread is 61 eV. FWHM energy spread is 73 eV.

where the plasma potential is modulated by a signal of amplitude equal to the energy separation between the peaks. In the case of a sinusoidal RF waveform the peaks of the energy distribution are easily understood as corresponding to the peaks and troughs of the RF cycle where the time derivative is smallest in absolute value and hence where most of the period is spent.

With the 500 Gauss permanent ring magnet installed, the energy spread decreases appreciably. It is recalled from chapter 4 that source density also increases under these conditions and a similar effect is noted as pressure is decreased. It is not clear what mechanism is responsible for the increased RF shielding.

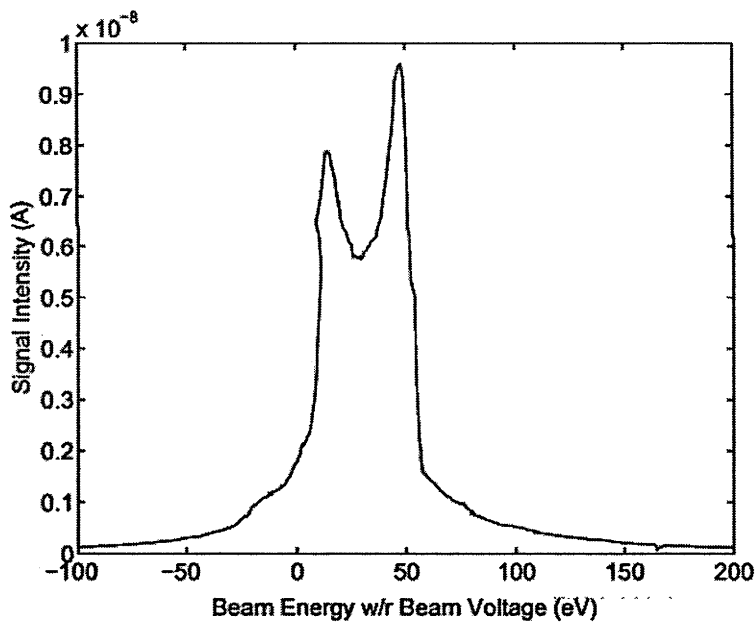


Figure 6.11: Energy spread for the source operating with 500 Gauss magnetic field and optimal pressure (5 mTorr). Peak-to-peak energy spread is 33 eV. FWHM energy spread is 40 eV.



### 6.2.2 Reducing Capacitive Coupling

A number of modifications were investigated to reduce the incidence of capacitive coupling on the plasma potential. The first and most basic improvement was to screen the feed cables for the electrodes. This was found to have an appreciable effect on energy spread. Operating under optimal pressure conditions (roughly 5 mTorr in the source) with the magnet installed, the peak-to-peak voltage was reduced from 33 eV to 27 eV, a reduction of almost 20%. Even at higher pressures and with the magnet removed significant reductions in plasma potential fluctuations were observed.

#### Balanced Antenna

After a suggestion by J. Keller, a circuit matching technique was developed which works by forcing either end of the plasma antenna to have the same peak-to-peak voltage with a phase difference of  $180^\circ$ . This results in a null point at the center of the antenna and hence the antenna is said to be “balanced”. Loading the antenna in this way ensures that opposite points on the antenna across the glass tube have equal and opposite voltages and destructively interfere to annul the net oscillation in the plasma potential. This modification, of all those tried, effected the greatest reduction in energy spread.

To obtain a balanced matching network for the phase 4 prototype, a high tension probe ( $\times 1000$ , 3 pF) was used to measure voltage and a resistor chain ( $10 \times 1 \text{M}\Omega$ ) in conjunction with a  $10 \times$  voltage probe was used to measure phase at various points on the antenna. A circuit diagram of the original impedance matching network is shown in figure 6.13(a) with the capacitance values as shown. With this circuit, and 200 W of applied RF power, the voltages at either end of the antenna were 370 V and 1600 V respectively with approximately zero phase shift. The voltage at the center of the antenna in this case was  $\pm 985$  V.

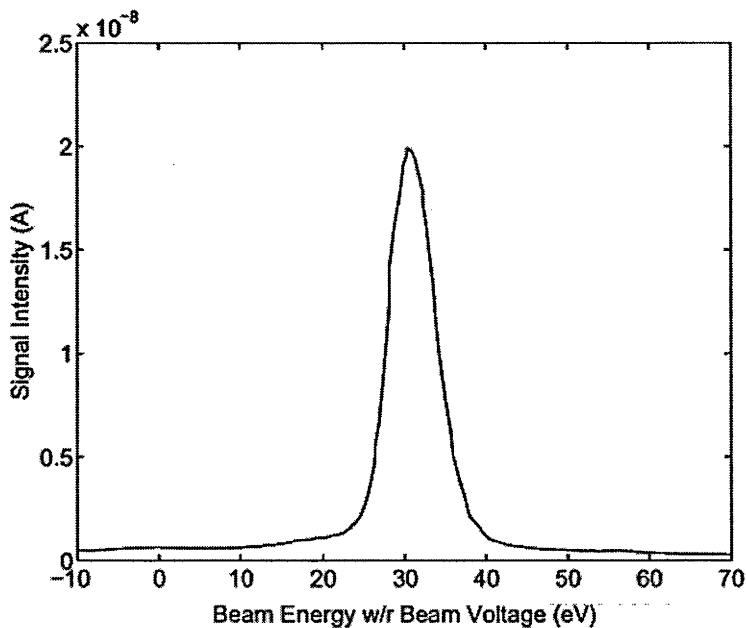


Figure 6.12: Energy spread for the source operating with optimal pressure (5 mTorr), 500 Gauss magnetic field and balanced antenna. The double peaked structure has been removed and the FWHM is about 6.5 eV unadjusted for the mass spectrometer transfer function.

By replacing the fixed 200 pF capacitor with a 50 pF capacitor and retuning the variable capacitors to 330 pF (Tune) and 340 pF (Load) as shown in 6.13(b), the required  $50\Omega$  impedance was achieved and the end voltages were 1020 V and 1040 V respectively with a  $180^\circ$  phase difference. This matching circuit had a dramatic effect on the extracted ion energy spread. Figure 6.12 shows that the distribution is approximately Gaussian with a FWHM of 6.5 eV and after substitution into 6.6 yields an energy spread of 5.6 eV.

### 200 $\mu\text{m}$ Extraction Aperture

As detailed in chapter 4, the intermediate goal of the source design is an inert gas plasma source with a brightness of  $2000 \text{ A}\cdot\text{cm}^{-2}\cdot\text{sr}^{-1}$  at 10 keV. This can be achieved with a plasma density of some  $10^{12}\text{cm}^{-3}$ . Limiting the current at the

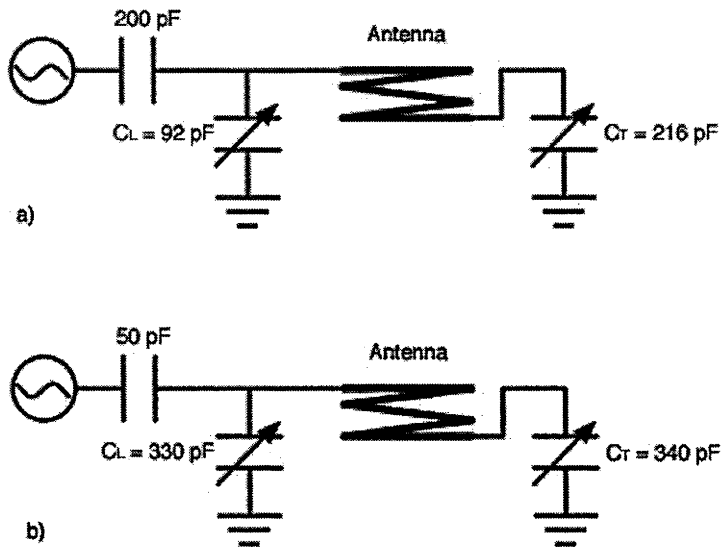


Figure 6.13: Top: unbalanced matching network. Bottom: balanced matching network.

source aperture is an efficient way to minimise space charge expansion and sputter erosion of the skimming apertures in the acceleration and drift regions of the column. Another advantage of the smaller extraction aperture is that the pressure differential between the source and the extraction region is increased decreasing the incidence of charge-exchange collisions, which tend to broaden the energy distribution. Moreover, the sensitivity of the system to micro-arcs is significantly reduced rendering the system more stable. To this end a  $200\ \mu\text{m}$  aperture was tested.

With the  $1\ \text{mm}$  aperture installed, the measured energy distribution could be reproduced 80% of the time. However, on occasions the distribution was significantly broadened and variable. It was found that the occurrence of these irregularities correlated with momentary fluctuations in the measured emission current, indicating that micro-arcs were possibly occurring in the extraction region. In any case, by replacing the  $1\ \text{mm}$  aperture with a  $200\ \mu\text{m}$  aperture these occurrences disappeared, with little variation in the acquired energy spread data. In addition, a significant reduction of the FWHM was observed, which could be explained by the reduction of

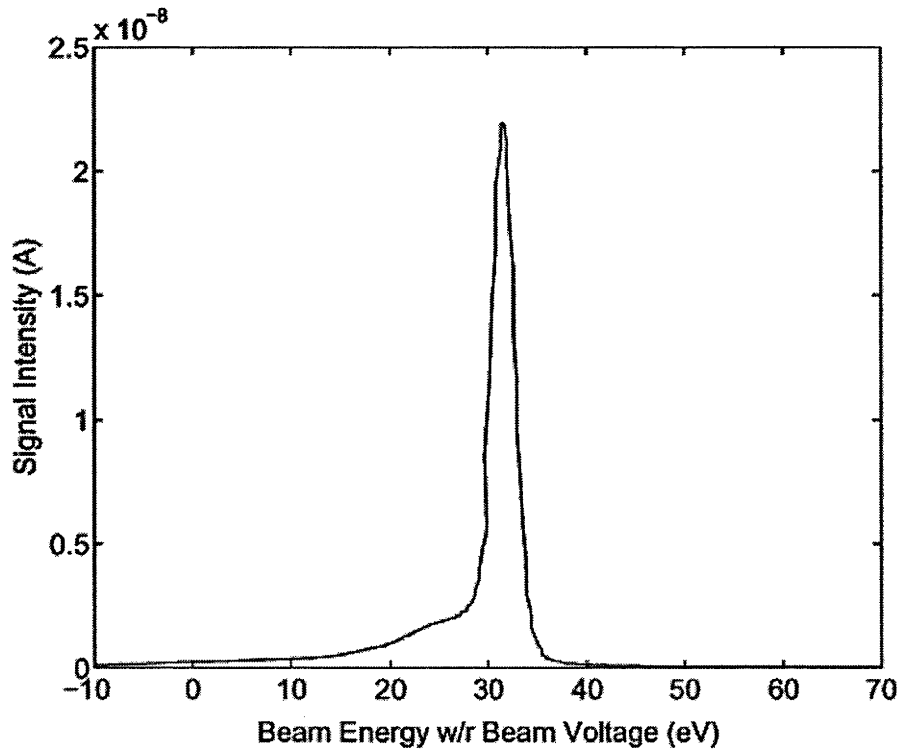


Figure 6.14: Energy spread for the source operating with 200 W forward power, optimal pressure (5 mTorr), 500 Gauss magnetic field, balanced antenna, 200  $\mu\text{m}$  source aperture diameter and split Faraday shield. The FWHM is 3 eV.

charge-exchange collisions in the extractor between the plasma and Accel electrodes where the ion velocity is still relatively small and the neutral pressure is relatively high.

Regardless of the exact mechanics of the situation, the measured energy spread has a FWHM of 3.5 eV without considering the broadening effect of the mass spectrometer.

#### Half Split Faraday Shield

Though an ion energy spread of 3.5 eV is competitive against alternative technologies, it would be desirable to reduce it even further. The energy distribution

function of the balanced antenna source set-up still showed some small amplitude structure in the low energy end of the distribution. It was reasoned by N. Smith that if this structure was due to residual capacitive coupling then it might be possible to further screen out the capacitive components of the antenna with a Faraday shield placed between the antenna and the source tube.

Four 90° aluminium sections were manufactured and installed between the antenna and the source tube leaving a small air gap to minimise Eddy currents in the shield. In principle, these shields should have almost totally eliminated all capacitive coupling between the antenna and the plasma leaving only induction fields to interact with the plasma. As capacitive coupling plays an important role in igniting the plasma initially, a Tesla coil was needed to strike the plasma. Unfortunately it was also found that the plasma could not be sustained with the shields in place, indicating that significant Eddy fields were being produced and effectively shielding the inductive fields from the plasma. It did, however, prove beneficial to leave two 90° sectors installed on opposite sides of the plasma tube, adjacent to each of the large tuning capacitors. With this set-up, the minimum FWHM energy spread measured was 2.8 eV which is an indication that the empirically determined 3.3 eV error in the transfer function is an over estimation. Thus, without further information on the mass spectrometer it can only be concluded that the ion energy spread for the balanced, 200  $\mu\text{m}$ , shielded plasma source is less than 3 eV and that the experiment has reached the resolution limit of the mass spectrometer (cf. figure 6.14).



## Concluding Remarks

The primary emphasis of this work has been to develop a physical understanding and provide techniques for the manufacture of a high brightness inert gas plasma ion source. In particular, this thesis has presented a new methodology for the extraction of low aberration FIBs as well as an investigation of ion heating mechanisms in helicon plasmas. Moreover, undertaken with-in the frame work of a major contract for the FEI Corporation of Oregon, U.S.A., four compact plasma ion source prototypes, suitable for use with existing FEI technologies, were developed and the first three were presented in this thesis.

The first prototype was used to determine basic plasma parameters in terms of pressure, magnetic field, power and antenna position. It was also used to callibrate two computer simulation codes employed for the design and quantification of the ion source's extraction electrodes. With the development of the second prototype, the emphasis shifted away from FIB extraction and onto the design of a compact, high density plasma source. It was shown that densities over  $10^{14} \text{ cm}^{-3}$  could be attained with 1 kW of RF power and a 700 Gauss magnetic field. The third prototype was then used to demonstrate that an ion energy spread of less than the 3 eV limit of the measurement technique could be achieved with 200 W of input power and 5 mTorr of pressure. During these ion energy experiments, no direct simultaneous measurements of the plasma density were made, but it is known from previous experiments that with these operating conditions, the plasma density was

in the low  $10^{12}$   $\text{cm}^{-3}$  range. Higher input powers could not be safely tested as the third prototype was not designed for high thermal loads. However, further, more precise testing of the fourth prototype due for late 2004/ early 2005 may show the ion energy spread to be considerably less than 3 eV. In addition, as this latest design employs glass-to-metal seals (instead of o-rings) it will also be possible to test higher powers.

As opposed to ion energy spread, no direct measurements of ion temperature were made. Experimentally, this quantity is difficult to measure with conventional probes and our laboratory was not equipped with a LIF system which might have been used to make an estimate. It is not, however, unreasonable to assume that the ion temperature in the prototype sources was on the order of 0.1 eV. PIC simulations undertaken for this work showed that for operating pressures below 10 mTorr ion heating due to collisions was well below 0.1 eV. Wave-particle interactions can also almost certainly be ruled out as ion cyclotron and ion acoustic waves were only observed (in WOMBAT) for a narrow range of operating conditions. In addition, LIF measurements in the University of West Virginia's helicon device, HELIX (similar to WOMBAT), have shown that for pressures between 2 and 9 mTorr, RF power of 500 W and a magnetic field of 1 kGauss ion temperature is between 0.09 and 0.11 eV [11].

Taking the experimentally demonstrated density of  $10^{14}$   $\text{cm}^{-3}$  and the estimated ion temperature of 0.1 eV, the inherent brightness of the A.N.U. ion sources with a 10 kV extraction potential is  $10^5$   $\text{A.cm}^{-2}.\text{sr}^{-1}$  and  $10^6$   $\text{A.cm}^{-2}.\text{sr}^{-1}$  at 100 kV. The low emittance growth extraction optic presented in this thesis had not been tested experimentally at the time of writing, but results from simulations were very encouraging, showing almost no emittance growth. If the extraction optic is shown to operate effectively early in 2005, then combined with these ion sources, it may well produce FIBs bright enough to challenge LMIS technology in a large number



of processes across the semiconductor industry where the use of inert gas ions is preferable to highly dopant liquid metals. In addition, it could be used in applications requiring the use of reactive gas ions. The relatively low ion energy spread also means that these sources are suitable for low energy FIB extraction.

## 7.1 Extraction Optics

### 7.1.1 Generalising the Langmuir-Blodgett Laws

An important first step in the development of a high brightness ion source is the design of low aberration extraction electrodes. In this work we have departed from many of the longly held “truths” about ion extraction from plasmas. This started with a review of the Langmuir-Blodgett laws as they apply to plasmas, in particular with regard to the boundary conditions at the plasma/beam interface known as the meniscus where a significant electric field exists. This field significantly alters the beam distributions but is assumed to be zero in the standard Langmuir-Blodgett assumptions for space-charge limited flow. Moreover, the field at the meniscus is sensitive to the plasma parameters so that flow between two differentially charged concentric or parallel plates is not unique but variable and dependent on the plasma density.

In addition, ion extraction from plasmas is not space charge limited in as much as particles are not extracted from plasmas (this is a misnomer) but fall down the sheath and through the extraction orifice with a flux determined by the plasma density. In this sense extraction from a plasma is source limited. It has been argued that the variation in the meniscus shape is a reorganisation of the extraction gap to ensure space-charge limited flow. However, experimental evidence of this by Rautenbach could only show that the current was proportional to  $V^{3/2}$  and was mistakenly interpreted as demonstrating the validity of the Langmuir-Blodgett laws. To make

the data “fit” he had to use a coefficient of proportionality  $k$  which subsumed the effect of the meniscus field. This effectively showed the invariance of particle extraction from plasmas to the ratio of charge and mass as well as showing that extracted current was proportional to a  $3/2$  power law on extraction potential. But it was not a sufficient proof that ion extraction from plasmas was best described by Langmuir-Blodgett’s laws for space-charge limited flow which, it is recalled, were originally devised to explain current flow from thermionic cathodes. In the assumptions for that system, emitted electrons are assumed to be unlimited in number and to have zero initial velocity. With the application of an extraction field, electrons stream into the extraction gap and their presence alters the vacuum potential distribution so that the electric field at the emission surface is zero. If this was not so then too many or too few electrons would flow into the extraction gap. If too many electrons are emitted, then the gap starts to develop a net negative charge repelling the entry of new electrons. If too few electrons are emitted, then the gap has a net positive charge and more electrons are attracted from the unlimited source of electrons in the emission surface. It is then clear that the equilibrium situation requires the electric field to be zero at the emission surface. In reality, electrons are emitted with a finite initial velocity as described by Richardson’s equation [73]. This means that the electric field at the emission surface can no longer be zero but must have some negative value to impede the flow of thermionic electrons. This requires the build up of a pool of negative charge adjacent to the emission surface called a virtual cathode. Even under these conditions the Child-Langmuir and Langmuir-Blodgett laws can still be applied because the potential distribution across the virtual cathode must have an inflexion point, where the electric field is zero, so that it connects smoothly with the extraction field in the rest of the gap. The net result is that the extraction gap is shortened by half the width of the virtual cathode in essence increasing the applied field to accommodate the flux from the emission surface. However, the vir-

tual cathode or anode has never been detected experimentally for plasmas nor has it been observed by the author in PIC or ray-tracing simulations [115].

Therefore the first step to designing low emittance growth electrodes as described in this thesis was the generalisation of the original Langmuir-Blodgett laws for cylindrical and spherical symmetries to accommodate the non-zero potential gradient across the plasma meniscus. In addition, these new relations were expressed in the same form as the original Langmuir-Blodgett laws in order to be used in conjunction with Radley's solutions to Laplace's equations.

### 7.1.2 Low Aberration Electrodes

In applying the Langmuir-Blodgett laws or the generalisation presented in this thesis, care must be taken to ensure that the beam geometry adheres strictly to the assumptions of planar, cylindrical or spherical symmetry in order that particles are not subject to azimuthal forces and hence have rectilinear trajectories. In the Pierce paradigm of electrode design, which appears to be the most popular approach in the literature, this is assumed to hold between the first two electrodes in the extraction system. The problem with this method is that it neglects the strong electric field that exists in the beam at the position of the second electrode, which balloons outwards from the aperture deflecting the flow of particles and hence increases emittance. More importantly, this change in the electric field geometry reshapes the equipotential surface at the electrode aperture which under normal application of the Child-Langmuir or Langmuir-Blodgett laws should be parallel or concentric with the plasma meniscus. In essence, this means that the beam is no longer flowing as if in an ideal diode and therefore no longer has standard beam distributions so that the Pierce electrode, the derivation of which is strongly based on the Child-Langmuir law, is no longer valid as a low aberration optic. In this thesis it was proposed that to avoid this, a second set of electrodes is required to bring

the electric field (as well as the beam potential) back to zero allowing the beam to flow throughout the *entire* extraction system as if in an ideal diode. Importantly, this means that both faces of every electrode must be shaped in accordance with Laplace's equation as solved by Radley.

The electrode design methodology as presented thus far is complicated by the presence of electrons produced in the transport region which tend to migrate into the extraction gap if not blocked by an appropriately large potential barrier. To this end, "blocking" electrodes are inserted into the extractor after the main extraction stage which are biased negatively (typically with a peak of about -400 V) relative to ground. This second stage is designed to have the same potential profile as the extraction electrodes, that is to say low field, high field, low field. This brings the total minimum number of electrodes for low aberration extraction to 5 comprising 2 stages:

- Stage 1: Plasma electrode aft face, Accel front and aft face, Decel front face.
- Stage 2: Decel aft face, Blocking electrode front and aft face, Ground electrode front face.

Low aberration extraction of FIBs from plasmas therefore requires generalised Langmuir-Blodgett laws, comprehensively shaped electrodes to ensure that *both* the potential and the electric field are brought to zero upon exit from the extractor and the addition of Blocking electrodes to repel electrons designed with the same principles as the electrodes of the extraction stage.

### 7.1.3 Electrons and the Extraction Optic

The presence of electrons has a further effect on the shape of the Blocking electrodes though this is quite small. As the electrons are assumed to have some distribution of energies, a population of electrons will exist in the Blocking stage of the extractor up to a certain position determined by their energy. This means that

the presence of electrons would need to be incorporated into the analytical modeling of the beam distributions in this portion of the extractor. This was not done in this present work but assuming a population of Maxwellian electrons in Boltzmann equilibrium this could be quite easily intergrated into the Langmuir-Blodgett generalisations.

## 7.2 Plasma Source

The theory presented here on extraction optics relies on the assumption of cold ions, which in any real plasma is impossible but is well approximated for temperatures less than 0.2 eV. In addition, the thermodynamic limit on brightness requires plasma densities of at least the order of  $10^{13} \text{ cm}^{-3}$  for intermediate brightnesses and  $10^{14} \text{ cm}^{-3}$  for high brightnesses. At these high densities, thermal stress of materials becomes a significant constraint on the design of a basic plasma source especially if it is to be compact. So some effort was made towards the design of a compact plasma ion source which could fit roughly into a space of  $2000 \text{ cm}^3$  (including matchbox), produce densities of up to  $10^{14} \text{ cm}^{-3}$  and have an ion temperature on the order of 0.1 eV. In this thesis, three prototype ion sources were presented. The source tube, antenna and electrode assembly of the second and third prototypes were designed to fit into the required volume, but as yet a compact matching network has not been designed and manufactured. With the second prototype, in particular, it was shown that the required density of  $10^{14} \text{ cm}^{-3}$  could be achieved using 1 kW of forward power, 5 mTorr of pressure and 500 Gauss of on axis magnetic field, but the RF had to be pulsed to avoid overheating. By mounting the third “balanced” prototype source onto an energy selective mass spectrometer with a  $200 \mu\text{m}$  extraction aperture, it was shown that an ion energy spread of less than the 3 eV resolution of the measurement technique could be achieved.

The forth prototype currently being designed, will feature glass to metal seals (in-

stead of rubber o-rings) so that higher RF powers can be injected CW. In previous designs it was observed that at powers much above 200 W, the source tube o-rings degraded contaminating the plasma and compromising the vacuum seal. The use of braised glass to metal seals will alleviate this problem and will allow the source to reach much higher temperatures so that densities on the order of  $10^{13} \text{ cm}^{-3}$  can be attained with roughly 500 W and 500 Gauss. For even higher powers alumina tubing will replace the current Pyrex source providing increased thermal stability. All the electrode systems presented in this thesis were manufactured from stainless steel which, due to thermal expansion, will most probably be replaced by Titanium in future designs. In addition, a compact, purpose built matching network will also be installed so that the total volume of the device is less than  $2000 \text{ cm}^3$ .

### 7.3 Ion Energy Spread

Parallel and perpendicular ion energy distributions are critical factors in the success of FIB systems as they can lead to significant aberrations in the extraction optics and therefore a reduction in brightness. Parallel energy spread causes chromatic aberration resulting in differential focusing of fast and slow ions and therefore places a limit on the smallest reproducible feature size. This problem is particularly salient at low energies ( $< 1 \text{ kV}$ ). Perpendicular ion heating and energy spread causes ions to exit the meniscus with a distribution of angles, making application of the standard diode model of electrostatic optical theory difficult. In particular, non-laminar trajectories lead to third-order forces and hence spherical aberration which can impact strongly on beam quality placing a further limit on the minimum reproducible feature size.

It was shown that the primary contribution to axial ion energy spread was from oscillations in the plasma potential resulting from residual capacitive coupling be-

tween the antenna and the plasma. This problem was alleviated by “balancing” the antenna so that the phase at its mid-point was zero and therefore had the effect that opposing segments of the antenna across the source tube were  $180^\circ$  out of phase and destructively interfered to reduce electrostatic coupling to the plasma. When combined with an axial magnetic field of 500 Gauss (in the plasma chamber) and a  $200\ \mu\text{m}$  extraction aperture (to reduce charge-exchange collisions in the extraction gap), it was shown that this reduced the parallel ion energy spread to less than the 3 eV limit of the measurement technique. Further high resolution testing may show the ion energy spread to be significantly less than this, though these experiments are only scheduled for late 2004 / early 2005.

Charge exchange and elastic scattering collisions were also shown to have some impact on perpendicular ion energy spread though for the parameter range proposed for the FEI source (5 mTorr) this could be kept to within 0.1 eV. Using a 1D PIC code it was shown that significant perpendicular ion energy was only gained in the presheath by collisions for pressures above 20 mTorr but never exceeded 1 eV.

Wave-particle interactions were also identified as having strong potential to couple into the perpendicular ion energy distribution. In particular, ion cyclotron and ion acoustic waves were detected in the large volume helicon reactor WOMBAT whilst operating under similar conditions to the proposed FEI source. It was shown that the ion cyclotron waves were produced in a four wave interaction with 3 helicons in a process that resembled a filamentation type instability which became particularly unstable within a narrow band of operating conditions but was otherwise difficult to detect. The second wave-particle interaction of interest was ion Landau damping of ion acoustic waves which were particularly salient but were limited to the outer layer of the plasma column. Though it has been proposed by other researchers that these waves can be produced by parametric decay of a helicon pump, the experimental data presented here could not be made to fit the minimum theoretical

requirements for such a process and instead it was proposed that free energy from strong pressure gradients at the edge of the plasma column drove this particularly strong instability. Importantly, the acoustic activity was not detected inside the plasma column, especially on axis and therefore is unlikely to have any significant effect on the plasma parameters at the extraction aperture and hence on the extraction itself.

## 7.4 Other implications of the work

Ion cyclotron and ion acoustic waves have been used to explain anomalous ion motion and ion heating in regions of the ionosphere believed to be responsible for auroral arcs and double layers and have previously been detected in laboratory helicon plasmas in conjunction with parallel flow shear and temperature anisotropies. In particular, Koepke *et al.* [68] have presented experimental evidence, based primarily on the measurement of ion energy distributions by laser induced fluorescence, supporting the seminal theoretical work of Ganguli *et al.* [42] and subsequent developments of Gavrishchaka *et al.* [43], Spangler *et al.* [110] and Scime *et al.* [105]. In this thesis, the ion cyclotron waves were measured using a floating Langmuir probe and detected in the presence of 3 helicons (a pump and two sidebands). In addition, the experimental data was well correlated with a theory based on filamentation instabilities developed by M. Giles which predicted (correctly) that the ion cyclotron frequency was roughly 0.7 the theoretical ion-gyro frequency. In light of this, detailed measurements of the ion distribution functions by LIF would be of some interest to determine if the plasma column in WOMBAT was undergoing parallel flow shear and if in addition temperature anisotropies existed.



# Bibliography

- [1] Y. Awad, E. Lavallee, J. Beauvais, D. Drouin, P. Yang, D. Turcotte, and L. Kien Mun. Fabrication of x-ray masks using evaporated electron sensitive layers for back patterning of membranes. *J. Vac. Sci. Technol. B*, 20(6):3040, Nov/dec 2002.
- [2] D. L. Barr. Gallium clusters from a liquid metal ion source. *J. Vac. Sci. Technol. B*, 5(1):184–189, Jan/Feb 1987.
- [3] R. Becker and W. B. Herrmannsfeldt. A program for the simulation of positive ion extraction including magnetic fields. *Rev. Sci. Instrum.*, 63(4):2756, Apr 1992.
- [4] Y. I. Belchenko and M. Bacal. Compact hollow cathode penning surface-plasma sources for steady-state negative ion production. *Rev. Sci. Instrum.*, 65(4), 1994.
- [5] B. Bertotti. Theory of an electrostatic probe in a strong magnetic field. *Phys. Fluids*, 4(8):1047, 1961.
- [6] B. Bertotti. Theory of an electrostatic probe in a strong magnetic field 2. *Phys. Fluids*, 5(8):1010, 1962.
- [7] C. K. Birdsall and A. B. Langdon. Plasma physics via computer simulation. 1985.

- [8] H. Blevin and J. Christiansen. Propagation of helicon waves in non uniform plasma. *Aust. J. Phys.*, 19(4):501, 1966.
- [9] Jack E. Boers. *PBguns, An Interactive IBM PC Computer Program for the Simulation of Electron and Ion Beams and Guns*. Thunderbird Simulations, v4.01 edition, June 1999.
- [10] D. Bohm. *The Characteristics of Electrical Discharges in Magnetic Fields*. McGraw-Hill, New York, 1949.
- [11] R. F. Boivin and E. E. Scime. Laser induced fluorescence in Ar and He plasmas with a tunable diode laser. *Rev. Sci. Instrum.*, 74(10):4352, 2003.
- [12] R. W. Boswell. *A study of waves in gaseous plasmas*. PhD thesis, Flinders University, 1974.
- [13] R. W. Boswell and F. F. Chen. Helicons-the early years. *IEEE Transactions on Plasma Science*, 25(6):1229, Dec 1997.
- [14] R. W. Boswell, P. J. Christiansen, and C. R. Salter. Non linear effects in an r.f. plasma. *Phys. Lett. A*, 38A(2):67, Jan 1972.
- [15] R. W. Boswell and M. J. Giles. Trapping of decay waves in whistler resonance cones. *Phys. Rev. Lett.*, 36(19):1142, May 1976.
- [16] R. W. Boswell and I. J. Morey. Self-consistent simulation of a parallel-plate rf discharge. *Appl. Phys. Lett.*, 52(1):21, Jan 1988.
- [17] R. W. Boswell and R. K. Porteous. Large volume, high density rf inductively coupled plasma. *Appl. Phys. Lett.*, 50(17):1130, April 1987.
- [18] R. Bowers, F. Rose, and C. Legendy. Oscillatory galvanomagnetic effect in metallic sodium. *Phys. Rev. Lett.*, 7(9):339, 1961.

- [19] C. Charles, A. W. Degeling, T. E. Sheridan, J. H. Harris, M. A. Lieberman, and Boswell. Absolute measurements and modeling of radio frequency electric fields using a retarding field energy analyzer. *Phys. Plasmas*, 7(12):5232, Dec 2000.
- [20] F. Chen. *Plasma Diagnostic Techniques*. Academic Press, New York, 1965.
- [21] F. Chen and G. Chevalier. RF production of long, dense plasma columns. In *International Conference on Plasma Physics III*, 1992.
- [22] F. F. Chen and D. D. Blackwell. Upper limit to Landau damping in helicon discharges. *Phys. Rev. Lett.*, 82(13):2677, March 1999.
- [23] C. D. Coath and J. Long. *Rev. Sci. Instrum.*, 66(2):1018, 1995.
- [24] C. Corr, N. Plihon, P. Chabert, O. Sutherland, and R. Boswell. Spatially limited ion acoustic wave activity in low-pressure helicon discharges. *Phys. Plasmas*, 11(10), 2004.
- [25] J. R. Coupland, T. S. Green, D. P. Hammond, and A. C. Riviere. A study of the ion beam intensity and divergence obtained from a single aperture three electrode extraction system. *Rev. Sci. Instrum.*, 44(9):1258, Sept. 1973.
- [26] C. Cui. *Experimental Study and Modelling of a Low Pressure RF Generated Magnetoplasma*. PhD thesis, Plasma Research Laboratory, RSPHysSE, Australian National University, 1992.
- [27] Z. Cui, P. D. Prewett, and J. G. Watson. Focused ion beam biased repair of conventional and phase shift masks. *J. Vac. Sci. Technol. B*, 14(6):3942, Nov/Dec 1996.
- [28] P. N. Daykin. Electrode shapes for a cylindrical electron beam. *Brit. J. Appl. Phys.*, 6:248, 1955.

- [29] F. J. de Heer, R. H. Jansen, and W. van der Kaay. Total cross sections for electron scattering by Ne, Ar, Kr and Xe. *J. Phys. B*, 10:3849, 1979.
- [30] A. W. Degeling. *Plasma Production in a Large Volume Helicon Wave Discharge*. PhD thesis, Plasma Research Laboratory, RSPHysSE, Australian National University, 1999.
- [31] A. W. Degeling, G. G. Borg, and R. W. Boswell. Transitions from electrostatic to electromagnetic whistler wave excitation. *Phys. Plasmas*, 11(5):2144, May 2004.
- [32] A. W. Degeling, C. O. Jung, R. W. Boswell, and A. R. Ellingboe. Plasma production from helicon waves. *Phys. Plasmas*, 3(7):2788, July 1996.
- [33] A. W. Degeling, C. O. Jung, R. W. Boswell, and A. R. Ellingboe. Plasma production from helicon waves. *Phys. Plasmas*, 3(7):2788, July 1996.
- [34] A. W. Degeling, T. E. Sheridan, and R. W. Boswell. Intense on-axis plasma production and associated relaxation oscillations in a large volume helicon source. *Phys. Plasma*, 6(9):3664, Sept 1999.
- [35] A. B. El-Kareh and J. C. J. El-Kareh. *Electron beams, lenses and optics*. Academic Press, 1970.
- [36] A. R. Ellingboe. *Wave and Power Absorption in a Magneto-Plasma*. PhD thesis, Plasma Research Laboratory, RSPHysSE, Australian National University, 1998.
- [37] A. R. Ellingboe and R. W. Boswell. Capacitive, inductive and helicon-wave modes of operation of a helicon plasma source. *Phys. Plasmas*, 3(7):2797, July 1996.

- [38] A. R. Ellingboe, R. W. Boswell, J. P. Booth, and N. Sadeghi. Electron beam pulses produced by helicon-wave excitation. *Phys. Plasmas*, 2(6):1807, June 1995.
- [39] D. J. Elliott. *Integrated Circuit Fabrication Technology*. McGraw-Hill Publishing, 2nd edition, 1989.
- [40] J. Ferch, B. Granitza, C. Masche, and W. Raith. Electron-argon total cross section measurements at low energies by time-of-flight spectroscopy. *J. Phys. B*, 18:967, 1985.
- [41] K. Gaff. Magfield v2.2, 1999.
- [42] G. Ganguli, M. J. Keskinen, H. Romero, R. Heelis, T. Moore, and C. Pollock. Coupling of microprocesses and macroprocesses due to velocity shear: an application to the low-altitude ionosphere. *J. Geophys. Res.*, 99(A5):8873, 1994.
- [43] V. V. Gavrishchaka, S. B. Ganguli, and G. I. Ganguli. Origin of low-frequency oscillations in the ionosphere. *Phys. Rev. Lett.*, 80(4):728, 1998.
- [44] V. Godyak. *Plasma-Surface Interactions and Processing of Materials*. Kluwer Academic, Boston, 1990.
- [45] G. Gross. Ion projection lithography: Next generation technology? *J. Vac. Sci. Technol. B*, 15(6):2136, Nov/Dec 1997.
- [46] G. Gross, R. Kaesmaier, H. Loeschner, and G. Stengl. Ion projection lithography: Status of the MEDEA project and United States/European cooperation. *J. Vac. Sci. Technol. B*, 16(6):3150, Nov/Dec 1998.
- [47] S. K. Guharay, E. Sokolovsky, and J. Orloff. Characteristics of focused beam spots using negative ion beams from a compact surface plasma source and

- merits for new applications. *J. Vac. Sci. Technol. B*, 16(6):3370, Nov/Dec 1998.
- [48] S. K. Guharay, W. Wang, V. G. Dudnikov, M. Reiser, J. Orloff, and J. Melngailis. High-brightness ion source for ion projection lithography. *J. Vac. Sci. Technol. B*, 14(6):3907, Nov/Dec 1996.
- [49] E. M. Gullikson, C. Cerjan, D. G. Stearns, P. B. Mirkarimi, and D. W. Sweeney. Practical approach for modeling extreme ultraviolet lithography mask defects. (1):81, Jan/Feb 2002.
- [50] E. R. Harrison. Approximate electrode shapes for a cylindrical electron beam. *Brit. J. Appl. Phys.*, 5:40, 1953.
- [51] A. V. Hayes, V. Kanarov, R. Yevtukhov, H. Hegde, B. Druz, D. Yakovlevitch, W. Cheesman, and V. Mirkov. Ion source for ion beam deposition employing a novel electrode assembly. *Rev. Sci. Instrum.*, 71(2):1163–1167, February 2000.
- [52] D. He, H. Solak, W. Li, and F. Cerrina. Extreme ultraviolet and x-ray resist: comparison study. (6):3379, Nov/Dec 1999.
- [53] S. Hector and P. Mangat. Review of progress in extreme ultraviolet lithography masks. (6):2612, Nov/Dec 2001.
- [54] N. Hershkovitz. *Plasma Diagnostics*. Academic Press, New York, 1989.
- [55] H. J. Hopman, B. Jurgens, J. H. A. van Wakeren, and F. F. F. F. F. F. Construction of a retarding field energy analyzer. *J. Phys. E Sci. Instrum.*, 10(3):936, 1977.
- [56] S. Humphries. *Charged Particle Beams*. Wiley and Sons, 1990.
- [57] Y. S. Hwang, I. S. Hong, and G. S. Eom. Conceptual design of a helicon ion source for high-current dc accelerators. *Rev. Sci. Instrum.*, 69(3):1344, 1998.

- [58] M. Irzyk. *Génération de Faisceaux d'Ions à Partir de Plasmas a Haute Densité*. PhD thesis, Université d'Orléans, 2001.
- [59] Michael Irzyk, Claude Laure, and Andre Bouchoule. Ion extraction from a helicon source and PIC simulation. *Plasma Sources Sci. Technol.*, 10:463, July 2001.
- [60] T. Ishitani, H. Koike, T. Yaguchi, and T. Kamino. Implanted gallium-ion concentrations of focused-ion-beam prepared cross sections. *J. Vac. Sci. Technol. B*, 16(4):1907, Jul/Aug 1998.
- [61] T. Ishitani, Y. Taniguchi, S. Isakozawa, H. Koike, T. Yaguchi, H. Matsumoto, and T. Kamino. Proposals for exact-point transmission-electron microscopy using focused ion beam specimen-preparation technique. *J. Vac. Sci. Technol. B*, 16(4):2532, Jul/Aug 1998.
- [62] Y. Jinxiang, S. Zhizhong, R. Xiaotang, and L. Renxing. Progress of pocket PIG ion sources with permanent magnet at peking university. *Rev. Sci. Instrum.*, 65(4), 1994.
- [63] R. Jones. Optimization and performance of electrostatic particle analyzers. *Rev. Sci. Instrum.*, 49(1):21, 1978.
- [64] R. Jones. Correction. *Rev. Sci. Instrum.*, 50(3):392, 1979.
- [65] R. Kaesmaier, H. Loeschner, G. Stengl, J. C. Wolfe, and P. Ruchhoeft. Ion projection lithography: international development program. *J. Vac. Sci. Technol. B*, 17(6):3091, Nov/Dec 1999.
- [66] J. L. Kline, E. E. Scime, R. F. Boivin, A. M. Keesee, X. Sun, and V. S. Mihailenko. Rf absorption and ion heating in helicon sources. *Phys. Rev. Lett.*, 88:195002-1, 2002.

- [67] J. P. Klozenberg, B. McNamara, and P.C. Thoneman. Dispersion and attenuation of helicon waves in a uniform cylindrical plasma. *J. Fluid Mech.*, 21(3):545, 1965.
- [68] M. E. Koepke, C. Teodorescu, E. W. Reynolds, C. C. Chaston, C. W. Carlson, J. P. McFadden, and R. E. Ergun. Inverse ion-cyclotron damping: Laboratory demonstration and space ramifications. *Physics of Plasmas*, 10(5):1605, 2003.
- [69] A. Komori, T. Shoji, K. Miyamoto, J.Kawai, and Y. Kawai. Helicon waves and efficient plasma production. *Phys. Fluid. B*, 3(4):893, 1991.
- [70] N. A. Krall and A. W. Trivelpiece. *Principles of Plasma Physics*. McGraw-Hill, 1973.
- [71] E. Krishnakumar and S. K. Srivastava. Ionisation cross sections of rare-gas atoms by electron impact. *J. Phys. B*, 21:1005, 1988.
- [72] L. Landau. *Journal of Physics (U.S.S.R.)*, 10, 1946.
- [73] I. Langmuir. The effect of space charge and residual gases on thermionic currents in high vacuum. *Phys. Rev.*, 2(6):450, 1913.
- [74] I. Langmuir and K. B. Blodgett. Currents limited by space charge between coaxial cylinders. *Phys. Rev.*, 22(4):347–356, 1923.
- [75] I. Langmuir and K. B. Blodgett. Currents limited by space charge between concentric spheres. *Phys. Rev.*, 24(1):49–59, 1924.
- [76] Y. Lee, R. A. Gough, K. N. Leung, J. Vujic, M. D. Williams, N. Zahir, W. Fallman, M. Tockler, and W. Bruenger. Plasma source for ion and electron beam lithography. *J. Vac. Sci. Technol. B*, 16(6):3367, Nov/Dec 1998.
- [77] Y. Lee, Q. Ji, K. N. Leung, and N. Zahir. Nanobeam production with the multicusp ion source. *Rev. Sci. Instrum.*, 71(2):722–724, February 2000.



- [78] C. R. Legendy. Macroscopic theory of helicons. *Phys. Rev.*, 135(6A):A1713, September 1964.
- [79] J. Lehane and P. Thonemann. An experimental study of helicon wave propagation in a gaseous plasma. *P. Phys. Soc. Lond.*, 85(544P):301, 1965.
- [80] Ka-Ngo Leung. Plasma sources for electrons and ion beams. *J. Vac. Sci. Technol. B*, 17(6):2776, Nov/Dec 1999.
- [81] Ka-Ngo Leung. The application and status of the radio frequency driven multi-cusp ion source (invited). *Rev. Sci. Instrum.*, 71(2):1064–1068, February 2000.
- [82] Y. Li, K. Ota, and K. Murakami. Thermal and structural deformation and its impact on optical performance of projection optics for extreme ultraviolet lithography. (1):127, Jan/Feb 2003.
- [83] M. A. Lieberman and A. J. Lichtenberg. *Principles of Plasma Discharges and Materials Processing*. John Wiley & Sons, New York, 1st edition, 1994.
- [84] H. Loeschner and G. Stengl. Characterization of a process development tool for ion projection lithography. *J. Vac. Sci. Technol. B*, 19(6):2520, Nov/Dec 2001.
- [85] P. K. Loewenhardt, B. D. Blackwell, R. W. Boswell, G. D. Conway, and S. M. Hamberger. Plasma production in a toroidal heliac by helicon waves. *Phys. Rev. Lett.*, 67(20):2792, Nov 1991.
- [86] W. Maly. SIA road map and design and test. Technical report, Carnegie Mellon University, 1997.
- [87] T. K. Mau. *IEEE Trans. Plasma Sci.*, PS-2:152, 1974.
- [88] J. Melngailis. Critical review: Focused ion beam technology and applications. *J. Vac. Sci. Technol. B*, 5(2):469, Mar/Apr 1987.

- [89] J. Melngailis, A. A. Mondelli, I. L. Berry, and R. Mohondro. A review of ion projection lithography. *J. Vac. Sci. Technol. B*, 16(3):927, May/June 1998.
- [90] R. Meunier. A new electrode geometry for the formation of diverging ion beams in the presence of space charge.
- [91] A. B. Mikhailovskii. *Theory of Plasma Instabilities*. Plenum Publishing Corp., 1974.
- [92] A. Mikkelsen, R. Engelstad, E. Lovell, K. Blaedel, and A. Claudet. Extreme ultraviolet lithography mask flatness and electrostatic chucking analysis. 21(6):3091, Nov/Dec 2003.
- [93] N. Mizusawa, K. Uda, Y. Tanaka, H. Ohta, and Y. Watanabe. Technology and performance of the Canon XRA-1000 production x-ray stepper. *J. Vac. Sci. Technol. B*, 18(6):2955, Nov/Dec 2000.
- [94] J. Orloff, J.-Z. Li, and M. Sato. Experimental study of a focused ion beam probe size and comparison with theory. *J. Vac. Sci. Technol. B*, 9(5):2609, Sep/Oct 1991.
- [95] J. Orloff, L.W. Swanson, and M. Utlaut. Fundamental limits to imaging resolution for focused ion beams. *J. Vac. Sci. Technol. B*, 14(6):3759, Nov/Dec 1996.
- [96] M. H. F. Overwijk, F. C. van den Heuvel, and C. W. T. Bulle-Lieuwma. Novel scheme for the preparation of transmission electron microscope specimens with a focused ion beam. *J. Vac. Sci. Technol.*, 11(6):2021, Nov/Dec 1993.
- [97] J. R. Pierce. Rectilinear electron flow in beams. *J. Appl. Phys.*, 11:548, 1940.
- [98] M. Porkolab, V. Aranasalam, and R. A. Ellis. Parametric instability and

- anomalous heating due to electromagnetic waves in plasma. *Phys. Rev. Lett.*, 29:1438, 1972.
- [99] R. K. Porteous and R. W. Boswell. Equilibrium in an rf generated magnetoplasma. *Australian Institute of Nuclear Science and Engineering 15th AINSE Plasma Physics Conference*, page 33, Feb 1985.
- [100] D. E. Radley. The theory of the pierce type electron gun. *J. Electron. Control*, 4:125, 1957.
- [101] D. Rapp and W. E. Francis. Charge exchange between gaseous ions and atoms. *J. Chem. Phys.*, 3(7):2631, 1962.
- [102] W. L. Rautenbach. Experimental verification of the space charge law  $i = k(e/m)^{\frac{1}{2}}v^{\frac{1}{2}}$  for ion beams from a plasma ion source. *Nucl. Instr and Meth.*, 12:169, Feb 1961.
- [103] H. Z. Sar-El, I. Chavet, and M. Kanter. Shape of pierce electrodes for divergent wedge-shaped beams. *Nuclear Instruments and Methods III*, page 613, 1973.
- [104] G. Schmidt. *The Physics of High Temperature Plasmas*. Academic Press, 2nd ed. edition, 1979.
- [105] E. E. Scime, R. Murphy, G. I. Ganguli, and E. Edlund. Electrostatic ion-cyclotron waves in a currentless, anisotropic plasma with inhomogeneous flow. *Phys. Plasmas*, 10(12):4609, Dec. 2003.
- [106] L. Scipioni, D. Stewart, D. Ferranti, and A. Saxonis. Performance of multicusp plasma ion source for focused ion beam applications. *J. Vac. Sci. Technol. B*, 18(6):3194, Nov/Dec 2000.
- [107] SEMATECH. International technology roadmap for semiconductors - lithography. Technical report, SEMATECH, 2003.

- [108] T. T. Sheng, G. P. Goh, C. H. Tung, and L. F. Wang. Precision transmission electron microscopy sample preparation using a focused ion beam by extraction method. *J. Vac. Sci. Technol. B*, 15(3):610, May/June 1997.
- [109] T. Shoji, Y. Sakawa, S. Nakazawa, K. Kadota, and T. Sato. *Plasma Sources Sci. Technol.*, 1993.
- [110] R. S. Spangler, E. E. Scime, and G. I. Ganguli. Parallel inhomogeneous flows in a thermally anisotropic plasma: the electrostatic ion-acoustic branch. *Phys. Plasmas*, 9(6):2526, 2002.
- [111] M. Steinberg, B. Yap, and H. H. Fleischmann. A low-current low-energy-spread duoplasmatron ion source. *Rev. Sci. Instrum.*, 42(3), 1971.
- [112] G. Stengl, H. Loeschner, W. Maurer, and P. Wolf. Ion projection lithography machine IPLM-01: A new tool for sub-0.5-micron modification of materials. (1):194, 1986.
- [113] T. H. Stix. *Waves in Plasmas*. American Institute of Physics, New York, 1992.
- [114] M. Sugawara. Electron probe current in a magnetised plasma. *Phys. Fluids*, 9(4):797, 1966.
- [115] O. Sutherland, J. Keller, M. Irzyk, and R. Boswell. A comparison between experiment and two simulation strategies for the extraction of focused ion beams. *Rev. Sci. Instrum.*, 75(6):2379, 2004.
- [116] L. W. Swanson and J. Z. Li. The influence of electrode geometry on liquid metal ion source performance. *J. Vac. Sci. Technol. B*, 6(4):1062, Jul/Aug 1988.

- [117] L. W. Swanson, G. A. Schwind, and A. E. Bell. Measurement of the energy distribution of a gallium liquid metal ion source. *J. Appl. Phys.*, 51(7):3453, 1980.
- [118] A. A. Talin, G. F. Cardinale, T. I. Wallow, P. Dentinger, S. Pathak, D. Chinn, and D. R. Folk. Extreme ultraviolet lithography based nanofabrication using a bilevel photoresist. 22(2):781, mar/Apr 2004.
- [119] G. I. Taylor. *Proc. R. Soc. London*, A280:383, 1964.
- [120] S. Tsuboi, Y. Tanaka, H. Sumitani, and Y. Nakayama. Recent progress in 1x x-ray mask technology: feasibility study using ASET-NIST format TaXN x-ray masks with 100 nm rule 4 Gbit dynamic random access memory test patterns. *J. Vac. Sci. Technol. B*, 19(6):2416, Nov/Dec 2001.
- [121] J. P. Verboncoeur, M. V. Alves, V. Vahedi, and C. K. Birdsall. Simultaneous potential and circuit solution for 1D bounded plasma particle simulation codes. *J. Comp. Physics*, 104:321, 1993.
- [122] V. F. Virko, G. S. Kirichenko, and K. P. Shamrai. *Plasma Sources Sci. Technol.*, 12:217, 2003.
- [123] K. Volk, M. Sarstedt, H. Klein, and A. Schempp. Energy spectra of ions and electrons of a duoplasmatron. *Rev. Sci. Instrum.*, 61(1), 1990.
- [124] von Ardenne. *Tabellan der Elektronenphysik und Übermikroskopie*, 1963.
- [125] A. Wagner, P. Longo, S. Cohen, and P. Blauner. Focused ion beam metrology. *J. Vac. Sci. Technol. B*, 13(6):2629, Nov/Dec 1995.
- [126] Z. Wang, T. Kato, T. Hirayama, K. Sasaki, H. Saka, and N. Kato. Focused-ion-beam preparation of wedge-shaped cross sections and its application to

- observing p-n junctions by electron holography. *J. Vac. Sci. Technol. B*, 21(5):2155, Sept/Oct 2003.
- [127] J. R. Woodworth, M. E. Riley, D. C. Meister, B. P. Aragon, M. S. Le, and H. H. Sawin. Ion energy and angular distributions in inductively coupled radio frequency discharges in argon. *J. Appl. Phys.*, 80(3):1304, 1996.
- [128] A. Yamaguchi and T. Nishikawa. Low-damage specimen preparation technique for transmission electron microscopy using iodine gas-assisted focused ion beam milling. *J. Vac. Sci. Technol. B*, 13(3):962, May/June 1995.
- [129] A. Yamaguchi, M. Shibata, and T. Hashinaga. Transmission electron microscopy specimen preparation technique using focused ion beam fabrication: application to GaAs metal-semiconductor field effect transistors. *J. Vac. Sci. Technol.*, 11(6):2016, Nov/Dec 1993.
- [130] P. Zhu and R. W. Boswell. Observation of nonthermal electron tails in an rf excited argon magnetoplasma. *Phys. Fluids B*, 3(4):1991, April 1991.